THE PHYSICS OF HIGH-DENSITY, HIGH-β REVERSED-FIELD PINCH PLASMAS

by

Max D. Wyman

A thesis submitted in partial fulfillment of the

requirements for the degree of

Doctor of Philosophy

(Physics)

at the

UNIVERSITY OF WISCONSIN–MADISON

2007

The Physics of High-Density, High-β Reversed-Field Pinch Plasmas

Max David Wyman

Under the supervision of Dr. Brett Chapman and Professor Stewart Prager

At the University of Wisconsin-Madison

Abstract

The use of pellet injection to achieve high-density, high-β discharges in the Madison Symmetric Torus has been investigated. The physics goals motivating this work are split into two primary and two secondary thrusts. The primary goals are the use of pellet-fueling in conjunction with improved confinement plasmas to attain higher plasma beta and to investigate the consequences for stability at the higher β. The secondary research thrusts are to compare pellet-fueling of standard RFP discharges to edge-fueled plasmas and to begin the search for a density limit in MST.

Following are the results of the primary and secondary goals. Pellet injection has been used to increase the density in improved confinement discharges fourfold while maintaining low magnetic fluctuations, and data suggest that even higher density is possible. A record plasma beta has been achieved for the improved confinement RFP in the process. A portion of the beta increase is attributed to a rising ion temperature (not seen in low density improved confinement) caused in part by the improved thermal coupling between electrons and ions. At this high beta, a new regime for instabilities is accessed. Both local interchange and global tearing instabilities are calculated to be linearly unstable. The tearing instability, normally driven by the current gradient, is driven by the pressure gradient in this case and appears to be the cause of a soft-β limit. This β-limit occurs as a reduction in the energy confinement time in moving to high beta during improved

confinement plasmas. In standard (non-improved) confinement discharges, pellet fueling can peak the density profile where edge fueling cannot. The core-fueling of pellet injection alters the nature of the MHD activity in a standard discharge, but confinement appears unchanged from an edge-fueled discharge. For a limited range of plasma currents, MST discharges with edge fueling are constrained to a maximum density corresponding to the Greenwald limit. This limit is surpassed in pellet-fueled improved confinement discharges.

Acknowledgments

Graduate school has truly been the snooze bar on the alarm clock of life. Having hit that bar for the past seven years, its hard to believe it's time to get up and act like an adult. I can't imagine that I would have had all the fun times and met all the great people in my stay here in Madison had I entered the workforce back at the turn of the century.

I've been dissuaded from writing the whole of the thesis in meter but not the acknowledgments. To those who've played a role in my graduate student career, I present haikus:

Brett Chapman and Stewart Prager:

Conned into pellets.
Maybe I learned a lot, but
I hold you to blame

Steve Combs and Charlie Foust:

Up from Tennesee
You guys brought the injector
I blame you as well

MST Staff:

I'm too lazy to
write each one a haiku but
thanks for your patience.

Boulders routesetters/staff:

Clay and plastic holds
comprise the routes you create
Non-plasma problems

Mr. Daniels:

Your grand elixir
Ingested at each day's end
Washed away the pain

Will, Zeke, Morgan + John:

Can't promise a beer
When we meet again but I
Can promise whiskey

Mom + Dad:

I'm done... finally
One day I will come over
solely to do chores.

Jess:

My partner in crime,
You made the trip... even more
May it continue

Lastly, I'd like to thank Agent Jack Bauer of the Counter-Terrorist Unit. You've kept our country safe from evil-doers, allowing me to enjoy the American way of life as I worked towards my doctorate. Thank you, good sir. You deserve more than a haiku, perhaps a series of rhyming couplets or even a limerick. if only there had been more time.

In memory of

Duane Richard Wyman

(August 26, 2005)

Contents

List of Tables

List of Figures

What's a pirate's preferred method of magnetically confining a plasma?

The Arrr-FP

Unknown

1 Introduction

1.1 Motivation

The primary foci of this thesis have been the achievement of high density, high plasma beta discharges with improved confinement and the investigation of the consequences for plasma stability due to the high β. To achieve the necessary plasma pressure, the technique of pellet injection was employed. This led to two secondary research thrusts: comparison of the pellet fueling and edge gas puffing techniques and investigation of the applicability of the Greenwald density limit scaling to the reversed field pinch (RFP).

The RFP's highest confinement plasmas have been achieved by reducing current driven instabilities through an inductive current profile control technique. These high confinement plasmas have also had high plasma beta, but not so high as to surpass any beta limits. At higher beta, the pressure should start to drive instabilities, both local (interchange) and global (tearing). As will be shown, injection of pellets in combination with the current profile control technique leads to the highest beta observed in the improved

confinement RFP. At this beta, both interchange and pressure-driven tearing modes are calculated to be linearly unstable, but a disruptive beta limit is not observed.

In developing the pellet injection technique for use on the Madison Symmetric Torus (MST), experimental comparisons to edge fueling techniques were undertaken. As expected, pellet fueling can lead to peaked density profiles compared to the hollow profiles that are the result of edge fueling to similar line-averaged densities.

Implementation of pellet injection and modification of the edge fueling system has allowed for the achievement of densities near the Greenwald density limit. In tokamaks, this limit on achievable density only applies to edge fueled discharges, i.e., with the application of pellet injection, it can be surpassed. For a limited range of plasma currents in MST, density limiting behavior near the limit was observed but its scaling with plasma current has yet to be confirmed. Pellet fueling of improved confinement discharges has led to sustained densities above this limit but thus far only at low plasma currents ($I_\phi \sim 0.2\ MA$).

This chapter will provide a foundation and overview of the thesis. An introduction to the RFP will be given followed by a brief description of the technique by which improved confinement is achieved. A brief history of pellet injection in tokamaks as well as the shorter history of pellet-fueled RFP experiments will be presented. Finally, the remainder of thesis will be outlined.

1.2 Confinement and β-limits in RFP

The RFP is one of many toroidal magnetic configurations being explored for the purpose of confining hot plasmas. The mainstay of such devices is the tokamak which has a large toroidal field and relatively weak poloidal field ($B_\phi >> B_\theta$). What separates the RFP

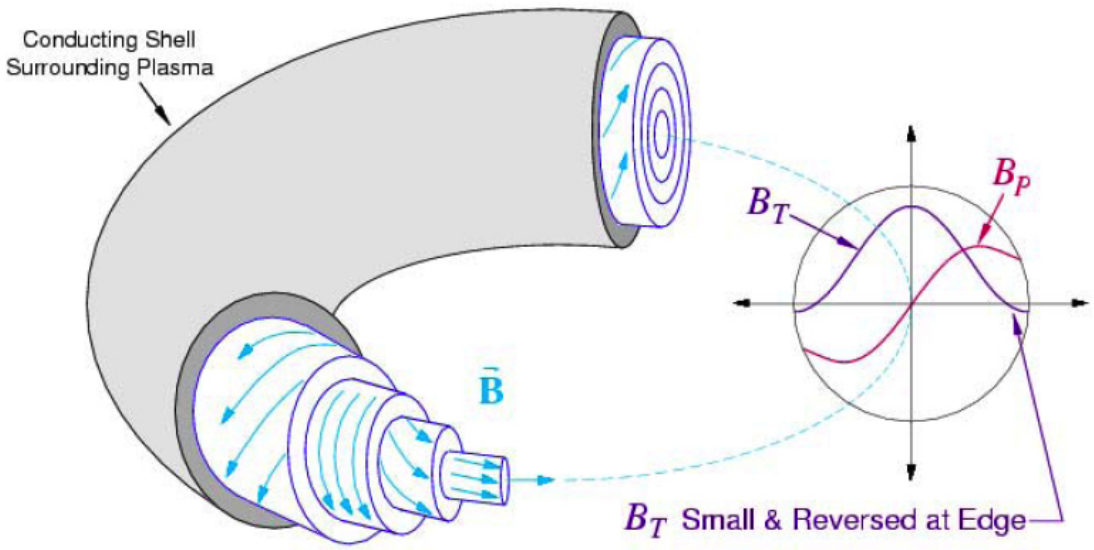

Figure 1.1: Magnetic Configuration of RFP.

from tokamaks is that for similar size and plasma current, $B_\phi^{tokamak} >> B_\phi^{RFP}$, and in the RFP, $B_\phi \sim B_\theta$ (shown in Fig. 1.1). Near the edge of the plasma, B_ϕ reverses, and the location of this change in direction is denoted as the reversal surface or reversal radius r_s. Toroidal field reversal is the product of a relaxation process wherein the plasma tends towards a minimum energy state [1]. The poloidal current necessary to sustain the field reversal is provided in part by a dynamo process [2] that draws on the unstable nature of the current profile. The profiles tend to be peaked, providing energy to drive m = 1 kink modes near the core, where m is the poloidal mode number. These modes nonlinearly drive fluctuations that produce an electromotive force. This additional electric field suppresses current in the core and drives current in the edge, simultaneously reducing current peaking and sustaining edge field reversal.

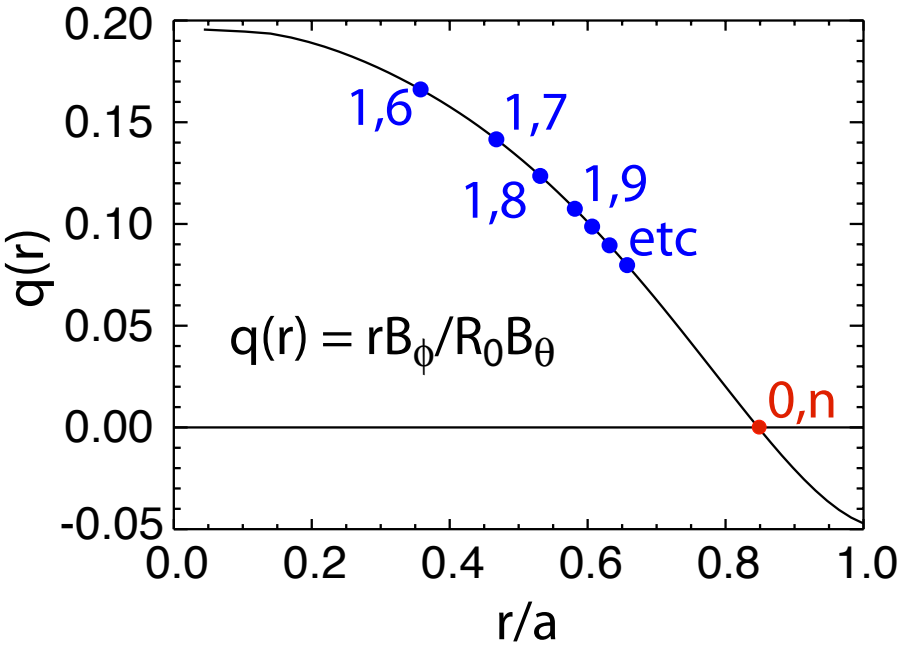

Figure 1.2: Safety Factor Profile in Standard Discharge

The high magnetic shear of the RFP makes confining a relatively high beta plasma possible, but the safety factor q (Figure 1.2) is less than unity everywhere and changes sign beyond the reversal surface, making a host of both m=0 and m=1 tearing instabilities internally resonant. The dominant tearing instabilities in the plasma core are driven primarily by a gradient in the plasma current and have poloidal mode number m = 1 and toroidal mode numbers $n \geq 2\frac{R}{a}$ [3] where R is the major radius, and a is the plasma minor radius. At the reversal surface, modes of the m = 0, n > 0 variety are resonant, and through an impulsive non-linear coupling process allow energy to flow between the edge-resonant and core-resonant modes, at which time these tearing instabilities manifest themselves as magnetic reconnection events ("sawteeth"). In this process the current and particle density profiles are flattened, and confinement of particles and energy is degraded.

These current-driven instabilities can be suppressed through an inductive current profile control technique referred to as pulsed parallel current drive (PPCD). Current is inductively driven in the edge, altering the current profile and reducing the free energy available to drive tearing instability. Application of the PPCD technique has led to improved confinement in several RFP devices [4, 5, 6] including MST [7].

The largest improvements in energy confinement and beta using PPCD, however, have been limited to relatively low density, $n_e \leq 10^{13}\ cm^{-3}$ [8, 9, 5, 6, 10, 11, 7, 12]. Above this density in the MST, edge resonant instability is triggered, thereby degrading the improved energy confinement. It is believed that this destabilization is due to an unfavorable change in the edge current or pressure profiles brought about by the additional flux of cold, neutral particles through the plasma edge needed to provide a larger plasma density. The only source of fuel for MST plasmas has been gas injection and wall-recycling. In these low density, ohmically heated plasmas, fluctuation reduction allows a rapid increase in the

electron temperature, but the ion temperature remains unchanged. One mechanism for heating ions is collisional energy transfer from the electrons, but the energy transfer time $\sim T_e^{\frac{3}{2}}/n_e$, where T_e is the electron temperature, is ten times longer than the PPCD pulse. The improvement in plasma beta has come about solely from an increase in the electron temperature.

Experiments on ZT-40M utilizing krypton gas injection indicated that energy confinement in standard RFP discharges was beta limited [13]. By varying the amount of krypton injected, the radiated power was varied from 15% to 95% of the ohmic input power. The poloidal beta was observed to remain constant ($\sim 12\%$) with respect to the changing radiated power fraction.

In previous PPCD experiments on MST, there was no sign of beta limiting behavior nor is any predicted in linear stability calculations. The poloidal beta in these experiments reached a maximum value of 18%. And as a matter of fact, these discharges are stable to both current and pressure driven instabilities. Stability to the former is due to the application of PPCD. Stability to the latter is due to the pressure gradient not being large enough to drive either global tearing or local interchange modes.

1.3 Pellet Injection

In magnetically confined fusion devices there is the problem, among other issues, of providing fuel to the hot core of what ideally would be a good "confiner" of energy and particles. Pellet injection, as has been thoroughly demonstrated on tokamaks, RFPs, and stellarators, can fuel the core with minimal energy requirements compared to other methods of deep fueling *e.g.* neutral particle beams.

Pellet injection has been applied to the tokamak to a greater extent [14] than the RFP. Two particular areas of interest to this thesis are pellet-fueled improved confinement RFP plasmas, and exceeding density limits using pellet injection. In edge-fueled tokamak discharges a density limit has been observed [15]. The sustainment of densities beyond this limit has been achieved through pellet injection. Though density limit research on the RFP is sparse, preliminary data indicates that the RFP is subject to a similar limit [15]. Tokamak discharges, when pellet-fueled, observe an improvement in confinement if the density profile becomes peaked (the result of deeply penetrating pellets). The mechanism for improvement is generally attributed to a favorable change in MHD behavior caused by the pellet altering the current profile. This has not been shown in the RFP, however, as particle confinement times are of the same order as the pellet life times. In the RFP's standard operating regime, the quick relaxation of the plasma profiles precludes pellet injection from having the same long lasting beneficial effects on the confinement and stability of the plasma.

While the scope of pellet injection experiments on the RFP has been limited, these initial experiments have shown that the technique can be beneficial to RFP performance. Pellet injection in the RFP was first attempted in the ETA-BETA II experiment [16]. In these experiments, the tendency of the discharge to progress to high I/N, where I is the plasma current, and N is the line density, was arrested by pellet fueling. The poloidal beta β_θ, however, was modestly increased (to 9%) over non-pellet cases (6%) even though T_e was initially decreased. The increased beta, however, was not large enough to excite pressure driven instabilities.

In experiments on the ZT-40 machine at LANL [17], they observed strong pellet deflection for radially injected pellets and "massive" increases (up to 6-fold) in the line-averaged

density $<n_e>$ $(= \int n_e dl)$ without deleterious effects on the discharge. Strong on-axis peaking of n_e was not observed with radial injection as pellets were deflected in both the poloidal and toroidal directions [18]. The deflection was attributed to "rocketing" wherein a population of fast electrons asymmetrically heats the pellet and produces a comet-like tail that extends poloidally (in the edge) and toroidally (in the core) [19]. If two pellets were fired in close temporal proximity, the 2nd pellet was not deflected due to a reduction in the fast electron population after impacting the first pellet. Though large densities could be obtained through pellet fueling, the high densities could not be sustained due to poor confinement.

Both the RFX and TPE-RX experiments have engaged in cursory pellet fueled PPCD experiments. In TPE-RX, the electron density was increased to 1.5×10^{13} cm^{-3} through pellet injection before the application of PPCD and then sustained by the auxiliary current drive [20]. During pellet-fueled PPCD discharges, RFX observed a 50% increase in the energy confinement time [21]. Though these pellet fueled, improved confinement experiments have been limited, they do indicate that there's room for improvement.

The injection of pellets has also been used for diagnostic purposes in the tokamak with parallel developments occurring in the RFP community. In particular, impurity pellets have been used to measure the q-profile in tokamaks. This is accomplished by measurement of the pellet cloud elongation where field line pitch is determined by comparing the spread of the cloud in both the poloidal and toroidal directions, and has been used on TFTR [22], TEXT [23], ASDEX-U [24], and Alcator C-Mod [25]. A similar method has been used at RFX [26]. To characterize the dynamo process in the RFP, experiments at RFX used the deflection of a hydrogen pellet to determine the electron distribution function [27]. One requirement for all these diagnostic uses of pellets is a good tracking

system of the pellet, either to measure its trajectory or the elongation of the ablation cloud. For the RFX dynamo experiment it was also necessary to have an accurate model of pellet ablation.

1.4 Thesis Overview

This thesis has four specific thrusts: use of pellet-fueling in conjunction with improved confinement plasmas to attain higher plasma beta; investigation of the consequences of high beta for stability; pellet-fueling of standard RFP discharges with comparison to edge-fueled plasmas; and searching for a density limit in MST. In Chapter 2, the techniques of pellet and gas injection will be discussed. Also included in Chapter 2 are detailed descriptions of MST, PPCD, and the diagnostics used in this thesis, along with notes on the (not-so-beneficial) effects of pellet-fueling on several of these systems. A comparison of the two fueling techniques applied to standard discharges will be the subject of Chapter 3. Chapter 4 will cover attempts to identify density limiting behavior in MST and determine the applicability of the Greenwald density limit to MST operation. The application of pellet fueling to increase the plasma beta of MST's improved confinement plasmas will be discussed in Chapter 5. Chapter 6 contains a discussion of the consequences of this higher pressure on plasma stability. Conclusions from the research presented will be the subject of Chapter 7. Also included are several appendices which should prove useful for future Pelleteers and Puffers, and will focus on the maintenance, testing, and use of both the pellet injector (Appendix A) and gas puffing (Appendix B) systems.

Bibliography

[1] J. B. Taylor, Rev. Mod. Phys. **58**, 741 (1986).

[2] S. Ortolani and D. D. Schnack, *Magnetohydrodynamics of Plasma Relaxation* (World Scientific, 1993).

[3] H. Bodin and A. Newton, Nuc. Fusion **20**, 1255 (1980).

[4] R. Bartiromo *et al.*, Phys. Rev. Lett. **82**, 1462 (1999).

[5] Y. Yagi *et al.*, Plasma Phys. Control. Fusion **44**, 335 (2002).

[6] M. Cecconello *et al.*, Plasma Phys. Control. Fusion **46**, 145 (2004).

[7] J. S. Sarff, N. E. Lanier, S. C. Prager, and M. R. Stoneking, Phys. Rev. Lett. **78**, 62 (1997).

[8] B. E. Chapman *et al.*, Phys. Rev. Lett. **87**, 205001 (2001).

[9] B. E. Chapman *et al.*, Phys. Plasmas **9**, 2061 (2002).

[10] J. S. Sarff, S. A. Hokin, H. Ji, S. C. Prager, and C. R. Sovinec, Phys. Rev. Lett. **72**, 3670 (1994).

[11] J. S. Sarff *et al.*, Phys. Plasmas **2**, 2440 (1995).

[12] M. R. Stoneking, N. E. Lanier, S. C. Prager, J. S. Sarff, and D. Sinitsyn, Phys. Plasmas **4**, 1632 (1997).

[13] M. Pickrell *et al.*, in *Controlled Fusion and Plasma Heating (Proc. 16th Eur. Conf. Venice, 1989)* Vol. 13B, pp. 749–752, European Physical Society, 1989.

[14] S. Milora, W. Houlberg, L. Lengyel, and V. Mertens, Nuc. Fusion **35**, 657 (1995).

[15] M. Greenwald, Plasma Physics and Controlled Fusion **44**, R27 (2002).

[16] V. Antoni *et al.*, in *Plasma Physics and Controlled Nuc. Fus. Res., 1986* Vol. 2, p. 441, 1987.

[17] R. G. Watt, G. A. Wurden, P. G. Weber, K. Buchl, and E. K. Spanos, Rev. Sci. Instrum. **58**, 1401 (1987).

[18] G. A. Wurden *et al.*, Nuc. Fusion **27**, 857 (1987).

[19] G. Wurden *et al.*, in *Proceedings of IAEA Technical Committee Meeting, Gut lsing 1988*, p. 67, 1989.

[20] H. Koguchi *et al.*, Japanese Journal of Applied Physics **45**, L1124 (2006).

[21] R. Bartiromo *et al.*, Nuc. Fusion **39**, 1697 (1999).

[22] J. L. Terry *et al.*, Rev. Sci. Instrum. **61**, 2908 (1990).

[23] R. D. Durst, P. E. Phillips, and W. L. Rowan, Review of Scientific Instruments **59**, 1623 (1988).

[24] H. W. Muller *et al.*, Review of Scientific Instruments **68**, 4051 (1997).

[25] D. T. Garnier, *Lithium Pellet Injection Experiments on the Alcator C-Mod Tokamak*, PhD thesis, Massachusetts Institute of Technology, 1996.

[26] L. Garzotti, P. Innocente, S. Martini, A. Reggiori, and G. B. Daminelli, Rev. Sci. Instrum. **70**, 939 (1999).

[27] L. Garzotti, B. Pégourié, R. Bartiromo, P. Innocente, and S. Martini, Phys. Rev. Lett. **84**, 5532 (2000).

Just because something doesn't do what you planned it to do doesn't mean it's useless.

Thomas A. Edison

2

Experimental Setup

2.1 Introduction

The mainstay of MST fueling has been wall recycling and edge gas puffing. The mechanics of the MST gas puff system will be discussed along with the changes made in order to improve fueling output. The details of a newly added single high-throughput valve will be included in the discussion of the edge fueling system. The physical processes underlying wall-recycling are not well-known quantitatively, but a qualitative discussion will be presented. Recently, a pellet injector was added to the quiver of MST fueling. The design and layout of the injector will be described, and then the reader will be regaled with (truthful) tales of the formation and injection processes. Appendices A and B contain detailed descriptions of the operation and maintenance of the injector and puff valve systems. The latter portion of the chapter will be dedicated to describing both the diagnostics that were used in characterizing the discharges and problems that arise when using some of the diagnostics at higher plasma densities. First, the target of the pellets,

the Madison Symmetric Torus, will be discussed.

2.2 The Madison Symmetric Torus

The Madison Symmetric Torus [1] (MST) is an RFP with the distinction that its 5-cm-thick aluminum shell serves both as a vacuum vessel and a single turn toroidal field winding (see Fig. 2.1). A cut in the shell (at the inboard midplane) that extends toroidally (the toroidal gap) around the vessel allows current to be driven poloidally in the shell producing the initial toroidal field (see Fig. 2.2). A cut at 0° toroidal and extending poloidally (the poloidal gap) around the vessel allows poloidal flux to enter from the B_θ transformer. The transformer induces current toroidally (along the seed field) with the plasma acting as the secondary. As the plasma current ramps up, image currents are induced on the shell. In order to reduce the field error at the poloidal gap, the toroidal path of the image currents must be complete. The continuity winding (also shown in Fig. 2.1) extends from one side of the poloidal gap, around the B_θ-transformer, and connects to the other side of the poloidal gap, completing the circuit and helping to reduce field errors at the poloidal gap.

The MST operates at plasma currents of $0.2 - 0.6$ MA and densities ranging from $0.4 - 4 \times 10^{13}\ cm^{-3}$. Plasma temperatures (both electron and ion) can reach up to 2 keV. Typical data from a standard MST discharge are shown in Fig. 2.3. Before the start of the discharge ($t < 0$), a toroidal field is produced as seen in the trace of the average toroidal field [Fig. 2.3(a)]. At $t = 0$, a voltage (V_ϕ) is induced across the poloidal gap [Fig. 2.3(b)] driving a current in the plasma [Fig. 2.3(c)]. Fluctuations of both velocity and magnetic field combine to produce a dynamo that reverses the edge toroidal field [Fig. 2.3(d)]. During sawtooth events toroidal flux is increased. As $\frac{d}{dt}B_\phi \propto V_\theta$, the surface

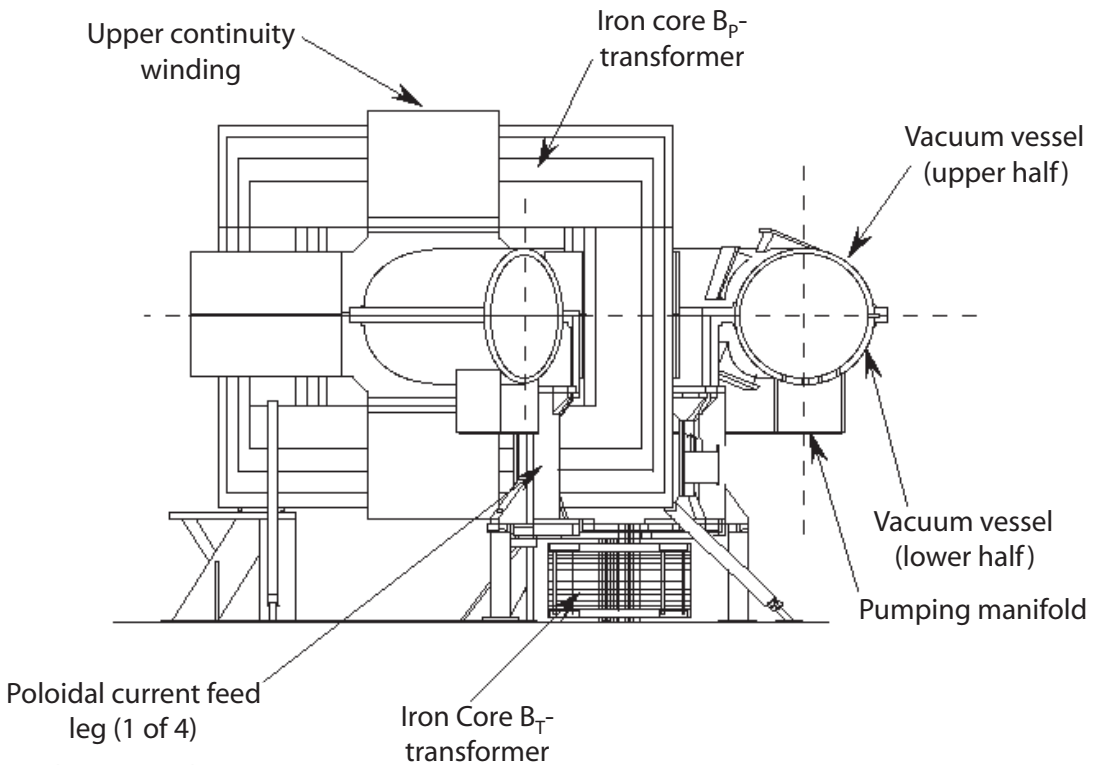

Figure 2.1: Side View of MST showing both poloidal and toroidal field circuits.

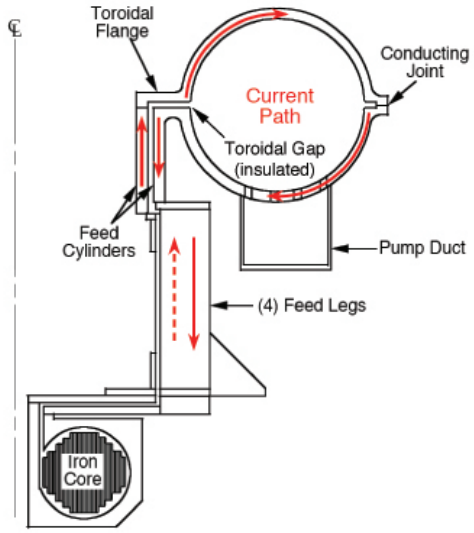

Figure 2.2: Vertical Cut of MST showing toroidal field circuit.

poloidal voltage (V_θ, measured across the toroidal gap) provides a measure of the magnetic fluctuation activity where the spikes correspond to sawteeth. Also shown in Fig. 2.3(g-h) are the reversal (F) and pinch (Θ) parameters which help to characterize RFP discharges, defined as

$$F = \frac{B_\phi(a)}{< B_\phi >} \tag{2.1}$$

and

$$\Theta = \frac{B_\theta(a)}{< B_\phi >} \tag{2.2}$$

with $< B_\phi >$ is the average toroidal field defined as $< B_\phi > = \int B_\phi dA / \int dA$.

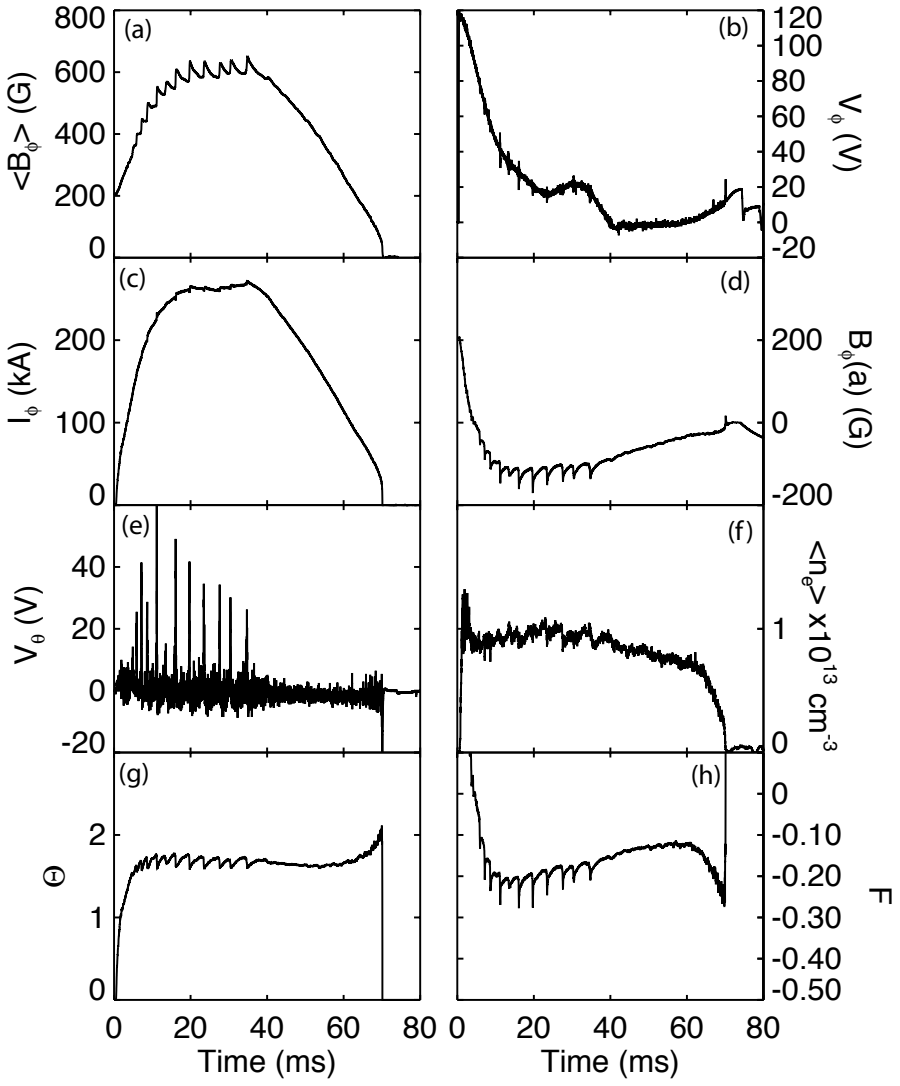

Figure 2.3: Operations signals during a standard MST discharge: (a) average toroidal magnetic field; (b) toroidal voltage measured at poloidal gap; (c) plasma current; (d) toroidal magnetic field measured at the wall; (e) poloidal voltage measured at toroidal gap; (f) line-averaged electron density as measured by CO_2 interferometer; (g) reversal parameter F; and (h) pinch parameter Θ.

2.3 Pulsed Parallel Current Drive

In its standard mode of operation (ohmically heated, self-relaxed), the ability of the reversed-field pinch (RFP) plasma to confine particles and energy is relatively poor. This is due to the fact that the internal magnetic field structure is largely stochastic, a result of the growth and spatial overlap of multiple internally resonant current driven tearing instabilities. One reliable means of reducing these instabilities and improving energy confinement is modification of the current profile via auxiliary inductive parallel current drive. In the MST, this technique is referred to as Pulsed Parallel Current Drive (PPCD - Figure 2.4) and has resulted in a ten-fold improvement in energy confinement and a doubling of plasma beta, the ratio of plasma pressure to the confining magnetic field pressure [2, 3]. This technique has also been successfully applied to other RFP experiments [4, 5, 6].

During PPCD, a voltage is applied across the toroidal gap. The resultant electric field drives current poloidally in the edge. The altered current profile has been calculated to be stable to current-driven tearing modes. The drop in tearing mode fluctuations leads to the improved confinement. In Figure 2.4 are typical operational signals from a PPCD discharge in MST. The startup phase is very similar to the standard discharge and begins with a seed toroidal field [Fig. 2.4(a)] and an applied toroidal voltage [Fig. 2.4(b)] driving toroidal current [Fig. 2.4(c)]. At $t = 10$ ms, however, an additional voltage is applied poloidally. Edge poloidal current is driven by the resultant edge parallel electric field $E_{||}$ in Fig. 2.4(g). As $E_{||}$ goes positive, the current profile is altered and fluctuations are reduced as seen in V_θ [Fig. 2.4(e)] during the period of improved confinement $t \sim 15 - 25$ ms. We also note the drop in the toroidal field at the wall as seen in Fig. 2.4(d). This technique is transient in that it "sucks" toroidal flux out of the machine [compare Figs. 2.3(a) and

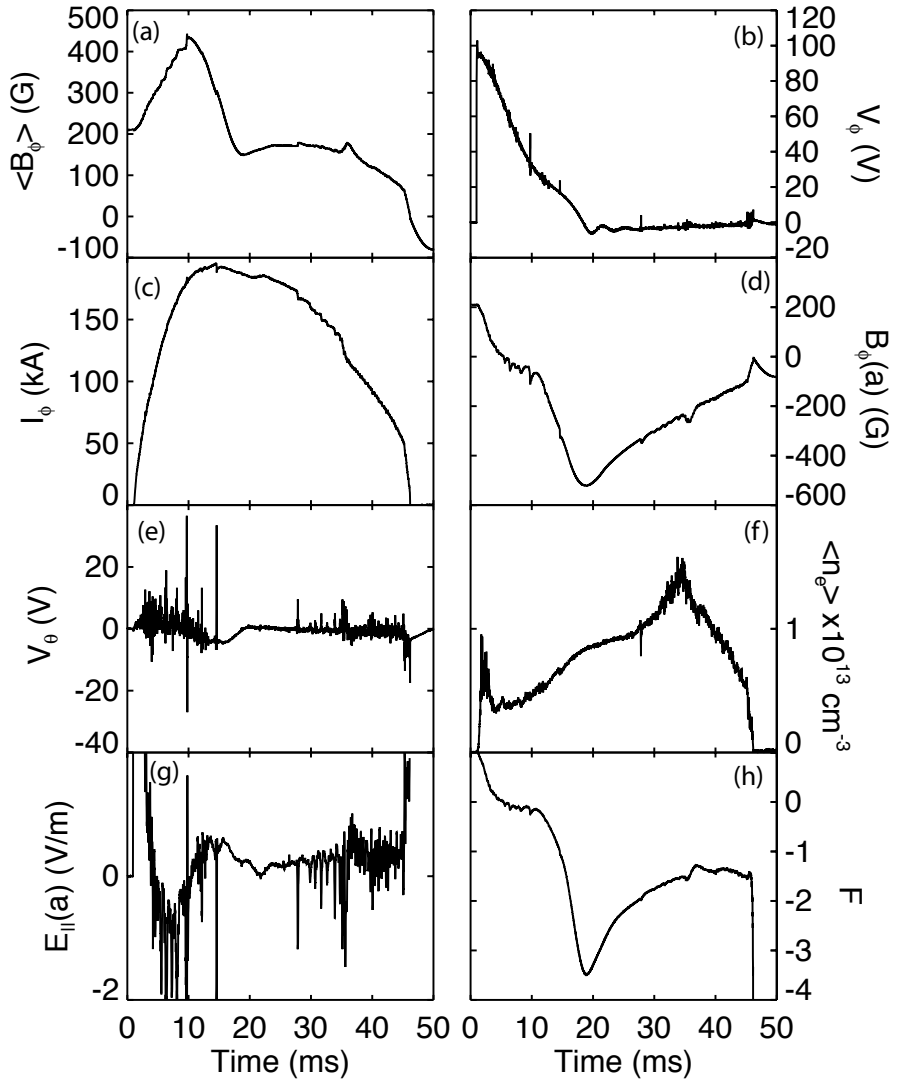

Figure 2.4: Operations signals during PPCD discharge: (a) average toroidal magnetic field; (b) toroidal voltage measured at poloidal gap; (c) plasma current; (d) toroidal magnetic field measured at the wall; (e) poloidal voltage measured at toroidal gap; (f) line-averaged electron density as measured by CO_2 interferometer; (g) parallel electric field at the wall; and (h) reversal parameter F.

2.4(a)]. If PPCD is applied long enough, the toroidal flux would completely reverse.

2.4 Fueling Methods

2.4.1 Wall Recycling

Fueling by the wall is referred to as wall recycling. Ten percent of the inner wall of the MST vacuum vessel is covered by graphite tiles that serve to protect the vacuum gaps and various diagnostics. The remainder of the plasma-facing wall is simply the inside of the vacuum vessel - aluminum. During a discharge, both deuterium and impurities are transported outwards and embedded in the wall. As power is lost to the wall of MST, any material embedded in it can be liberated ("recycled"). Deuterium and impurities can then re-enter the plasma through this process. Material can be stored in the walls between discharges and then recycled to be used as fuel in subsequent discharges. When running at lower densities, wall-recycling is relied upon more heavily as a source of fuel. To limit the fueling from wall-recycling, the walls must be "cleaned". This is accomplished through conditioning of MST which amounts to creating discharges at high current ($I_\phi \rightarrow 0.6\ MA$) with limited gas puffing. In this way, the plasma temperature is high, and the increased power to the walls removes much of the stored material which can then be pumped out following the discharge. Typically conditioning is only necessary following a vent of the vacuum vessel (when the machine is brought up to atmospheric pressure) or extensive probe runs (when material from probes can become embedded in the wall only to be recycled later as a source of impurities). As higher densities are reached, wall-recycling becomes less controllable i.e. fueling from the wall outpaces fueling from the gas puff system. Occasionally lots of fuel will be liberated from the walls, and the discharge

disrupts (more on this in Chapter 4).

2.4.2 Gas puffing

MST has nine puff valves - one for dopant, one for puffing helium during pulsed discharge cleaning (PDC), and seven for fueling RFP discharges with deuterium. One of the D_2 valves has been modified for larger throughput. The remaining six fueling valves are capable of providing multiple pre-programmed gas puffs. The fueling valves are all Veeco PV-10s as pictured in Fig. 2.5, and are spread toroidally about MST in order to provide even fueling. Use of the high throughput valve will be referred to as "single valve fueling," and use of the remaining six MST fueling valves will be referred to as "multi-valve fueling".

MST Fueling System

The six main fueling valves are actuated by one central controller which is programmed before a discharge. They provide both pre-fill before and active fueling during the discharge. Previously, the valves were actuated with 150 V pulses of length between 0.25 to 5 ms (adjustable in 0.25 ms increments). In order to increase the fueling capability of the system the amplitude was increased to 250 V. It was found that at 250 V, along with higher throughput (Fig. 2.6), there is finer control over the opening and closing of the valves. The computer control program was updated and now allows increments of 0.125 ms with the minimum pulse now being 0.125 ms. Valves have been tested with pulses up to 375 V. PV-10s have been pulsed up to 800 V [7], but the probability of inducing a valve failure increases. When one fails, it can either fail open or closed, neither route beneficial for consistent operation of MST, but the valve can be repaired. To repair damage, it must be removed from the fueling system and disassembled, and screws supporting the peizoelec-

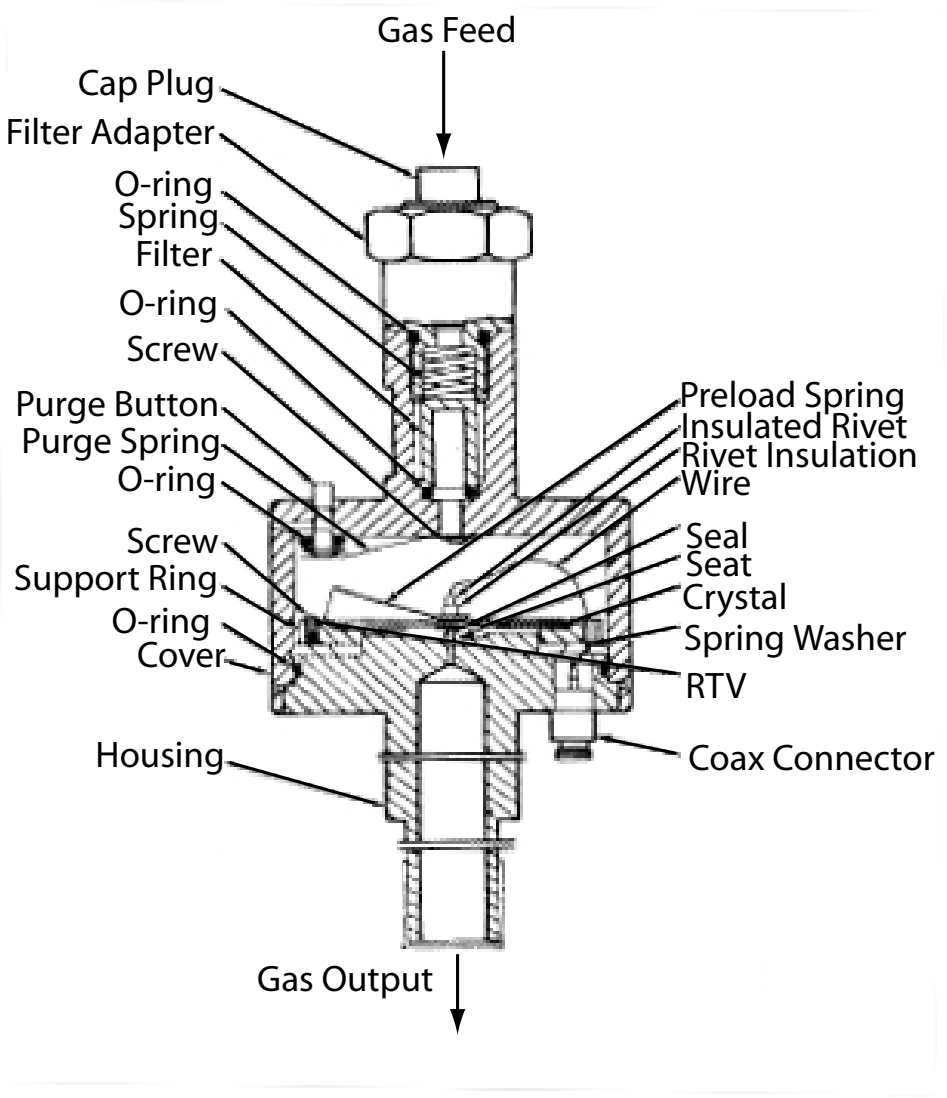

Figure 2.5: Cutaway of the Veeco PV-10 puff valve

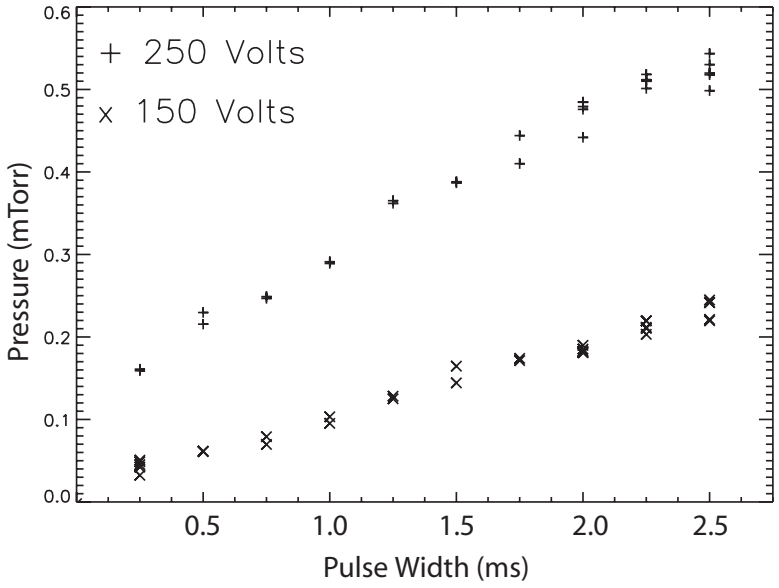

Figure 2.6: MST puff valve system output for differing pulsing voltages and pulse widths. The pressure is measured with a fast ion gauge with the output adjusted for D_2 and represents the equilibrium pressure in the MST vacuum vessel following the gas puffing.

tric crystal must be adjusted to regain proper sealing and opening characteristics (more details of Veeco PV-10 repair/adjustment are in Appendix B).

High Throughput Gas Valve

A single Veeco PV-10 has been modified for high throughput. Its throat has been drilled out to 0.042" (the standard valve has a throat diameter of 0.019"), and the valve is pulsed at higher voltage. It is actuated by a variable voltage power supply capable of providing pulses up to 400 V. In practice, a 350 V pulse of 10 ms duration is used. The flow characteristics (Fig. 2.7) of the modified valve and several standard valves were tested at different voltages (but with constant pulse width, 9.9 ms) using a variable power supply, test volume ($\sim$ 86 L), and convectron gauge. Its flow-voltage characteristics exceed that

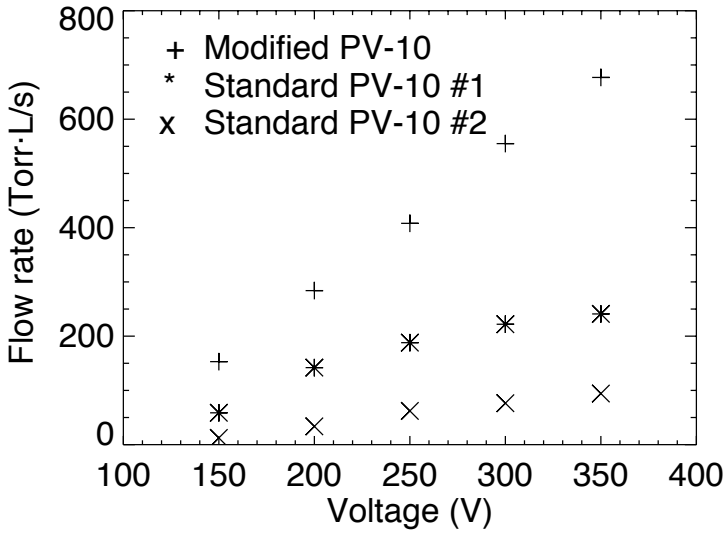

Figure 2.7: Comparison of flow rate response of the modified valve and two standard PV-10s when using deuterium gas.

of a standard PV-10, providing up to seven times the amount of gas.

2.4.3 Pellet Injection

MST has a prototype four barrel pellet injector [8] built in collaboration with Oak Ridge National Laboratory's Pellet Fueling Group. The support structure and surge tanks were recycled from a previous attempt at pellet injection on MST. The gunbox, injection line, and feed manifold were designed by ORNL. The remainder of the injector's development (pellet speed/size optimization, timing of pellet firing, etc.) occurred during MST experiments.

The pellet injector utilizes the "the pipe gun" formation technique with deuterium pellets formed directly in the barrel. The pellet diameter is restricted to that of the barrel being used (1.0 to 1.6 mm). Pellet length is controlled, albeit poorly, by the amount of feed gas let into the barrel. Nominal lengths can be varied from 1 to 4 mm. The speed

of the pellet is dependent on the method of acceleration: high pressure propellant gas, mechanical punch, or a combination of the two. The ideal pellet speed is that which carries the pellet to the core and allows it to fully ablate before reaching the far edge of the plasma. This ideal speed is dependent on both the pellet size and plasma parameters, most notably the electron temperature (and plasma current). Using propellant gas (H_2 at ~ 1100 *psi*), pellets attain speeds of 1200 m/s. Using only a mechanical punch, pellet speeds fall to 100 - 200 m/s but with the addition of propellant gas are sped up to 250-400 m/s.

In developing the injector for use on MST several problems arose, *e.g.*, non-optimal pellet deposition, high propellant gas flux, and irreproducibility of pellets. The last two issues have been solved with the use of close-coupled valves and the implementation of the "dry-fire" technique, respectively, and will be described later in greater detail. In some experiments, pellet deposition has not been optimal, which is to say that the pellets either don't penetrate deeply enough (fully ablated in the near edge) or cross the whole plasma striking the far wall of the vacuum vessel, resulting in what looks like a large localized gas puff. Optimizing the pellet's speed such that it ablates between the core and the far edge is an on-going task but inroads have been made (at minimum, several possible solutions have been ruled out).

Injector Layout

The layout of the pellet injector is depicted in Fig. 2.8. The pellets are injected radially, 30° above the horizontal mid-plane and are aimed at the plasma center. At the rear of the injector is the feed manifold, consisting of an array of computer controlled valves providing both the pellet feed gas (deuterium) and the propellant gas (hydrogen). The feed side of

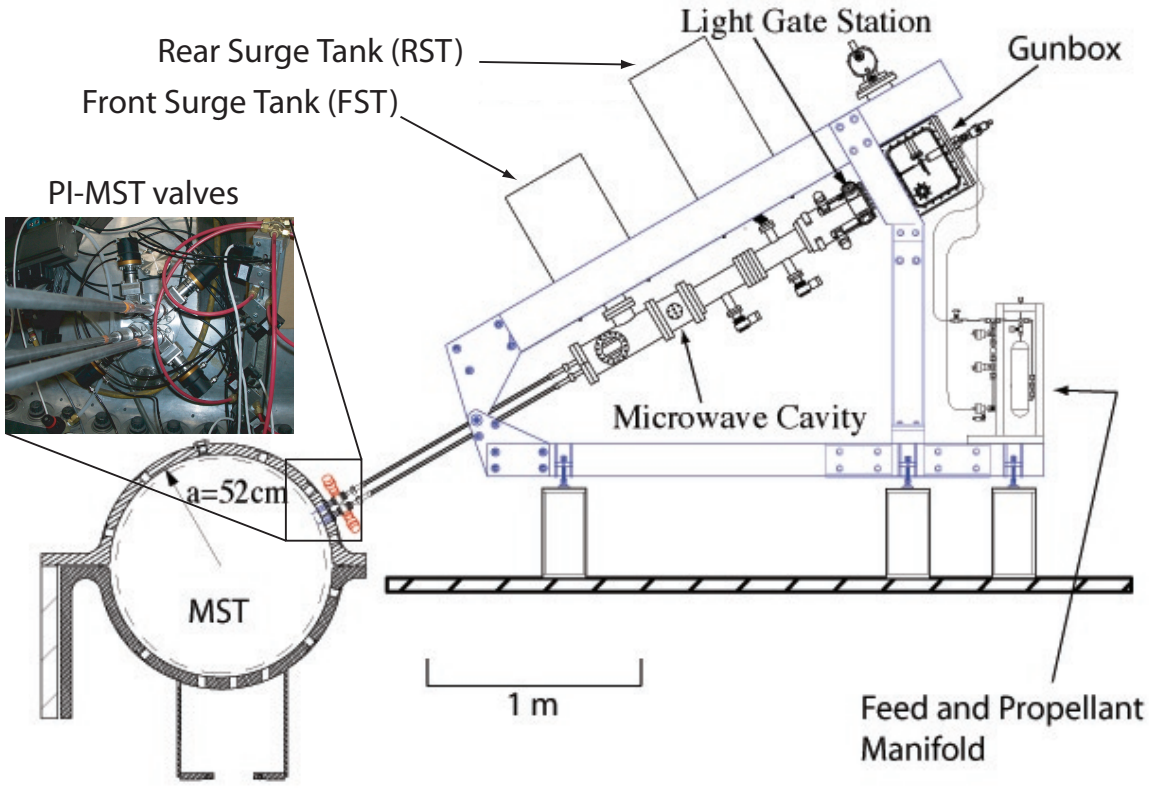

Figure 2.8: Pellet injector layout

the manifold is kept at 1-2 psi (∼80 Torr) while the propellant side is at 1100 *psi*. The manifold valves are controlled via a Labview program on a computer situated in the MST control room.

The manifold provides feed and propellant gas to the gunbox of the injector (shown in closeup in Fig. 2.9). During the formation phase both feed and propellant gas flow are controlled via slow valves in the manifold, but during the injection phase, fast-acting valves [9] at the gunbox control the flow of the propellant gas. The triple point for deuterium is 18.7 K, and in order to freeze pellets, the barrels are cooled to 10.5 K, typically. To accomplish this, each barrel is brazed to a copper disk that fits to the coldhead of the closed-loop cryogenic refrigerator. To decrease the conduction of heat to the barrels, the

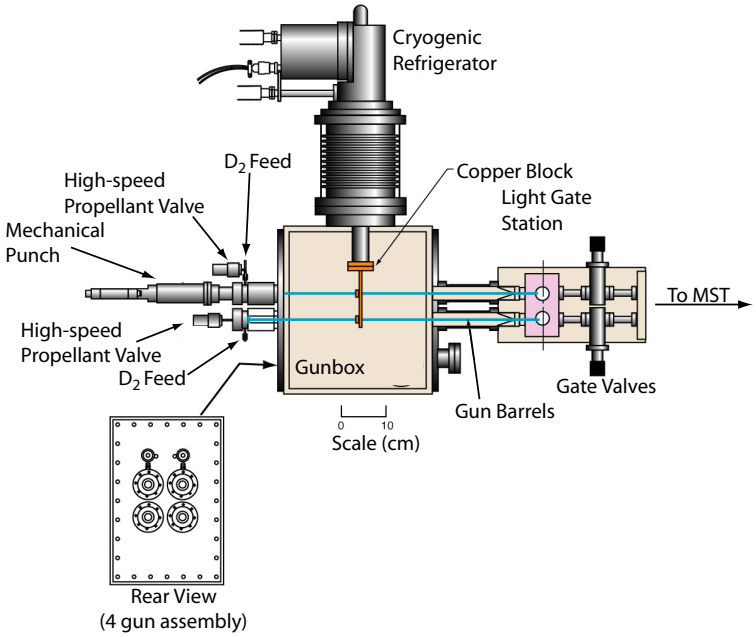

Figure 2.9: Gunbox layout

coldhead and its attachment to the barrels are kept in a vacuum vessel, i.e., the gunbox. The gunbox pressure is only monitored to ensure that it is below 1 mTorr.

Downstream and outside of the gunbox is the lightgate and photography station. Each barrel has an LED and photodiode in order to signal the pellet's passing as it breaks the LED's beam. Pellets can be photographed in flight as they leave the muzzle at the photography station (Fig. 2.10). Downstream of the photography station, each injection-line has a valve separating it from the rear surge tank.

The two large ($\sim$ 100 L) surge tanks provide ballast to limit gas throughput to the MST vacuum vessel. Each is pumped on by a turbomolecular pump and kept at base pressures of $< 10^{-6}$ Torr between injections. Between the two surge tanks the four injection lines pass through a single, toroidally-shaped microwave cavity. A microwave oscillator

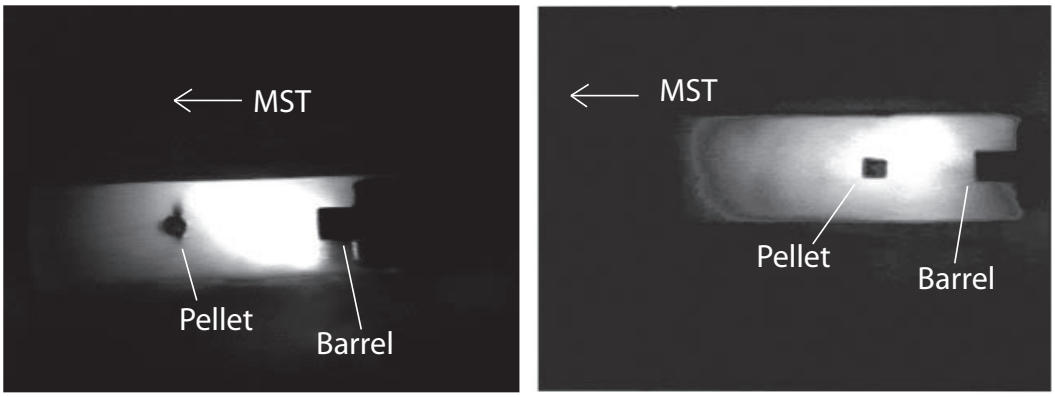

Figure 2.10: Pictures, taken at the light-gate station, of a fast (left) and a slow (right) pellet leaving the barrel and entering the injection line. The gunbox is to the right of the pellet (end of the barrel is visible) and MST is to the left. The blurry region around the fast pellet is "blowoff" from the propellant gas.

is connected to the cavity, and its operating frequency is chosen to be near the resonant frequency of the cavity. The cavity is located 93 cm downstream of the lightgate station and provides a relative measurement of pellet mass [10] far from the location of pellet formation and acceleration. As the pellet passes through the cavity, it serves as a small dielectric perturbing the resonant frequency of the cavity. The frequency of the oscillations is changed, and the shift in frequency is proportional to ratio of the pellet volume to the cavity volume. The frequency shift is observed as a voltage pulse which is used as a measure of the relative pellet mass (relative to other pellets) and also serves as a second time point for determining the pellet's speed (Figure 2.11).

Nearly 2.9 m from the point of the formation are valves (depicted in the inset of Fig. 2.8) separating the injection lines from the MST vacuum vessel. Even though the pressure in the front surge tank is equal to or lower than that of MST, the valves are kept closed until seconds before a plasma discharge. This is accomplished by having the valves' controllers linked to MST's own timing system (the PLC). To ensure that the MST

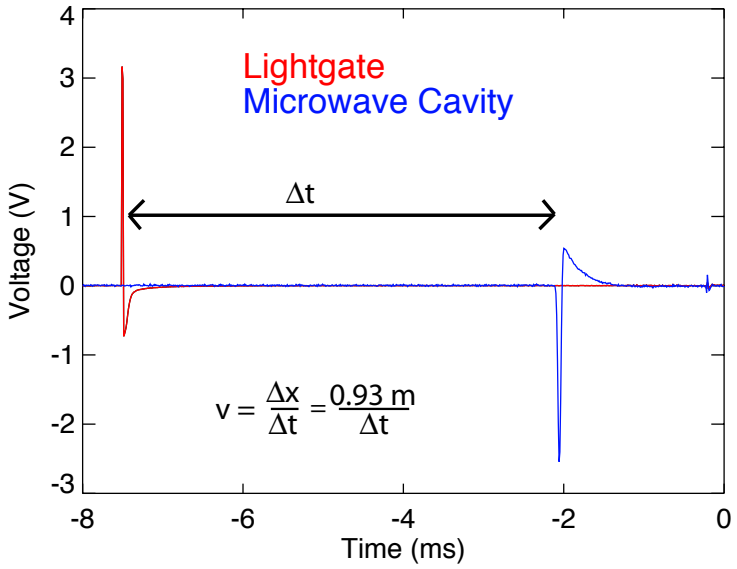

Figure 2.11: Pellet speed measurement where $\triangle x$ is the distance between the lightgate station and the microwave cavity. (Shot 1060224046)

vacuum is not exposed to a leak in the pellet system, the valves are interlocked to the pressure monitors on the injection lines. If the pressure in any of the surge tanks should surpass a preset value, the valves will not open. Following the discharge, these valves are closed again until the next pellet-fueled discharge.

Formation Phase

The formation process begins with the introduction of deuterium gas at a pressure of 80 Torr from the back of the gunbox. The pellet begins forming at the contact point of the barrel and coldhead as depicted in Fig. 2.12. At each contact point, there is a thermocouple for monitoring the freezing process. To ensure that solid pellets (instead of long hollow tubes of frozen deuterium, i.e., "lifesavers") are formed, braided copper heat shorts (not shown Fig. 2.9) connect the barrels to the wall of the gunbox. Shorts are

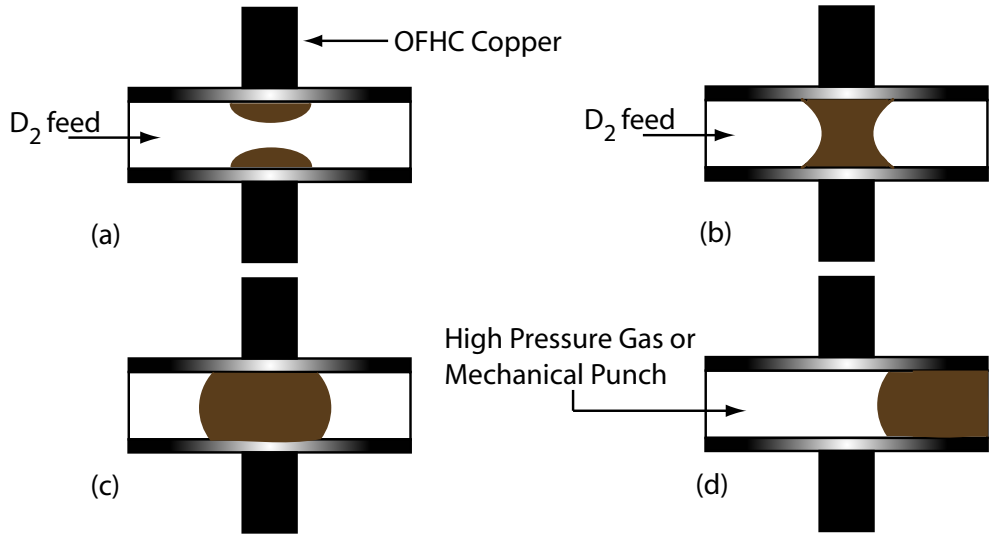

Figure 2.12: Pellet formation process: (a) Room temperature D_2 is introduced into the barrell, (b) as the freezing process continues, the center of the pellet is formed, (c) feed manifold is closed off from barrel and pellet sits in barrel until (d) when the pellet is accelerated with some combination of mechanical punch and high pressure propellant gas.

connected to the barrel both fore and aft of the brazed connection to the coldhead using cable ties. The use of cable ties as fasteners ensures that the proper placement of the heat shorts, which is critical to successful pellet formation, will remain more of an art than a science. Pellet size can be adjusted through one of two methods: (1) varying the amount of gas introduced; or (2) by adjusting the temperature gradient along the barrel with heat shorts. As the heat shorts are inaccessible during operation, the former method is used. Once the desired amount of gas has been introduced, the barrel is closed off from the feed system, and the pellet sits until fired.

Injection Phase

Pellets can be accelerated using either a mechanical punch, high pressure gas, or both. The mechanical punch consists of a stiff wire mounted on a solenoid. Actuation of the

solenoid pushes the wire down the barrel so that it breaks the pellet free of the barrel, imparting to it a velocity of 100-200 m/s. The addition of high pressure gas (∼1000 psi of H_2) will increase the speed to 250-400 m/s. The gas is added by pulsing the high speed valve several milliseconds after actuation of the punch. In this setup the valve is located off center of the barrel line (see upper gun in Fig. 2.9). For this technique, timing is everything: the impulse provided by the high pressure gas isn't enough to break the pellet free from the barrel due to the valve being located far from pellet formation. The pellet will be melted by the room temperature propellant gas if it has not been broken free by the punch.

The high speed valve can also be used alone as in the lower gun of Figure 2.9. In this instance, the sealing surface is placed within the gunbox, closer to the formation point of the pellet, so that the valve is in line with the barrel. This setup is referred to as "close-coupled." Earlier configurations had the sealing surface outside the gunbox, far from pellet formation (similar to the configuration of the valves on the punch barrels). Consequently, a larger impulse of propellant gas was required to break the pellet free causing the surge tanks to work harder, and the pressure in the MST vacuum vessel would rise to a small degree. Opening the close-coupled valve for 3-4 ms, the propellant gas provides enough impulse to break the pellet away and accelerate it to 1100-1200 m/s. The barrel extends for 37 cm past the point of formation, so that afterwards the pellet is effectively in free flight for the remaining 2.6 m to the plasma vessel. For gas propelled pellets this 37 cm is the length over which the pellet is accelerated.

The acceleration of a high speed pellet down the barrel is analogous to the motion of a piston in an infinite pipe with a vacuum on one side of the piston and gas at pressure p_0 on the other. The speed of the pellet as a function of time, neglecting nonideal effects

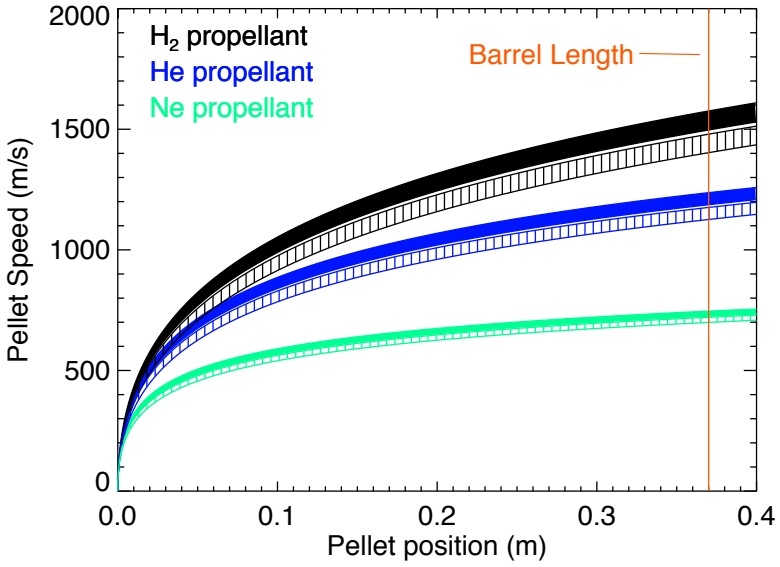

Figure 2.13: Pellet speed vs position in the barrel for three different propellant gases (hydrogen, helium, and neon) for different pellet sizes: 1.6 mm diameter by 3.2 mm length (solid) and 2.0 mm diameter by 4.0 mm length (line-filled).

(*e.g.*, friction and heat transfer) is then [11]:

$$U(t) = \frac{2C_0}{\gamma - 1}(1 - [1 + \frac{\gamma + 1}{2\rho l C_0} p_0 t]^{-\frac{\gamma-1}{\gamma+1}}), \tag{2.3}$$

where C_0 is the sound speed of the propellant gas, γ is the ratio of the specific heats, ρ is the mass density of the pellet, and l is the length of the pellet. Integrating Eq. (2.3) over time to get the pellet position $x(t)$, the velocity of a pellet at a given point in space is determined by plotting $U(t)$ against $x(t)$ (shown in Fig. 2.13). The calculation has been done for propellant pressures of 1000 to 1200 psi and two different pellet sizes: the 1.6 mm diameter already in use and 2.0 mm diameter to be installed for use in future high current experiments.

Along with propellant pressure and barrel length, the choice of the propellant gas is

Table 2.1: Pellet speeds (v), measurement error for pellet speeds ($\triangle v$) and estimated arrival times ($\triangle ETA$). Pellet A is accelerated by high pressure gas only. Pellets B and C are accelerated by mechanical punch only. The error is based on uncertainty in the measurement of the locations of the lightgate station and microwave cavity relative to the MST vacuum vessel.

	Pellet speed, v	$\triangle v$	$\triangle ETA$
A	1200 m/s	30 m/s	70 μs
B	200 m/s	2.5 m/s	0.25 ms
C	100 m/s	1.2 m/s	0.6 ms

another knob for controlling pellet speed. As Eq. (2.3) shows, the pellet speed is strongly dependent on the sound speed of the propellant gas, $C_0 = (\frac{\gamma k_b T}{m})^{\frac{1}{2}}$. Figure 2.13 depicts this variation in $U(x)$ for different mass gases. As nonideal effects have been neglected, the estimated speeds are overestimates. The barrels on the pellet injector are 37 cm in length, predicting velocities of 1500 m/s for the 1.6 mm pellets. In the lab, typical speeds are 1200 m/s with a variation of 50 m/s.

Table 2.1 summarizes the acceleration regimes for the injector. The error in speed ($\triangle v$) is determined by the error in the measurement of the time at which the pellet passes the lightgate and microwave cavity and the error in the length measurement between the two. Using the speeds and the speed measurement error, the error in the arrival time estimates ($\triangle ETA$) is determined.

For low current ($I_\phi < 0.3\ MA$) experiments, both 1.3 mm and 1.6 mm slow pellets can penetrate to the core (shown in Chapter 3) but as Figure 2.14 shows there is a variation in mass and speed of the pellets. As slow pellet velocities range from 100 to 200 m/s, the variation in arrival time is on the order of 10 ms (*much greater than* $\triangle ETA$). With the target window for injection having a duration $<$ 2 ms, the number of discharges with proper pellet timing is reduced. In low current experiments, 1.6 mm fast pellets are too

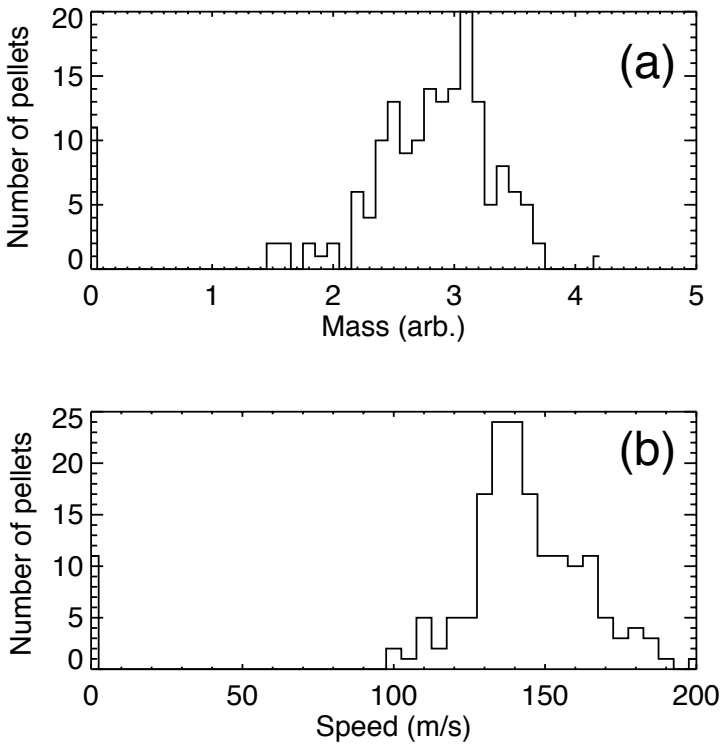

Figure 2.14: Histogram plot of 1.6 mm slow pellets showing the variability in mass (a) and speed (b)

fast, i.e., they cross the whole plasma usually impacting the far wall, resulting in a large gas puff. However, these fast pellets are the most reliable, with a variation in arrival times of $\sim 100\ \mu s$, which is comparable to their $\triangle ETA$.

The ideal situation is to somehow slow down the fast pellets. To this end, the propellant gas and pressure have been varied as well as the barrel length, but to no avail. One requirement of the propellant gas is that it have its triple point below or equivalent to that of the gas used for the pellets. If it were greater, the possibility of a frozen blockage forming in the barrel increases. To remove the blockage, the gunbox must be brought up to above the offending gas's freezing point, generally a lengthy process. Both helium and neon fit the requirement, but the fast valves had trouble opening so that not enough gas was available to break the pellet away.[1] Variation of the H_2 propellant pressure was also attempted. It was found that as the pressure was decreased, keeping $p_0 > 500$ psi, pellet breakaway became less predictable, and pellet speed fell to $\sim 900\ m/s$.

Two attempts were made at varying the barrel length using a "snub-nosed" barrel and a vented barrel (Fig. 2.15). For the former, the barrel was shortened to 5 cm, and the resulting pellets speeds were between 550 and 600 m/s. However, the number of pellets reaching the plasma dropped off precipitously. With the shorter barrel length, the pellet would tumble more, and the flight angle variability increased such that most of the time it did not make it into the injection line after the light-gate station. In the latter, drilled vents were placed in the barrel after ∼5 cm allowing propellant gas to escape but still providing a direct flight path to the injection line. Initial experiments showed pellet speeds between 500 and 600 m/s. The complexity of a barrel with the vents made it very fragile, and though initial experiments were promising, it proved unreliable in subsequent

[1]It should be noted that this was the first attempt to use a propellant gas other than hydrogen with these valves *i.e.* the valve's opening voltage characteristics aren't known for heavier gases.

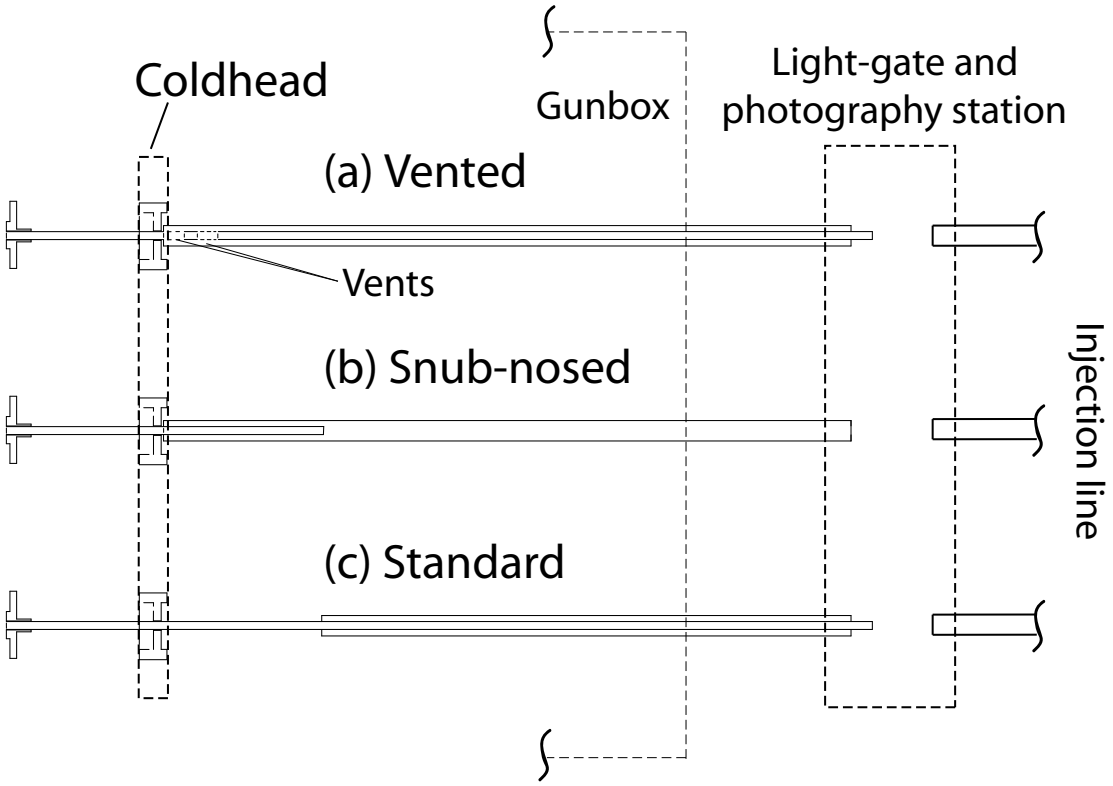

Figure 2.15: Diagrams of the 3 different barrel types: (a) vented, (b) snub-nosed, and (c) standard. Pellets are formed in the region of the coldhead with both feed and propellant gases entering from the left. Pellet are in free flight after leaving the barrel - at the light-gate station for barrels (a) and (c), and while still in the gunbox for barrel (b).

experiments[2]. Either the barrel was damaged during installation, or the vents themselves affected the pellet.

Using both propellant gas and the punch does not solve the situation, as this technique relies on the punch to break the pellet free from the barrel. While moderate increases in speed are seen, the combination of punch timing variability and warm H_2 gas makes melting of the pellets more likely so that the mass variability is greater. Without recourse for slowing down the fast pellets, low current experiments have resulted in campaigns with lots of "bad" shots, *i.e.*, pellet arrival times were not ideal, in order to get a handful of "good" shots.

Though the situation looks dire for low current, pellet-fueled experiments, it is an improvement over the experiments done during the injector's infancy. Until recently, slow pellet reliability was suspect at best with the punch not always breaking pellets free of the barrel. Fast pellet breakaway wasn't always assured either, but when they did break away, their speeds were consistent. It was found that if the experimenter launched a zero-mass pellet after a pellet-fueled discharge and before the next discharge, pellet breakaway was more consistent. This "dry-firing" of the injector consists simply of actuating the punch or high speed propellant valve between shots for the barrel in use with formation of a pellet.

2.5 Diagnostics

The characterization of pellet-fueled discharges, *e.g.* determining the normalized pressure, β, and the confinement times for particles and energy, has required the use of all major diagnostic systems on MST. The layout of the diagnostics, in both the toroidal and

[2]Discovery of the "dry-fire" technique may resurrect the vented barrel.

poloidal planes, is shown in Figures 2.16 and 2.17.

Electron density is measured both with a single chord CO_2 interferometer and a far-infrared (FIR) interferometer array [12]. The former yields the time evolution of the line-averaged density which can be viewed following each discharge. The latter also measures the line-averaged density along each of 11 chords. This data can be inverted to determine the radial profile evolution.

There are two methods for measuring electron temperature profiles in MST: Thomson-scattering (TS) [13] and soft-x-ray (SXR) tomography [14]. There are two methods for measuring ion temperature in MST, and both employ neutral beams [15]: Rutherford scattering (RS) and charge exchange recombination spectroscopy (CHERS). The bulk ion temperature evolution at r/a = 0.35 is measured using the Rutherford scattering system. Ion temperature profile evolution can be constructed using data from the CHERS system.

Internal measurements of the magnetic field (from which the current profiles can be calculated) are done using the FIR polarimeter [$B_\theta(r,t)$] [12] and motional Stark emission diagnostic or MSE [$B_\phi(r=0)$] [15]. The particle source rate is determined from D_α emission using the bremsstrahlung array. Colinear with the D_α detectors on a couple of chords are near infrared (1040 nm) detectors. The combination is used to determine Z_{eff}. The runaway electron population is determined from hard-x-ray measurements (another profile diagnostic) [16]. A CCD camera is used to characterize the trajectory of the pellet.

In the course pellet-fueling experiments, it was found that the high density inflicted on MST discharges had both beneficial and detrimental effects on diagnostics. Whether high density was advantageous or not, the diagnostics could be split into two categories: those that relied on transmission of a beam and those that relied on the scattering of a beam. The CHERS and FIR systems fall into the former, depending on transmission

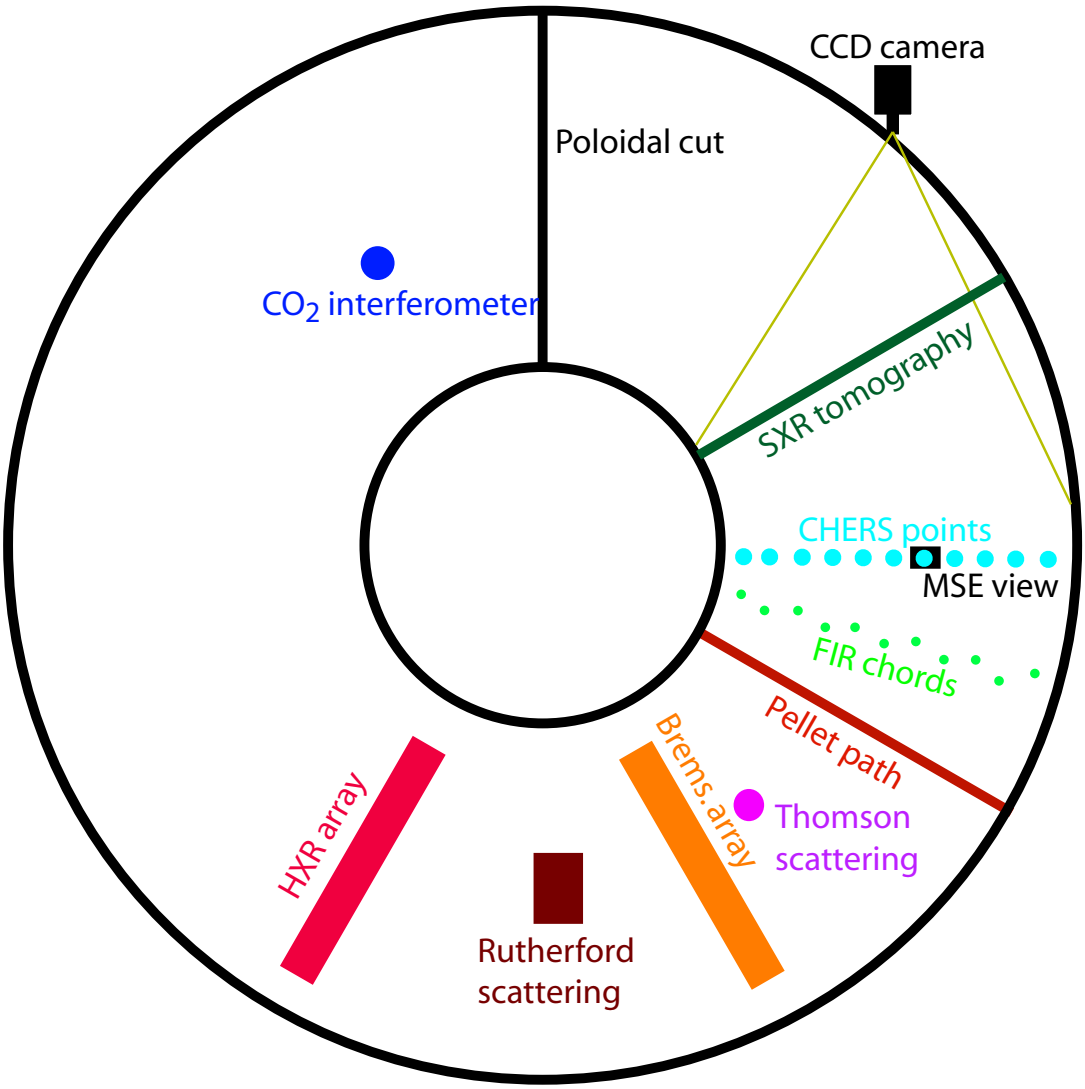

Figure 2.16: The pellet injector sits aside the FIR interferometer. The CCD camera has a good view of poloidal deflection of the pellet trajectory. Toroidal deflection is inferred. The CO_2 interferometer is far from the injector.

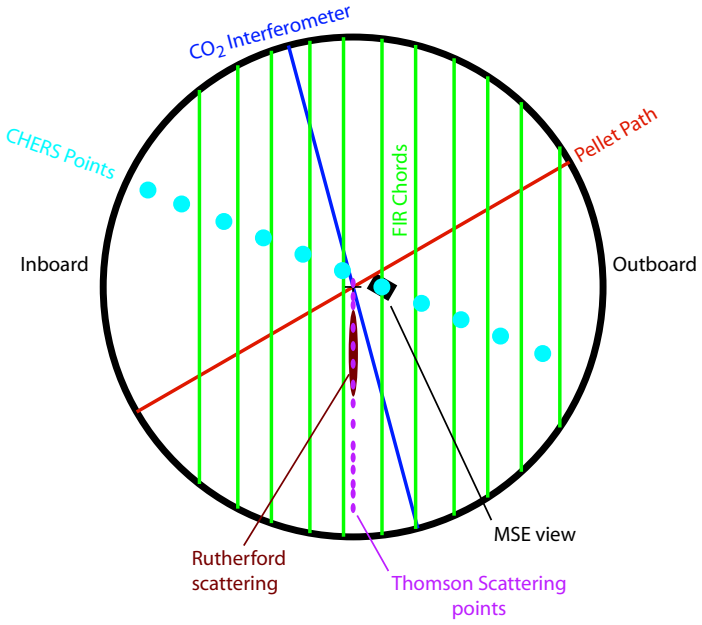

Figure 2.17: Poloidal cross section of diagnostic coverage

of a neutral beam and array of lasers, respectively, and as such, pellet fueling can have a malignant effect on the measurements. Into the latter group falls the Rutherford and Thomson systems. They, too, use a neutral beam and laser. Again, attenuation could be an issue, but due to the technique's dependence on the scattering of the beam, the two appear unaffected during higher density operation. Following is a discussion of the diagnostic systems and in some cases, the effect of pellet injection on the measurements.

2.5.1 Measuring the density profile

The FIR interferometer works by comparing the phase of a laser beam (of which there are 11, each at a different major radius) passing through the plasma to a reference beam that passes outside the plasma. To get an absolute density, this phase shift is compared to the

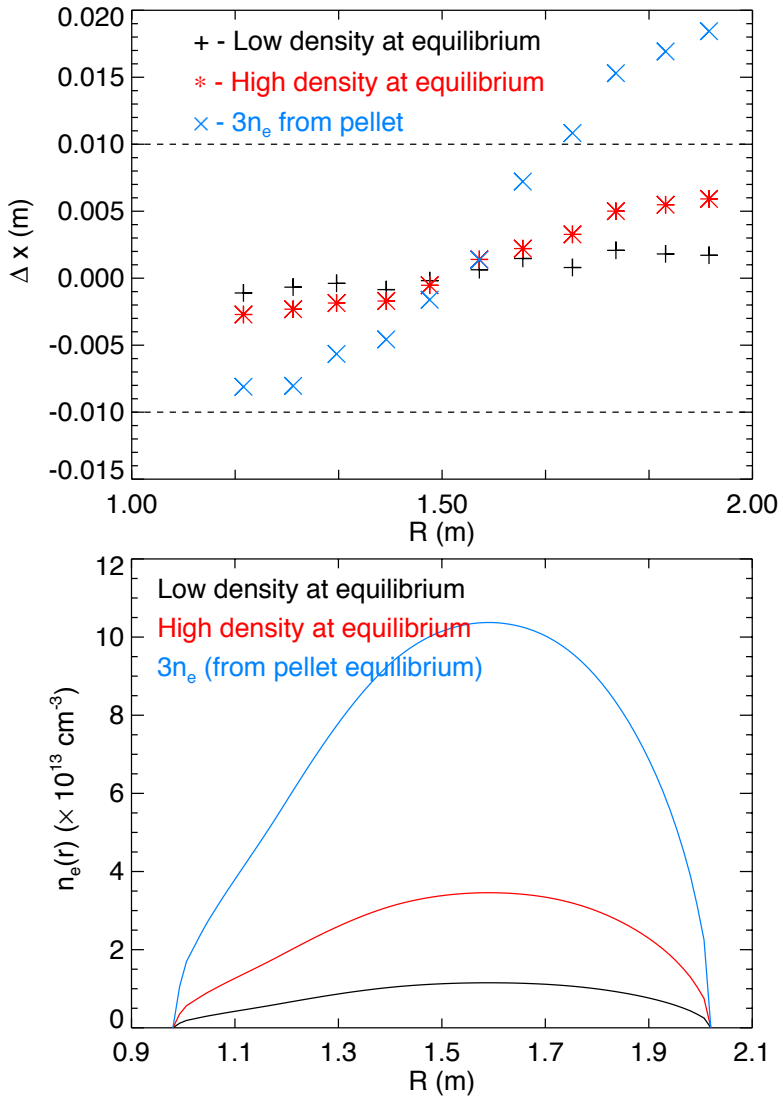

Figure 2.18: Calculated deflection ($\triangle x$) of FIR laser beams becomes stronger as the density (and density gradient) increases. Plotted (upper plot) are deflections of each chord for 3 cases: the low density case, high density pellet fueled case (long after ablation), and a higher density case (theoretical profile during the ablation period - though not necessarily an upper bound) along with the associated density profiles (lower plot). The dotted line on deflection plot represent the maximum deflection allowed before signal is lost.

initial (or final) shift before (or after) the discharge, when the beam passing through the plasma sees only vacuum. Of note is that the refractive index N in the plasma is related to the density by [17]:

$$N^2 = 1 - \frac{n_e}{n_c} \tag{2.4}$$

where n_c is the cut-off density (above which the beam will not propagate) and is simply the density corresponding to a plasma with an electron plasma frequency equal to the beam frequency. The FIR system uses lasers at a frequency of 694 GHz correlating to a cut-off density, $n_c = 6.0 \times 10^{15}\ cm^{-3}$. This however is not the limiting factor for the interferometry system nor is there any danger in broaching it in MST. The detectors and the portholes through which the beams pass are of limited size, so significant refraction of the beams can result in no signal. Deflections less than 1 cm can be tolerated [18].

While injecting similarly sized pellets, RFX (an RFP $\sim 10\%$ larger in volume than MST) was able to show local density increases near the pellet of $3-4\times10^{14}\ cm^{-3}$ [19]. In MST, the capability doesn't exist to make local measurements of pellet ablation, but the two sets of FIR interferometer chords are located at 10° and 15° toroidally away from the injection line (Fig. 2.16). Similar deposition in MST results in FIR beam refraction with displacements greater than the detector area (Fig. 2.18). Considering that the ablated material spreads toroidally and poloidally from the injection line, both clockwise and counterclockwise around MST, an upper bound on the density seen by the FIR can be estimated. The volume between the first set of chords and the injection line represents $\sim 5.6\%$ of the volume of MST. For the second set of chords it is $\sim 8.3\%$. As an upper bound then, the FIR "sees" between 12 and 18 times the equilibrium density or about $4-6\times10^{14}\ cm^{-3}$.

During a period of no signal it is possible to a have a phase change greater than 2π

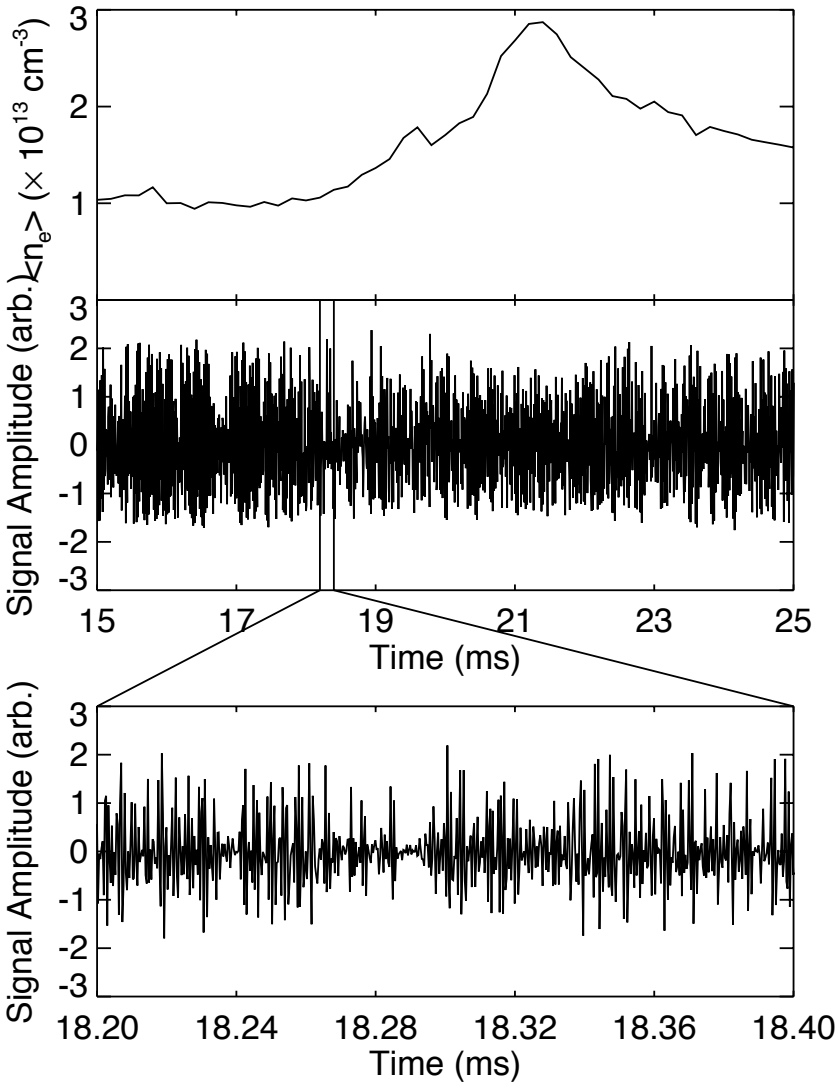

Figure 2.19: The deflection of the FIR lasers manifests itself as a drop in signal at the detectors. Plotted above are the (a) line-averaged density measured by the CO_2 interferometer, (b) the detector signal for the p36 chord (impact parameter is 1.86 m), and (c) a blow up of the detector signal. At t = 18.24 and t = 18.29, the detector signal becomes too low for analysis and "phase jumps" will occur. (Shot 1050518097)

thereby losing information concerning the phase between the two beams. Discharges with "phase jumps" show unrealistic density changes that must be manually corrected. An example of such a situation is shown in Fig. 2.19. The line averaged density from the CO_2 interferometer shows the rise due to double pellet injection. The signal from an outboard FIR chord (10° from the injection line with an impact parameter of 36 cm) has steady amplitude until 18 ms when the ablatant material arrives, attenuating the FIR signal at 18.24 ms and 18.29 ms. Due to the large number of phase jumps during pellet ablation, particularly when attempting to double or triple the density, it can take up to several days to process FIR data from a single discharge if the information during pellet ablation is desired. Though it may strain the abilities of the FIR system, pellet fueling has not made the system obsolete but does make processing the data difficult.

2.5.2 Electron temperature diagnostics

SXR tomography

The SXR tomography system measures the 2-D electron temperature profile evolution using the measured emission as seen through filters of differing thickness. Using four cameras, split into pairs that utilize identical filters, the 2-D emission profile can be resolved. With sufficiently thick filters, the emission is solely from bremsstrahlung radiation. The two sets of bremsstrahlung emission profiles are compared, and the electron temperature is calculated. Filter thickness is chosen such that line radiation from impurities does not pollute the signal, otherwise the measured temperature would be an underestimate. However, for this technique to work, the bremsstrahlung emission must be large so that enough photons make it through the filters. Due to this lower bound on emission, 2-D profiles are presently only available inside $r \sim 20\ cm$ and for sufficiently hot discharges.

For this reason the SXR technique is not used in the low-current, pellet-fueled discharges. At high current ($I_\phi > 400\ kA$), however, both SXR tomography and Thomson Scattering are used.

Thomson Scattering

The Thomson scattering (TS) system measures the electron temperature at up to 20 radial points at one or two time points during the discharge. Unlike the FIR system, which requires its lasers to propagate through the plasma and pass through small detectors opposite where they enter, the TS laser must only make it to the volume in the plasma where measurement is desired. The spectrum of scattered photons from this volume is then measured. The larger the number of electrons within the target volume, the larger the scattering. Typically for pellet-fueled PPCD discharges, gains on the photo-multipliers need to be turned down to prevent the signal saturation. Difficulties might then arise when trying to make multiple measurements during a single discharge, *e.g.*, taking T_e-profiles before and after pellet injection.

2.5.3 Ion temperature diagnostics

CHERS

The CHERS (CHarge Exchange-Recombination Spectroscopy) system measures the temperature of fully stripped carbon ions at one radius (can be varied over 11 chords each with a width 2 cm) for a period of 20 ms. The CHERS diagnostic uses a neutral hydrogen beam to charge exchange with the background fully-stripped carbon. The carbon captures an electron in an excited state. The electron transitions down to a lower energy emitting light that is used to gauge the temperature of the carbon population. Two spectra are

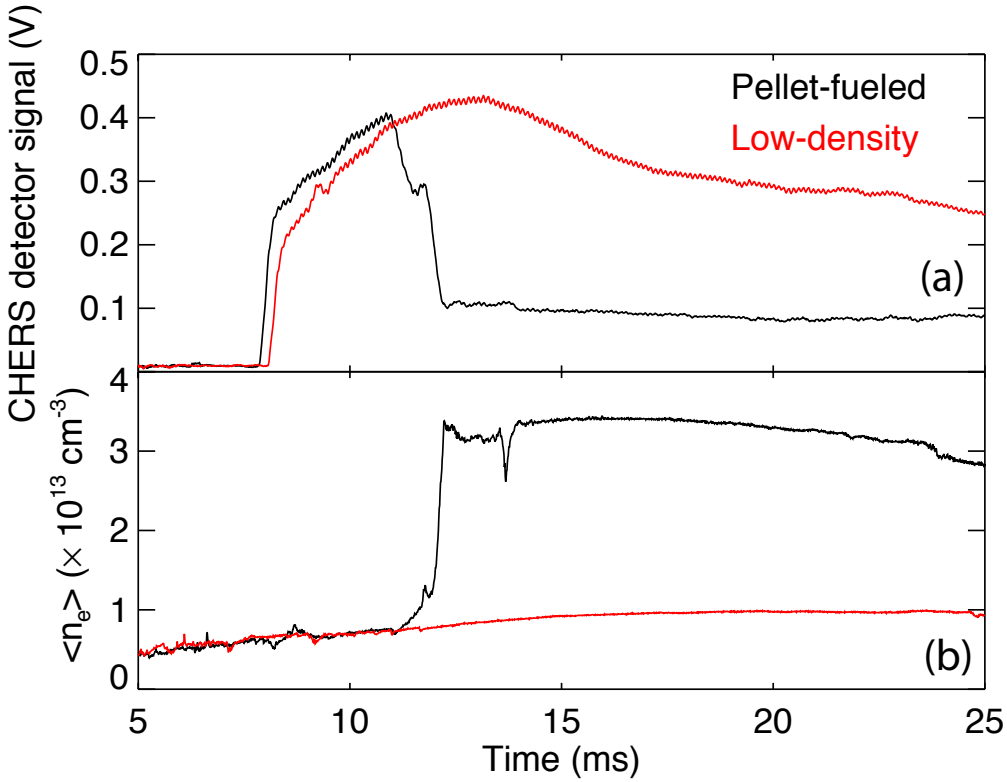

Figure 2.20: The DNB transmission (a) is measured on the inboard edge opposite of where it enters the plasma. The pellet-induced density change (b) reduces the transmission four-fold.

taken: one of a small radial extent (2 cm) of the beam and another just beside the beam in order to measure the background emission. The background is subtracted from the on-beam signal. The resultant spectrum's width is the temperature of fully stripped carbon. For the most part, the CHERS temperature is used to represent the ion temperature due to the greater spatial and temporal coverage of the diagnostic and the difficulty in directly measuring the bulk ion temperaure[3].

Figure 2.20 shows the CHERS beam signal (measured as the beam exits the plasma) for low and high density discharges. Pellet injection increases the density threefold and decreases the beam signal by a factor of four compared to the low density case.

Beam attenuation between r_0 and r can be calculated by [17]:

$$I(r) = I(r_0) \int_{r_0}^{r} \alpha dl \tag{2.5}$$

with:

$$\alpha \;=\; \frac{<\sigma_e v_e>}{v_a} n_e + (\sigma_{pi} + \sigma_{CX}) n_i \tag{2.6}$$

where v_a is the speed of beam neutral and $<\sigma_e v_e>/v_a$, σ_{CX}, and σ_{pi} are the cross sections for electron impact ionization, charge exchange, and ion impact ionization, respectively. For a 50 keV hydrogen beam, $v_a \sim 3\times10^8\ cm/s$. For this ion energy, the charge exchange and ion impact ionization cross-sections have values of $1.2\times10^{-16}\ cm^2$ and $1.8\times10^{-16}\ cm^2$. The electron impact cross-section for typical target plasmas is $1\times10^{-16}\ cm^2$.

Figure 2.21 shows a profile of the beam attenuation for two cases (similar to those used in Fig. 2.20). In order to measure T_i, there needs to be a large enough population of fully

[3]A testament to this difficulty is that MST is one of just a few experiments around the world that has a tool for measuring bulk ion temperature - the Rutherford scattering diagnostic, which however is much more limited in measuring capabilities.

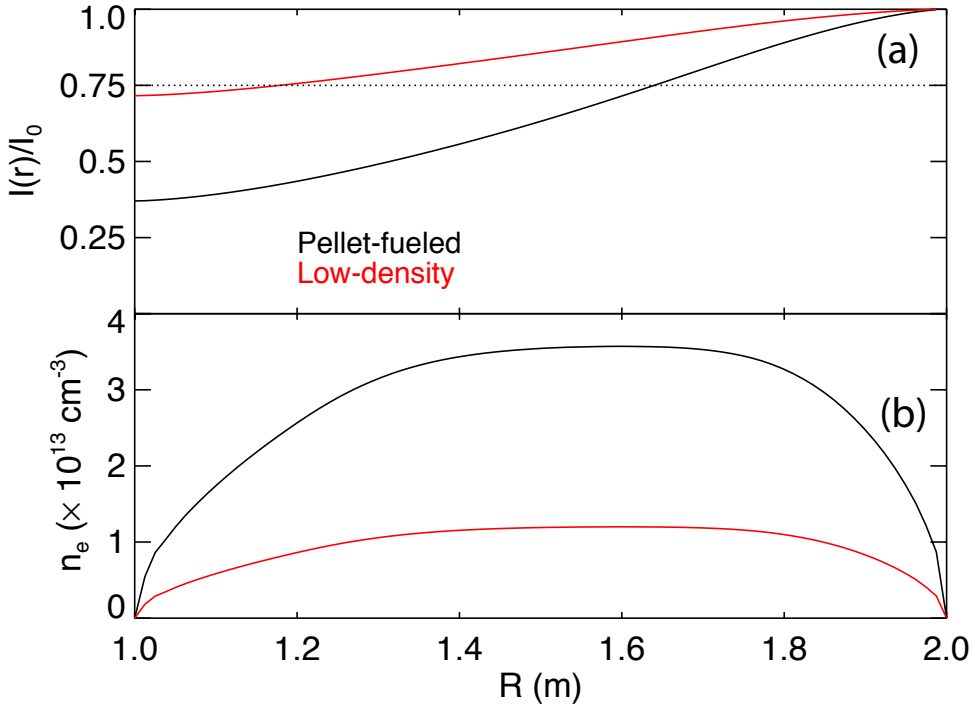

Figure 2.21: Computation of the DNB transmission at different points in the plasma indicates that R must be greater than 1.6 m for the measurement to be reliable. This corresponds to a point between the r/a = 0.0 and r/a = 0.2 chords.

stripped carbon and enough fast beam neutrals to charge exchange with them. Figure 2.21(a) shows that for the high density case the attenuation at $R \sim 1.6$ is equivalent to that at the far wall for the low density case. Typically measurements (even at low density) have focused on the outboard half of the machine. At high density, measurements inside $R < 1.6$ are fairly poor (larger error bars) than those from outboard edge. In the near future, the CHERS diagnostic neutral beam will be upgraded to be more intense.

Rutherford Scattering

The Rutherford scattering diagnostic measures the temperature of the bulk ions (deuterons) at one radius (r = 17 cm with total spatial width of 14 cm) for a period of 3 ms. The RS system uses a 20 keV neutral helium beam that as it passes through the plasma collides with the bulk ions (deuterons). The ion temperature can then be calculated from the width of the resulting energy distribution of the Coulomb-scattered helium atoms. While the RS system also needs its neutral beam to penetrate to the region being measured, the increased density following pellet fueling also provides more deuterium ions from which to scatter the helium neutrals. In this struggle, the increased scattering wins out and the measurement is affected to the experimenter's benefit. Another factor in the experimenter's favor is the use of a helium beam. Helium, with its higher ionization potential than hydrogen, can penetrate deeper into the plasma.

2.5.4 Internal magnetic field diagnostics

MSE

Using the same neutral beam as CHERS, the MSE (Motional Stark Effect) diagnostic measures the Stark splitting of the emission from the beam neutrals' interactions (col-

lisions) with the plasma (primarily the electrons). The splitting is due to the motional electric field $E = v_{beam} \times B$ where v_{beam} is the velocity of neutrals in the beam, and B is the local magnetic field. The diagnostic uses a CCD camera to image the spectra of the emission and determine E. As v_{beam} is known, and the view of the beam is focused on the core, the MSE diagnostic measures $B_\phi(r = 0)$. For the data presented, the measurement was only capable of getting $B_\phi(r = 0)$ for a single time point. However, the diagnostic has since been upgraded to provide multiple time points of the central toroidal field during a discharge. Though it relies on the same neutral beam as CHERS, it is not yet apparent if higher density operation is having an effect on the measurement.

Polarimetry

The FIR system was designed to provide simultaneous interferometry and polarimetry data. Faraday rotation of a circularly polarized beam goes as $\int n_e B_\parallel dl$, where $B_\parallel$ is the component along the beam's path [17]. Since $B_r \ll B_\theta$, Faraday rotation measurements determine the poloidal component of the magnetic field which in turn can be used in Ampere's Law to calculate the toroidal component of the plasma current, J_ϕ. As it uses the same beams as the interferometer, the same problem arises during pellet-fueling. Care must be taken when processing Faraday rotation data as well.

2.5.5 Z_{eff} and τ_p

Determining the plasma resistivity requires measurement of both the electron temperature and Z_{eff} (the effective ionic charge). Z_{eff} is defined:

$$Z_{eff} = \frac{1}{n_e} \sum_\alpha n_\alpha Z_\alpha^2, \ \alpha = \text{all ions present} \tag{2.7}$$

Measurement of Z_{eff} is a difficult task but in the case of MST works rather well in one particular operating regime: high current, pellet-fueled PPCD. The method used makes use of the dependence of bremsstrahlung emission on Z_{eff}:

$$\epsilon_{brems} = A\frac{g_{ff}n_e^2 Z_{eff} e^{\frac{-hc}{\lambda k T_e}}}{\lambda^2\sqrt{T_e}}\left[\frac{\mathrm{W}}{\mathrm{cm^3 nm\ sr}}\right] \tag{2.8}$$

Line radiation from deuterons and impurities in MST coincides with the bremsstrahlung spectrum and can interfere with the measurement. In particular D_α radiation from neutrals makes the measurement unfeasible in standard discharges. During PPCD, the neutral density drops, and consequently D_α emission falls as well. Coupling PPCD with pellet-fueling can increase bremsstrahlung emission 20-fold. Even when looking at near-infrared (NIR) emission far from the D_α line, this line is still a pollutant, but during PPCD it can be removed. In MST, NIR emission at 1040 nm has been used to measure Z_{eff} [20]. NIR emission can be plotted as a function of D_α, and a fit made to the comparison is a straight line:

$$\epsilon_{1040nm}(t) = m\gamma_{D_\alpha}(t) + b(t) \tag{2.9}$$

where b(t) is the unpolluted bremsstrahlung emission at 1040 nm, and m is a constant. Measurement of both NIR and D_α emission, the density profile (using the FIR system), and the temperature profile (using Thomson scattering) provides the necessary ingredients for the calculation of the line-averaged Z_{eff} in MST.

Measurement of the D_α emission profile is also key in determining the particle confinement time τ_p :

$$\tau_p = \frac{\int n_e dV}{\int (S - \frac{dn_e}{dt})dV} \tag{2.10}$$

where S is the source term [17]:

$$S = n_e n_0 < \sigma v >_{ion} \tag{2.11}$$

where n_0 is the neutral density and $< \sigma v >_{ion}$ is the cross section for ionization of neutral deuterium. The measurement of the particle source rate S, is made using the D_α array. The electron source rate can be written in terms of D_α emission [17] which goes as:

$$\gamma_{D_\alpha} = n_e n_0 < \sigma v >_{exc} \tag{2.12}$$

where γ_{D_α} is in units of $\frac{photons}{cm^3 \cdot s}$, and $< \sigma v >_{exc}$ is the cross section for the excitation of bound electrons to n = 3 which then fall to n = 2, emitting a 656.1 nm photon. Combining Eqs. 2.11 and 2.12 yields:

$$S = \gamma_{D_\alpha} \frac{< \sigma v >_{ion}}{< \sigma v >_{exc}} \tag{2.13}$$

where the ratio $(\frac{<\sigma v>_{ion}}{<\sigma v>_{exc}})^{-1}$ is $\sim 0.08 - 0.09$ [21]. The particle confinement time can then be calculated using interferometry and a radial array of D_α detectors [22]. It's known that the particle sourcing in MST is not toroidally symmetric due to asymmetry in recycling. Previous measurements of the particle confinement utilized an array of D_α detectors that were colinear with the interferometer chords [21]. Also, local measurements of τ_p are difficult due to the 3-D nature of the emission (weighted to the outboard midplane and varying toroidally). Integrating over the whole plasma volume to get the global confinement time is much more straightforward as inversion of the line-averaged data is not required:

$$\tau_p = \frac{N_e}{S_{tot} - \frac{dN_e}{dt}} \tag{2.14}$$

where $N_e = \int_V n_e(r)dV$ and $S_{tot} = \int_V SdV$.

2.5.6 Energetic electrons

The runaway electron population in MST is observed through the measurement of hard-x-rays with a radial array of CdZnTe detectors capable of resolving emission in the range of $10 - 300$ keV. The runaway electrons can carry significant current and energy. Their energy is not available for heating the bulk due to their reduced collisionality. Pellet fueling can in principle effect either an increase in the runaway population (by providing targets electrons to be "knocked on" to runaway energies) or reduce the number of runaways (by increasing collisionality). Observation of a significant population of runaways also has implications for both the Thomson scattering measurement which assumes a Maxwellian population and the calculation of resistivity which has been assumed to be neo-classical.

2.6 Summary

There are three methods of fueling MST; in two of them, the experimenter can exert a wide range of control. At higher densities, wall-recycling remains more an art than a science. Gas puffing and pellet injection are more predictable. MST has two variants to its gas puffing: a localized single high throughput valve and a toroidally-spaced set of lower throughput valves. The pellet injector can provide similar amount of material, but with the ability to fuel the core plasma more than it does the edge, as will be shown in Chapter 3.

Diagnostic coverage of pellet-fueled discharges is good. Two diagnostic systems have difficulty with the high density (CHERS and FIR), and future increases in density may

limit the utility of these diagnostics. However it is unclear how much of an effect pellet fueling is having (and in the future, will have) on the MSE diagnostic.

Bibliography

[1] R. N. Dexter, D. W. Kerst, T. W. Lovell, S. C. Prager, and J. C. Sprott, Fusion Technol. **19**, 131 (1991).

[2] B. E. Chapman *et al.*, Phys. Rev. Lett. **87**, 205001 (2001).

[3] B. E. Chapman *et al.*, Phys. Plasmas **9**, 2061 (2002).

[4] R. Bartiromo *et al.*, Phys. Rev. Lett. **82**, 1462 (1999).

[5] Y. Yagi *et al.*, Plasma Phys. Control. Fusion **44**, 335 (2002).

[6] M. Cecconello *et al.*, Plasma Phys. Control. Fusion **46**, 145 (2004).

[7] S. Oliva, Private communication.

[8] S. K. Combs *et al.*, Fusion Technol. **44**, 513 (2003).

[9] S. L. Milora, S. K. Combs, and C. R. Foust, Rev. Sci. Instrum. **57**, 2356 (1986).

[10] V. Talanker and M. Greenwald, Rev. Sci. Instrum. **59**, 1085 (1988).

[11] L. D. Landau and E. M. Lifshitz, *Fluid mechanics* (Course of theoretical physics, Oxford: Pergamon Press, 1959).

[12] D. L. Brower *et al.*, Rev. Sci. Instrum. **72**, 1077 (2001).

[13] H. Cummings, J. A. Reusch, R. O'Connell, and D. J. Den Hartog, Bull. Am. Phys. Soc. **50**, 37 (2005).

[14] P. Franz *et al.*, Rev. Sci. Instrum. **75**, 4013 (2004).

[15] D. J. Den Hartog *et al.*, Rev. Sci. Instrum. **77**, 122 (2006).

[16] A. Almagri, D. Clayton, and R. O'Connell, Bull. Am. Phys. Soc. **51**, 73 (2006).

[17] I. Hutchinson, *Principles of Plasma Diagnostics* (Cambridge University Press, 1987).

[18] B. Deng, Private communication.

[19] A. Canton, B. Pégourié, P. Innocente, L. Garzotti, and S. Martini, Plasma Phys. Control. Fusion **43**, 225 (2001).

[20] J. K. Anderson, *Measurement of the Electrical Resistivity Profile in the Madison Symmetric Torus*, PhD thesis, University of Wisconsin - Madison, 2001.

[21] N. E. Lanier, *Electron Density Fluctuations and Fluctuation-Induced Transport in the Reversed Field Pinch*, PhD thesis, University of Wisconsin - Madison, 1999.

[22] J. K. Anderson, P. L. Andrew, B. E. Chapman, D. Craig, and D. J. Den Hartog, Rev. Sci. Instrum. **74**, 2107 (2003).

You can slay the wicked beast,

But you can't ignore my techno.

Electric Six

3

Comparison of pellet injection and edge-fueling in standard discharges

3.1 Introduction

This chapter will focus on the operational basics of pellet injection. To this end, the effect of pellet fueling on standard discharges will be characterized, *e.g.*, the effect of the pellet on plasma current and magnetic fluctuations, the evolution of the particle and current density profiles, and the effect of the plasma on pellet trajectory.

The effect of pellet injection on plasma evolution will also be compared to edge fueling to similar densities. The edge-fueled discharges to be described in this chapter are the result of either "single valve" fueling (*i.e.*, using the high throughput valve) or "multi-valve" fueling (*i.e.*, using MST's standard fueling system altered for higher throughput). In both cases, the resultant electron density profiles are hollow, whereas pellet-fueled

discharges can have peaked density profiles. For a more direct comparison to pellet-fueling, the density profile evolution and effect on magnetic fluctuation behavior following single valve fueling will be the primary foci.

3.2 Fueling comparison in standard discharges

For this comparison, plasmas of similar global parameters (I_p and $<n_e>$) are sought using the two fueling methods. Adjusting the current is a simple matter, but the expected densities are a bit more problematic and depend on the fueling efficiency of the source.

Empirically, the measured MST particle inventory change due to pellets is less than the estimated pellet particle inventory N_p. The estimated N_p is calculated from the pressure drop in the feed manifold during the freezing of the pellet. It is possible that some of the material is frozen, but not as part of the pellet. Also, the pellet may not always break away cleanly from the barrel, and some material can be lost in flight. A complete inventory of pellet material loss mechanisms has yet to be done. Using interferometry measurements to calculate the total material deposited by the pellet indicates that roughly two-thirds of the pellet material is not incorporated into the plasma. Taking this into account, an estimate of the delivered pellet material can be made. In the following experiments, double-pellet injection was employed using 1.6 mm diameter (large) and 1.3 mm diameter (medium) pellets. Both pellets have nominal lengths twice their diameter, 3.2 mm and 2.6 mm, respectively, and are accelerated using a mechanical punch. The mass density of solid deuterium is 0.2 $\frac{g}{cm^3}$, so that the combined particle count of the two pellets is 5.9×10^{20}. The estimated particle inventory change in MST due to pellet injection is then $\sim 2 \times 10^{20}$.

For gas-injection, the throughput of the modified valve is $\sim$ 680 $\frac{Torr \cdot L}{s}$ (Fig. 2.7 at

350 V), which translates into a particle source rate of 2.2×10^{22} $\frac{1}{s}$. The valve can be actuated in increments of 0.1 ms up to 9.9 ms, so the maximum pulse length would be necessary to reproduce the total particle flux of the pellets. The volume of MST[1] is 8×10^6 cm^3, so injecting 2×10^{20} particles should result in an average density change $\triangle n \sim 2.5 \times 10^{13}$ cm^{-3}.

3.2.1 Single valve fueling

Edge fueling using the high throughput gas valve introduces a large amount of cold particles. Figure 3.1(a) shows a tripling of the line averaged density over the course of the single valve fueling (orange box). As a consequence, there is a drop in temperature[2] resulting in higher resistivity which is reflected in the 12% drop in the plasma current [Fig. 3.1(b)]. During the period of higher density ($<n_e> \gtrsim 1.5 \times 10^{13}$ cm^{-3}), sawtooth activity becomes more frequent but lower in amplitude as seen in both the V_θ and in the level of magnetic fluctuations [Fig. 3.1(c) and the red traces of Fig. 3.10, respectively].

The FIR system (combined interferometer and polarimeter) was used to measure the density profile (Fig. 3.2) evolution during the discharge depicted in Fig. 3.1. The poor penetration of particles is evidenced by the edge peaking of the profile where the maximum density is about 15 cm from the wall and reaches $\sim 4 \times 10^{13}$ cm^{-3}. Due to profile-flattening during sawtooth crashes and short transport times between crashes ($\tau_p \sim 1$ ms), there is some core penetration of the gas puff as the central density does exceed 2×10^{13} cm^{-3} by the end of the gas puff.

[1] This is just the volume of the torus, $V = 2\pi^2 a^2 R_0$. The pumping duct is not included.
[2] This assertion is supported by measurements taking during similar edge-fueled discharges.

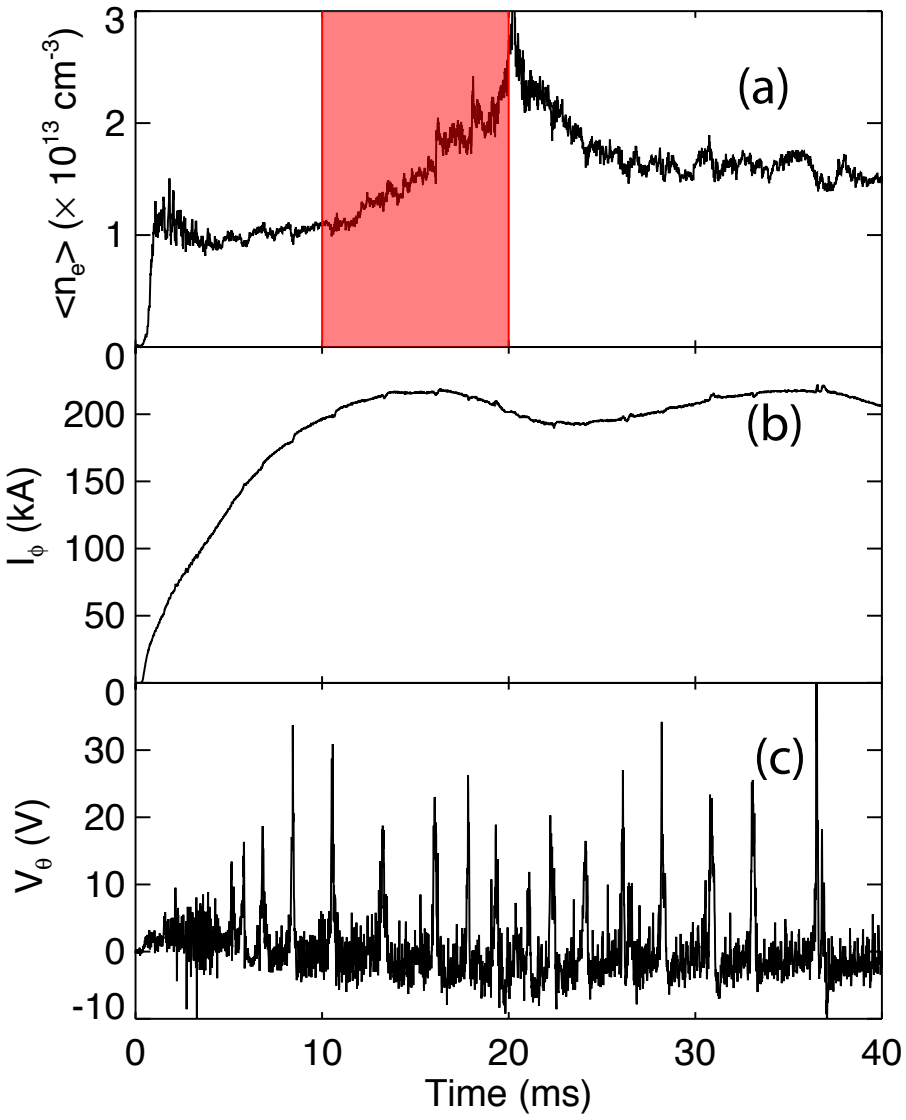

Figure 3.1: A large gas puff (indicated by shaded box) injected into a standard discharge. In single valve fueling the density rise time is long and constrained by the valve's throughput. Due to the large influx of cold gas, the plasma current (b) drops as resistivity increases. The surface poloidal voltage (c) shows an increase in sawtooth frequency. (Shot 1050924127)

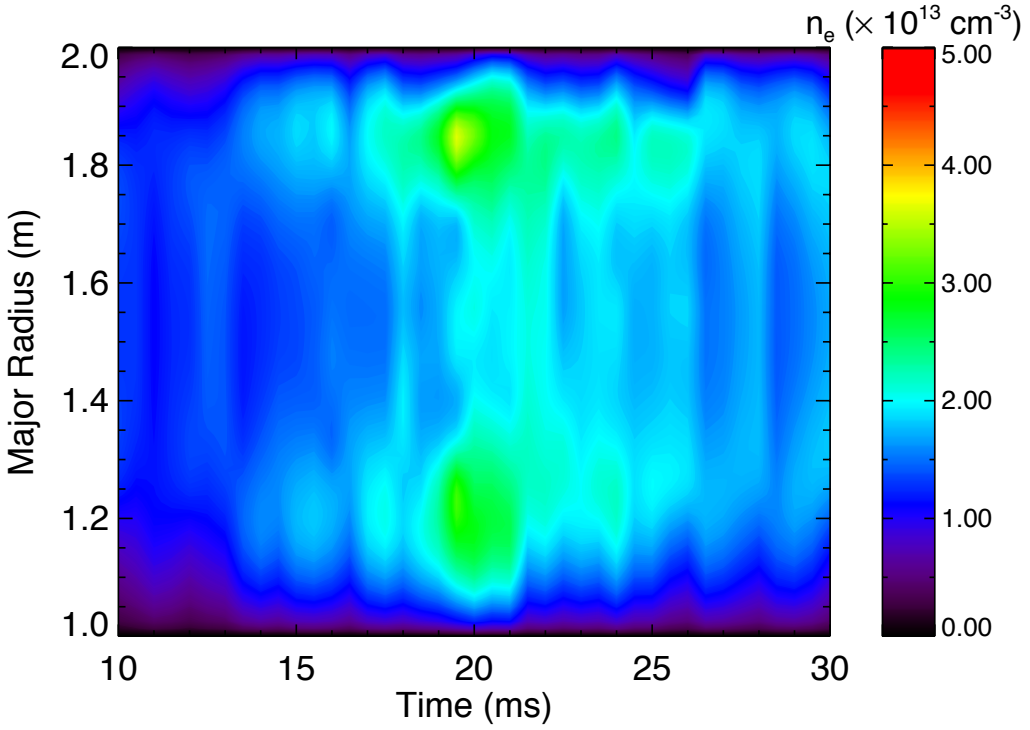

Figure 3.2: Density profile evolution for a discharge with a large gas puff. Single valve fueling begins at 10 ms and ends at 20 ms. Sawtooth crashes flatten profile, but with intense gas puffing, discharges are always flat or hollow. (Shot 1050924127)

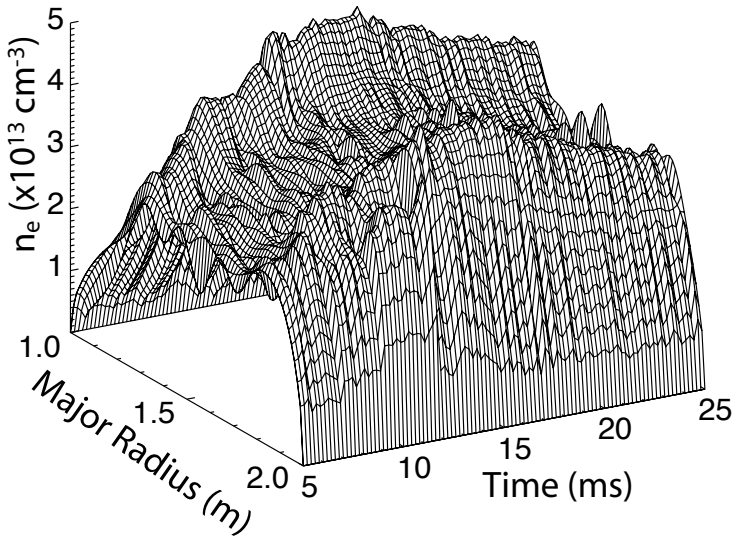

Figure 3.3: Density profile evolution for 0.5 MA standard discharge. Fueling was a result of wall-loading, and extended gas puffing from the standard MST fueling system. (Shot 1060912085)

3.2.2 Multiple valve fueling

The combination of wall loading and multiple valve fueling (using MST's fueling system without the single high throughput valve) has been used to increase density in an attempt to achieve densities similar to pellet injection. The results have been poor as it takes many discharges to produce a single stable, high density discharge due to the lower throughput of the valves and the reliance on wall recycling. Figure 3.3 shows a surface plot of density for a 0.5 MA standard discharge, again another hollow profile. To arrive at this discharge, it was necessary to go through a series of 20+ discharges, alternating between multiple valve fueling and very little puffing at all. In this way, terminations, *i.e.*, an accelerated decay of the plasma current, can be averted, and the density is increased nearly three-fold.

These terminations can be either fast or slow depending on the rate at which the current decays.

3.2.3 Pellet injection

Pellet fueling has the ability to produce similar densities as gas puffing but in shorter times and with peaked profiles. In Figure 3.4, data are shown for a low current pellet injected discharge. In this shot, two pellets were injected, and their arrival times are indicated by the red vertical lines.

The delay between the arrival time and the jump in density (measured by the CO_2 interferometer which is located $\sim 180°$ from the injector, as shown in Fig. 2.16) can be broken into two parts, although the first is the larger of the two: (1) the time it takes the pellet to reach a particular magnetic surface and deposit material and (2) the time it takes that material to flow along the surface and reach the interferometer. The amount of material deposited at a given surface is a strong function of the electron temperature (the ablation rate goes as $\sim n_e^{\frac{1}{3}} T_e^{1.64}$ [1]). With the target plasmas typically having peaked n_e and T_e profiles, the pellet ablation rate would be greatest in the core. In the discharge depicted in Figure 3.4, the pellet speeds are 194 m/s and 170 m/s, making the time to reach the plasma core $2 - 3\ ms$. The density impulse provided by an ablating pellet at a given radius will travel at the speed of sound c_s [2, 3] along field lines. For MST plasmas, $c_s \sim 10^7\ cm/s$ over most of the plasma, falling to zero outside the reversal surface. Given the magnetic field profiles of the RFP, the shortest toroidal path between the pellet injector and the interferometer is found in the core. In standard discharges, the edge field is strongly poloidal, and the core field is strongly toroidal. As a pellet enters the plasma, the material deposited in the edge has a much longer distance ($> 10\times$)

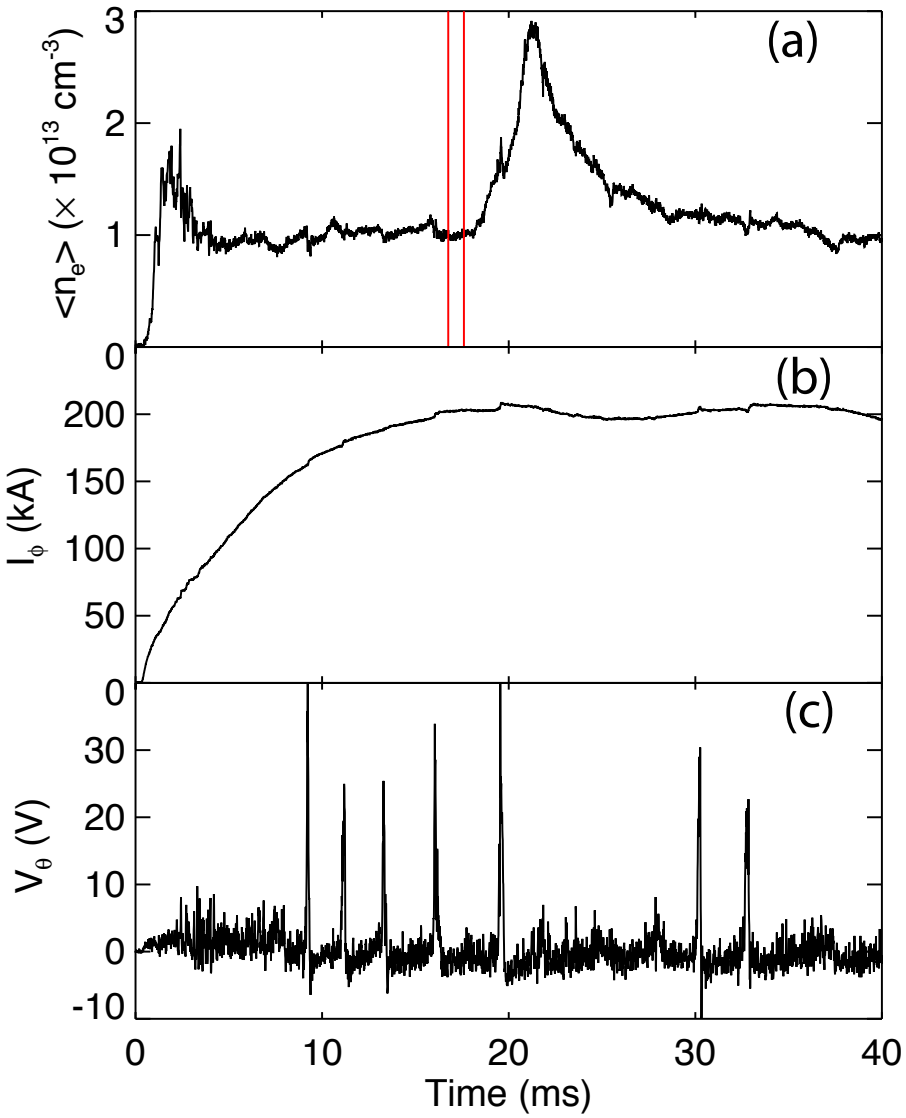

Figure 3.4: Two pellets (vertical red lines) are injected into a standard discharge. They rapidly increase the density (a) as measured by the CO_2 interferometer located 180° from the pellet injector. The plasma current (b) also drops due to the sudden decrease in plasma temperature. The voltage measured across the toroidal gap (c) shows a drop in the sawtoothing activity following pellet injection. (Shot 1050518097)

to travel to reach the interferometer compared to material deposited in the core. When material is deposited in the core, the density impulse will take $\sim 50\ \mu s$ to travel from the pellet's toroidal location to the interferometer. For slow pellets ($v_p < 200\ m/s$), the major factor in the delay is the pellet's speed. The delay depicted in Fig. 3.4 is ~ 3 ms and is consistent with the time it takes for the pellets to reach the core. Even for fast pellets ($v_p \sim 1000\ m/s$), the time to reach the core is still $10\times$ larger than the time it takes for the density impulse to spread toroidally to the interferometer.

Through pellet injection, the density profile can be tailored, *i.e.*, a flat, peaked, or even hollow profile can be created. The pellet data presented in this section will focus on peaked profiles. Flat and hollow profiles will be shown in Chapter 5. In the case of the discharge shown in Fig. 3.4, the two injected pellets penetrate to the core as observed from CCD imaging of the pellets. The 1.3 mm diameter pellet arrives at t = 16.8 ms with speed of 194 m/s, followed shortly thereafter at t = 17.6 ms by a 1.6 mm pellet moving at speed of 170 m/s. There is an early rise in density at t = 19.5 ms where it reaches $1.8 \times 10^{13}\ cm^{-3}$, and then quickly drops. This initial rise and then drop in density is coincidental with both a sawtooth crash and the smaller pellet reaching the core. The drop in density indicates that the crash is responsible for some of the rise. The short drop in density is quickly succeeded by a rise in density, most likely due to the large pellet, where the density peaks at t = 21.5 ms with a value of $2.9 \times 10^{13}\ cm^{-3}$. These estimated times-of-flight (2.7 ms and 3.9 ms, respectively) indicate penetration depths of 52 and 66 cm, respectively, which would place them in the core of MST.

Interferometry measurements show the evolution to a peaked density profile in this discharge (Fig. 3.5). Assuming no significant pellet deflection,[3] the estimated pellet

[3]For significant poloidal deflection, the pellet doesn't breach the reversal surface. There is a more detailed discussion of pellet deflection in Section 3.3.

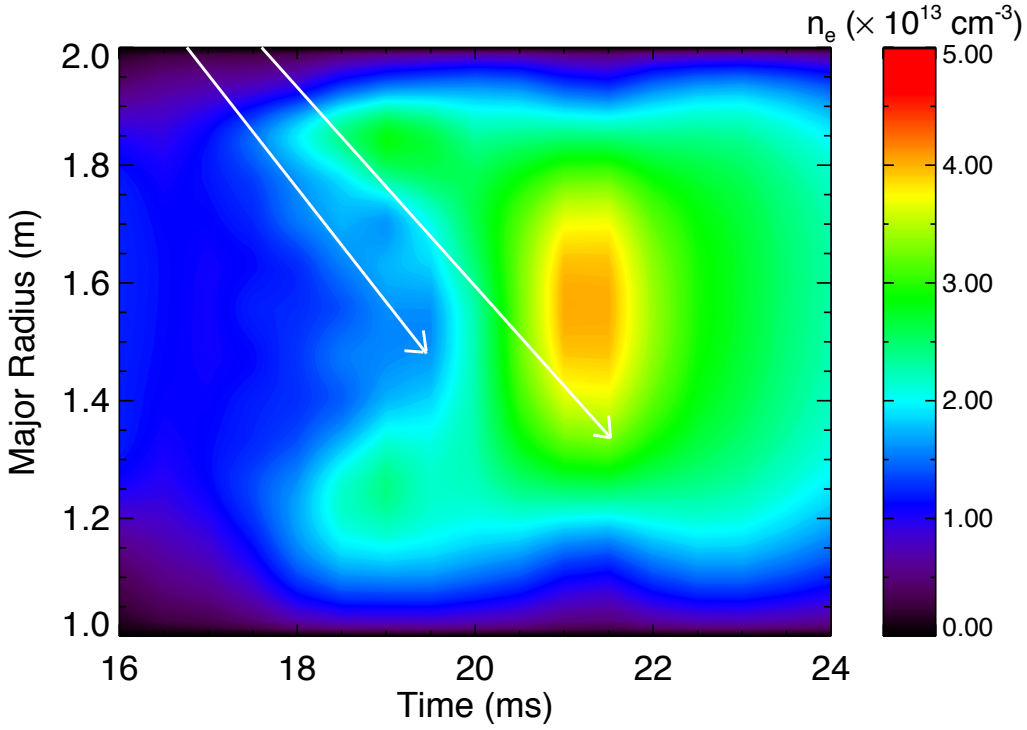

Figure 3.5: Density profile evolution for a pellet-fueled discharge. In this discharge, two pellets were injected. Their estimated positions in time are shown as the white lines. (Shot 1050518097)

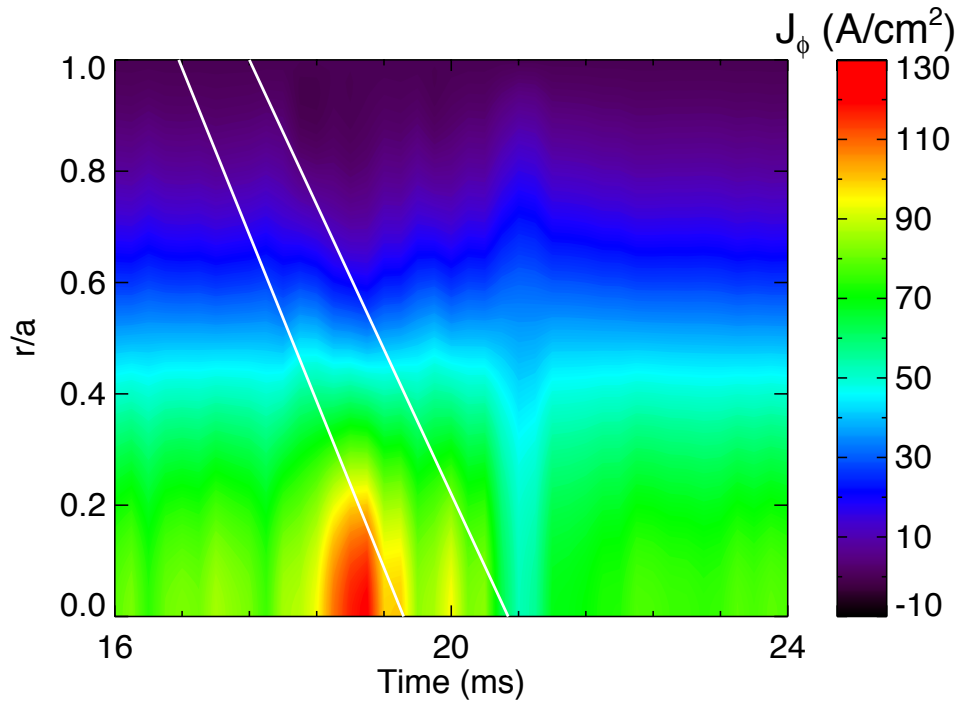

Figure 3.6: Toroidal current density evolution for a pellet-fueled discharge. In this discharge, 2 pellets were injected. Their positions in time are shown as the white lines. (Shot 1050518097)

positions in time (white lines) are also depicted. Just like gas puffing, as the pellets enter the plasma, the profile becomes very hollow with edge densities $2-3\times$ the value in the core. Following full ablation of the second pellet, the profile is peaked and then begins to decay as the particle confinement time is fairly short in standard plasmas (~ 0.6 ms [4]).

During pellet ablation the total plasma current is relatively constant[4], however, the current profile is undergoing significant changes. In Fig. 3.6, the toroidal current density

[4]Figure 3.7(a) shows that during ablation, there is a jump in plasma current at t = 19 ms due most likely to pellet-induced changes in the current and/or pressure gradients in the edge. These sharp, small increases in plasma current are seen during sawteeth with and without pellet injection and at low and high density. These sawteeth-related changes in plasma current also happen on timescales of 10s to 100s of microseconds, whereas the subsequent resistive decay due to pellet or single valve fueling occurs over milliseconds.

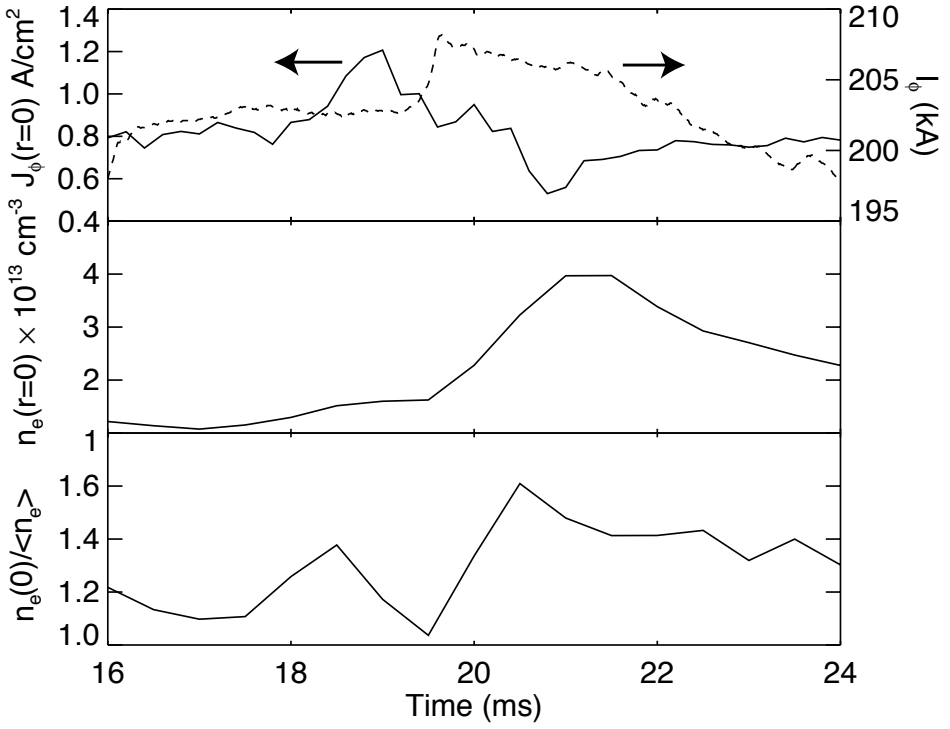

Figure 3.7: Central current density and total current (a), central particle density (b), and profile peakedness (c) before, during, and after pellet ablation. (Shot 1050518097)

as measured by polarimetry is plotted versus normalized radius and time. It appears that the smaller pellet, also the first to arrive, has little effect on the current density. However as the second, larger pellet reaches r/a = 0.6 (at 19 ms)[5], the edge current drops and the central density begins to peak. As this pellet reaches the core there is a large drop in the central current density, and an overall flattening of the profile. These effects are more pronounced when focusing on the time traces for the central particle and current densities during this discharge (Fig. 3.7) which show an increase in the central current density [Fig. 3.7(a)] just after pellets enter the plasma (beginning at t = 18 ms). At t = 19 ms, the central current density peaks just as the central particle density [Fig. 3.7(b)] begins to increase, coinciding with the first pellet reaching the core. In [Fig. 3.7(c)] the peakedness of the profile is plotted and the profile is most peaked at t = 20.5 ms, before the highest central density. This corresponds to the second pellet passing the core and the subsequent relaxation of the density profile.

3.2.4 Comparison of gas and pellet injection

Pellet injection can produce peaked density profiles whereas gas-injection leads to hollow profiles (Fig. 3.8). Direct comparison of the gas and pellet injection (Figs. 3.9 and 3.10) shows the benefits, albeit temporary, of core fueling in standard plasmas. The density rise time is quicker, and the drop in plasma current is smaller. It is interesting to note that there is a also change in MHD behavior in which sawtooth crashes are suppressed, although the baseline magnetic fluctuations are unchanged indicating the level of fluctuation-induced transport is the same.

The difference in density rise time can be attributed to the fact that it takes the pellet

[5]It is possible that a minor deflection experienced by the first pellet allows the second pellet to have a less perturbed trajectory.

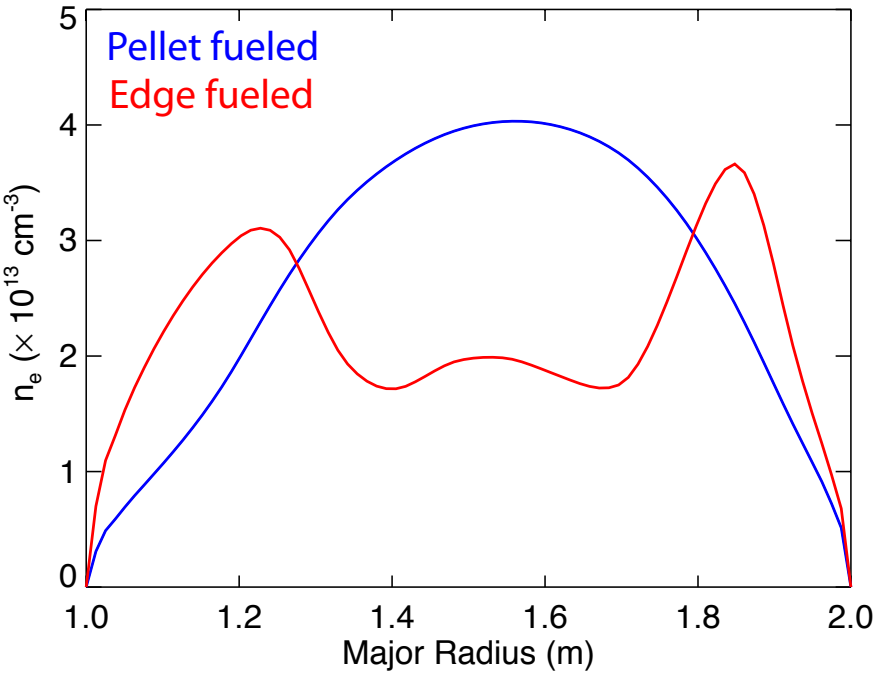

Figure 3.8: Time slice of density profiles for pellet (blue) and gas-injected (red) discharges chosen at time of peak line-averaged density. (Shots 1050518097 and 1050924127)

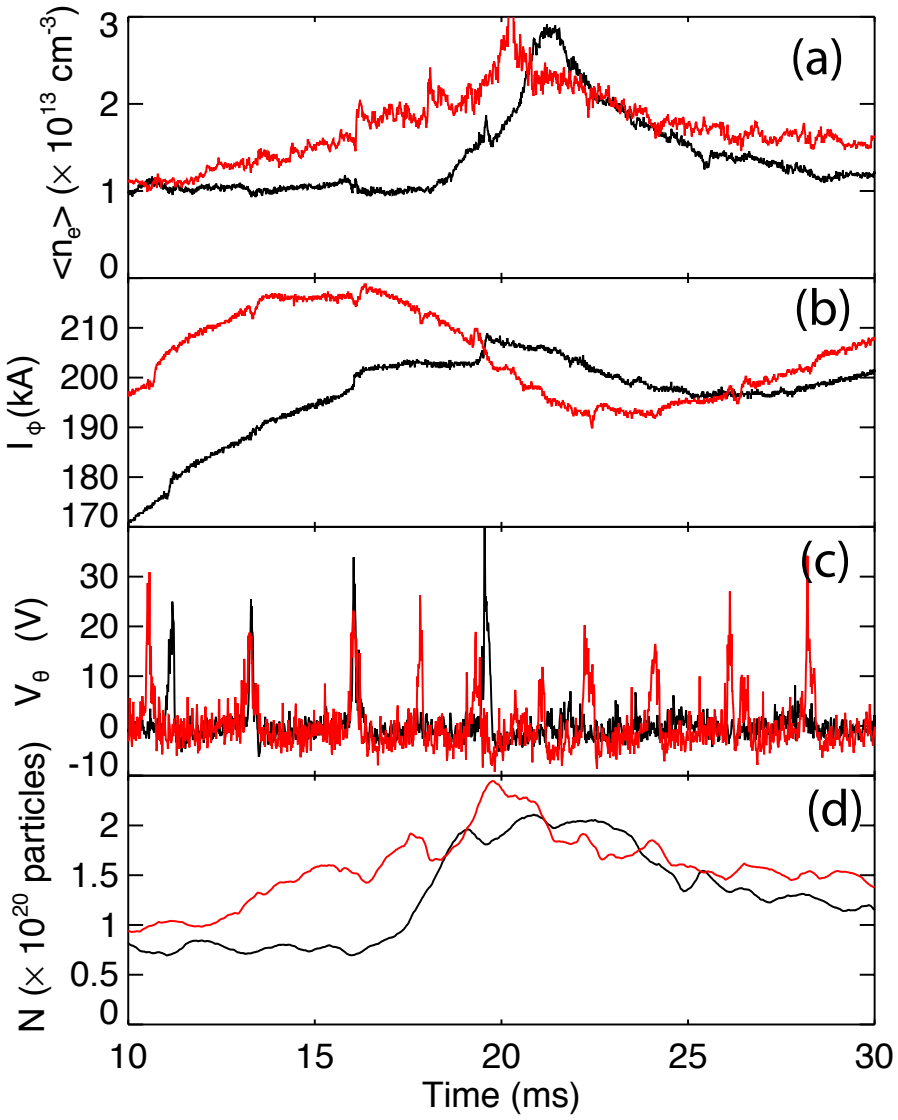

Figure 3.9: Comparison of pellet fueled (black) and gas-injected (red) standard discharges. In (a) the density rise time is much quicker for pellets. The drop in I_ϕ (b) following pellet injection is 5% compared to 12% for the gas-injected case. There appears to be beneficial effects on MHD activity due to pellets as well shown in the cessation of V_θ spikes. The time evolution of particle inventory (d) shows a slight flat-top for the pellet case. This plateau occurs after the second pellet has fully ablated (21 ms). (Shots 1050518097 and 1050924127)

life-time (< 5 ms) to deposit all of its material. Single valve fueling is limited by the valve's throughput, and to replicate the particle number change of the pellets requires ~ 10 ms of fueling. The fall-off of $<n_e>$ is quicker following pellet injection indicating either a decrease in wall recycling or a drop in τ_p. However, comparison of the total particle inventory N [Fig. 3.9(d)], shows that the pellet case experiences a "flat-top" for several milliseconds following the full ablation of the second pellet (t = 21 ms). This is in contrast to the gas-injection case, where N begins to fall immediately following the cessation of single valve fueling. The total particle inventory was calculated directly from integrating the profile of the chord line-averaged densities. This technique has the benefit of not being affected by any shift in the plasma. The larger drop in plasma current in the gas-injected case can simply be due to the larger influx in particles. Though $<n_e>$ is similar in the two cases, the particle inventory differs by nearly 20%.

There is a change in MHD activity between the two cases, as shown in Fig. 3.10, that, while not significant, may be of interest for future pellet fueling experiments. After 20 ms, there are no longer any large amplitude bursts in the edge resonant (m=0) fluctuations for the pellet case. In the gas-injected case, bursts still occur but at greater frequency than earlier in the discharge. The core-resonant activity in both cases loses the discrete behavior seen before 15 ms. The drop in m = 0 bursts in the pellet case are indicative of a favorable change in the current and/or pressure profiles. The resumption of sawtoothing activity [V_θ spike at 30 ms in Fig. 3.4(c)] indicates that by this time the profiles have relaxed to a pre-pellet/less stable state. However, the baseline level of m = 0 fluctuations remains unchanged during the sawtooth suppression indicating that confinement is similar to that between crashes of the non-pellet discharge.

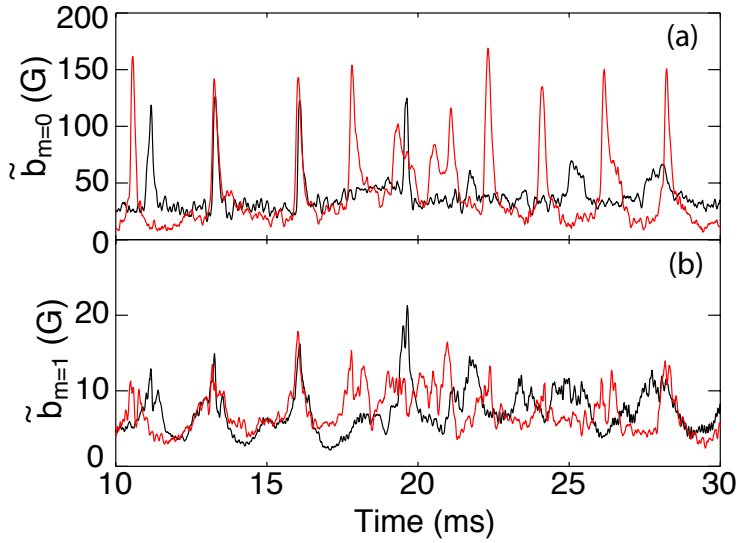

Figure 3.10: Mode comparison for pellet-fueled (black) and gas-injected (red) standard discharges. In (a) the edge resonant m=0 modes are shown (RMS sum of n=1-4 fluctuations). In (b) the core resonant m=1 modes are shown (RMS sum of n=7-14 fluctuations). (Shots 1050518097 and 1050924127)

3.3 Pellet deflection

The deflection of pellets, both poloidally and toroidally, in the RFP has been well documented by both RFX [5] and ZT-40M [6]. Tokamaks see very little deflection of pellets [7, 8]. Pellet deflection in the RFP is due to preferential heating of one side of the pellet due to the presence of suprathermal electrons [9]. Their presence can produce as much as a 60% asymmetry of heat flux on a pellet. Also in the RFP, the ablatant cloud is less dense compared to the cloud in a tokamak by two orders of magnitude, as measured in the RFX experiment [10], leading to a much higher ablation rate.

The CCD image of a pellet in flight is shown in Figure 3.11 with a cutaway of the MST for reference. In this case the injection angle was 30° above the horizontal midplane (earlier pellet injection experiments were through a different port with an injection angle

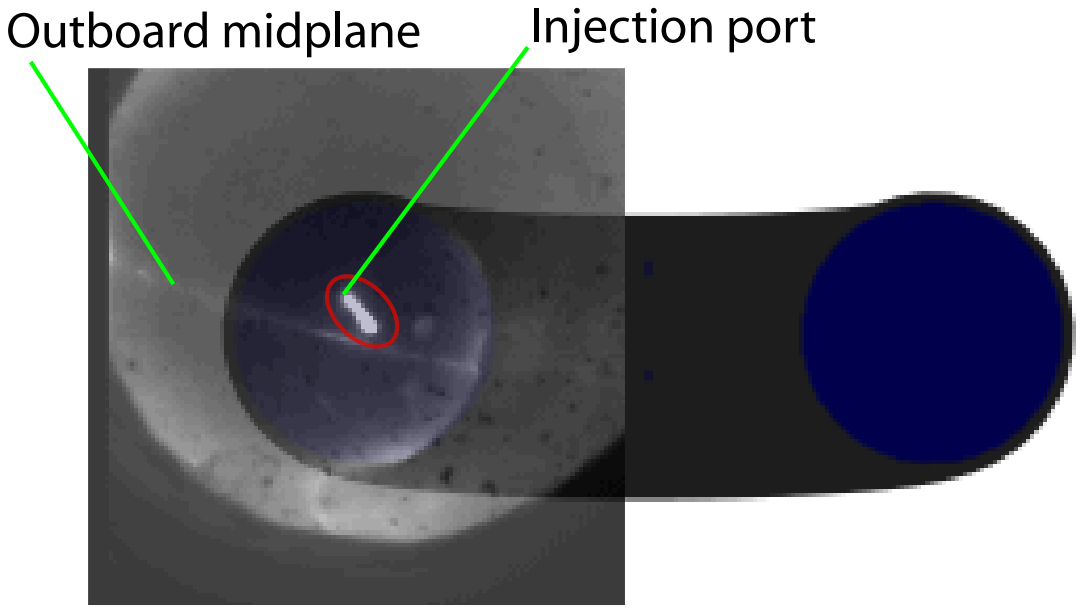

Figure 3.11: Cutaway of torus (grey/blue) with CCD picture (single frame) of slow pellet overlayed. The pellet (circled in red) is shown just entering the plasma's edge. Outboard side and injection port are shown on the left.

of 15° above the midplane). The CCD exposure time is 1.26 ms (its minimum value) such that fast pellets can cross the whole plasma in a single frame, and slow pellets can take 4-5 frames to cross the vacuum vessel (Fig. 3.12). In this setup, the poloidal deflection of pellets can be characterized but not toroidal deflection which is assumed based on other RFP pellet injection experiments. The pellet deflection in the edge of the machine is consistent with the direction of the suprathermal electrons in the region [11]. By changing the direction of the toroidal field, the direction of the poloidal current is changed as well, altering the deflection of the pellet as it passes through the edge (Figs. 3.12 and 3.13). The small deflections of pellets in MST closely resemble that seen in RFX but do not come close to the severe deflections (upwards of 90°) observed in ZT-40M.

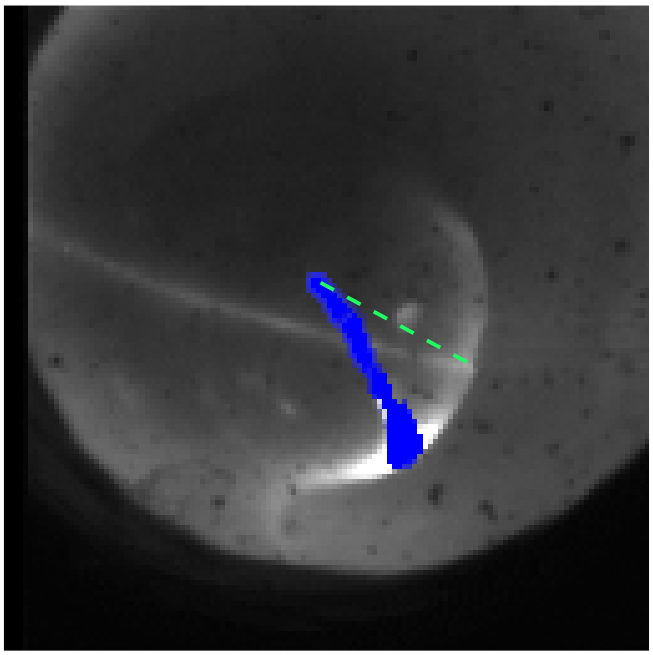

Figure 3.12: Pellet deflection in edge of machine shown here is due to fast electrons preferentially heating one side of the pellet. In the edge these electrons are moving primarily in the poloidal direction. The pellet is deflected downwards when initial B_ϕ on-axis is reversed from standard configuration. Compilation of four consecutive frames with pellet trajectory highlighted in blue and unperturbed trajectory in green. The bright area that extends along the bottom of MST is believed to be a "hard gas puff" due to the pellet impacting the wall. Outboard side and injection port are on the left. (Shot 1050308023)

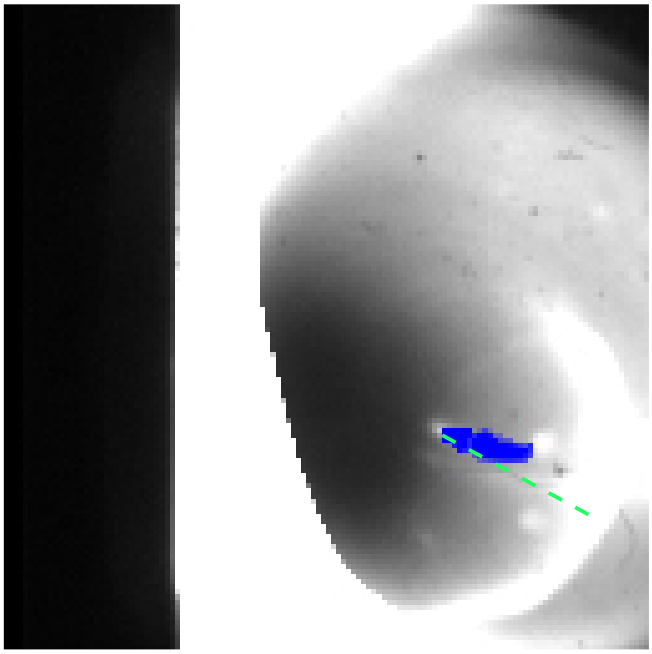

Figure 3.13: The deflection direction is consistent with the direction of the fast electrons. In this discharge, B_ϕ is in its standard orientation. Compilation of two consecutive frames with pellet trajectory highlighted in blue and unperturbed trajectory in green. Outboard side and injection port are on the left. Camera alignment and iris diameter are different in this compilation than previous images. White region surrounding image is saturation of the CCD. (Shot 1021025077)

3.4 Summary

As expected, pellet injection can produce peaked density profiles whereas gas-injection leads to hollow profiles. Pellet fueling reduces MHD activity, *e.g.*, the frequency of sawtooth crashes. Tokamaks see an analogous effect, and correlate it to the peaking of the density profile. Due to the longer particle confinement times of tokamaks, however, the effect is prolonged and more pronounced. Though the sawtooth behavior is suppressed following pellet injection, the baseline level of magnetic fluctuations is unchanged, and consequently, confinement is unchanged.

Bibliography

[1] P. B. Parks and R. J. Turnbull, Phys. Fluids **21**, 1735 (1978).

[2] V. Rozhanskij and I. Veselova, Nuc. Fusion **34**, 665 (1994).

[3] B. Pegourie and J.-M. Picchiottino, Phys. Plasmas **3**, 4594 (1996).

[4] N. E. Lanier *et al.*, Phys. Rev. Lett. **85**, 2120 (2000).

[5] P. Innocente, B. Boscolo, S. Martini, and L. Garzotti, Rev. Sci. Instrum. **70**, 943 (1999).

[6] G. A. Wurden *et al.*, Nuc. Fusion **27**, 857 (1987).

[7] C. A. Foster, R. J. Colchin, S. L. Milora, K. Kim, and R. J. Turnbull, Nuc. Fusion **17**, 1067 (1977).

[8] S. L. Milora *et al.*, Nuc. Fusion **20**, 1491 (1980).

[9] M. R. Stoneking, *Fast Electron Generation and Transport in a Turbulent, Magnetized Plasma*, PhD thesis, University of Wisconsin - Madison, 1994.

[10] A. Canton, B. Pégourié, P. Innocente, L. Garzotti, and S. Martini, Plasma Phys. Control. Fusion **43**, 225 (2001).

[11] M. R. Stoneking *et al.*, Phys. Rev. Lett. **73**, 549 (1994).

I have not failed. I've just found 10,000 ways that won't work.

Thomas A. Edison

It could be that the purpose of your life is only to serve as a warning to others.

Despair, Inc.

4

The search for a density limit

4.1 Introduction

There exists a limit on the achievable density in current-carrying, edge-fueled, toroidal magnetic confinement configurations above which the plasma disrupts, and it is not well understood theoretically [1]. As the fusion reaction rate scales as n^2, the upper limit for density is of interest for fusion devices. The Greenwald limit [2] represents an empirical relationship between plasma current density and particle density for edge-fueled discharges. It is defined as:

$$n_{GW} = \kappa \bar{J}, \tag{4.1}$$

where n_{GW} is the limiting line-averaged density in units of 10^{20} m^{-3}, κ is the plasma elongation, and $\bar{J}$ is the average current density in units of MA/m^2. For a device without

shaping *i.e.* one with a circular cross-section, the limit can be re-written as:

$$n_{GW} = \frac{I_\phi}{\pi a^2}, \tag{4.2}$$

where I_ϕ is the plasma current in MA, and a is the minor radius of the current-carrying plasma in meters. Above this density, tokamak discharges will exhibit large amplitude MHD fluctuations and disrupt.

In MST, the use of either the single high throughput valve or the pellet injector can bring MST densities up to the Greenwald limit but only for a limited range of plasma current ($0.2\ MA\ < I_\phi < 0.3\ MA$). These discharges are observed to terminate early for densities near and above the Greenwald limit, but the scaling with plasma current over the full range of MST's plasma current has not been confirmed. In this research the focus has been on determining if there's such a limit on MST operation and to describe it phenomenologically. As evidenced by the tokamak research on the Greenwald limit, the physical mechanisms of the limit are quite complex, and their investigation in the RFP is beyond the scope of this thesis.

4.2 The Greenwald limit in tokamaks

In tokamaks, the high density limit is characterized by the onset of phenomena detrimental to the plasma. As the Greenwald limit is approached, cooling of the plasma edge leads to any of the following: a drop in H-mode confinement, a transition from H-mode to L-mode, change in ELM behavior, poloidal detachment, divertor detachment, a local radiative collapse, or finally a plasma disruption. Of particular interest is the disruptive density limit as the RFP doesn't have an H-mode or a divertor. More importantly,

the disruptive limit represents the maximum achievable density, whereas other density-limiting phenomena can occur at lower densities [1]. Like other effects of the density limit, the tokamak disruption begins with a cooling of the plasma edge as $n_{GW} \rightarrow 1$. This region of cool plasma expands from the edge into the core leading to a shrinkage of the current channel. The current profile becomes unstable, and the subsequent growth of large amplitude MHD fluctuations breaks flux surfaces and connects field lines to the wall. Heat now flows along field lines leading to a "thermal quench" as particles and heat are dumped to the wall, sometimes damaging in-vessel components. With the plasma temperature reduced, it can no longer carry the plasma current as well. The current is then inductively transferred to the vessel or to runaway electrons [3]. This "current quench" can damage devices through two routes: mechanical forces exerted on the vessel from the induced currents or the impact of runaways on the vessel walls. Though the mechanism of the limit is well described, it is not understood why the density corresponding to its onset scales with plasma current.

Surpassing the Greenwald limit has been accomplished through the modification of the density profile. In particular, by peaking the profile, the limit is exceeded, indicating that physics in the plasma edge is responsible for the limit. Profile peaking can be accomplished through deep pellet fueling, edge pumping, neutral beam injection, or transport modification. Pellet fueling has led to densities up to $1.5n_{GW}$ in improved confinement (H-mode) tokamak discharges [4].

4.3 Previous RFP density limit experiments

Historically, the operating range of the RFP has been characterized by the ratio I_ϕ/N [5], where N is the particle count per unit length. Typically, RFPs operate with $I_\phi/N > 1 \times 10^{-14}\ A \cdot m$ which if after changing units and substituting for $N = \pi a^2 <\mathrm{n}>$, the Greenwald limit is obtained. Most RFP experiments [5, 6, 7] apparently exceed the Greenwald limit during both the startup and decay of the plasma current.

Early RFP experiments in ETA-BETA II reported a "quiescent" phase for I_ϕ/N values of $1.0 - 1.5 \times 10^{-14}\ A \cdot m$ [5]. The start of this phase corresponded to the reversal of the edge magnetic field signaling the formation of an RFP configuration. Later work showed that there was a high density limit corresponding to an increase in radiated power that scaled with plasma current [8].

The most in-depth look at RFP density limits has been undertaken by the RFX group [7]. RFX has seen fast terminations (lasting $\sim 5\ ms$) at densities as low as $0.5 n_{GW}$ but only at higher currents ($I_\phi > 0.9\ MA$). These fast terminations begin with a thermal quench wherein the core temperature drops over a period of several milliseconds. At this time, both the loop voltage and MHD activity increase. Field reversal is then lost, and the plasma's energy is dissipated on the walls of the vessel liberating particles and resulting in a density spike. At lower currents, RFX would experience a slow termination wherein the current would decay slowly. The upper bound on density for these slow terminations corresponded to the Greenwald limit.

Like the tokamak, the cause of the limiting behavior in the RFP is still unclear. For instance, one mechanism that has been investigated is radiative power loss outpacing the input power. At higher densities, low Z impurity radiation was observed to increase in some experiments [8] but in others the radiative losses comprised only a small fraction of

the input power [9].

4.4 MST density limit experiments

While achieving densities near or exceeding the limit has been a goal in MST, so has determining how the plasma current behaves near/above the limit, *e.g.*, does it decay as the limit is reached or remain unchanged? There are multiple scenarios and techniques that approach and/or exceed the Greenwald limit in the MST. The scenarios include plasma startup (when I_ϕ is ramping up), ramp-down (when I_ϕ is decaying), in an "over-recycled" shot, and during a "poor discharge." The techniques employed to reach the Greenwald limit include single valve fueling, multi-valve fueling, and pellet injection. For MST the Greenwald limit can be expressed as:

$$n_{GW}[10^{13}\ cm^{-3}] = 1.27 \times I_\phi[100\ kA]. \tag{4.3}$$

In the calculation of the Greenwald limit for MST, the plasma minor radius (0.5 m) is used as opposed to the vacuum vessel minor radius (0.52 m). The difference arises due to both the toroidal nature of MST and in-vessel components, *e.g.* tiles, b-dot coils, and limiters covering the inboard toroidal gap.

It is quite possible that the current channel doesn't occupy this full volume during startup, ramp-down, and other times of interest. This shrinking could be a result of instability, the edge being too cool to support current during startup, or simply part of the ramp-down process. Regardless of mechansim, n_{GW} would increase. Not having investigated any contraction, the current channel will be assumed to have a radius of 0.5 m.

The Greenwald limit has been defined as the non-disruptive upper bound on the achievable line averaged density for edge-fueled, current-carrying toroidal plasmas. Through pellet injection, tokamaks can exceed this limit due to peaking of the density profile. As seen in Chapter 3, pellet injection can peak the density profile of the RFP as well, but the effect is short-lived in standard plasmas due to the comparatively poor confinement. After several milliseconds, the profiles lose their peakedness, gaining the shape of an edge-fueled profile, albeit with higher particle content (Fig. 4.1). For the pellet injected case in Figure 4.1, peakedness ($\frac{n_e(0)}{<n_e>}$) falls back to pre-pellet value within 5 ms of the peak density. The Greenwald scaling, then, can be tested using pellet injection along with the single- and multi-valve fueling techniques.

4.4.1 Ramp-up and ramp-down

In its standard mode of operation, MST apparently exceeds the Greenwald limit at the beginning of a discharge[1] (current ramp-up) and at the end of a discharge[2] (ramp-down phase) as seen in Figure 4.2. Concerning the ramp-up phase, the large initial density is referred to as the "ionization spike," and can be up to three times larger than the density later in the discharge. The experimenter can control the magnitude of the ionization spike by altering either the pre-fill pressure and initial seed toroidal field $B_\phi(0)$. By increasing $B_\phi(0)$, it is easier to instigate plasma breakdown. As more gas is ionized, the ionization spike is then larger.

During current ramp-up, the density typically starts out higher than n_{GW} [Fig. 4.3(a)], however, there are two caveats. The first is that it is quite possible that the radius of the

[1]The limit is exceeded barring the current channel contraction caveat.

[2]The current is decaying already, so it's unclear whether the density limit is exceeded without consequence.

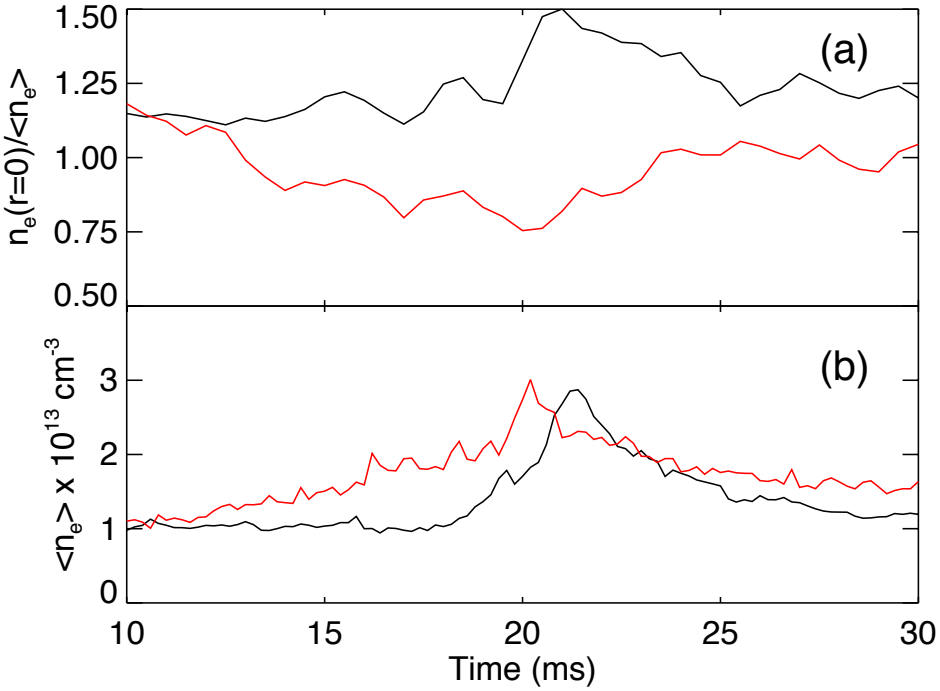

Figure 4.1: Peakedness values for different fueling techniques: pellet fueling of standard 200 kA discharge (black) and single-valve fueling of a 200 kA standard discharge (red). [Shots 1050518097 (black) and 1050924127 (red)]

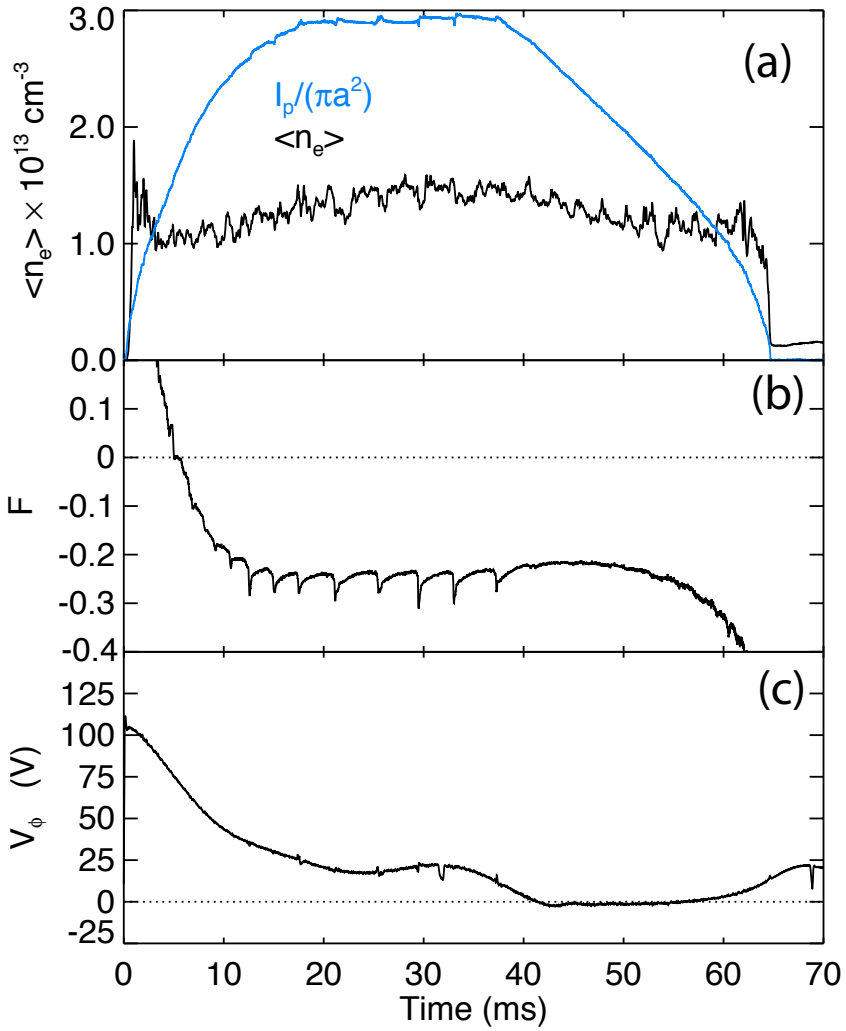

Figure 4.2: Data for typical low current discharge ($I_\phi \sim 250\ kA$). In (a) the $<n_e>$ is compared to the Greenwald density n_{GW}. During the ramp up phase, $<n_e> > n_{GW}$, but the plasma has yet to reverse (b). During ramp-down, the plasma is still reversed and $<n_e> > n_{GW}$. The surface toroidal voltage (c) is shown to indicate that the beginning of the ramp-down phase ~ 40 ms occurs when V_ϕ reaches zero *i.e.* no current drive. (Shot 1050924017)

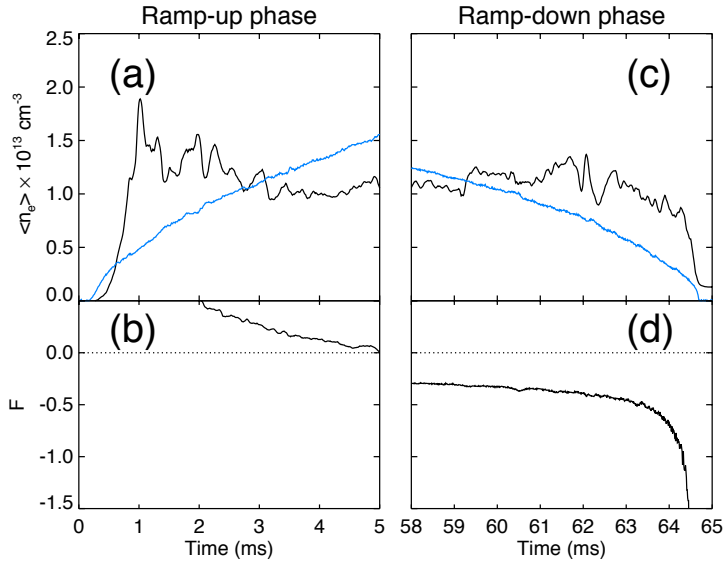

Figure 4.3: Close-up of density and reversal data in Fig. 4.2. Again the Greenwald limit is depicted in blue for (a) and (c)

current channel is less than 0.5 m, which would increase n_{GW}. Second, during the current ramp-up, the magnetic field reversal has yet to occur [Fig. 4.3(b)]. This may be more of a technicality, but an RFP, by definition ($\frac{B_\phi(a)}{<B_\phi>} < 0$), has yet to be formed.

Perhaps a more interesting situation occurs at the end of a discharge where the current is ramping down as the density is staying relatively constant [Fig. 4.3(c)] while $F < 0$. During current ramp-down, there's no longer any "drive," *i.e.* the surface toroidal voltage V_ϕ goes to zero [the period between t = 40 and 60 ms in Fig. 4.2(c)]. With the drop in current drive, sawtoothing behavior falls off as seen in the evolution of the reversal parameter F in Figure 4.2(b). For higher density discharges ($<n_e> > 2 \times 10^{13}\ cm^{-3}$) achieved through intense gas-puffing, sawtoothing behavior during the decay phase generally does not disappear, possibly due to unfavorable changes to edge current and pressure profiles.

4.4.2 Approaching the limit in the middle of standard discharges

Through wall-loading and multi-valve fueling, $N_{GW} \rightarrow 0.7$ can be achieved during the current flat-top in MST, where $N_{GW} = \frac{<n_e>}{n_{GW}}$. However, creating these high-density, edge-fueled discharges is challenging. To arrive at line-averaged densities approaching and exceeding $2 \times 10^{13}\ cm^{-3}$ using MST's standard fueling system requires a series of discharges with the degree of gas-fueling gradually increased. The gradual increase is necessary in order to achieve a controllable balance between wall-recycling and gas puffing. Occasionally, the experimenter will need to decrease the gas puffing for a few discharges in order to draw excess fuel from the walls (effectively conditioning the walls).

In the event that there is over-fueling due to some combination of wall-loading and gas-puffing, the density can run away and quench the current as shown in Fig. 4.4 – an "over-recycled" shot. Shown are two consecutive shots with the second (red) discharge appearing like its predecessor until 30 ms, when the density begins to rise. At $\sim 38\ ms$, the density approaches the Greenwald density, and $|\frac{d}{dt} I_\phi|$ suddenly increases with the discharge terminating shortly thereafter. The density increase began at 30 ms without active fueling implying that some wall interaction led to excess recycling, the rising density, and the eventual termination of the discharge. The sudden increase in $|\frac{d}{dt} I_\phi|$ may be related to the Greenwald limit, but the red discharge's decline began much earlier. The initial decline began when the density was 50% of the Greenwald density indicating that either the limit could be lower for the RFP, or something has changed relative to the black discharge that is not related to density.

Some discharges, however, can best be described as "poor," and their maximum non-disruptive density may be lower than that predicted by the Greenwald limit. In these discharges, increased fueling (be it gas puffing or wall recycling) during the startup phase

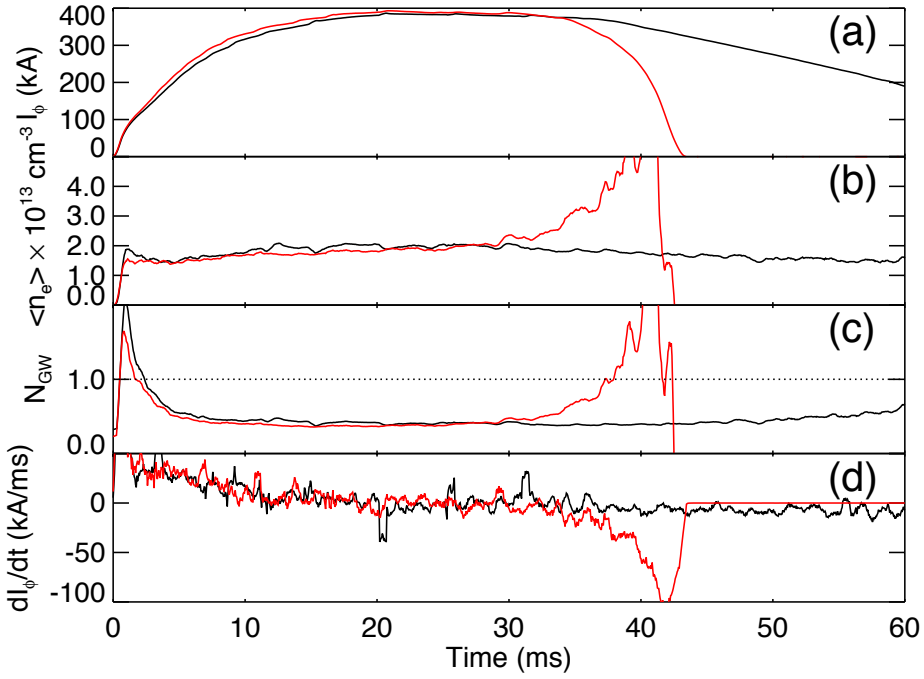

Figure 4.4: Line-averaged density (a) and plasma current (b) for consecutive shots. The first shot (black) exhibits a normal current and density evolution. In the subsequent shot (red), the gas programming was unchanged but at t = 30 ms, the density rises quickly due to an influx of material from the wall. [Shots 1041030127 (black) and 1041030128 (red)]

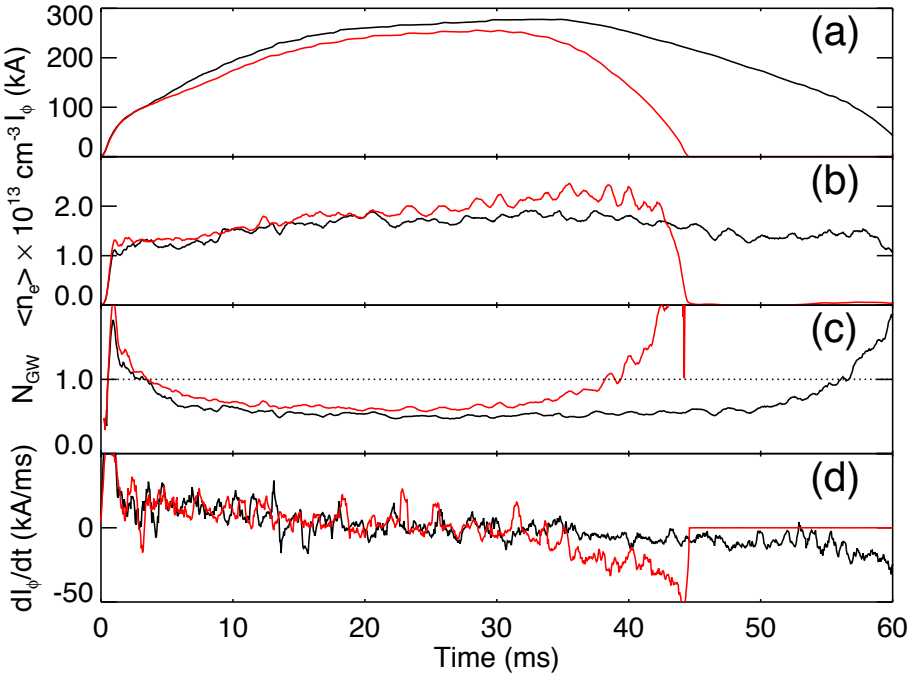

Figure 4.5: Comparison of "good" (black) and "poor" (red) discharges. Plasma current ramp-up is the same for the two shots until t = 5 ms. At this point, the poor discharge's ramp-up is retarded and reversal delayed. It also a cooler discharge inferred from the level of CIII and CV emission as compared to the good shot. [Shots 1041022091 (black) and 1041022092 (red)]

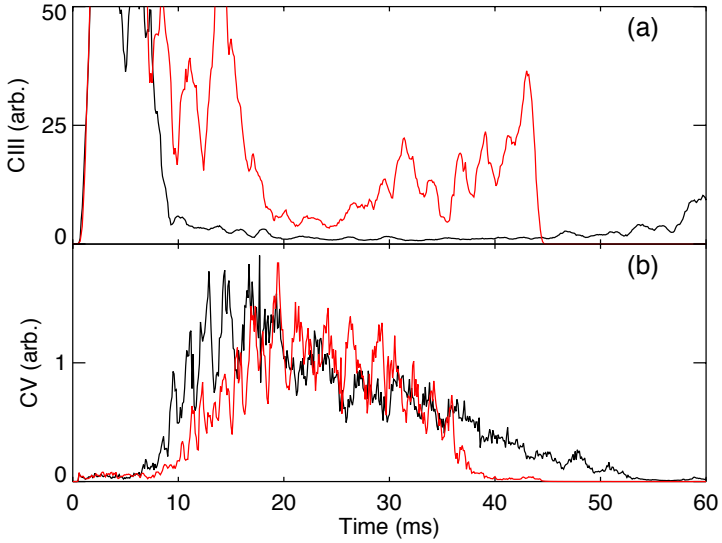

Figure 4.6: The increase in CIII emission and drop in CV emission in the red discharge relative to the black discharge indicate that it is cooler than the black discharge both early (before 20 ms) and late (after 35 ms) in the discharge. [Shots 1041022091 (black) and 1041022092 (red)]

slows the current ramp-up due to the increased resistivity (red discharge of Fig. 4.5), and the peak current is lower compared to the previous discharge (the two discharges are consecutive). The current decay begins much earlier, and consequently the Greenwald limit is approached much earlier than in the black discharge. For the red discharge, $|\frac{d}{dt}I_\phi|$ begins to increase at $t \sim 32\ ms$ when $N_{GW} \sim 0.7$. Using the emission levels of the CIII and CV lines [Figs. 4.6(a-b)], the relative temperatures can be inferred. The good discharge burns through the lower energy carbon more rapidly (earlier drop in CIII) moving to higher charge state of carbon (CV) than in the poor discharge indicating that the former is hotter. At $t \sim 35\ ms$ when $N_{GW} \sim 0.8$, there's a resurgence in CIII emission and CV emission falls off indicating that the plasma is cooling.

Exploration of the density limit using the multi-valve system has resulted in many

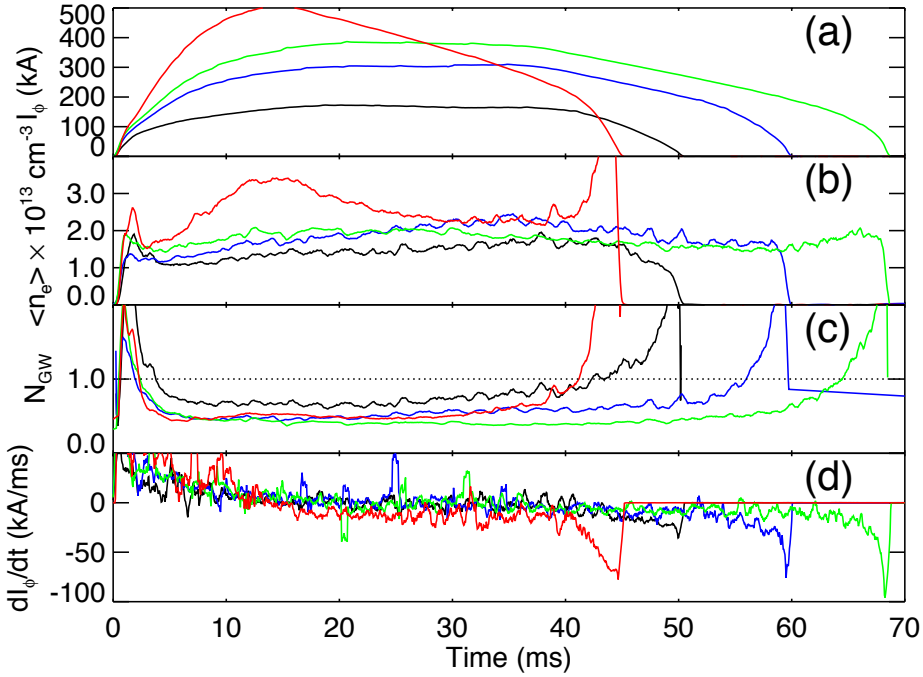

Figure 4.7: Compilation of highest densities achieved with multi-valve fueling at different nominal currents: 200 kA (black), 300 kA (blue), 400 kA (green), 500 kA (red). Voltage programming was different for 500 kA case, hence the altered current evolution. Again all discharges exceed Greenwald during ramp-up and ramp down. [Shots 1041022017 (black), 1041025050 (blue), 1041030127 (green) and 1060912085 (red)]

over-recycled and poor discharges. Onset of density-limiting behavior in these discharges corresponds to $N_{GW} \leq 1$. However, this maximum density will be shown to be more of an engineering problem (not enough fueling) as opposed to some physical limit (Greenwald-related mechanism). Figure 4.7 shows N_{GW} for different currents, and the maximum value ($N_{GW} \sim 0.7$) occurs at the lowest current). The 500 kA case is the only one in which a 250 V supply was used to actuate the valves but N_{GW} only reaches ~ 0.5 during the middle of the discharge. The evidence for it still being an engineering problem is indicated by the ability to achieve densities near n_{GW} using the single valve.

High densities were easily achieved in RFX at all currents, as nearly 100% of the plasma-facing wall is graphite tile. The prevalence of carbon on the wall increases the amount of wall-fueling possible but also makes density control difficult. For MST, the wall is predominantly aluminum with $\sim$ 10% covered by graphite tiles making the densities naturally lower than RFX. To overcome this, two other fueling techniques have been applied to the density limit search: single valve fueling and pellet injection.

Using the single high throughput valve, the Greenwald limit can be reached and fast terminations of the current are observed (Fig. 4.8). Due to the influx of cold material, both discharges experience a current decay, but the first shot (black) recovers. In both cases, the Greenwald density is reached [Fig. 4.8(c)] near the end of the gas injection phase (t = 10 to 20 ms). However, in the terminating case, the limit is breeched (t = 18 ms) before the end of the gas puff and coincides with an acceleration in the rise of plasma density.

Standard MST discharges with pellet fueling have reached the Greenwald limit for currents up to 300 kA. As in the single-valve discharges, there are cases where an accelerated decay of the plasma current occurs following injection (but only after some delay).

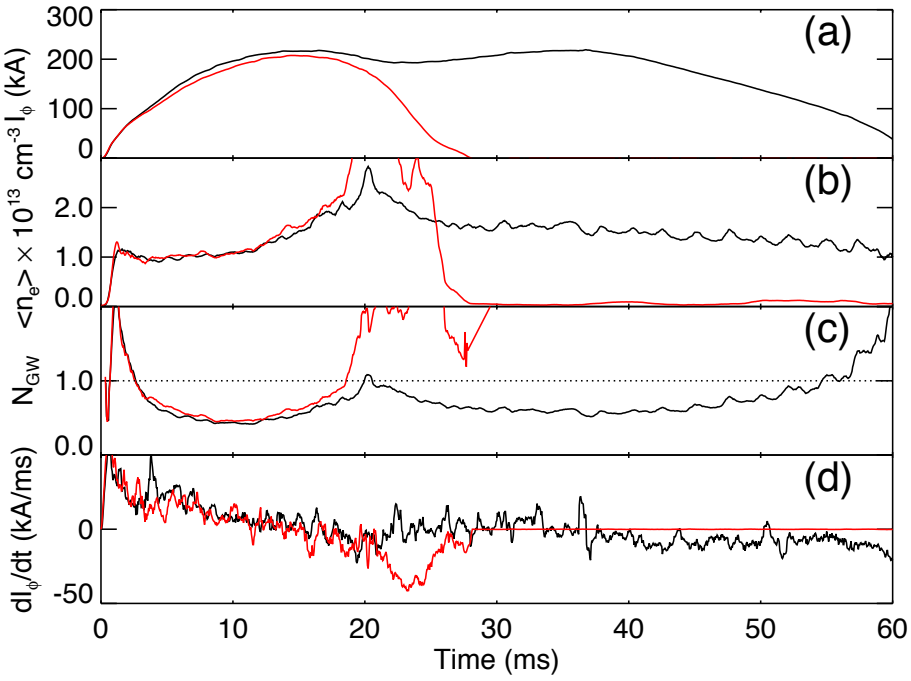

Figure 4.8: Data for two consecutive shots using single-valve fueling. The red discharge (second in this progression) has a slightly lower plasma current (a). In both discharges, single-valve fueling occurs from t = 10 to 20 ms. In the red discharge, the density (b) deviates from what was seen in the black discharge at t = 17 ms. $N_{GW} \sim 1$ in both discharges (c) but when the red discharge reaches n_{GW}, there's a knee in the density's temporal evolution. At t = 21 ms, $\frac{dI_\phi}{dt}$ (d) is the same for both discharges until the density rises again in the red discharge after which $|\frac{d}{dt}I_\phi|$ quickly rises. [Shots 1050924127 (black) and 1050924128 (red)]

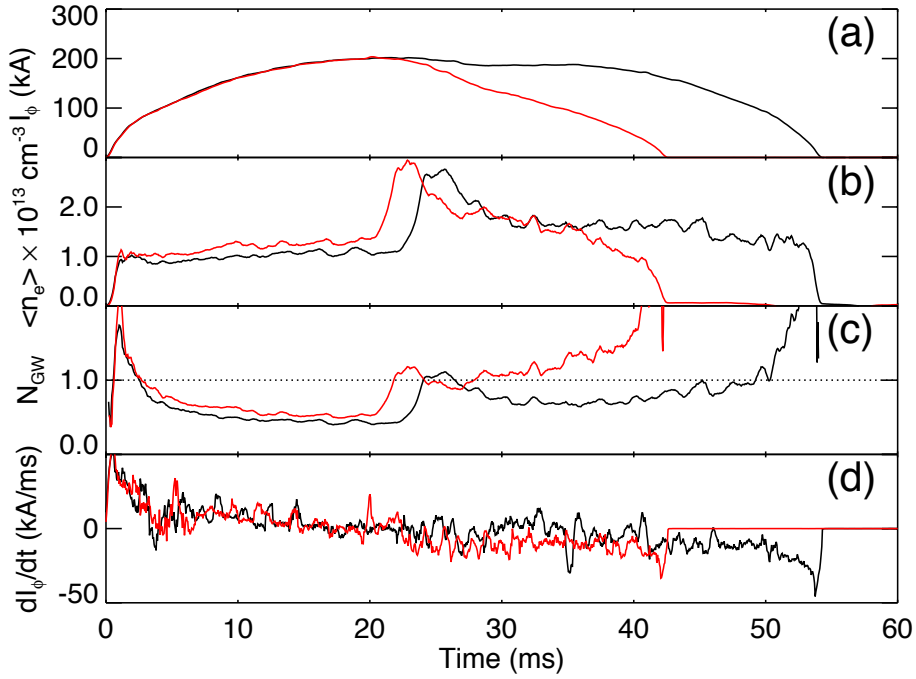

Figure 4.9: Data for two similar pellet-injected shots at 200 kA with standard programming. A single 1.6 mm pellet was injected into each discharge with speeds of 154 m/s (black) and 143 m/s (red). According to microwave cavity measurements, the mass of the second pellet (red) was $\sim 5\%$ larger than the first (black). In both discharges, pellet injection more than doubles the density (b) leading to $N_{GW} > 1$ (c) and a slight drop in current (a). The shot depicted in red does not recover, and there's a soft-termination. [Shots 1041030072 (black) and 1041030076 (red)]

Pellet fueling can also result in a slow decay of the discharge wherein both the current and density slowly ramp down. This decay is still quicker than the standard discharge without impulsive fueling (pellet injection or single valve fueling).

In Figure 4.9, two pellet-fueled, standard discharges are shown, both with nominal plasma currents of 200 kA. Pellets are injected at t $\sim$ 20 ms, and in both cases, the line-averaged density is nearly tripled [Fig. 4.9(b)]. Plasma current evolution is the same for the two cases [Fig. 4.9(a)], and both experience a drop in current due to increased

resistivity following the cooling effect of the pellets. The second shot (red), however, doesn't recover and slowly terminates. This slow termination lasts $\sim 20\ ms$, much longer compared to the fast termination shown in gas-injected case (Fig. 4.8). The decay begins during a period when N_{GW} remains near unity but after the pellet has fully ablated.

Similar to the 200 kA case, pellet-induced terminations have been observed at 300 kA when N_{GW} approaches unity (Fig. 4.10). However, in this case the termination results in the density of the red discharge rapidly increasing [Fig. 4.10(b)] - contrary to the result in the 200 kA case. The termination has the evolution of an "over-recycled" discharge (*e.g.* red discharge of Figure 4.4). This isn't to say that slow terminations don't occur at 300 kA, as they do. However, these fast-terminations or "over-recycled" discharges haven't been observed while pellet fueling 200 kA standard discharges. It appears that getting to the Greenwald density during pellet ablation doesn't hurt the discharge, but remaining near the limit after the pellet has been fully ablated does. This effect is due to the short particle confinement time ($\sim 1\ ms$) which causes the density profile to relax (*i.e.*, flatten) following pellet ablation.

4.4.3 PPCD discharges

MST has a method for transport modification – PPCD. Combining pellet injection with PPCD, sustainment of low current discharges above the Greenwald limit has been achieved (black trace in Fig. 4.11). In this discharge, a single 1.6 mm diameter, slow pellet was injected, arriving just as PPCD was applied (10 ms). The density is quickly quadrupled, reaching $N_{GW} = 1$ [Fig. 4.11(c)]. As fluctuations are reduced (at 15 ms), the density rises even more reaching its peak at 20 ms with $N_{GW} \rightarrow 1.3$ without any sign of termination.

During PPCD, fluctuation-induced transport is reduced, increasing the particle con-

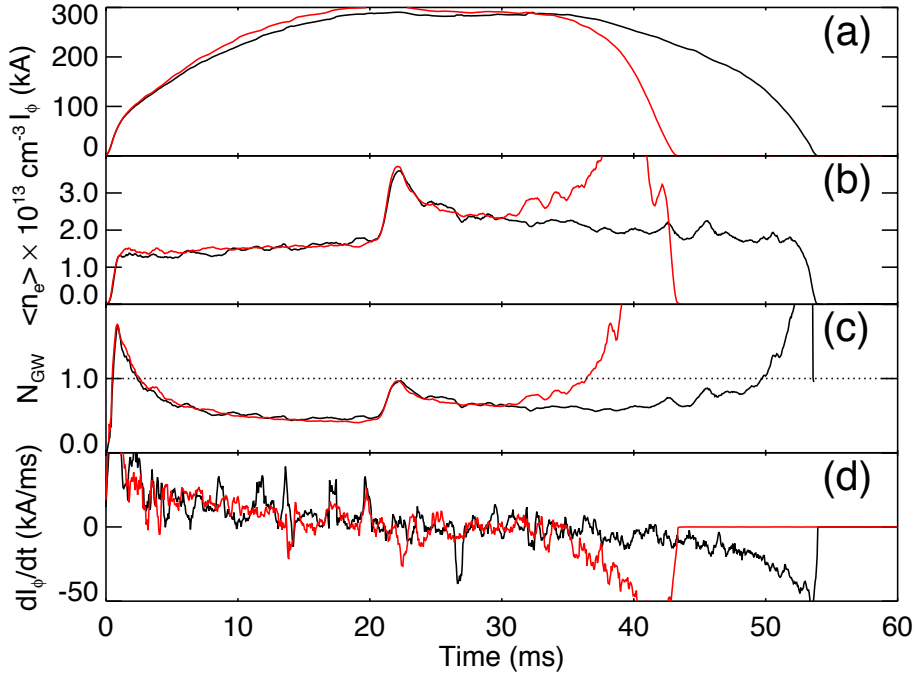

Figure 4.10: Data for two similar pellet-injected shots at 300 kA with standard programming. A single 1.6 mm diameter pellet is responsible for the density change in each shot. However, in both cases, a 1.3 mm pellet was fired as well. Neither 1.3 mm pellet was observed entering the plasma. Both of the 1.6 mm pellets had speeds of 330 m/s, and the second pellet (red) was $\sim 8\%$ larger than the first (black). In both discharges, pellet injection leads to $N_{GW} \sim 1$ (c) and slight drop in current (a). It is interesting to note that in the case of the red discharge, as $N_{GW} \rightarrow 1$ near the end of the discharge (t = 37 ms), there's a distinct change in the behavior of $\frac{dI_\phi}{dt}$ resulting in the fast termination. [Shots 1041030114 (black) and 1041030121 (red)]

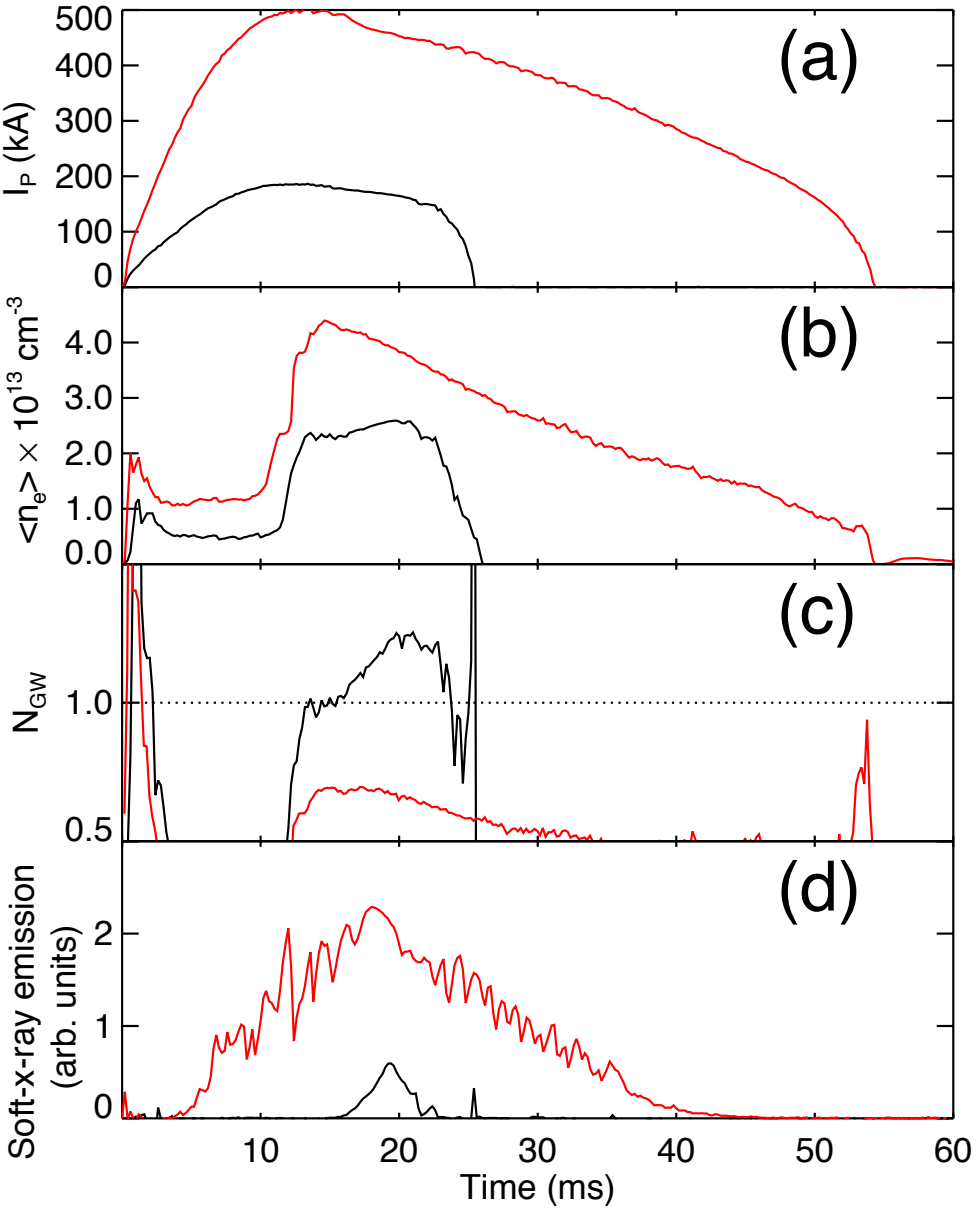

Figure 4.11: Comparison of highest densities achieved with pellet injection into PPCD discharges at different currents: 200 kA (black) and 500 kA (red). In the 200 kA discharge, a slow 1.6 mm pellet was injected, and for the 500 kA case, a slow 1.6 mm pellet and fast 1.6 mm pellet were injected. [Shots 1060224046 (black) and 1060912035 (red)]

finement time. The sustainment of the high density following pellet ablation (compared to the falling density observed after the pellet is done ablating in a standard discharge) can be attributed to the improved confinement. Additionally the density profile remains unchanged for the period of PPCD so that it remains peaked. Even as the density is at its highest, the temperature is still rising as inferred from the rising soft-x-ray emission [Fig. 4.11(d)]. This particular discharge will be discussed in more detail in Chapters 5 and 6, but it should be noted that for all pellet-fueled PPCD experiments, there is no gas puffing aside from pre-fill and a puff near the end of the current ramp-down.

Also shown (red trace) in Figure 4.11 is the highest density case at 500 kA where pellet-fueling was combined with PPCD. The evolution of both density and current are very similar but in this case one fast and one slow pellet (both 1.6 mm in diameter) are injected. Due to the limited size of the pellets and the higher current, however, this discharge's Greenwald number only reaches ~ 0.7. This discharge represents the highest achieved density for pellet injection in MST.[3]

4.5 Summary

To avoid disruptions, edge-fueled tokamak plasmas operate below the empirical Greenwald limit. The limit can be surpassed through core fueling techniques like deep pellet injection. Using either single valve fueling or pellet injection, the Greenwald limit has been approached for a small range of currents ($0.2\ MA \leq I_\phi \leq 0.3\ MA$) in MST. In these discharges, both fast and slow terminations have been observed for densities near the limit. In pellet fueled discharges, terminations will start only after the pellet has been

[3]Higher densities can be achieved without pellet injection during a disruption but due to their uncontrollable nature and poor confinement characteristics are considered less useful for research.

fully ablated, but for edge-fueled discharges, terminations can begin while the fueling source is still on. This delay is explained by the poor particle confinement in a standard discharge, i.e. shortly after the pellet's ablation, the density profile will have relaxed from a peaked to a flat profile resembling an edge-fueled discharge.

If pellet fueling is combined with the tearing mode control of PPCD, densities exceeding the Greenwald limit ($n_{GW} = 1.3$) can be sustained for the length of PPCD without any sort of termination. The suppression of the tearing modes reduces transport, and the peaked density profile produced by pellet injection is sustained. In standard discharges, the tearing modes degrade confinement causing the density profile to evolve quickly following pellet ablation. Along with the increased transport, there appears to be a rise in tearing mode fluctuations during early terminations in standard discharges. Because PPCD both reduces fluctuations and consequently transport, it is difficult to decouple the effects of a peaked density profile from that of the reduced fluctuations.

Although a density limit corresponding well with the Greenwald limit has been observed, its scaling with plasma current has not been confirmed. In order to access Greenwald densities for the full range of MST plasma currents ($I_\phi \leq 0.6\ MA$), changes to the fueling systems are required. The addition of two more high throughput puff valves would allow for densities approaching $7 - 8 \times 10^{13}\ cm^{-3}$ while if spaced properly, would allow for a more toroidally symmetric fuel source. The next upgrade of the injector will add the capability of producing 2.0 mm diameter pellets whose particle inventories, N_{pellet} will have an upper bound of 7.5×10^{20} compared to the 1.6 mm diameter pellet in which $N_{pellet} \sim 3.9 \times 10^{20}$. This increase in particle content for a single pellet indicates that it would take 1 or 2 of the these large pellets to produce Greenwald numbers approaching unity for the highest currents in MST.

Bibliography

[1] M. Greenwald, Plasma Physics and Controlled Fusion **44**, R27 (2002).

[2] M. Greenwald *et al.*, Nuc. Fusion **28**, 2199 (1988).

[3] J. Wesson *et al.*, Nuc. Fusion **29**, 641 (1989).

[4] R. Maingi *et al.*, Phys. Plasmas **4**, 1752 (1997).

[5] A. Buffa *et al.*, in *Proc. 8th International Conference on Plasma Physics and Contr. Nuclear Fusion Research (Brussels, 1980)* Vol. 2, p. 275, 1981.

[6] H. Bodin *et al.*, Nuclear Fusion Supplement **1**, 641 (1983).

[7] R. Bartiromo *et al.*, in *27th EPS Conference on Contr. Fusion and Plasma Phys. (Budapest, 2000)* Vol. 2, p. 1380, 2000.

[8] S. Costa, R. De Angelis, S. Ortolani, and M. Puiatti, Nuc. Fusion **22**, 1301 (1982).

[9] A. M. L. Marrelli, P. Martin and G. Spizzo, Nuc. Fusion **38**, 649 (1998).

With my lighting bolts a-glowing

I can see where I'm going

Arcade Fire

5

Confinement at high-β

5.1 Introduction

The RFP's highest confinement plasmas have been achieved using the Pulse Parallel Current Drive (PPCD) technique but have been limited to low density ($n_e \sim 1 \times 10^{13}\ cm^{-3}$). Attempts to raise the density through gas puffing resulted in increased m = 0 fluctuations thereby degrading confinement. It is believed that the increased edge fueling during PPCD alters the edge current and/or pressure profiles in such a way as to destabilize the edge-resonant m = 0 modes. Because of the low density, ion heating from collisions with electrons is small, resulting in electron temperatures that can be as much as four times larger than the ion temperature, *e.g.*, in previous high current PPCD experiments [1], T_e increased during improved confinement to $\sim 1300\ eV$ while T_i was constant at 300 eV.

These high confinement, low density plasmas have had high plasma beta ($\beta_{tot} = 15\%$). It is not believed that this represents a β-limit as these discharges are most likely con-

finement and heating power limited.[1] In fact a β limit (in the form of pressure-driven tearing modes or disruptions) has not been established experimentally for the RFP. For the RFP to progress as a fusion reactor concept, improved confinement must be achievable at substantially higher density. To gauge its attractiveness as a fusion reactor, the β limit and its cause must be known.

The application of pellet-fueling to MST was hoped to bring about higher density during PPCD while maintaining low magnetic fluctuations. Accomplishing this, it was assumed that the higher density would improve coupling between electrons and ions. During improved confinement, the electron temperature would rise, and now the ion temperature would increase as well. Improved confinement at higher density then could lead to higher plasma beta.

The first experiments carried out on MST comparing pellet fueling to gas puffing during PPCD discharges showed that for modest increases in density (Fig. 5.1), magnetic fluctuations were unaffected by the pellets. In Figure 5.1, improved confinement for pellet-fueled (blue) and no-active-fueling (black) occurs between 15 and 20 ms. Figure 5.1(c) shows that for the gas-puffed case (red), fluctuations still exhibit discrete bursts while the both the pellet-fueled and non-fueled cases exhibit low m = 0 fluctuations.

In this chapter, the results of an extensive campaign investigating the effect of pellet fueling on PPCD discharges at both low (0.2 MA) and high (0.5 MA) current will be presented. It will be shown that the density can be quadrupled through pellet injection while retaining fluctuation reduction, and the confinement remains improved over standard (non-PPCD) discharges. The measurements and subsequent data ($n_e, T_e, T_i, Z_{eff}, D_\alpha$, etc.) necessary for computation of β and the confinement times (τ_E and τ_p) show that β_{tot}

[1] There isn't any evidence (early terminations, increased fluctuations, etc) to suggest that if the confinement time were longer, beta wouldn't increase further.

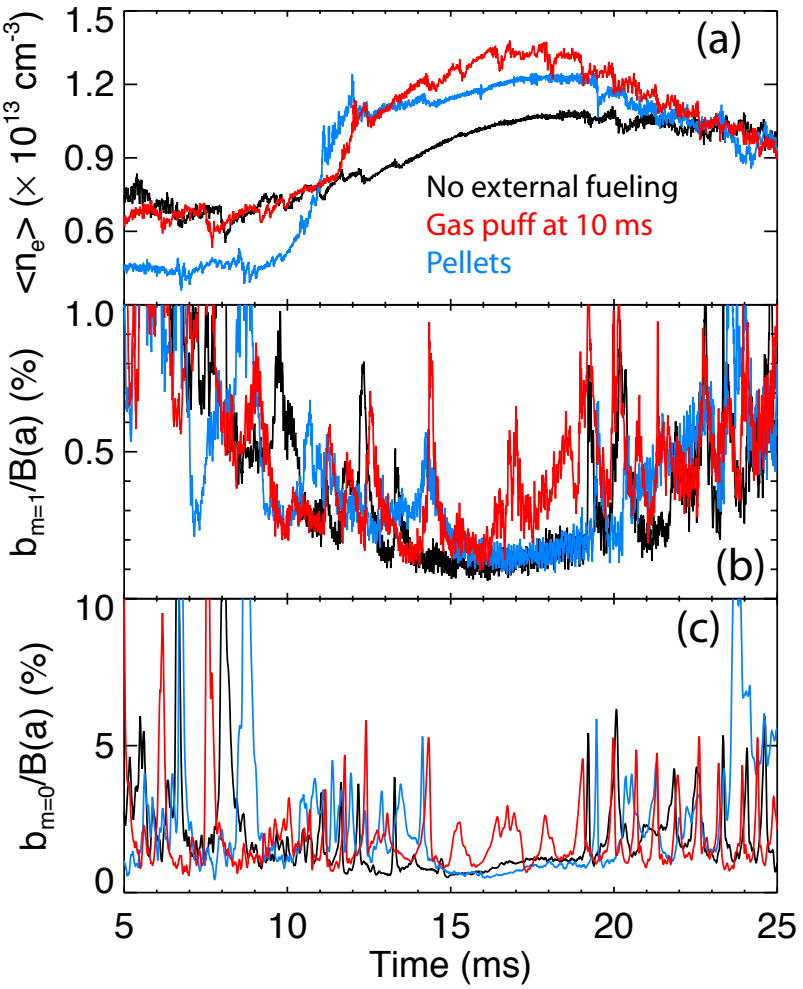

Figure 5.1: (a) the line averaged density, (b) core-resonant m=1, n=7-15 fluctuations normalized to the field at the wall, and (c) the edge-resonant m=0,n=1-4 fluctuations from representative shots are shown for the three fueling techniques available for PPCD discharges: no active fueling of any kind; a large gas puff at 10 ms; and 2 small pellets injected before the start of PPCD. For these discharges, PPCD starts at 10 ms. The period of best confinement in each discharge is $\sim 15 - 20$ ms, when fluctuations have become reduced. In the case of the gas-puffing, the confinement is not improved as fluctuations aren't reduced as much. [Shots 1030417015 (black), 1030417098 (red) and 1030528068 (blue)]

is increased to the highest value yet observed in MST and in any improved confinement RFP plasma. Concurrently, the confinement of particles and energy is comparable to low-density PPCD plasmas. Comparison of the confinement parameters to scalings relevant to RFPs and fusion devices indicate that indeed pellet injection is good for the RFP (in most cases). In the high current discharges, a significant increase in the ion temperature has been observed for the first time, though, it may be due to more than classical ion heating. As expected for a higher density plasma, the increased collisionality leads to changes in the nature of the plasma resistivity along with reduced production of runaway electrons.

The details of the achieving high-β discharges at both low ($I_\phi = 0.2\ MA$) and high ($I_\phi = 0.5\ MA$) plasma currents will be the subject of Section 5.2. Section 5.3 will cover measurements of the n_e, T_e, T_i, and J profiles for these discharges. Plasma quantities related to the heating of the electrons (measurements of Z_{eff}, calculation of the plasma resistivity, and hard-x-ray emission) will be discussed in Section 5.4. In Section 5.5, the attempts to carry out the ion power balance analysis for the high current discharges will be detailed. The calculation of confinement parameters (β, τ_E, and τ_p) and how they compare to several different scalings will be presented in Section 5.6. A summary of the key results will then be given.

5.2 High density PPCD operation

In low current (0.2 MA), improved confinement discharges, the highest plasma beta in MST is achieved. The largest density, electron temperature and ion temperature is observed in high current (0.5 MA), improved confinement discharges. What follows is a

detailing of how pellet-fueling was applied to each regime.

5.2.1 Low current

In low current discharges, pellets are injected so as to arrive at about the time that PPCD begins (generally at t = 10 ms). Too early, and the centrally peaked profile will relax to a flat "edge-fueled" density profile. Too late and it's in the middle of improved confinement, and upon entry, pellets will induce MHD activity. Typically the first few milliseconds of PPCD are noisy (MHD-wise) and make a good time for the pellet to enter. It was reasoned that any perturbation caused by the pellet would not matter as the disturbance is short-lived, typically lasting $< 3\ ms$.

For the case of injecting early into low current discharges, fast ($v_p \sim 1000\ m/s$) pellets (of any size) traverse the entire plasma. Large diameter ($\geq 1.3\ mm$), slow ($v_p < 200\ m/s$) pellets, however, can reach the core ablating before getting to the far edge and thus were ideal for these experiments.

In Figure 5.2, data from a pellet-fueled, low current (nominal $I_\phi = 0.2\ MA$) PPCD discharge are shown. A single 1.6 mm diameter pellet with $v_p = 170\ m/s$ was injected and arrived at approximately t = 10 ms as shown in Fig. 5.2(a) in both the central density $n_e(r = 0)$ (from the inverted FIR data) and line-averaged density $<n_e>$ (from CO_2 interferometer). Though it appears to arrive at t = 12 ms according to the CO_2 interferometer, calculations of pellet speed and arrival time put it just before 10 ms. The discrepancy is due to the time it takes the pellet to reach the core (the time response of the CO_2 interferometer to pellet injection was detailed in Section 3.2.3). As for the discrepancy with the FIR system, FIR data during ablation is difficult to process. For the most part this analysis is avoided due to the time it takes to remove fringe-skips for

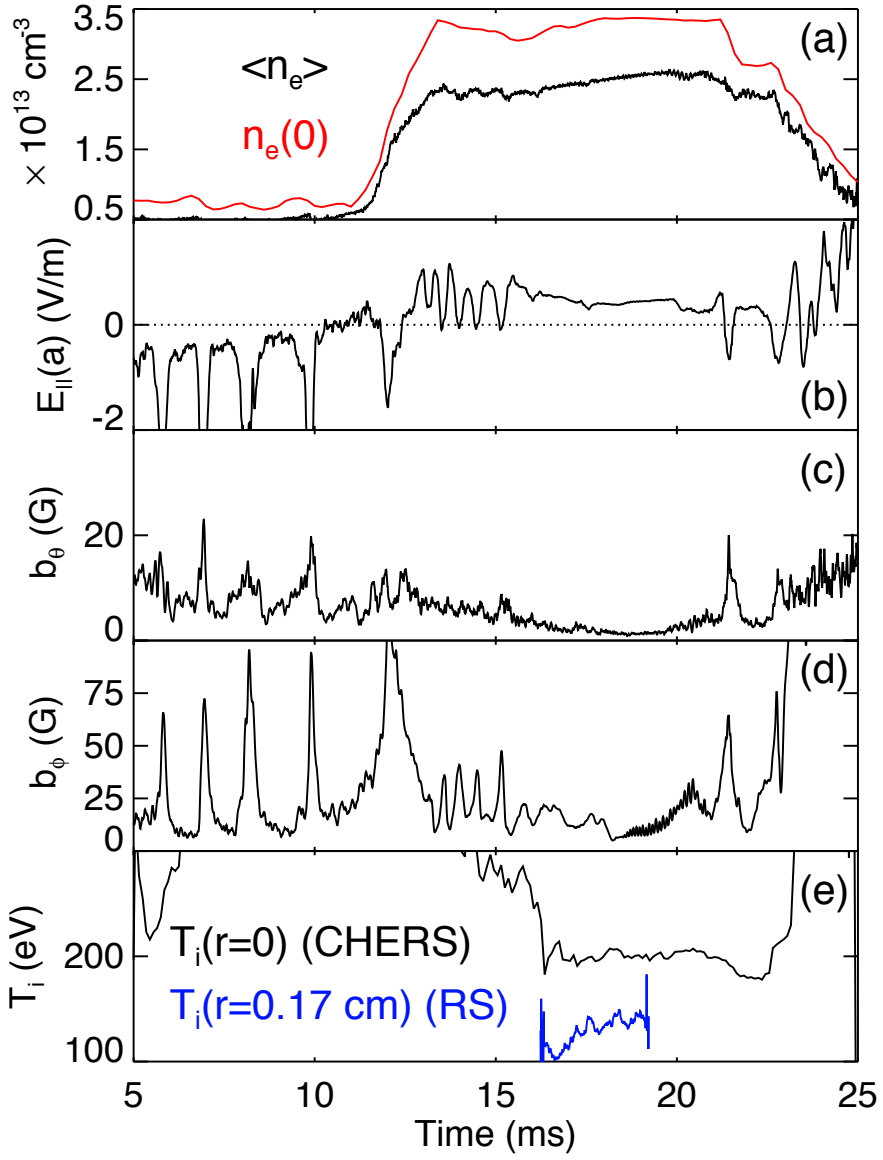

Figure 5.2: Data from a pellet-fueled, low current (nominal $I_\phi = 0.2\ MA$) PPCD discharge with pellet arriving at $\sim 10\ ms$: (a) the central density (from the inverted FIR data) in red and line-averaged density (from CO_2 interferometer) in black, (b) the parallel electric field at the edge, (c) core-resonant (m = 1, n = 8-14) magnetic fluctuations, (d) edge-resonant (m = 0, n =1-4) magnetic fluctuations, and (e) temperature of the impurity and majority ions as measured by CHERS (black) and RS (blue), respectively. (Shot 1060224046)

a single shot (up to a couple of days). In this case, however, it was done. In order to do it, though, the FIR chord densities are compared to the CO_2 interferometer so that any drastic changes in density will have the same time history as the CO_2 interferometer.

Unlike injection into standard discharges, pellet injection coupled with PPCD results in high densities that are sustained for the period of improved confinement. Comparing $<n_e>$ and $n_e(0)$, the density profile is flat before injection, and afterwards the profile becomes peaked, i.e., $n_e(0)/<n_e>$ increases. At the end of improved confinement ($t \sim$ 20 ms) the profile flattens out.

The parallel electric field at the edge [Fig. 5.2(b)] is shown to indicate the beginning of PPCD [$E_{||}(a) > 0$] and when fluctuation reduction is expected to begin. At t = 15 ms, $E_{||}(a)$ goes and stays positive. With PPCD having the desired effect, both the core-resonant (m = 1, n = 7-14) [Fig. 5.2(c)] and edge-resonant (m = 0, n =1-4) [Fig. 5.2(d)] magnetic fluctuations are reduced, and sawtoothing behavior is absent for the period of t = 15-21 ms. During PPCD operation the safety factor in the edge [$q(a)$] drops much further than during standard operation. In fact it is normal for an m = 1, n = -6 mode to become resonant in the edge. Care must be taken to separate the two sets of m = 1 modes. Separation of the core and edge m = 1 is possible due to the change in direction of mode velocities across the reversal surface. In this discharge, ion temperatures were measured with both the Rutherford scattering and CHERS systems [Fig. 5.2(e)].

5.2.2 High current

For high current discharges, the improved confinement period can be longer as the duration of PPCD can be varied. Two methods were tried for pellet fueling: injecting before the start of improved confinement (just like at low current) and injecting into an established

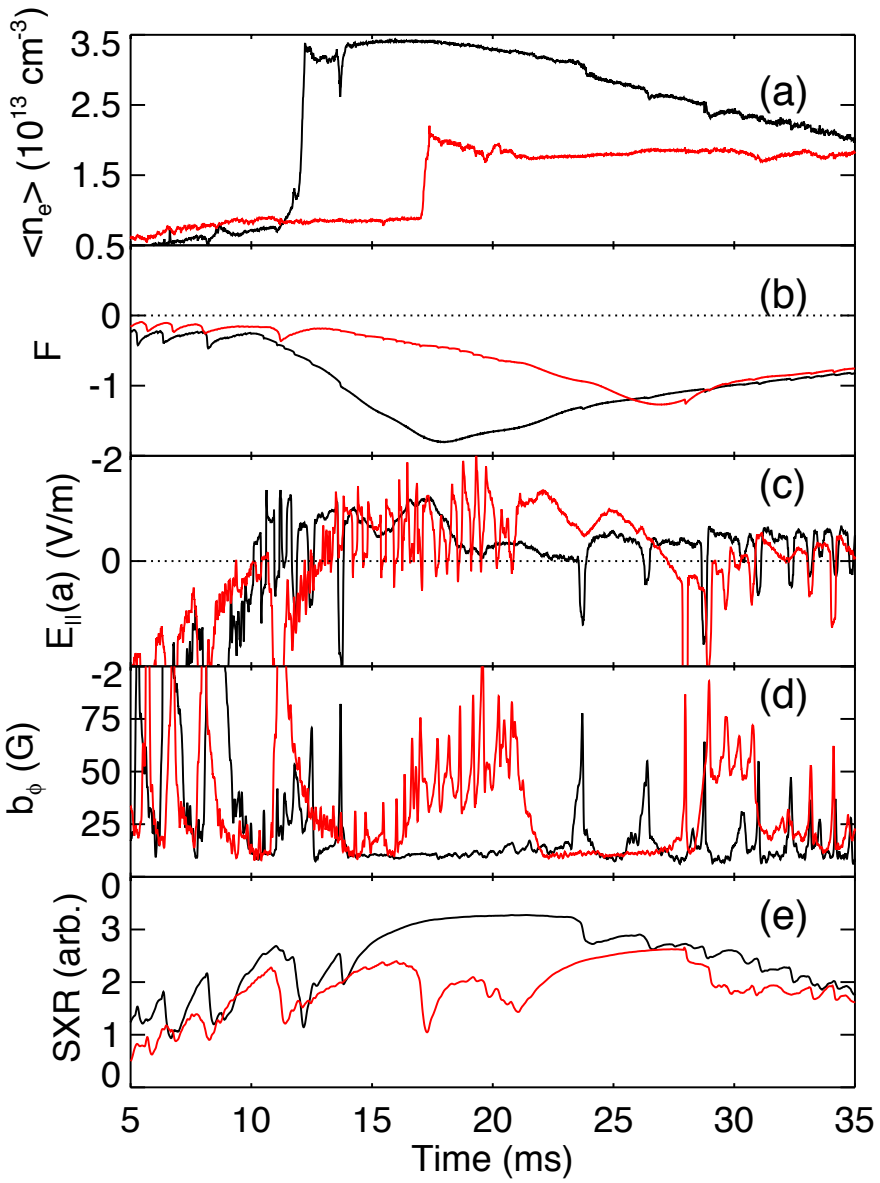

Figure 5.3: Data from two pellet-fueled, high current (nominal $I_\phi = 0.5\ MA$) PPCD discharges: (a) line-averaged density (from CO_2 interferometer), (b) the reversal parameter F, (c) the parallel electric field at the edge, (d) edge-resonant (m = 0, n =1-4) magnetic fluctuations, and (e) soft-x-ray emission. [Shots 1060517081 (red) and 1060523021 (black)]

improved confinement period. However it turns out that the former was more reproducible, and fully-diagnosed discharges were created using this method. In either case though, two 1.6 mm diameter pellets were usually injected. One pellet would be fast and the other slow. Due to the variability in pellet size and the differing penetration depths of the two pellets, different profile shapes were possible.

In Figure 5.3, the two methods are shown for comparison. Pellets were injected before the start of PPCD (black) and during PPCD (red). In the black discharge, two pellets were injected - each 1.6 mm diameter with velocities of 166 m/s and 1150 m/s. In the red discharge, only one pellet (1.6 mm diameter $v_p = 1160$ m/s) made it to the plasma although two pellets had been formed and fired. The second pellet was also 1.6 mm in diameter. Pellet diagnostics observed it traveling with a velocity of 147 m/s. At it happens (a little too often) a pellet can break up during flight, occasionally between the microwave cavity and plasma as in this case. Due to increased fueling of the black discharge, its line-averaged density is higher [Fig. 5.3(a)]. The onset of improved confinement occurs later for the red discharge [Figs. 5.3(c) & 5.3(d)], but the fluctuation reduction is comparable. The black discharge has a somewhat higher level of soft-x-ray emission, though in both cases, the emission level rises during improved confinement – a good indicator of rising electron temperatures.

In the end, "early injection" was used for the experimental campaign. When injecting during PPCD, there's a shortening of the length of improved confinement. Though the pellet injector appeared to be more reliable during early injection operation, trials of this mode of operation coincided with the development of the "dry-fire" cleaning technique between pellet shots (described in Chapter 2).

Figure 5.4 shows an early injection discharge (the same as in Fig. 5.3). The line-average

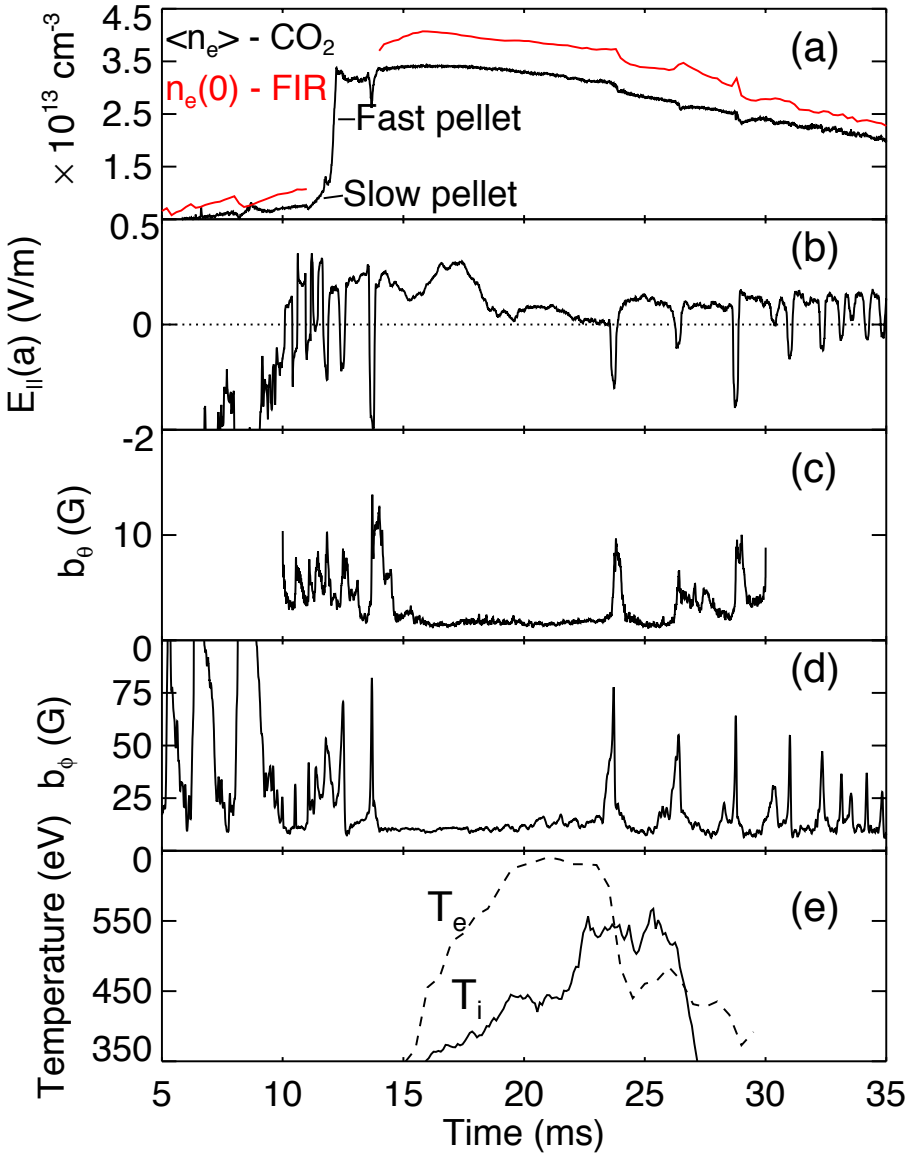

Figure 5.4: Data from a pellet-fueled, high current (nominal $I_\phi = 0.5\ MA$) PPCD discharge with pellets arriving at $\sim 11\ ms$: (a) the central density (from the inverted FIR data) in red and line-averaged density (from CO_2 interferometer) in black, (b) the parallel electric field at the edge, (c) core-resonant (m = 1, n = 7-14) magnetic fluctuations, (d) edge-resonant (m = 0, n =1-4) magnetic fluctuations, and (e) central electron temperature (broken line) as measured by SXR tomography and central ion temperature as measured by CHERS (solid line). FIR data during pellet ablation is removed due to the time-intensiveness of fringe-skip removal. (Shot 1060523021)

density is shown again but with the central density (from inverted FIR measurement) overlayed in red [Fig. 5.4(a)]. PPCD takes hold at t = 14 ms as seen in the reduction of both the core-resonant (m = 1, n = 7-14) and edge-resonant (m = 0, n =1-4) magnetic fluctuations [Figs. 5.4(c) & 5.4(d)]. During PPCD, the electron temperature rises due to the drop in fluctuation-based transport which is seen here in the plot of the central electron temperature [broken trace in Fig. 5.4(e)] as measured with soft-x-ray tomography. What hasn't been seen before during the improved confinement period induced by PPCD is a rising ion temperature. Due to pellet injection and mechanisms to be discussed in Section 5.5, ion temperatures are for the first time observed to rise during improved confinement [solid trace in Fig. 5.4(e)].

5.3 Profile measurements of equilibrium quantities

In order to calculate the confinement times and plasma beta, the density, temperature, and current profiles were measured for both high and low current, pellet-fueled improved confinement discharges.

5.3.1 Density profiles

As discussed in Section 2.5, evolution of the density profile is measured with the FIR system. The discharges with the highest densities and lowest fluctuations were achieved when pellets arrived in the t = 8-13 ms window (the beginning of PPCD). Due to the variation of slow-pellet arrival times, a single slow pellet was injected in low current experiments. If the second pellet's arrival time wasn't optimal, the discharge (already doing well due to proper arrival of the first pellet) would be degraded. Figure 5.5(a)

shows a 0.2 MA discharge where a single 1.6 mm diameter slow ($v_p = 170\ m/s$) pellet is injected. From CCD imaging, the pellet is observed to reach the core, and the resulting density profile confirms this.

For high current discharges, two large pellets (1.6 mm diameter) were injected in order to reach the highest densities possible: one fast ($v \sim 1200\ m/s$) and the other slow ($v \sim 100-200\ m/s$). The arrival time of the fast pellets was controllable to within several hundred microseconds, whereas the slow pellets arrived in a window of $\sim 5-10$ ms. This large variation in arrival time for the slow pellet in conjunction with the poor control of pellet mass introduced a crude sort of profile shape "control." By virtue of the number of shots taken, it was possible to get profile shapes that ranged from peaked to flat to hollow. At high current, profiles with the peaking observed at low current were not obtained. The definition of "peaked" for high current discharges has been altered to mean a profile with no off-axis peaking and can be somewhat flat in the core [Fig. 5.5(b)]. Flat profiles are flat in the core but as seen in [Fig. 5.5(c)] still possess some off-axis peaking. Hollow profiles possess the off-axis peaking but aren't flat near the core [Fig. 5.5(d)]. From CCD imaging, slow pellets were observed to fully ablate in the edge, and the larger, well-formed fast pellets cross the whole plasma. If the fast pellet were to break up or somehow be smaller than expected, it would not cross the entire plasma and would ablate in the near edge or core. The sum of these ablation characteristics is that regardless of pellet quality, the edge is preferentially fueled although the core does receive fuel so that the resultant profile is different from that derived from gas puffing.

Later, calculation of τ_p will show that, regardless of the density profile shape, each of these discharges exhibited improved particle confinement. Other characteristics of low density PPCD discharges are also observed following pellet injection into PPCD dis-

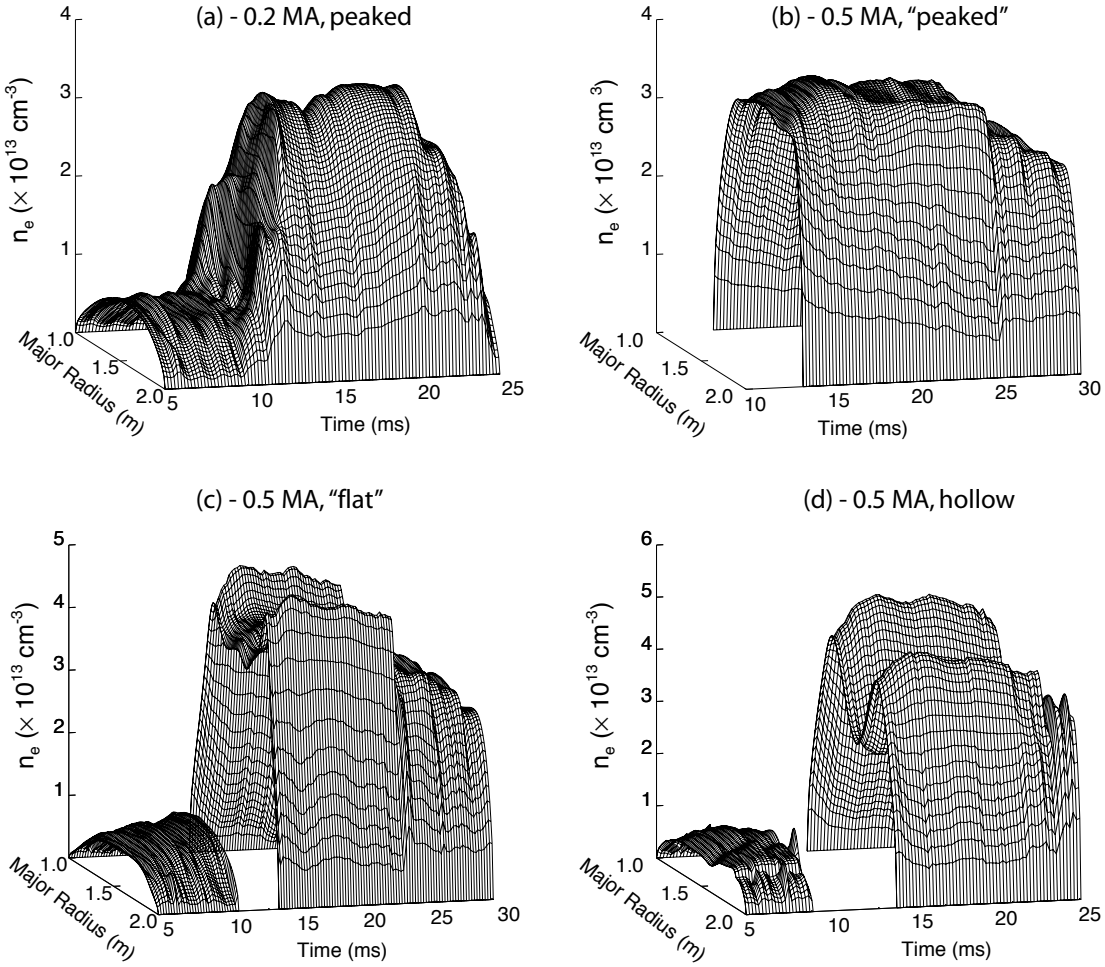

Figure 5.5: Density profiles for pellet-fueled PPCD. In (a) a single slow pellet is capable of reaching the core, resulting in a peaked density profile at low current (0.2 MA). Data for this discharge are shown in Fig. 5.2. Though not as peaked as at 0.2 MA, "peaked" profiles (b) can be obtained at 0.5 MA during PPCD. With two healthy pellets - fast pellet depositing material in the core, and slow pellet, the edge, a "flat" profile (c) is produced in 0.5 MA discharge. Data for this discharge are shown in Fig. 5.4. In a "hollow" discharge (d), most of the pellet material is deposited in the edge for this 0.5 MA discharge due either to a small, broken or non-existent fast pellet. In all the 0.5 MA discharges, gaps in data are due to pellet ablation. [Shots 1060224046 (a), 1060912048 (b), 1060523021 (c), and 1060523029 (d)]

charges. The electron temperature is increased, magnetic fluctuations are reduced, and both energy confinement and β are improved over standard discharges.

5.3.2 Electron temperature profiles

During improved confinement, the electron temperature rises due to the drop in fluctuation-induced transport. In Figure 5.6, the electron temperature and density profiles at two time points are shown for a low-current, pellet-fueled PPCD discharge (same as described in Fig. 5.2). The first time point occurs before both pellet injection and the start of PPCD. The second time point is near the peak temperature (inferred from single filter soft-x-ray emission). Even with the large increase in density, enhanced confinement can lead to higher temperatures than in a standard discharge.

At high current a comparison between the SXR tomography and TS measurements can be made. Figure 5.7 shows the T_e and n_e profiles for the discharge depicted in Figs. 5.4 and 5.5(c). There was only one TS profile taken in this discharge. The SXR temperature data is averaged[2] over 0.5 ms whereas the TS data gets the temperature over a period commensurate with the TS system's Nd:YAG laser pulse-width ($\sim$ 10 ns). The systems are in good agreement on the core electron temperature. In the case of the hollow discharge depicted in Figure 5.5(d), the electron temperature profile (Fig. 5.8) becomes much more peaked. In the case of a "peaked" density profile [shown in Figure 5.5(b)], the electron temperature profile from the Thomson scattering diagnostic (Fig. 5.9) exhibits an odd structure persisting for several milliseconds. TS data shows some off-axis hollowing of the T_e-profile.

[2]Data concerning soft-x-ray emission profiles (needed to get the electron temperature in the SXR setup) can be processed on smaller timescales in order to resolve MHD dynamics (*e.g.* rotating islands) that occur on the tens of microseconds time scale.

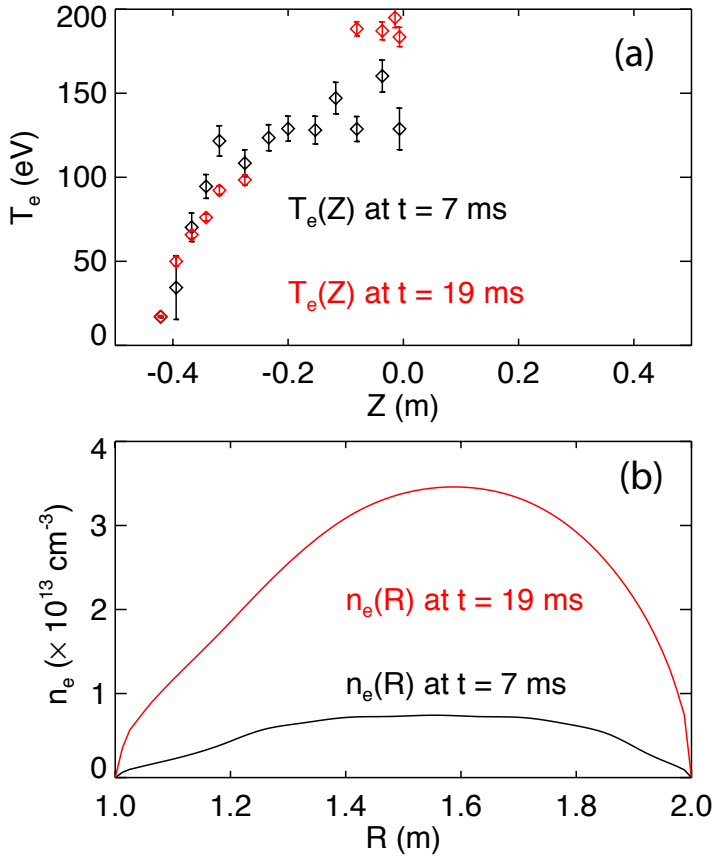

Figure 5.6: TS measurements (a) for a low current pellet-fueled PPCD discharge. Density profiles (b) at the times of the temperature measurement. A single 1.6 mm pellet was injected at $t = 10\ ms$. Temperatures are measured along a vertical line (Z-direction) passing near the plasma's center. At $t = 19\ ms$, four mid-radius points ($Z \sim -0.25\ m$ to $-0.1\ m$) of TS data are unavailable due to the detectors being saturated. Density profiles are measured along horizontal line (major radius) passing through the plasma center. (Shot 1060224046)

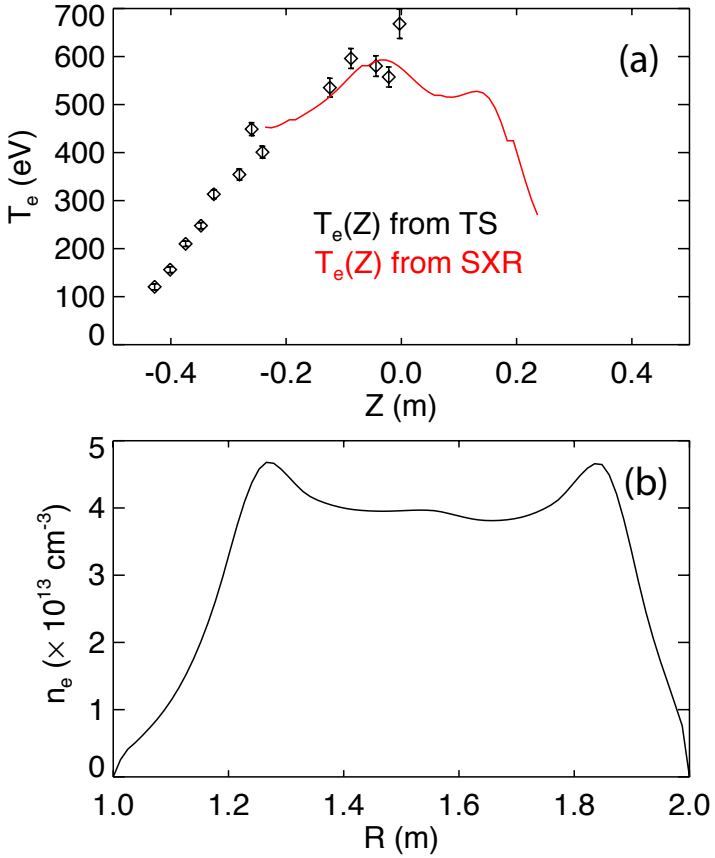

Figure 5.7: SXR tomography and TS measurements (a) for "flat" density profile (b). Same discharge as depicted in Fig. 5.5(c). Measurement taken at 18 ms. (Shot 1060523021)

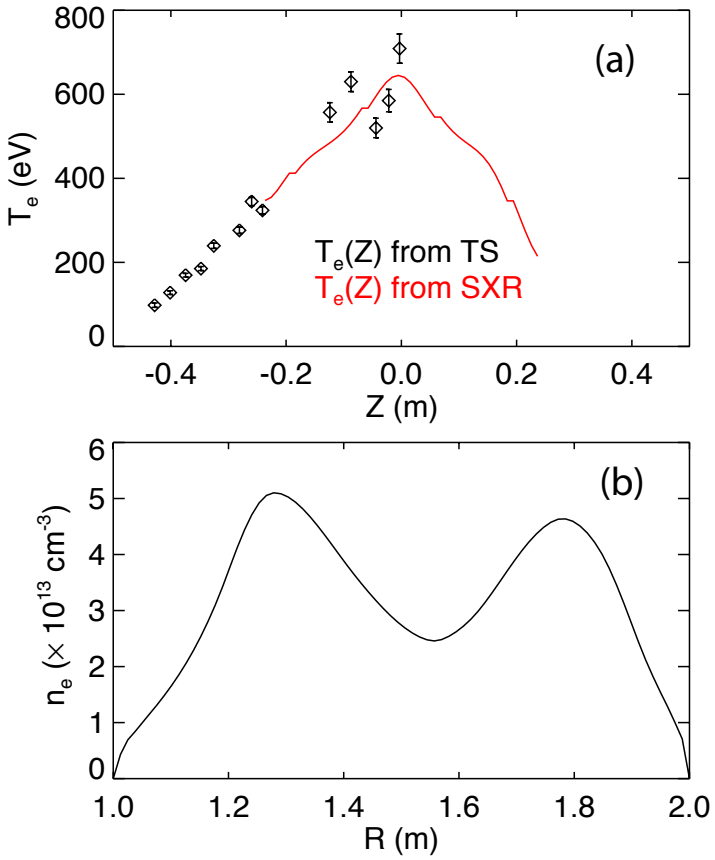

Figure 5.8: SXR tomography and TS measurements (a) for hollow density profile (b). Same discharge as depicted in Fig. 5.5(d). Measurement taken at 16 ms. (Shot 1060523029)

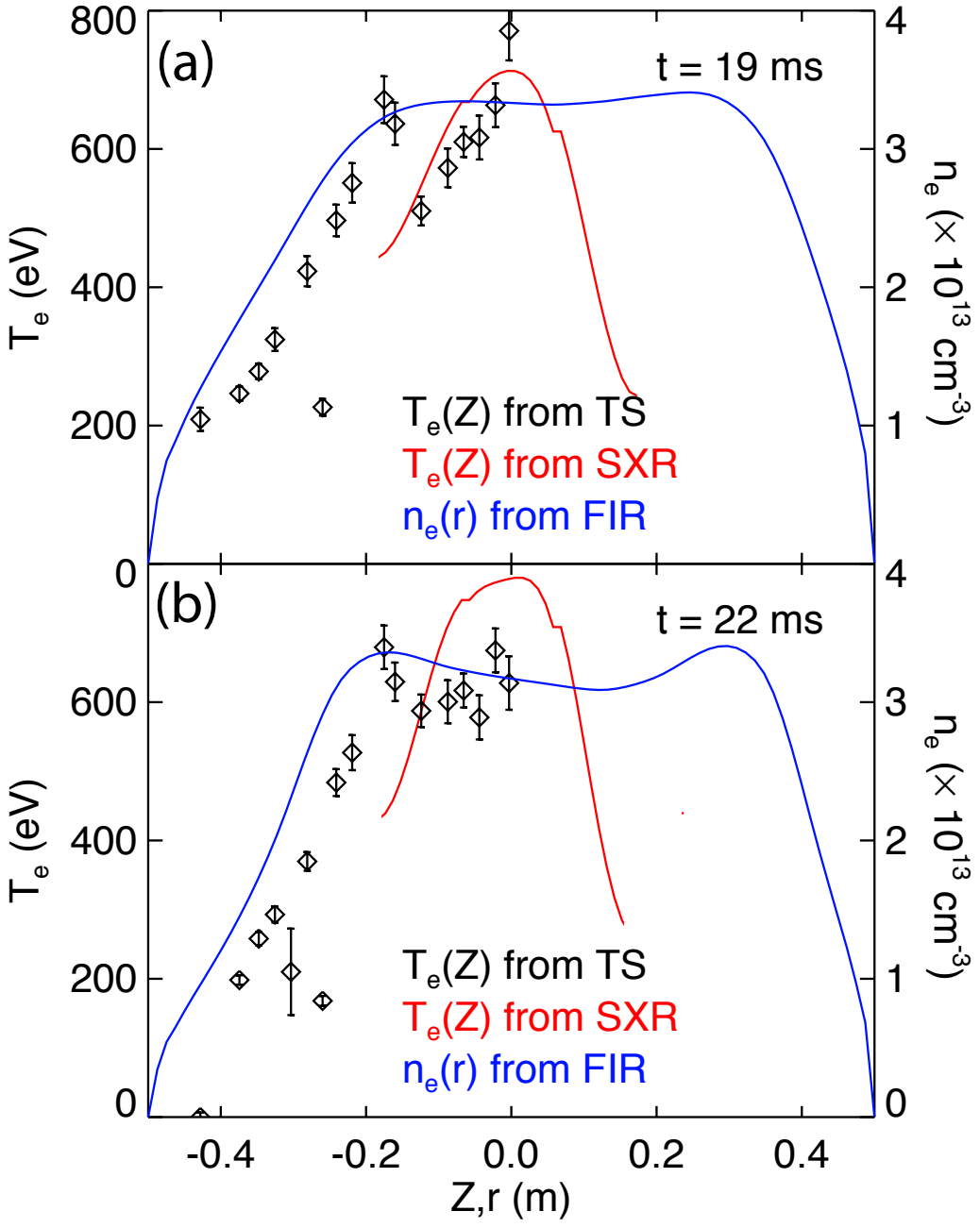

Figure 5.9: SXR tomography and TS measurements for "peaked" density profile [Fig. 5.5(b)] discharge shows interesting structure to T_e profile. Measurements taken at 19 ms (a) and 22 ms (b). (Shot 1060912048)

5.3.3 The ion temperature profile

Historically, ion temperatures have remained roughly constant during improved confinement. This however is not the case during pellet-fueled PPCD discharges.

Ion temperature measurements in high current pellet-fueled PPCD discharges (Fig. 5.10) using both the CHERS and RS systems show significant ion heating. At all radii, the ion temperature is observed to rise during improved confinement, regardless of density profile shape. The progression of the measurements going from the core (r/a = 0.0) to the outboard (r/a = 0.75) chords shows that the error bar decreases as the outboard edge is approached. As the CHERS beam is located at the outboard edge, attenuation of the beam becomes significant for inboard and even core measurements in these discharges.

During low-current, pellet-fueled PPCD, the ion temperature measured by the RS system shows a small amount of off-axis heating (Fig. 5.11). Data from the CHERS system is a bit more ambiguous due to the measurement being on-axis (Section 2.5.3 has a discussion on the problem of CHERS beam attenuation during pellet-fueled discharges). Even so, the central ion temperature measured at the time of the second TS measurement (Fig. 5.6) shows that $T_e(0) \sim T_i(0)$. Measurements at other radii are difficult due to the need for a sufficiently large fully-stipped carbon population for the CHERS measurement.

In all discharges, the RS system is measuring the deuteron temperature at r/a = 0.35. Partially due to the large radial window, the temperature measured by the RS system is lower than that at the CHERS chord that overlaps the RS. The larger window leads to an averaging of the temperature which with a decreasing temperature profile leads a lower measured value than that from a more spatially localized measurement like CHERS. Regardless, the temperature dynamics are similar, in that in all cases the ion temperature is rising.

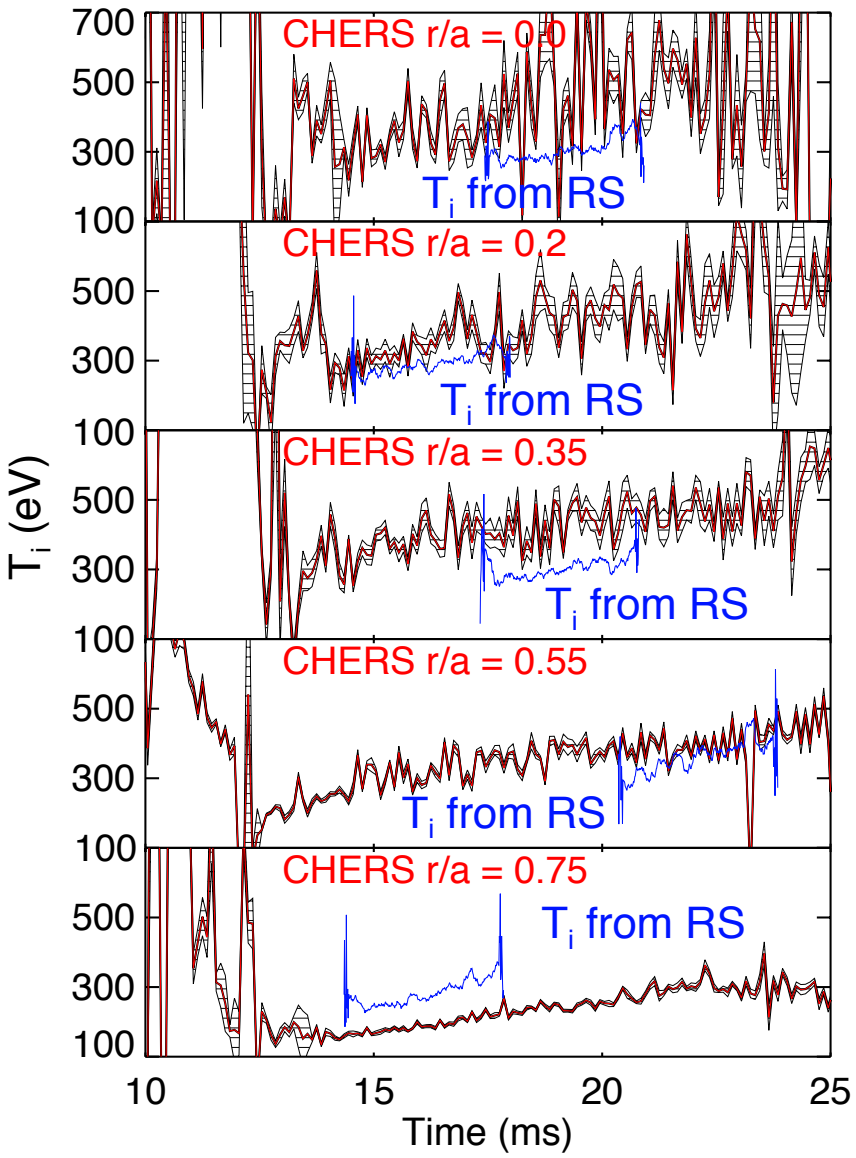

Figure 5.10: CHERS (in red with error bars) and RS (in blue) measurements for high density 0.5 MA discharge indicate increasing ion thermal energy during improved confinement at all radii. All discharges had $<n_e> \sim 3.0 \times 10^{13}\ cm^{-3}$. [Shots 1060522031 (r/a = 0.0), 1060523021 (r/a = 0.2), 1060522075 (r/a = 0.35), 1060522048 (r/a = 0.55), and 1060522047 (r/a = 0.75)]

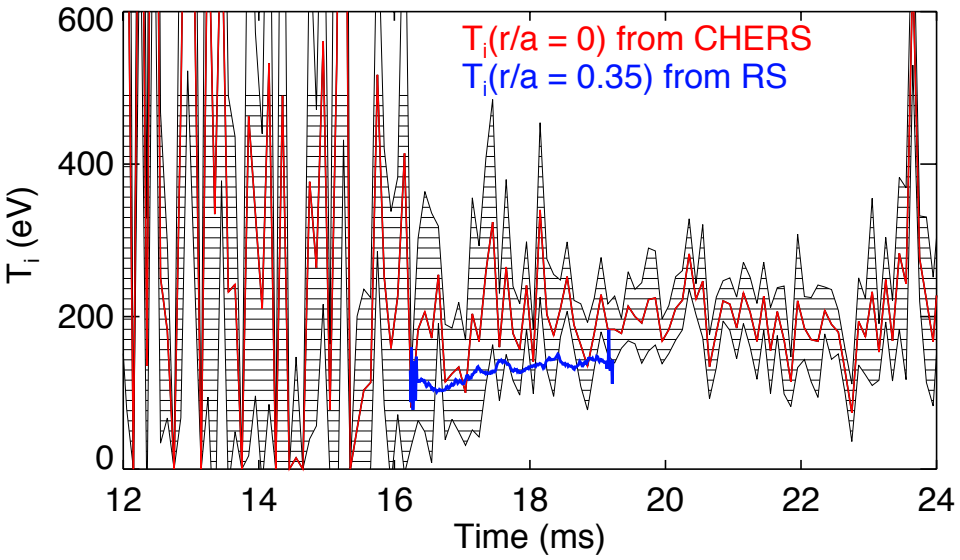

Figure 5.11: CHERS and RS measurements for high denstiy 0.2 MA discharge (Fig. 5.2) indicate heating during improved confinement (t = 15 to 20 ms). The region of horizontal stripes represent the error in the CHERS measurement. (Shot 1060224046)

5.3.4 λ profile

Control of the current profile with PPCD alters the λ profile, where $\lambda = \frac{\mu_0 J \cdot B}{B^2}$. This change of the λ profile reduces the free energy available to drive tearing instability. The parallel current profile $J_{||}(r)$ is reconstructed using the toroidal equilibrium code MSTFit [2]. The calculation is constrained by internal (polarimetry, interferometry, MSE, TS) and edge (magnetic loop array) measurements.

Axisymmetric toroidal equilibria are described by the Grad-Shafranov equation [3]:

$$\triangle^* \psi = -2\pi\mu_0 R^2 \frac{dp}{d\psi} - 2\pi F \frac{dF}{d\psi} \tag{5.1}$$

where $\triangle^*$ is the elliptic operator $[= R^2 \nabla \cdot (\frac{\nabla}{R^2})]$, ψ is the poloidal magnetic flux, R is the radius in cylindrical coordinates (Fig. 5.12), and $F = RB_\phi$. In MSTfit, the Grad-

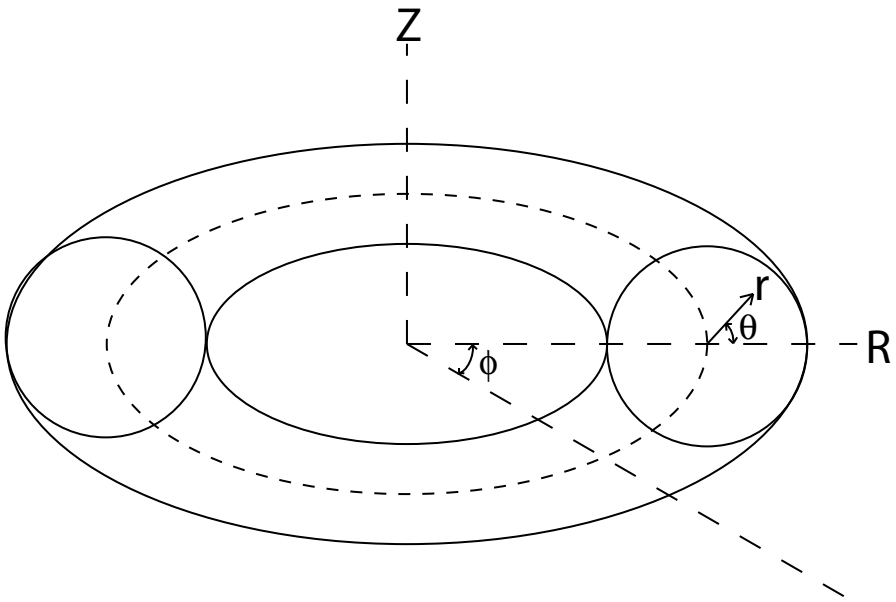

Figure 5.12: Cylindrical coordinate system for a torus

Shafranov equation is reduced to [4]:

$$J_\phi = \frac{2\pi F F'}{\mu_0 R} + 2\pi R p', \tag{5.2}$$

where $()' = \frac{d}{d\psi}$. F and p profiles are determined by fitting the data which can then specify J_ϕ. With J_ϕ in hand, other profiles can be calculated. As such, λ can be written as:

$$\lambda = 2\pi F' + \frac{2\pi\mu_0 F p'}{B^2}. \tag{5.3}$$

Although MSE is a good constraint on the MSTfit reconstructions, it is not available in low current discharges. As $B_\phi(0)$ or $q(0)$ are not measured at low current, the current profile fits near the core can have larger variation. In order to get a better fit, examination of the magnetic fluctuation data can yield what resonant surfaces exist in the plasma. In

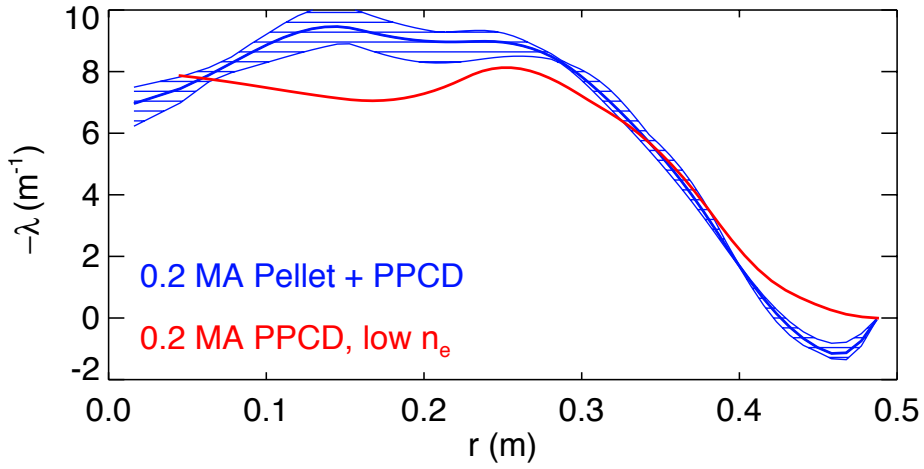

Figure 5.13: At low current, pellet-fueled PPCD operation (blue) results in an increased off-axis parallel current compared to low-n_e PPCD (red). Associated β values for the two cases: 26% for pellet case and 16% for low-n_e. [Shots 1060224016 (red) and 1060224046 (blue)]

particular, if the m = 1, n = 6 is observed but the m = 1, n = 5 is not, $q(0)$ will lie between 1/6 and 1/5.

Shown in Figures 5.13 and 5.14, are comparisons of the λ-profiles at low and high current for pellet-fueled and low-n_e PPCD discharges. For the pellet-fueled cases, multiple fits were done due to increased variation in the polarimetry measurement (in both high current and low current cases some chords, typically edge chords, had large errors) and lack of MSE (low current case). The error bars are from the multiple fits. At low current, the pellet-fueled discharge experiences an off-axis increase in λ with some hollowness that exceeds the error bars. As will be shown in Chapter 6, the mid-radius region is where the pressure gradient has its largest magnitude (Fig. 6.4). It's expected to have a larger role in the equilibrium (Eq. 5.2) in this region.

The higher pressure doesn't have much of an effect in the high current case (Fig. 5.14).

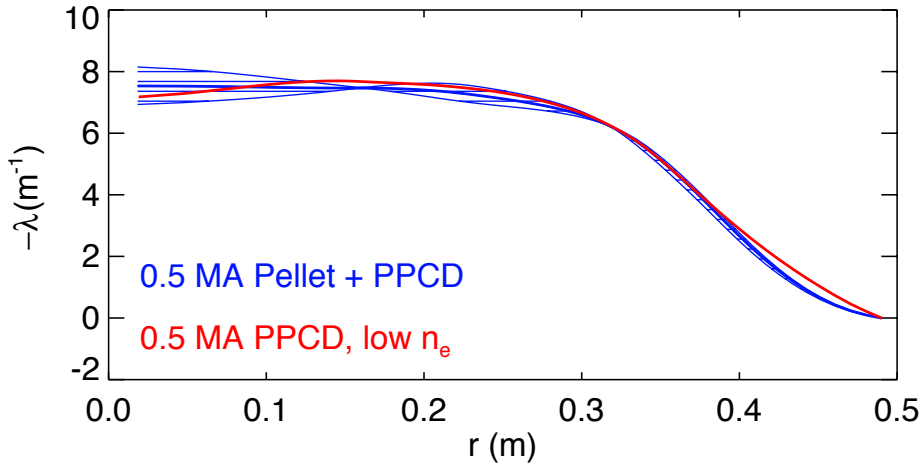

Figure 5.14: At high current, the λ-profiles for PPCD operation with and without pellet-fueling are within error bars. Associated β values for the two cases: 15% for pellet case and 12% for low-n_e. Low n_e profile (red) is from ensembled data and pellet-fueled data (blue) is from a single shot (1060522021).

However, it is remarkable, despite differences in the shape and magnitude of the n_e, T_e, and Z_{eff} profiles and the runaway populations, that the λ profile does not change due to pellet fueling at high current.

5.4 Electron heating

Typically, electrons are heated ohmically in the RFP, as $T_e > T_i$. The ohmic input power P_{ohmic} can be calculated using two methods: from measurements of resistivity and the current profile:

$$P_{ohmic} = \eta J^2 \tag{5.4}$$

or from global power balance:

$$P_{ohmic} = P_{IN} - \frac{dW_{mag}}{dt}, \tag{5.5}$$

where P_{IN} is the total input power or Poynting flux, and W_{mag} is the stored magnetic energy. This section will focus on the details of the first method with results of the calculation shown in Section 5.6. The measurement of Z_{eff} will be discussed so that the resistivity can be calculated. The results of hard-x-ray measurements are included as well in order to demonstrate that pellet fueled discharges do not possess a significant non-Maxwellian population of electrons that could alter the calculation of the resistivity.

5.4.1 Z_{eff}

Using the emission at 1040 nm (with D_α subtraction) at two radii (impact parameters of -0.089 and 0.4), temperature profiles from the Thomson system, and density profile information from the FIR system, a line-averaged Z_{eff} has been calculated for high current, pellet-fueled PPCD discharges. It is a line-averaged measurement due to both ϵ_{1040nm} and D_α being line-integrated measurements. The neutral density profile is very hollow, so that reconstruction of $D_\alpha(r)$ is not done. However given enough chords of the Z_{eff} a profile could be reconstructed. Figure 5.15(a) shows the time-evolution for the two radii of the line-averaged Z_{eff} using this method. In Fig. 5.15(b), ϵ_{1040nm} and D_α are compared showing how much larger the latter's emission is. From SXR tomography measurements, the core is known to be getting hotter, and the drop in D_α emission indicates that (after all the deuterium is burned through) higher Z impurities will begin losing more electrons resulting in the increasing Z_{eff} during improved confinement.

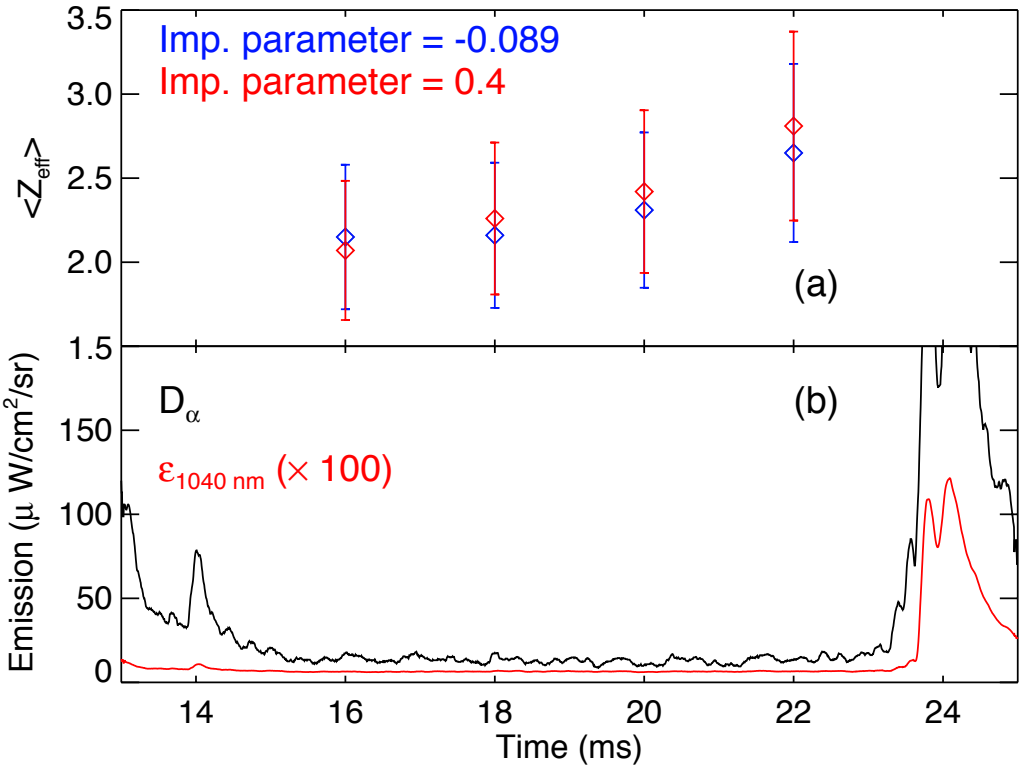

Figure 5.15: As expected from the increasing electron temperature during improved confinement, the line-averaged Z_{eff} also increases (a). The profile appears flat within the core. Measurements were made at impact parameters of 0.089 (just inboard of magnetic axis) and 0.40 (outboard mid-radius). An ensemble of discharges with similar $<n_e>$ was used in order get the necessary number of T_e profiles (from TS) for computing Z_{eff}. In (b) the bremsstrahlung emission and pollutant D_α emission are shown. The period of improved confinement lasts from ∼15 ms to 23 ms.

5.4.2 Plasma resistivity

In a collisional plasma the resistivity is given by the Spitzer expression:

$$\eta_{Spitzer} = 1.04 \times 10^{-4} \frac{Z\ ln\Lambda}{T_e^{3/2}}\ [\Omega \cdot m] \tag{5.6}$$

In toroidal devices, trapping of particles effectively reduces the number of current carriers, thereby increasing the resistivity. This "neo-classical" resistivity can be written in terms of the Spitzer resistivity, Z_{eff}, the trapped particle fraction f, and the de-trapping rate, ν_{*e}:

$$\eta_{neo} = \frac{\eta_{Spitzer}}{[1 - \frac{f_t}{1+\xi(Z_eff)\nu_{*e}}][1 - \frac{C_R(Z_{eff})f_t}{1+\xi(Z_eff)\nu_{*e}}]}, \tag{5.7}$$

where both ξ and C_R are corrections due to the presence of impurities [5]. The trapped particle fraction is calculated in MSTFit, and after including the de-trapping rate, gives $\frac{\eta^{neo}}{\eta^{Spitzer}} < 1.4$ for pellet-fueled discharges. For non-pellet plasmas, the neoclassical resistivity can be twice as large as the Spitzer resistivity (Fig. 5.16). The temperature drop in moving to higher density (a factor of $2-3$) results in the Spitzer resistivity increasing by a factor of $\sim 3-5$. Though the neo-classical correction is much smaller, the plasma resistivity is still larger for the pellet-fueled discharges.

5.4.3 Runaway electrons

Runaway electrons are "collisionless" in that the drag force due to collisions is less than the force due to the electric field. They can carry significant current and energy. Being collisionless, this energy is unavailable for heating the bulk plasma. At the end of discharges, during a disruption or even through gradual diffusion to the boundary, large populations

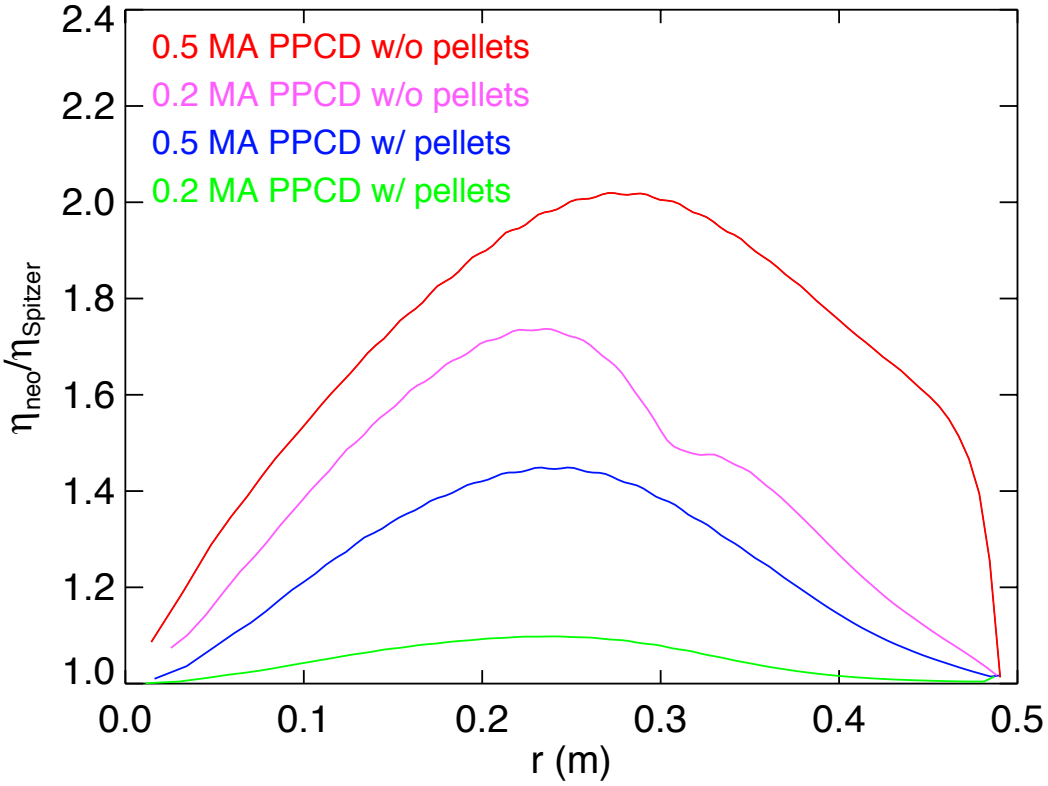

Figure 5.16: Due to the increase in plasma collisionality following pellet injection, particle de-trapping increases. The neoclassical correction to the plasma resistivity decreases, making the resistivity more Spitzer-like. 0.5 MA profiles are from ensembled data, and 0.2 MA profiles are from single shots. [Shots 1060224016 (yellow) and 1060224046 (green)]

of runaways can damage vessel walls. Their presence will also raise the resistivity. A lack of runaways at higher density during PPCD would indicate that the resistivity could be well-modeled as neoclassical.

In tokamaks, pellet injection can effect either a decrease or an increase in the runaway population relative to lower density plasmas. In the former case, the mechanism for reduction is that by increasing density, the drag force felt by the electrons is increased [6]. To increase the population, however, runaways must already exist, and the pellet, by increasing the density, provides cold target electrons that can be "knocked-on" to runaway velocities by existing runaways in an avalanching effect [7, 8]. In the case of MST, pellets can be fired at the start of PPCD - a period when runaways are rarely observed or during PPCD - when runaways are observed.

In PPCD discharges at higher current, runaway electrons have been observed whereas in standard discharges they are not [9]. As magnetic fluctuations are reduced, so is the field line stochasticity, allowing runaway electrons to be confined. Figure 5.17(a) depicts the evolution of the hard-x-ray flux for discharges with and without pellet injection. In all cases, PPCD is started at 10 ms. In one pellet-fueled case (blue) pellets are injected before the onset of improved confinement [Fig. 5.17(b)]. In the other pellet-fueled case (green), a single pellet is injected during improved confinement. Initially, improved confinement is lost but then recovers in this case. The increased density reduces runaway electron production.

There are two mechanisms by which the increased density can reduce the runaway population – (a) the fluctuations are slightly increased (due to changes in the current and/or pressure profile) raising the level of field line stochasticity or (b) the collisionality is increased such that the drag force exceeds the force due to the parallel electric field.

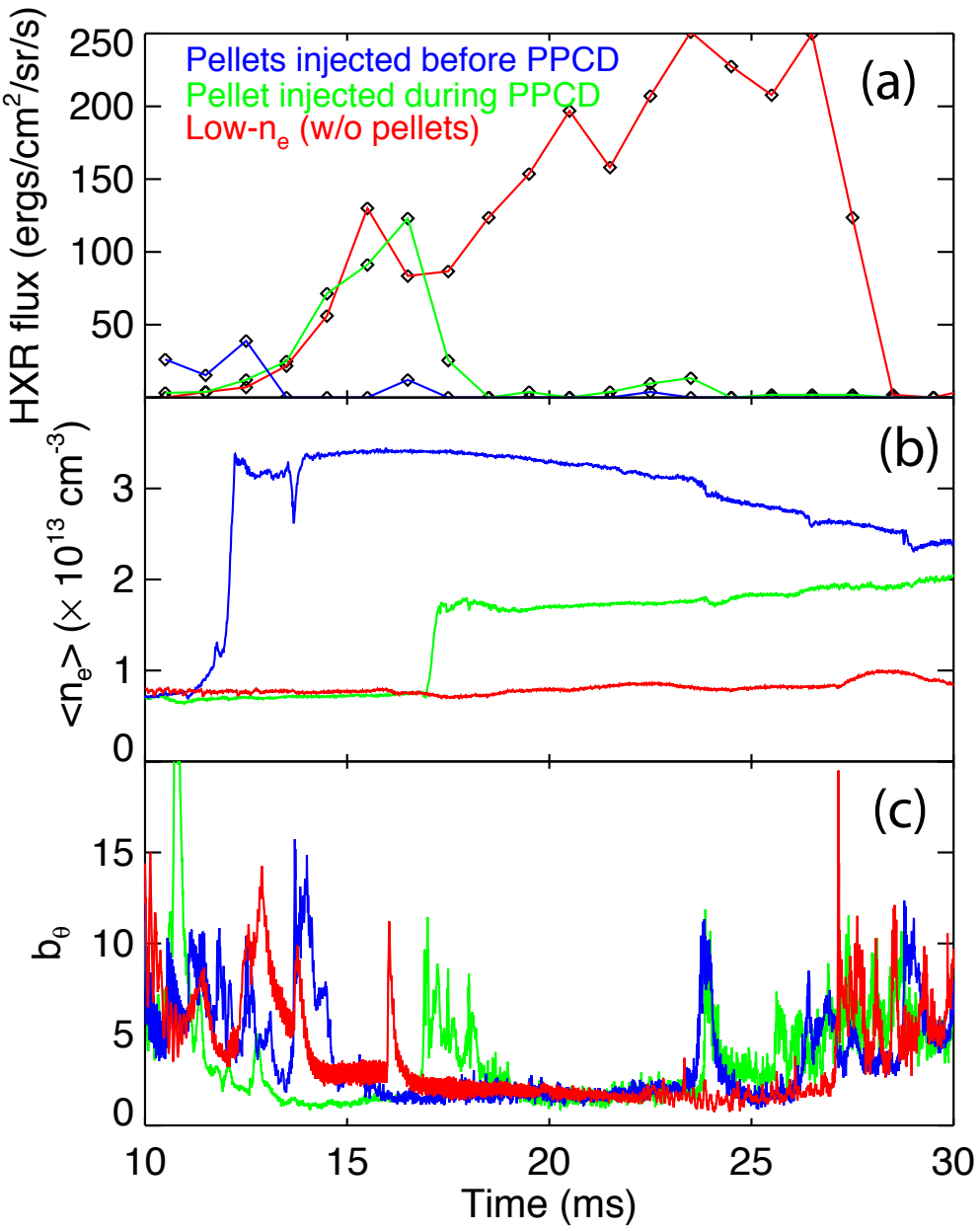

Figure 5.17: (a) The hard-x-ray flux from a centrally-looking detector and (b) line-averaged density (b) is shown for three cases: PPCD at low-n_e (red), pellets injected during PPCD (green), and pellets injected before PPCD (blue). Core m = 1, n = 7-14 fluctuations (c) are reduced in all three cases. [Shots 1060517014 (red), 1060517048 (green), and 1060523021 (blue)]

The threshold energy for an electron to runaway is [6]:

$$W_C \simeq 2 \times 10^4 \left(\frac{n_e}{10^{13}}\right) \left(\frac{0.001}{E}\right) \left(\frac{ln\Lambda}{15}\right) \left(eV, cm^{-3}, V \cdot cm^{-1}\right) \tag{5.8}$$

which in the low density case corresponds to $W_C \sim 10\ keV$. The injection of pellets brings the threshold to $\sim 30\ keV$ ($\sim 20\ keV$) for the injection before (during) PPCD case. The core fluctuations at high density remain comparable to the level at low density. These high density discharges have the hallmarks of being capable of confining runaway electrons, but a significant population is not observed.

5.5 Ion power balance

The observation of a rising ion temperature following pellet injection into PPCD has motivated a search for the source(s) of the ion heating. On the surface, it would seem to be a simple matter of having dramatically increased the collisional heating power from the electrons by increasing the density. However, as will be shown in this section, it remains unclear if collisional heating power can account for all of the temperature rise. As a consequence, there may be an ion heating anomaly during PPCD.

First the sources and sinks of ion energy will be detailed. Both a global and local calculation of the ion power balance will then be presented. The reason for the two treatments is that some parts of the power balance equation are easily measurable locally but not globally, while others are well known globally but not locally. When a source or sink is not well known, an approximation will be used.

5.5.1 Sources and sinks

The ion power balance equation for MST is:

$$\frac{dW_{th,i}}{dt} = P_{e-i} - P_{conv} - P_{cond} - P_{CX} + P_{anom} \tag{5.9}$$

where P_{e-i} is power lost or gained due to collisions with electrons, P_{conv} is power lost due to convection, P_{cond} is power lost due to conduction, i.e., thermal diffusion, P_{CX} is power lost due to charge exchange, and P_{anom} is the anomalous heating power whose mechanics are murky but are related to magnetic fluctuations. Due to the difficulty (it has not yet been done) of calculating χ_i, P_{cond} is neglected in the calculations to follow.

Though sawtooth crashes in the RFP are correlated with confinement degradation, significant heating of ions is also observed [10, 11, 12]. This anomalous heating is associated with the combined excitement of m = 1 and m = 0 activity during the crash [12]. In PPCD discharges, sawtoothing activity ceases, but it is unknown if this anomalous heating power disappears as well.

Energy transfer to the ions can also be accomplished through collisions with electrons:

$$P_{e-i} = \frac{3}{2} n_i \frac{(T_e - T_i)}{\tau_{e-i}} \tag{5.10}$$

where the equilibration time for a generic two species system is [13]:

$$\tau_{\alpha-\beta}^{-1} \;=\; \nu_{\alpha-\beta} = 1.8 \times 10^{-19} \frac{(m_\alpha m_\beta)^{1/2} Z_\alpha^2 Z_\beta^2 n_\alpha ln\Lambda}{(m_\alpha T_\beta + \; m_\beta T_\alpha)^{3/2}} \frac{1}{sec} \tag{5.11}$$

Table 5.1: Thermal equilibration times (electron-deuteron and deuteron-carbon) for the four PPCD operating regimes: (a) low-n_e, low-I_p, (b) high-n_e, low-I_p, (c) low-n_e, high-I_p, and (d) high-n_e, high-I_p.

Case	(a)	(b)	(c)	(d)
I_P (kA)	210	170	500	480
$n_e(0)$ (10^{13} cm^{-3})	1.0	3.5	1.2	4
$T_e(0)$ (keV)	600	200	1500	800
$T_i(0)$ (keV)	200	190	1000	700
τ_{e-D} (ms)	63	3.6	187	23
τ_{D-C} (μs)	54	15	440	82

which for electron-deuteron interactions is:

$$\tau_{e-D} \sim 6.1 \times 10^8 \frac{T_e^{3/2}}{n_e ln\Lambda} \; sec \tag{5.12}$$

and for carbon-deuteron:

$$\tau_{C-D} = 4.1 \times 10^4 \frac{(12T_D + \; 2T_C)^{3/2}}{n_D ln\Lambda} \; sec \tag{5.13}$$

where for Eqs. 5.11-5.13, all quantities are in cgs except for T which is in eV. Representative equilibration times for the four PPCD operating regimes are calculated in Table 5.1. As the equilibration time goes as $\sim \frac{T^{3/2}}{n}$, and since T is largest on axis, the quoted values also represent the upper bound on $\tau_{\alpha-\beta}$ over the plasma radius. Included are the equilibration times between deuterons and carbon to show that the bulk ion temperature dynamics should be reflected by CHERS measurements. For the cases considered the Coulomb logarithm $ln\ \Lambda$ varies from 13.7 to 15.8 for electron-deuteron interactions and 13.1 to 15.9 for deuteron-carbon.

When $T_i < T_e$, there are only two loss channels (again, ignoring ion thermal diffusion)

to consider for ion energy: convective power loss P_{conv} and charge exchange loss P_{CX}. The convective loss channel is simply energy lost due to diffusion of particles and is defined as:

$$P_{conv} = \bar{\epsilon}\Gamma \tag{5.14}$$

where $\bar{\epsilon}$ is the average energy of ions leaving a volume, and Γ is the flux of the those same ions through the surface bounding the volume. The particle flux is determined from the continuity equation:

$$\frac{dn}{dt} + \nabla \cdot \Gamma = S \tag{5.15}$$

Rearranging and integrating:

$$\int_S \Gamma \cdot dA = \int_0^r \left[S(r) \; - \; \frac{dn}{dt} \right] dV \tag{5.16}$$

which represents particle losses for (in the case of MST) a torus of minor radius r. For total convective losses, it can be re-written as:

$$\int_S \Gamma \cdot dA = S_{tot} - \frac{dN}{dt} \tag{5.17}$$

As for the energy carried by the lost ion, it is taken to be the temperature at that particular radius, so that $\bar{\epsilon}(r) \; = \; \frac{3}{2} T_i(r)$. The total convective power loss is then:

$$\int_V P_{conv} dV = \frac{3}{2} \left(S_{tot} - \frac{dN}{dt} \right) T_i(a). \tag{5.18}$$

In MST, $T_i(a) \sim \; 30 \; eV$ [14].

The other sink for ion energy is charge exchange loss wherein a thermal ion charge

exchanges with a neutral, gaining an electron but keeping its energy. Not bound by the magnetic fields of the plasma, it can then leave the plasma taking with it the difference in energy between it and the neutral it ionized. The local charge exchange power loss P_{CX} can be computed by multiplying the loss rate of ions by the energy difference between the ion and neutral:

$$P_{CX} = \frac{3}{2} n_0 n_i < \sigma v >_{CX} (T_i - T_0) \tag{5.19}$$

where n_0 is the neutral density, $< \sigma v >_{CX}$ the charge exchange cross-section, and T_0 is the energy of the neutral. At the plasma boundary, neutrals are liberated when particles collide with the wall. These neutrals typically have $T_0 \leq 4\ eV$. Through successive charge exchange interactions, neutrals gain energy and can penetrate deeper into the plasma. As the neutral temperature profile is not known, and ion temperatures are $200 - 1000\ eV$, T_0 is assumed to be zero for the calculation of charge exchange losses and will then provide an upper bound on P_{CX}. The neutral density profile can be calculated from D_α emission and put into terms of $\alpha = \frac{<\sigma v>_{ion}}{<\sigma v>_{exc}}$ and $< \sigma v >_{ion}$ using Eqs. 2.12 and 2.13:

$$n_0 = \frac{\gamma_{D_\alpha}}{\alpha n_e < \sigma v >_{CX}} \tag{5.20}$$

With the assumption of constant Z_{eff} and only one impurity species (fully-stripped carbon), $n_i(r)/n_e(r)$ is constant:

$$\frac{n_i}{n_e} = \frac{6 - Z_{eff}}{5} \tag{5.21}$$

so that 5.19 becomes:

$$P_{CX} = \frac{3}{2} \left(\frac{\gamma_{D_\alpha} < \sigma v >_{CX}}{< \sigma v >_{ion}} \right) \left(\frac{6 - Z_{eff}}{5} \right) T_i \tag{5.22}$$

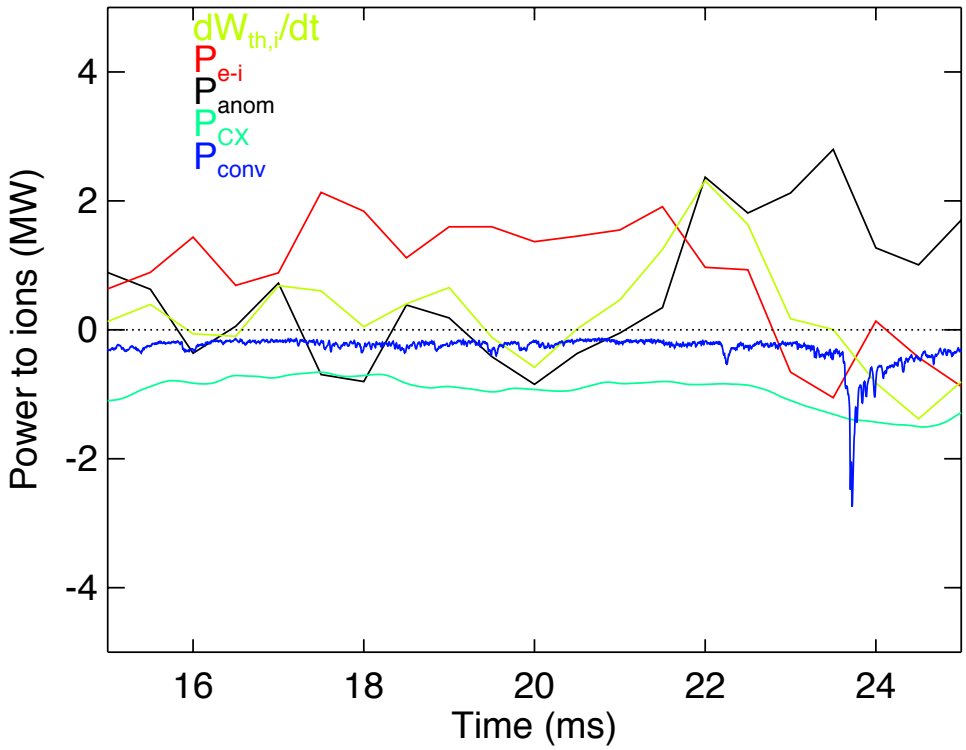

Figure 5.18: **Case A** - Comparison of ion power sources and sinks during improved confinement ($t < 22\ ms$). $dW_{th,i}/dt, P_{e-i}, P_{CX}$, and P_{conv} are all from measurements as detailed in the text. The anomalous heating power P_{anom} is calculated by balancing Eq. 5.9. Prior to $t = 22\ ms$, the anomalous power is zero within error bars but increases at $t = 22\ ms$ due to increased magnetic fluctuations (Shot 1060523021)

5.5.2 Global power balance

Completing the power balance globally takes advantage of the methods of measurement for both convective and charge exchange power losses. As explained in the discussion of τ_p, the neutral particle profile is 2-D and hollow, so that profiles accurate within the reversal radius are difficult to reconstruct. Integrating over the volume (Eq. 5.18) using line-averaged data from the FIR and D_α array gives the global picture and is unencumbered by the details of the profile in the core. Determining the total charge exchange losses in MST can be accomplished with a pair of bolometers - a pyrobolometer measures the

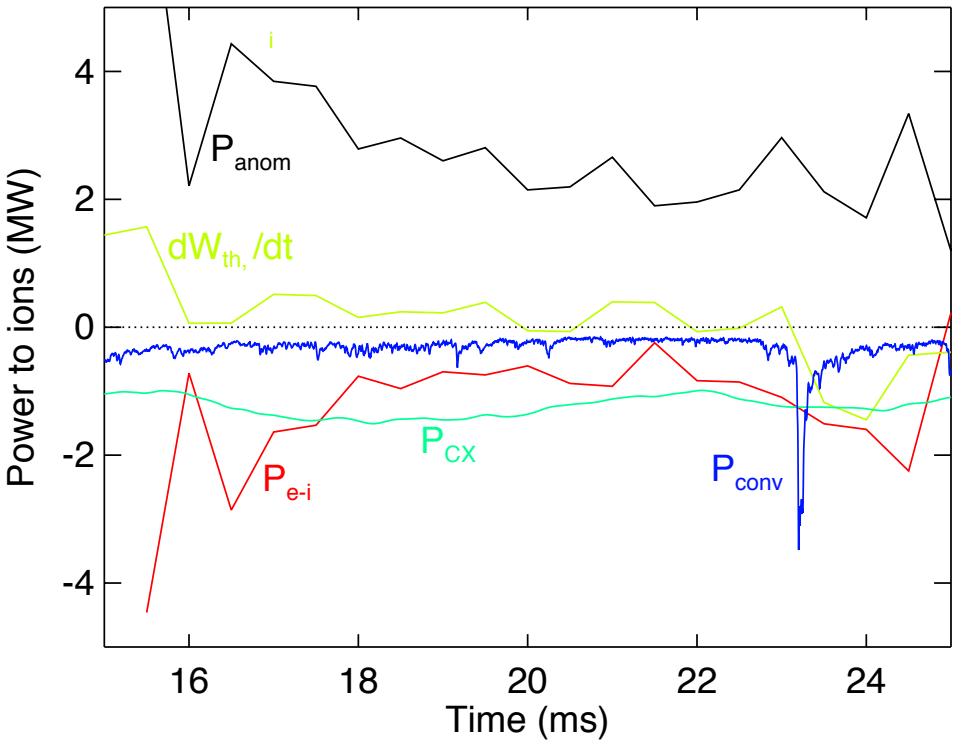

Figure 5.19: **Case B** - Comparison of ion power sources and sinks during improved confinement. $dW_{th,i}/dt, P_{e-i}, P_{CX}$, and P_{conv} are all from measurements as detailed in the text. The anomalous heating power P_{anom} is calculated by balancing Eq. 5.9. (Shot 1060522048)

energy flux due to radiation and neutrals, while an XUV photodiode measures radiation. When calibrated properly, the difference between the two measurements is the energy lost through the escape of charge-exchange neutrals.

There are disadvantages to the global calculation. In order to calculate the energy gained through collisions with the electrons, the evolution of electron temperature profile must be known. However, the electron temperature profile evolution is only well known for $r/a < 0.4$ (from SXR tomography). To get the full profile, Thomson scattering measurements (which extend to $r/a \sim 0.85$) are compared to the same time slice of SXR data. Since there are slight differences in the two profiles, a ratio is taken and averaged over the

region of the plasma where the measurements coincide. This ratio is used to extrapolate the SXR-tomography T_e-profiles to the wall for the remaining time of the discharge. Ion temperature profiles must either be ensembled from multiple shots or inferred from a single chord of CHERS data and extrapolated using the electron temperature profiles just described. Herein lies a problem: the assumption that the T_i and T_e profiles will evolve co-linearly. A big assumption, but due to a lack of full profile evolutions, one that will have to do.

Figures 5.18 and 5.19 show the global ion power balance calculation (Eq. 5.9 with P_{cond} neglected) for two high current, pellet-fueled PPCD discharges. For the purposes of discussion, the two are referred to as Case A and Case B, respectively. Both cases feature two pellets injected into a 0.5 MA PPCD discharge raising $<n_e>$ to $\sim 3 \times 10^{13}$ cm^{-3}. The difference between the two cases is diagnostic coverage which highlights the problem of calculating P_{e-i} and $\frac{dW_{th,i}}{dt}$. In case A, the ion temperature was measured in the core, so that comparison with the SXR-tomography data could be used to extrapolate the profile at each time point. In case B, however, the CHERS measurement was outside the view of the SXR cameras so that the profile extrapolation was done with a single profile from the TS diagnostic.

For each case, charge exchange loss is measured using the bolometer pair and convective loss is calculated using D_α emission (for the source rate) and FIR measurements (for density evolution) as detailed in Eq. 5.18. Calculation of $\frac{dW_{th,i}}{dt}$ is accomplished using the FIR data and an extrapolated (as described above) CHERS profile:

$$\frac{dW_{th,i}}{dt} = n_i \frac{dT_i}{dt} + T_i \frac{dn_i}{dt}, \tag{5.23}$$

where n_i is the deuteron density estimated using Eq. 5.21. The collisional heating is calculated as described in Eq. 5.10, and the anomalous heating is the difference between the thermal energy change and the summation of the sources and sinks. For case A, the collisional heating balances the two loss channels until t = 22 ms when fluctuations increase as PPCD ends. Until this point anomalous power is zero within the error bars but as the fluctuations increase so does P_{anom}. Case B highlights the difficulty in this technique of determining the source of ion heating. In the short time period of measurement of T_e, the electron and ion temperatures were close enough to be within the error bars. As the ions were hotter at this radius and point in time, though, the reconstructed T_i-profile is then hotter everywhere and on the global scale, the collisional power flows to the electrons from the ions. While the edge ion temperature was observed to be within error bars of the electron temperature, observations in similar discharges to Case B have not shown the ions to ever be hotter than the electrons in the core of the discharge. The end result of this is that balancing the ion power equation results in a very large, but not necessarily reliable, anomalous heating power of $\sim 2\ MW$. For comparison, typical ohmic heating powers for MST at this plasma current are $2 - 4\ MW$.

5.5.3 Local Power balance

The calculation of the local power balance has the opposite problem as the global case. At least for the core, both $T_i(t)$ and $T_e(t)$ are well known (from CHERS and SXR tomography, respectively). Outside the core, the electron temperature at a given radius is determined at one time point (during the TS measurement). It's time evolution is inferred from the evolution of radial points measured by SXR tomography. The assumption is that the electron temperature at two separate points will evolve co-linearly – a big assumption but

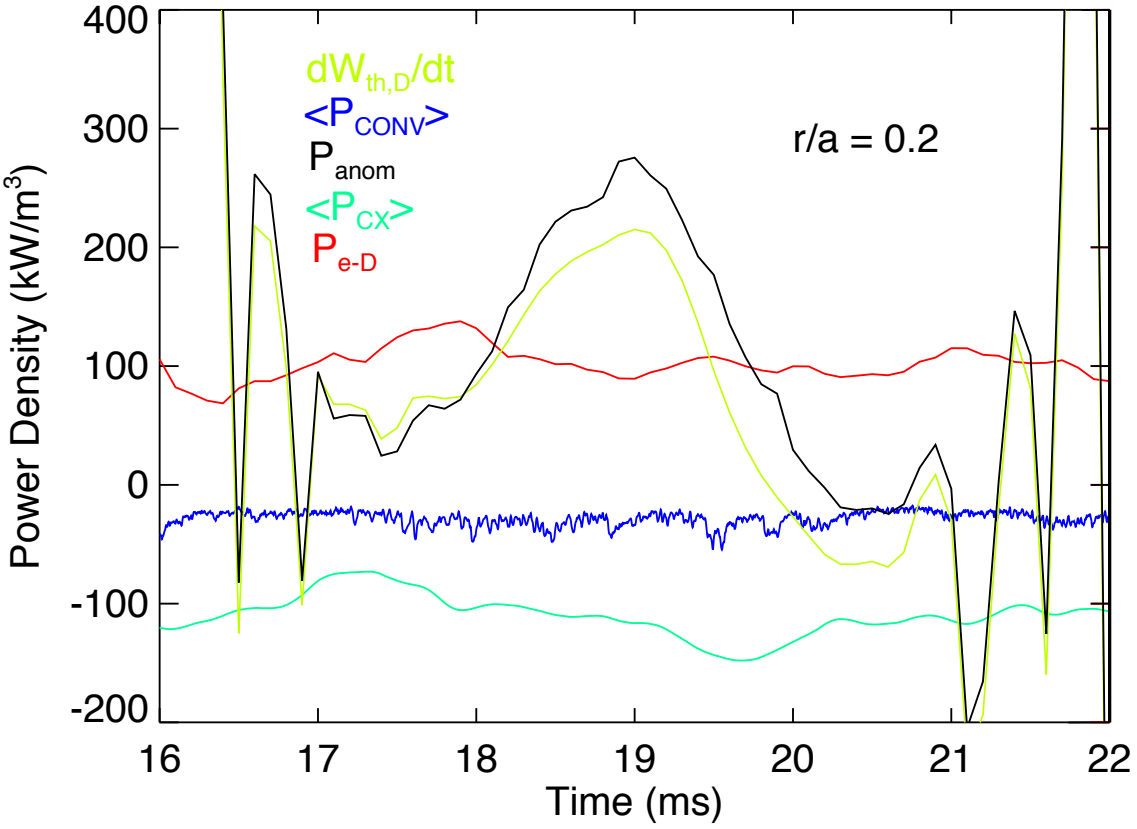

Figure 5.20: The time evolution of ion energy sources and sinks for the plasma core. The rate of deuteron thermal energy change $dW_{th,D}/dt$ is computed from FIR and CHERS measurements. The collisional heating power P_{e-D} is calculated from SXR tomography, CHERS and FIR measurements. The plotted charge exchange $<P_{CX}>$ and convective power $<P_{conv}>$ losses are volume averaged from global quantity. As it is, though, comparison of the sources and sinks indicate that substantial anomalous power P_{anom} is needed to account for the rising T_i. (Shot 1060523021)

one that'll again have to do (for the calculations outside the core anyway).

Accurate local measurements of both the convective and charge exchange losses are difficult as well. As noted in Eq. 5.16, particle flux calculations are dependent on the notoriously difficult measurement of the source profile. As calculation of the charge exchange loss profile also requires the measurement of the D_α-emission profile, it too can be difficult to pin down. Instead for the local ion power balance, the volume averaged losses will be shown. The energy exchange between the electrons and the ions via collisions, however, will be based on local measurements.

Figure 5.20 shows the ion power sinks and sources in the core ($r/a = 0.2$) for a high current, pellet-fueled PPCD discharge. The energy is flowing from the electrons to the ions through collisions with a local heating power near 100 kW/m^3. For comparison, the calculated collisional heating power in low density, PPCD discharges is typically $<$ 5 kW/m^3. For high density PPCD, the volume-averaged convective and charge exchange losses balance the collisional heating, indicating that anomalous heating is required to account for the positive $\frac{dW_{th,i}}{dt}$. Again, however, the loss channels are volume averaged. It's difficult to draw any conclusions from the data aside from the new observation of rising ion temperatures.

5.6 Confinement parameters

Previous PPCD experiments (all at low n_e) led to improvements in confinement of both particles and energy and higher plasma pressures compared to standard discharges. The coupling of PPCD with pellet-fueling has further improved β beyond low-n_e PPCD values while maintaining energy and particle confinement times longer than their standard values.

Table 5.2: Confinement and other parameters for standard, low-density PPCD, and pellet-fueled PPCD at low current, $I_\phi \sim 0.2\ MA$. Data for standard and low-n_e PPCD discharges are from [1]. Z_{eff} for low current discharges is assumed to be 2.

	Standard	Low n_e PPCD	PPCD + pellets
I_P (MA)	0.21	0.21	0.17
$<n_e>$ $(10^{13}\ cm^{-3})$	0.8	0.7	2.4
$T_e(0)$ (eV)	200	600	200
$T_i(0)$ (eV)	150	200	190
β_{tot} (%)	9	15	26
β_θ (%)	9	18	40
Z_{eff}	2	2	2
P_{ohmic} (MW)	2.0	1.0	2.2
τ_E (ms)	1	10	> 5
τ_p (ms)	0.6	4.7	4.3

Tables 5.2 & 5.3 summarize the results of these experiments and calculations.

5.6.1 Normalized pressure (β)

Pellet-fueled PPCD discharges attain total beta of 17% at high current and 26% at low current, where β_{tot} is defined as:

$$\beta_{tot} = \frac{\int_V p dV}{\frac{B^2(a)}{2\mu_0}\int_V dV}, \tag{5.24}$$

with the pressure calculated as:

$$p = n_e T_e + n_i T_i. \tag{5.25}$$

Figure 5.21 shows the pressure profiles for the four PPCD cases described in Tables 5.2 and 5.3. The total beta, measured near the end of auxiliary current drive, improves at low and high current when pellet-fueling is applied. Shown also in the tables is the poloidal

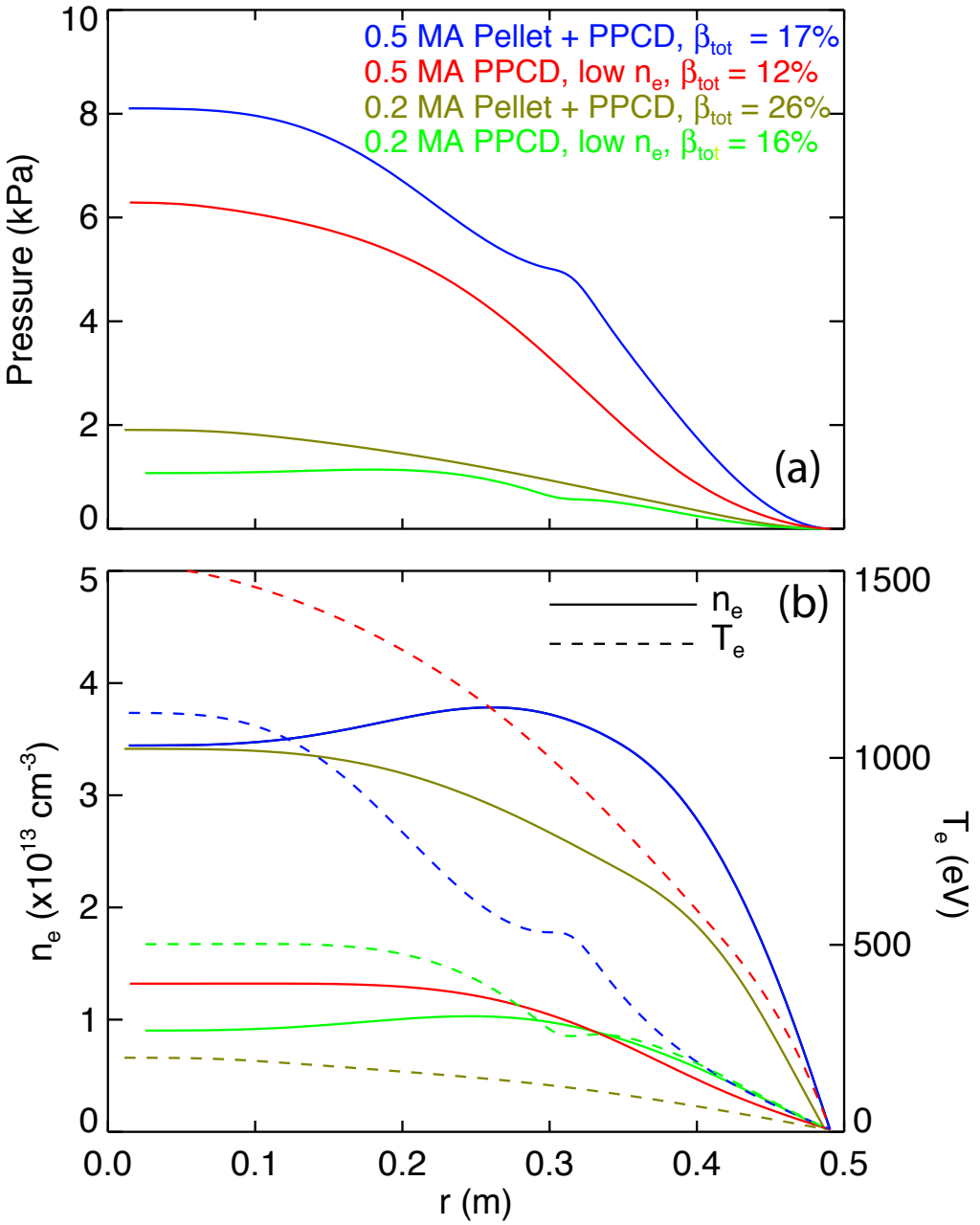

Figure 5.21: Pressure profile (a) comparison for PPCD operation. At both high and low current, pellet-fueling increases the pressure. 0.5 MA profiles are from ensembled data, and 0.2 MA profiles are from single shots. Shown in (b) are the corresponding electron temperature (dashed lines) and density profiles (solid lines). [Shots 1060224016 (green) and 1060224046 (brown)]

Table 5.3: Confinement and other parameters for standard, low-density PPCD, and pellet-fueled PPCD at high current, $I_\phi \sim 0.5\ MA$. Non-pellet fueled discharges are from same campaign as pellet-fueled discharges. Z_{eff} was assumed to be 2 for the standard case and 3 for the low n_e PPCD case. In each case P_{ohmic} was calculated assuming neoclassical resistivity and using current profile reconstructions from measurements.

	Standard	Low n_e PPCD	PPCD + pellets
I_P (MA)	0.50	0.51	0.48
$<n_e>$ $(10^{13}\ cm^{-3})$	3.4	1.0	3.4
$T_e(0)$ (eV)	250	1500	800
$T_i(0)$ (eV)	250	1200	700
β_{tot} (%)	9	10	17
β_θ (%)	9	12	21
Z_{eff}	2	3	2
P_{ohmic} (MW)	16	~ 2.1	4
τ_E (ms)	1.2	~ 6	7
τ_p (ms)	0.8	6	5.5

beta, defined as:

$$\beta_\theta = \frac{\int_V p dV}{\frac{B_\theta^2(a)}{2\mu_0}\int_V dV}. \tag{5.26}$$

For the calculation of both β and τ_E, electron temperature profiles were measured using the Thomson scattering diagnostic. At high current, there were a sufficient number of shots with the CHERS diagnostic at different chords in order to ensemble shots with similar densities and calculate $T_i(r,t)$. Deuteron densities are inferred from Z_{eff} under the assumption that the only impurity is fully stripped carbon. Using Eq. 5.21, leads to n_i/n_e ratios of 0.8 and 0.6 for Z_{eff} of 2 and 3 respectively.

At low current the T_i-profile was constructed using the CHERS central temperature and scaling the ion temperature to the electron temperature:

$$T_i(r) = T_e(r)\frac{T_i(0)}{T_e(0)}. \tag{5.27}$$

The ensembled profiles from high current discharges indicate that Eq. 5.27 is a lower bound for ion temperature.

The error in the electron temperature and density measurements is small (several percent). The main source for error in the calculation of beta is reconstruction of the ion temperature profile. Error in the CHERS measurement is typically 5-10%. The beta calculation then has an error of 1-2 percentage points, though due to the method of T_i profile reconstruction, the quoted values of beta are slightly on the low side.

The larger Ohmic heating power in both pellet-fueled cases contributes to the higher T_i (through the tighter coupling with the electrons) and consequently the higher beta. At low current, the electron pressure does not change when pellet fueling is applied to PPCD; what is gained in density is lost in temperature. The ion component of beta is responsible for the improvement, for while the ion temperature is still the same for the two PPCD cases (Table 5.2), the density has more than tripled. At high currents, both the electron and ion components of beta increase.

5.6.2 Energy confinement time (τ_E)

In pellet-fueled improved confinement plasmas, τ_E exceeds that for standard plasmas (1 ms), and is within a factor of two or better of the best-measured confinement at low density (10 ms). The energy confinement time τ_E is given by:

$$\tau_E = \frac{\int_V W_{th} dV}{\int_V (P_{ohmic} + P_{anom} - \frac{dW_{th}}{dt}) dV} \tag{5.28}$$

where $W_{th} = \frac{3}{2}p$. It is assumed that P_{anom} is zero as attempts to calculate it have been inconclusive. If it's not zero, the calculated τ_E would be an overestimate. For high current

pellet-fueled discharges, $\frac{dW_{th}}{dt}$ can be calculated directly from ensembled data where along with $T_i(r,t)$, the electron temperature evolution is pieced together from ensembling shots with the Thomson system looking at different time-points. At low current, the $n\frac{dT}{dt}$ portion of $\frac{dW_{th}}{dt}$ was not measurable. Single filter soft-x-ray measurements and RS data indicate both T_e and T_i are rising, so that $\frac{dW_{th}}{dt}$ and consequently, the calculated τ_E are lower bounds.

Equations 5.4 and 5.5 detailed the two methods by which the ohmic input power can be calculated. For the first method, the neoclassical resistivity is calculated directly from measurements of T_e and Z_{eff}. This method is used for both the high and low current cases. The second method is dependent on reconstructing the time evolution of the stored magnetic energy. In the high current case, the two methods yield an energy confinement time of 7 ms. Using the first method, the confinement time for low current pellet-fueled PPCD discharges is estimated to be 5 ms, calculated with Z_{eff} assumed to be 2.0 and spatially constant. Due to limited measurements of the current and magnetic profiles (MSE data is unavailable for low current discharges) and a limited number of shots (no possibility for ensembling), the second method was not used for computation of τ_E for low-current pellet-fueled PPCD. The assertion that $Z_{eff}(r) = 2.0$ is based on a past comparison of the two aforementioned methods for determining P_{ohmic} [1] in standard discharges. In this study, Z_{eff} was varied in order to match the results, and $Z_{eff}(r) = 2.0$ worked.

5.6.3 Particle confinement time (τ_p)

Improved particle confinement is implied by the stationary density profiles [Figs 5.5(a)-(d)] and reduced D_α emission [Fig. 5.15(b)]. The particle confinement time τ_p is given

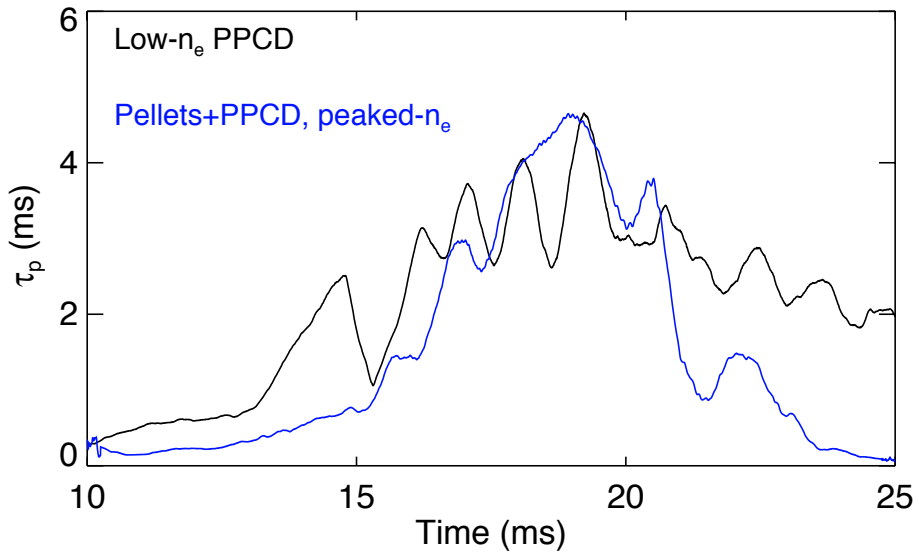

Figure 5.22: Particle confinement time τ_p evolution during low current PPCD. The peak particle confinement time for PPCD discharges is unaffected by pellet-fueling. However, the period of time for which it exceeds the standard value (1 ms) is greater at low density due to the longer duration of improved confinement. [Shots 1060224016 (low n_e) and 1060224046 (pellet-fueled)]

by:

$$\tau_p = \frac{\int n_e dV}{\int (S - \frac{dn_e}{dt}) dV} \tag{5.29}$$

Figures 5.22 and 5.23 show the evolution of τ_p for low and high current PPCD discharges. In the low current case, both pellet-fueled and low-n_e discharges show particle confinement times increasing from $<$ 1 ms before the start of PPCD to greater then 4 ms near the end of improved confinement. At high current, the "profile-shape scan" reveals that the better particle confinement occurs for flat or hollow profiles. In fact the low-n_e case is also slightly hollow. All pellet-fueled cases are a substantial improvement over the $\sim$ 0.6 ms confinement times measured in standard plasmas. Low-n_e cases and the best cases at high density remain comparable to the value ($\sim$ 4.7 ms) in previous low density

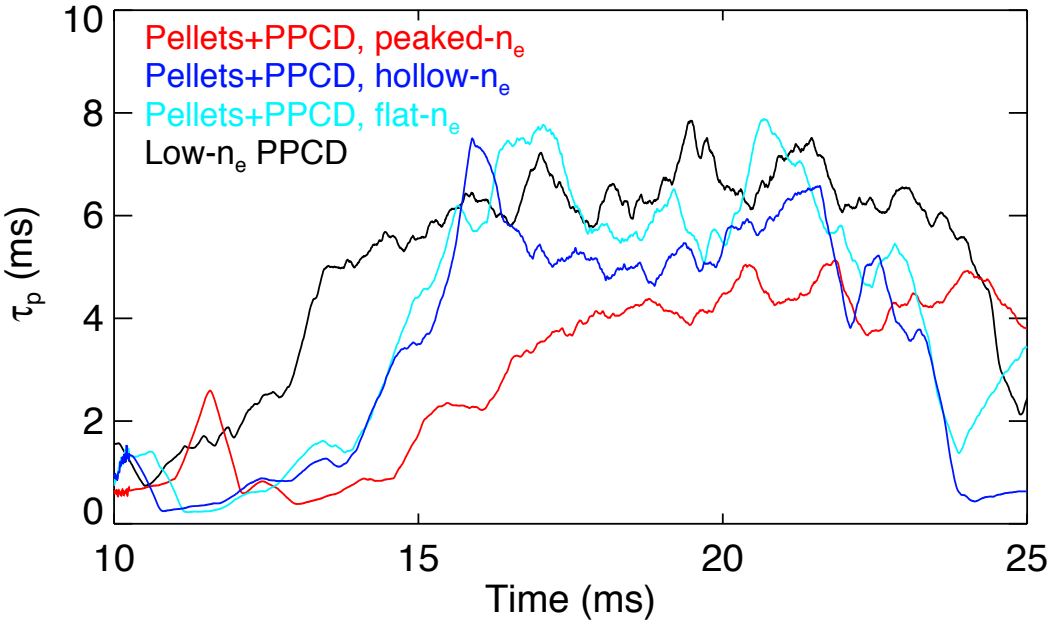

Figure 5.23: Particle confinement time τ_p evolution during high current PPCD. With the exception of the peaked profile case (red), pellet-fueling of high current PPCD results in similar particle confinement times as seen in low-n_e PPCD (black). [Shots 1060912014 (low n_e), 1060912048 (peaked), 1060523021 (flat), and 1060523029 (hollow)]

improved confinement plasmas [15].

5.6.4 Parameter scaling

Standard RFP confinement times have been shown to be bounded by the Connor-Taylor scaling [16]. Connor-Taylor scaling presumes the energy confinement of the conventional RFP to be limited by pressure-driven resistive fluid interchange turbulence [17]. Assuming losses due to turbulence induced by resistive interchange modes, the theory predicts that the confinement time goes as:

$$\tau_E \sim \frac{a^2}{6\eta}\left(\frac{m}{M}\right)\frac{1}{\beta^2}, \tag{5.30}$$

where a is the minor radius, η is the plasma resistivity, m is the electron mass, and M the mass of the bulk ion. Balancing these losses with the ohmic input power ($\eta J^2 \sim nT/\tau$) yields a maximum (constant) beta for the RFP [17]:

$$\beta_{tot} \cong \left(\frac{m}{M}\right)^{\frac{1}{6}}. \tag{5.31}$$

Coincidentally, this amounts to a maximum beta for MST of 25.4%, within the error bars of the measured value at low current with pellets. The theory also indicates that in an ohmically heated RFP, the temperature scales as I^2/N, i.e., beta is constant. With a classical resistivity ($\eta \sim T^{-\frac{3}{2}}$) and $T \sim I^2/N$, Eq. 5.30 becomes [16]:

$$\tau_E^{C-T} \sim \; I_p^{1.5}\left(\frac{I_p}{N}\right)^{1.5} a^2. \tag{5.32}$$

Previous improved confinement, low density discharges produced global energy confinement times exceeding the prediction of Connor and Taylor [1]. The achieved confinement times with pellet fueling also exceed the scaling. The confinement data in Fig. 5.24 were taken from [16] and Fig. 12 of [1] with the solid line ($\tau_E = 10.2a^2I^3/N^{1.5}$) representing the best fit found therein to standard RFP results (+). Both MST and RFX experiments show that as current is increased for standard discharges the experimental confinement times fall short of those predicted by the scaling. Previous PPCD results from MST are denoted by points (a)-(c), and points (d) and (e) are from the experiments detailed in this thesis. The observation of improved confinement plasmas, both past and present, exceeding the scaling implies interchange mode turbulence isn't limiting the energy confinement at high beta. In fact, as will be shown in Chapter 6, the pressure-driven tearing mode may be limiting confinement at the highest betas.

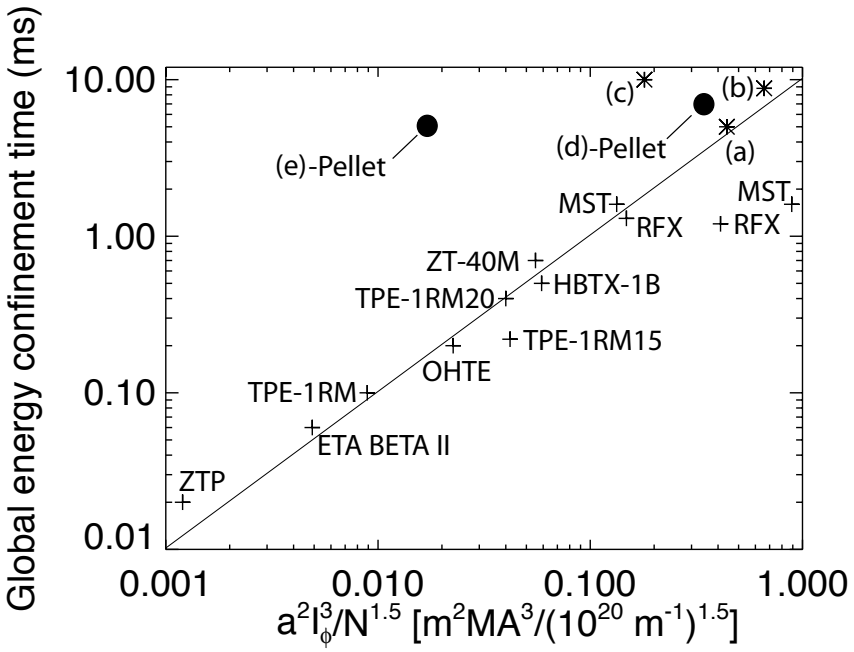

Figure 5.24: Connor-Taylor scaling of confinement for various RFP devices (+) including standard MST plasmas and previous improved confinement results (∗) at plasma currents of (a) 340 kA, (b) 390 kA, and (c) 210 kA. Recent improved confinement results using pellet injection (•) are shown for plasma currents of (d) 480 kA and (e) 170 kA. Each data point represents the best case τ_E for a given plasma current.

Recent work at the TPE-RX experiment has produced an empirical scaling for energy confinement in RFPs that use the PPCD technique [18]:

$$\tau_E^{TPE} = (8.1 \pm 2.9) \times 10^{-3} a^{1.63\pm0.21} I_p^{0.78\pm0.23} \left(\frac{I_p}{N}\right)^{0.33\pm0.40} \Theta^{2.97\pm0.78}. \quad (5.33)$$

(in ms, m, kA, and 10^{-14} Am). Pellet fueled discharges are predicted to have confinement times of 24 ms and 11 ms for low and high current, respectively. The Θ-dependence for the scaling was determined from the database of PPCD discharges and varied from 1.5 to 3.5. In high current PPCD, $\Theta \sim 3 - 3.2$ but in low current $\Theta > 5$. This divergence between the expected (from TPE scaling) and measured (in MST) confinement times in low current experiments could be quickly explained away by the lack of data at high Θ used for the scaling. However, in low-current, pellet-fueled PPCD discharges, the poloidal beta has been increased by a factor of 2-3 over what was observed in the database of PPCD discharges. It's possible that plasma pressure is playing a larger role (in this case limiting confinement) for which the scaling can't account. Chapter 6 will focus on the effect of the increased pressure on stability.

The application of PPCD and the subsequent fluctuation reduction has led to energy confinement comparable to that of the tokamak [19]. Figure 5.25 shows how past and present MST data compare with the IPB98(y,2) ELMy H-mode empirical scaling. This scaling projects ELMy H-mode confinement times to be:

$$\tau_E^{ELMy} = 0.0562 I_p^{0.93} B^{0.15} P^{-0.69} n^{0.41} M^{0.19} R^{1.97} \epsilon^{0.58} \kappa^{0.78}. \quad (5.34)$$

(in s, MA, T, MW, 10^{19} m^{-3}, AMU and m) where M is the atomic mass of the bulk ions, R is the major radius, ϵ is the inverse aspect ratio $\frac{a}{R_0}$, and κ is the plasma elongation

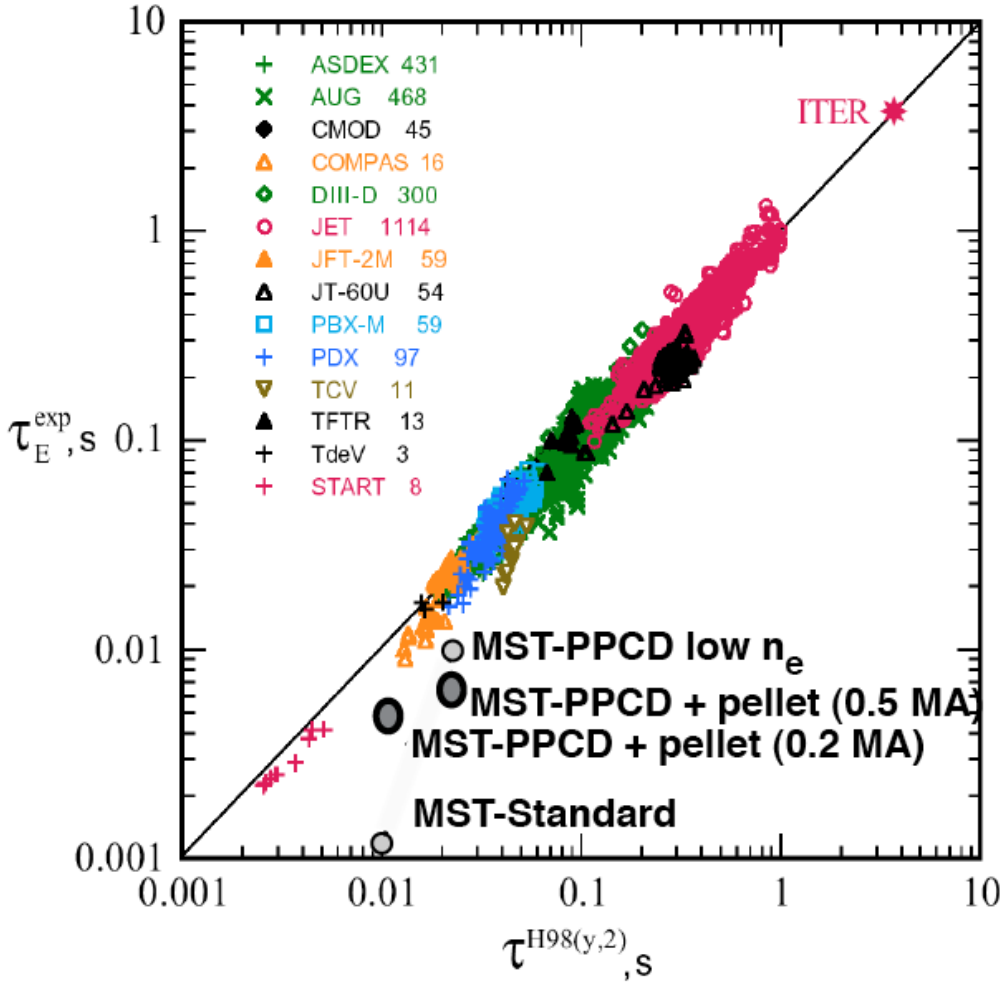

Figure 5.25: Improved confinement discharges approach ITER energy confinement scaling. Reprinted with (pellet data added) from [19] which was reprinted (with MST standard and MST PPCD low-n_e data added) from Ref. [20].

which for a circular device is 1. Pellet fueled discharges at 0.2 and 0.5 MA have projected confinement times of 9 ms and 22 ms respectively, using IPB98(y,2) scaling. Though it is an improvement over standard MST discharges, pellet fueling doesn't fit the scaling as well as low density PPCD discharges.

A measure of a device's fusion capability is the Lawson criterion or fusion triple product:

$$L_C = n_i(0)T_i(0)\tau_E \ [10^{20} \ m^{-3} \cdot keV \cdot s]. \tag{5.35}$$

Figure 5.26 shows the placement of many fusion devices using the criterion. The use of pellet-fueling in PPCD discharges has resulted in the RFP moving (barely) into the Proof-of-Principle regime of the Lawson criterion plot of fusion devices. The older RFP data point used the central electron temperature instead of ion temperature. MST's vertical departure from the previous RFP data point is due to the increasing T_i ($\sim$ 700 eV), four-fold increase in n_i (again Z_{eff} is assumed to $\sim$ 2 so that $n_i/n_e \sim 0.8$, leading to $n_i(0) > 3 \times 10^{13} \ cm^{-3}$), and long τ_E ($\sim$ 7 ms) observed in high current discharges.

5.7 Summary

The density during improved confinement discharges has been increased four-fold through the coupling of pellet injection to PPCD. Edge-resonant tearing modes are not excited with the extra fueling, and magnetic fluctuations remain low, limiting fluctuation-induced transport of particles and energy. At low current, a record $\beta_{tot} = 26\%$ for improved confinement RFP plasmas has been achieved. The energy confinement time in pellet-fueled, low current discharges (> 5 ms) is comparable to the value in low density PPCD discharges (10 ms) and remains well above the value in standard discharges ($\sim$ 1 ms).

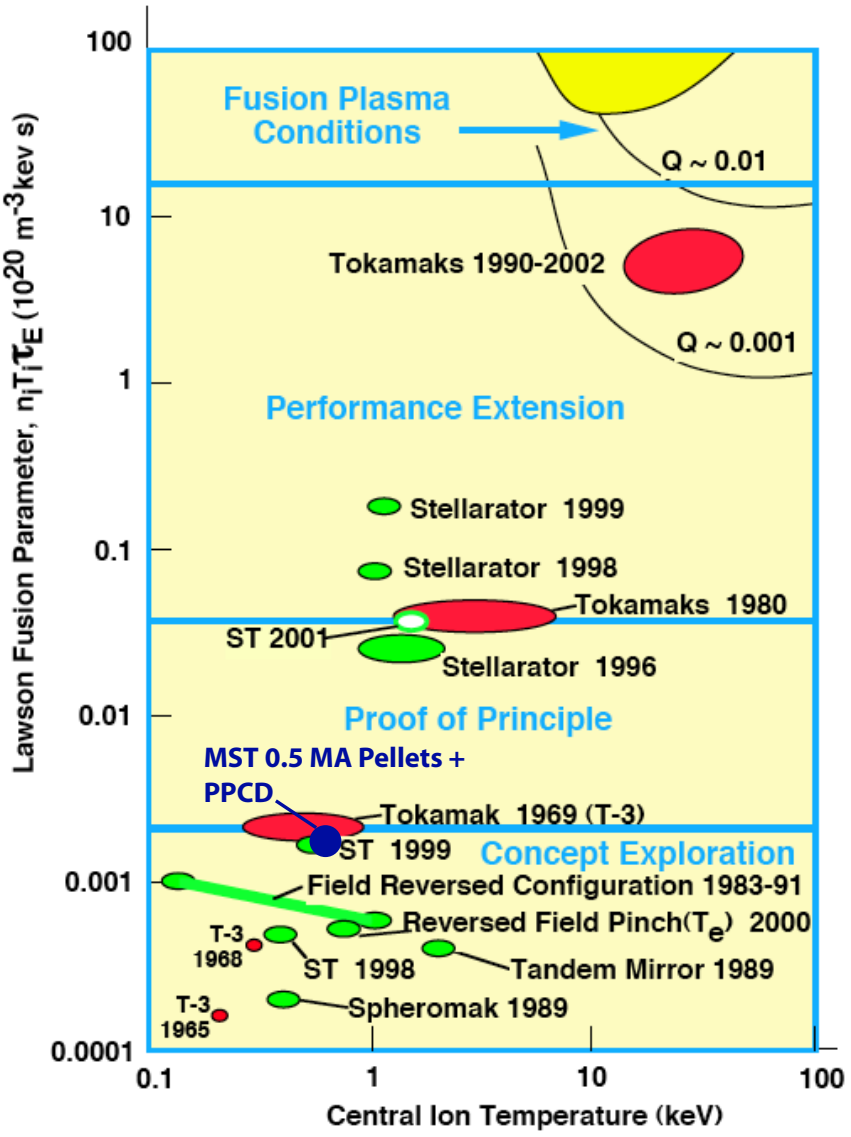

Figure 5.26: The use of pellet-fueling in PPCD discharges has resulted in the RFP moving (barely) into the Proof-of-Principle regime of the Lawson criterion plot (reprinted from http://fire.pppl.gov) of fusion devices.

At high current, β_{tot} is increased to 17% from 12%, and τ_E is 7 ms. A good portion of the increase in beta (at both currents) is attributable to the increase in ion pressure. For the first time during improved confinement, the ion temperature is observed to rise. A portion of the rise is attributed to improved thermal coupling of ions and electrons but it may not fully account for the increase. Particle confinement times at both high and low current remain unchanged ($\tau_p \sim 4-6\ ms$) at higher density when compared to low density improved confinement discharges. Similar to low density PPCD discharges, pellet-fueled PPCD discharges exceed the Connor-Taylor scaling prediction. The higher density and rising ion temperatures have also lead to an increase in the Lawson fusion parameter for RFP discharges.

Bibliography

[1] B. E. Chapman *et al.*, Phys. Plasmas **9**, 2061 (2002).

[2] J. Anderson, C. Forest, T. Biewer, J. Sarff, and J. Wright, Nuc. Fusion **44**, 162 (2004).

[3] J. Freidberg, *Ideal Magnetohydrodynamics* (Plenum Press, 1987).

[4] J. K. Anderson, *Measurement of the Electrical Resistivity Profile in the Madison Symmetric Torus*, PhD thesis, University of Wisconsin - Madison, 2001.

[5] S. P. Hirshman and D. J. Sigmar, Nuc. Fusion **21**, 1079 (1981).

[6] H. Knoepfel and D. Spong, Nuc. Fusion **19**, 785 (1979).

[7] B. Kuteev and A. Kostryukov, Tech. Phys. Lett. **25**, 606 (1999).

[8] R. Harvey *et al.*, Phys. Plasmas **7**, 4590 (2000).

[9] R. O'Connell *et al.*, Phys. Rev. Lett. **91**, 045002 (2003).

[10] G. Wurden *et al.*, in *Physics of Mirrors, Reversed Field Pinches and Compact Tori: Proceedings of the Course and Workshop, 1987, Varenna, Italy*, p. 159, 1988.

[11] E. Scime *et al.*, Physics of Fluids B: Plasma Physics **4**, 4062 (1992).

[12] S. Gangadhara *et al.*, Physical Review Letters **98**, 075001 (2007).

[13] L. Spitzer, *Physics of Fully Ionized Gases* (Physics of Fully Ionized Gases, New York: Interscience (2nd edition), 1962, 1962).

[14] G. Fiksel, Private communication.

[15] N. E. Lanier *et al.*, Phys. Rev. Lett. **85**, 2120 (2000).

[16] K. A. Werley, J. N. DiMarco, R. A. Krakowski, and C. G. Bathke, Nuc. Fusion **36**, 721 (1996).

[17] J. W. Connor and J. B. Taylor, Phys. Fluids **27**, 2676 (1984).

[18] Y. Yagi, H. Koguchi, Y. Hirano, H. Sakakita, and L. Frassinetti, Nuc. Fusion **45**, 138 (2005).

[19] J. Sarff *et al.*, Nuc. Fusion **43**, 1684 (2003).

[20] I. P. E. G. on Confinement, Transport, I. P. E. G. on Confinement Modelling, Database, and I. P. B. Editors, Nuc. Fusion **39**, 2175 (1999).

To be a rock and not to roll.

Led Zeppelin

6

Stability at High Beta

6.1 Introduction

Previous PPCD experiments have led to increased beta and longer confinement times but not to the identification of a β-limit, disruptive or otherwise. These low density PPCD experiments were able to attain improved confinement by limiting the fluctuation induced transport produced by current gradient driven tearing modes. Pellet-injection experiments have shown that even higher β can be obtained while maintaining stability to the current gradient driven tearing mode. However, the increase in plasma pressure (particularly in 0.2 MA discharges) leads to the possibility that the pressure gradient could have a deleterious effect on plasma stability. In these experiments, the higher betas are attained without disruptive events that would be related to a β-limit. These discharges, however, are calculated to be unstable to pressure gradient driven modes, both local (interchange modes) and global (tearing modes). There is however a drop in τ_E in going to higher betas.

In this chapter a brief introduction to both the interchange and tearing modes will be given. This will be followed by the results of stability calculations for high-β, pellet fueled discharges. Experimental observations (and lack thereof) of the predicted instabilities will be discussed along with a possible "soft β limit" for MST.

6.2 The interchange mode

When a heavy fluid is placed above a lighter fluid in a gravitational field, the system is unstable to the Raleigh-Taylor instability. If excited, the Raleigh-Taylor instability results in the two fluids exchanging places and a reduction in the system's potential energy. If the fluids are replaced with a magnetized plasma having a gradient in pressure, the gravitational force is replaced with the magnetic field curvature. In this case, the instability to be excited is the interchange mode, and stability is determined by the direction of magnetic field curvature in relation to the pressure gradient (Fig 6.1).

In the case of bad curvature, the plasma wishes to expand further (down the pressure gradient) and the magnetic field decreases in the same direction. Plasma expansion has to work against the tension of the magnetic field in a region of good curvature. One drawback of the RFP is that the curvature is bad everywhere resulting in the possibility of interchange instability if the pressure gradient is large enough. For comparison, the tokamak has good curvature on the inside of the torus and bad curvature on the outside, but in general has good average curvature. Stellarators also have regions of good and bad curvature. As the average curvature can either be good or bad, the stellarator can be subject to interchange instability.

Magnetic shear ($\frac{1}{q}\frac{dq}{dr}$) can stabilize the interchange mode. In a cylindrical plasma,

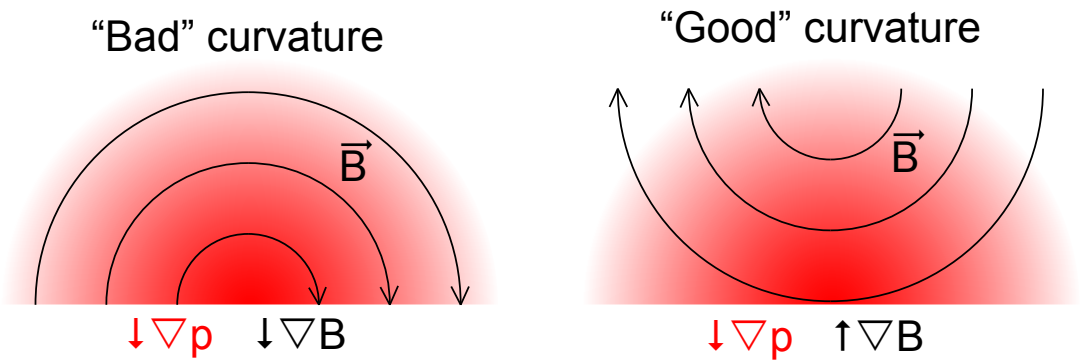

Figure 6.1: Quality of curvature depends on the direction of the pressure gradient relative to the curvature of the magnetic field. In bad curvature both point radially inward. In good curvature case, they are anti-parallel.

addition of magnetic shear alters the stability criterion, and is known as the Suydam criterion [1]:

$$\frac{rB_z^2}{4\pi}\left(\frac{q'}{q}\right)^2 + 8p' > 0, \tag{6.1}$$

where $(\ )' = \frac{d}{dr}$, and all quantities are evaluated at the resonant surface for a particular set of mode numbers (m,n). The growth rate of the interchange mode is larger for shorter wavelengths [2]. Consequently, the mode numbers for interchange instability are typically large, and the mode is localized. In toroidal geometry, stability to interchange is governed by the Mercier criterion and is determined by the expression [3]:

$$\frac{rB_\phi^2}{4\pi}\left(\frac{q'}{q}\right)^2 + 8p'\left(1-q^2\right) > 0, \tag{6.2}$$

which can be written in the form:

$$D_M = -\frac{8\pi q^2(1-q^2)}{rB_\phi^2 q'^2}\nabla p > 0.25. \tag{6.3}$$

Note that for the RFP, $q < 1$ so that the $(1-q^2)$ term approaches unity, and the Mercier criterion reduces to the cylindrical limit.

Experimentally, stellarators have achieved plasma betas that exceed the Mercier criterion without observation of plasma instability [4]. Previous RFP experiments haven't resulted in pressure gradients exceeding the Mercier criterion. However, reconstructed pressure profiles from standard confinement RFP discharges appear to be limited to the Mercier critical profile in the edge [5].

Recent theoretical work for the RFP has shown that the interchange instability would be weak near marginal stability ($D_S \sim 0.25$) [6], and that no sudden changes in the growth rate occur near the limit [7]. Furthermore, the localized mode remains resistive at plasma betas several times the Suydam limit before becoming ideal at very high beta [7].

6.3 The tearing mode

In ideal MHD, the kink instability is the result of plasma current parallel to magnetic field. Figure 6.2 shows an m = 1 kink mode becoming unstable for a plasma column and the shifting of the plasma column. On the inner part of the perturbation the poloidal field is stronger than it is on the outside of the bend resulting in a force that enhnances the perturbation. Though field lines are bent, they are not "broken" until resistivity is introduced.

In a resistive plasma, the kink mode can break and reconnect field lines. Capable

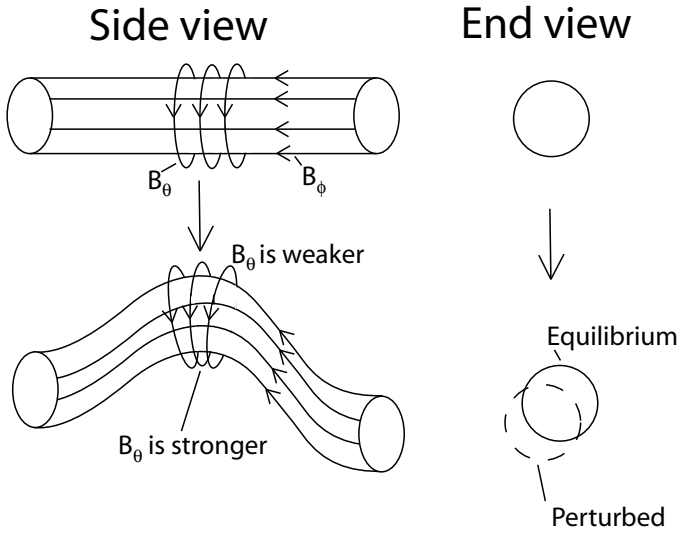

Figure 6.2: The m = 1 kink instability

of rearranging the plasma's magnetic topology, the resistive kink mode is referred to as the tearing instability. The tearing instability occurs at a resonant surface. Figure 6.3 shows the creation of magnetic islands following magnetic reconnection. Following reconnection, transport is enhanced, and particles and energy can flow along field lines across the resonant surface.

In the RFP, $q < 1$ everywhere and multiple m = 1 and m = 0 modes are resonant within the plasma. The close proximity of the resonant surfaces leads to overlap of magnetic islands creating a large volume of stochasticity across which particles and energy can move from the core to the edge. Tearing mode fluctuations are the dominant source of transport degradation in the RFP.

In most experimental cases to date, the tearing mode is driven by the gradient in the plasma current but can also be driven by the pressure gradient. Alteration of the current profile to reduce the free energy available to drive the fluctuations has been ex-

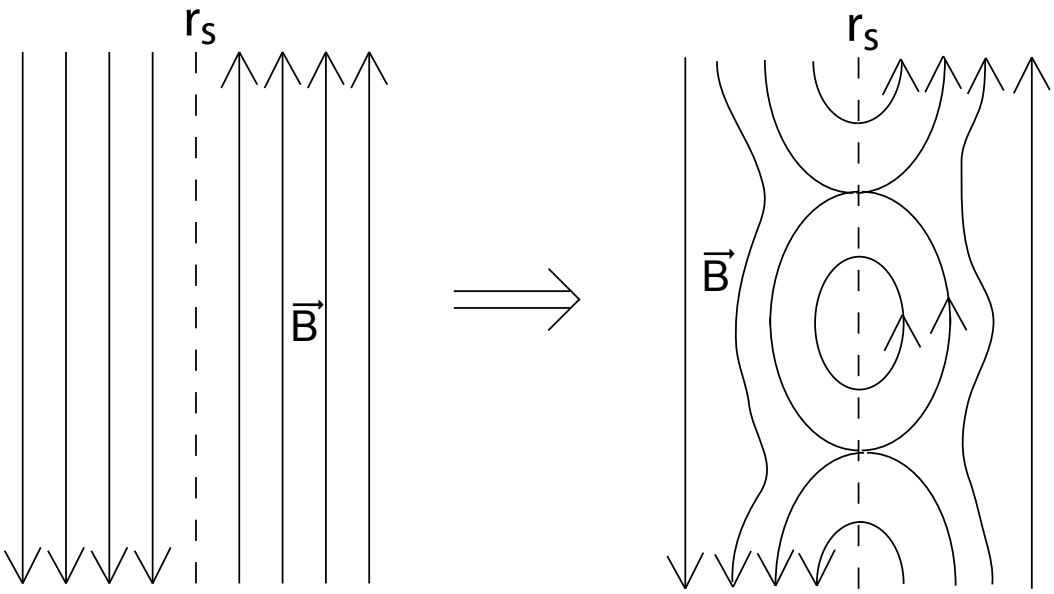

Figure 6.3: Tearing instability breaks and reconnects field lines altering the magnetic field topology

plored experimentally (PPCD) and has resulted in an order of magnitude increase of the confinement time.

6.4 Interchange stability in pellet-fueled discharges

Pellet fueled, improved confinement discharges are observed to exceed the Mercier criterion. Figure 6.4 shows the Mercier critical and measured pressure (from density and temperature measurements) gradients. For $r/a < 0.4$ the criterion is exceeded.

Stability calculations provide the growth rates for the unstable Mercier-like local interchange modes (Fig. 6.5) [8]. The stability calculations were done with the DEBS code [9]. The code was used to do a linear resistive MHD calculation with a Lundquist number $S = 5 \times 10^5$ where S is defined as the ratio of the resistive diffusion and Alfvenic time

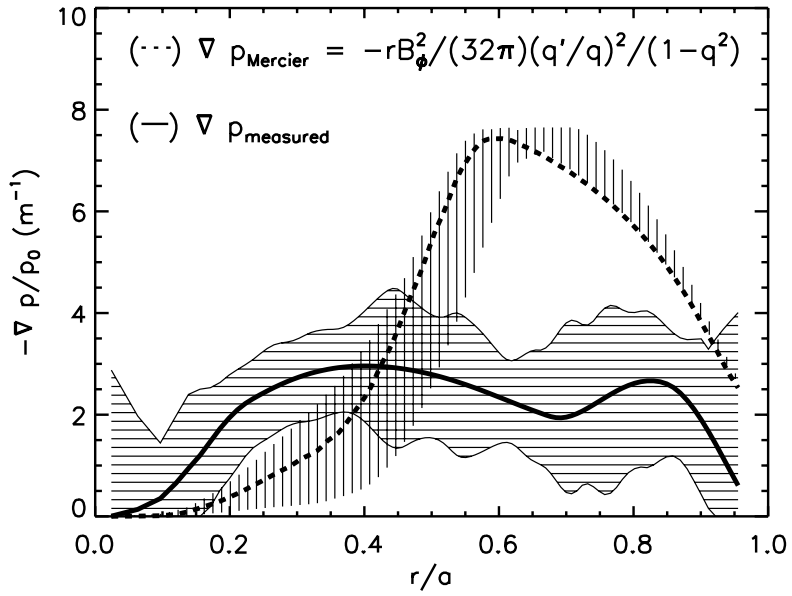

Figure 6.4: Mercier Criterion and pressure gradient for a single time point (t =19 ms) in a 0.2 MA pellet-fueled PPCD discharge. At this time $\beta_{tot} = 26\%$. Striped regions represent error bars.

scales, $\tau_R = \mu_0 a^2/\eta$ and $\tau_A = a/v_A$, respectively. The experimentally observed Lundquist number for pellet-fueled PPCD discharges is $S \sim 10^6$, and in low density PPCD, S can approach 10^7.

The calculation is performed in cylindrical geometry whereas the experimental equilibrium reconstruction is toroidal. In order to fit the measured pressure and λ profiles, the q-profile was altered. This led to the m = 1, n = 6, and consequently high-n modes with corresponding m-to-n ratios of 1/6 (*e.g.* the m = 3, n = 18), no longer being resonant, so their growth rate is not calculated. The modes left resonant with $D_M > 0.25$ where those with m-to-n ratios of 1/7 and 1/8. Both of these modes (m/n = 3/21 and 3/24) are calculated to be resistive and unstable. The calculations predict that localized, Mercier-like (high-n) interchange modes resonant in the core are unstable with growth times $\leq 200\ \mu s$, as shown in Fig. 6.5 for m = 3 modes.

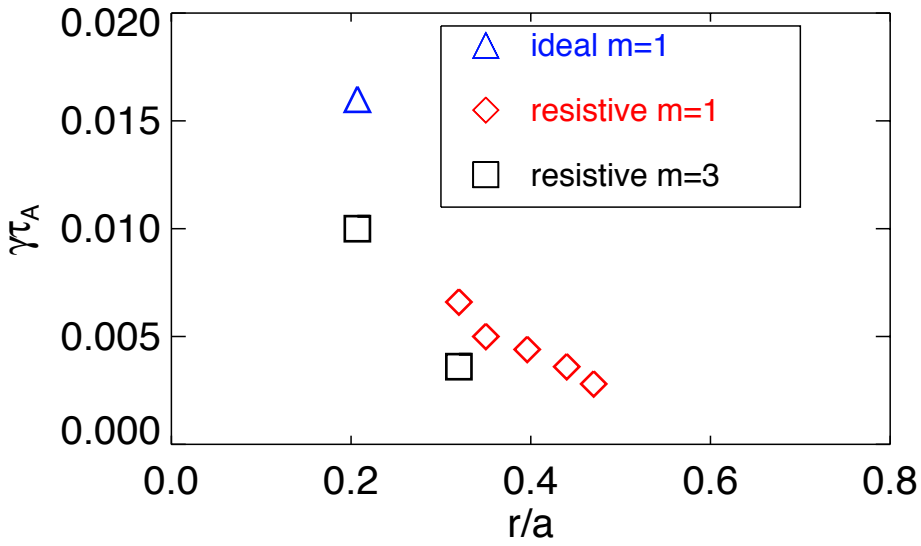

Figure 6.5: Growth rates (in terms of the Alfvén time $\tau_A \sim 1\ \mu s$) for instabilities calculated with a linear resistive MHD code indicate that both global tearing (m = 1) and local interchange (m = 3) are unstable for a pellet-fueled PPCD discharge at low current where $\beta_{tot} = 26\%$. Calculations are courtesy of Fatima Ebrahimi.

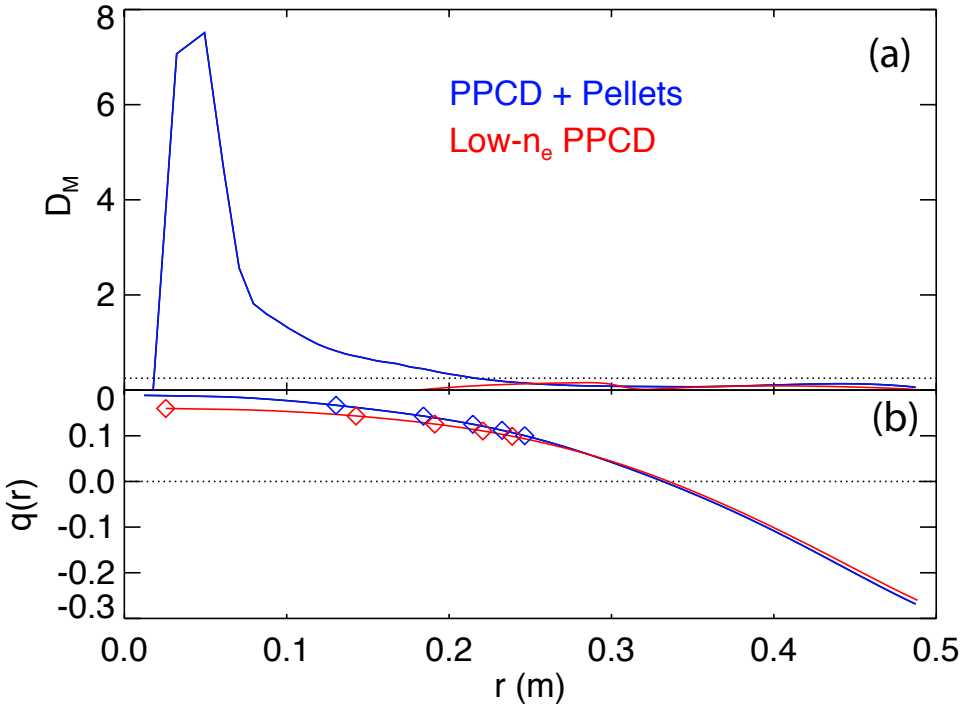

Figure 6.6: (a) The Mercier criterion parameter D_M exceeds resistive instability threshold ($D_M = 0.25$) only during the pellet-fueled case. (b) Plot of $q(r)$ for both low and high density PPCD.

These shorter wavelength, local modes are calculated to be growing on time scales (hundreds of microseconds) much shorter than the period of improved confinement (up to 10 milliseconds). Although instabilities are predicted, we do not observe any effects that would be indicative of interchange activity, *e.g.*, flattening of the pressure profile, indicating that either the modes are saturated at low amplitude or that the spatial scale of the effect is smaller than we can resolve. As noted in Chapter 5, the Connor-Taylor scaling assumes confinement to be limited by resistive interchange turbulence but these high-β, pellet-fueled discharges exceed the scaling.

Figure 6.6 shows $D_M(r)$ and the safety factor profile for low and high density PPCD.

The measured values ($D_M = 0.45,\ 0.26$ for the m/n = 3/21 and 3/24 modes respectively) and those used in the calculation ($D_M = 0.76,\ 0.35$) are just above marginal stability. For the instability to become more robust, D_M should exceed 0.5 [6] at the mode's resonant surface.

6.5 Tearing stability in pellet-fueled discharges

In standard confinement discharges, tearing modes are present and are driven by the current gradient. The application of PPCD modifies the current gradient in order to reduce the free energy that drives global tearing instability. However, plasma pressure is also a source of free energy for these modes. Stability calculations utilizing the equilibrium profiles from high-β pellet discharges show that these long wavelength modes (m = 1) are now becoming unstable to pressure (Fig. 6.5). With one exception, the tearing modes calculated to be unstable were resistive. In the case of the m = 1, n = 7, the eigenmode is ideal, *i.e.*, the associated B_r goes to zero at it's resonant surface (r/a = 0.2). Similar calculations for low-n_e PPCD discharges show that these modes are stable. Similarly, if the pressure is reduced for the stability calculation of the pellet-fueled, high-β discharges, the m = 1 modes become stable indicating that the modes are indeed driven by the pressure gradient and not the current gradient.

The tearing modes are predicted to be linearly stable in low density improved confinement discharges; m = 1 modes are experimentally observed to be saturated at a low level compared to the between-sawtooth-crash value in standard discharges. Comparison of the experimental m = 1 magnetic fluctuation spectra (Fig. 6.7) for three regimes shows the reduction with PPCD, at both low density (w/o pellets) and high density (w/ pellets)

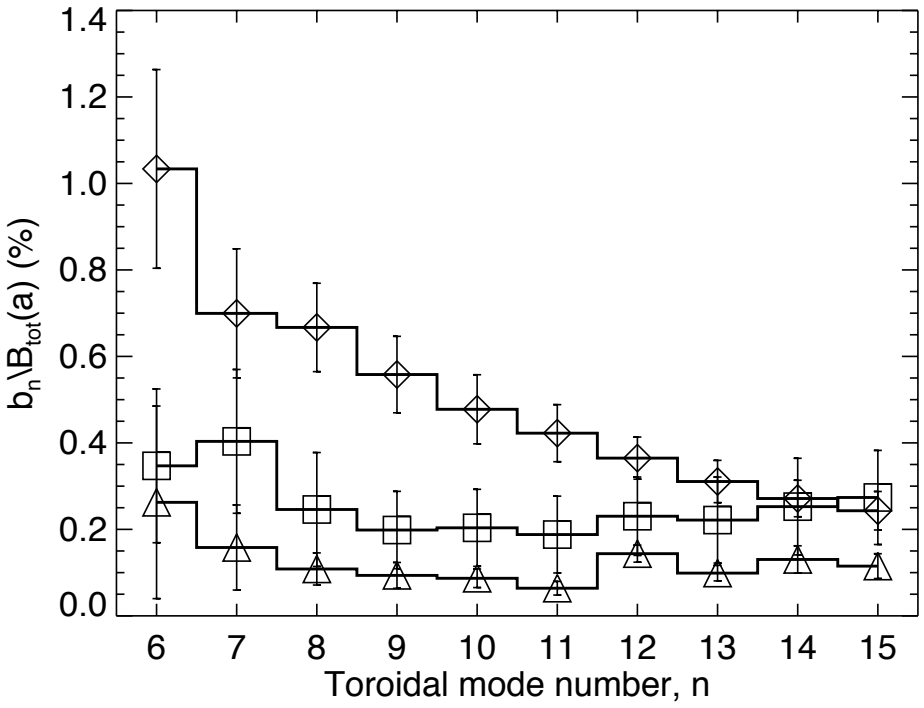

Figure 6.7: Low current mode spectrum comparison for (⋄) standard confinement, (△) low density PPCD, and (□) high density PPCD. For standard confinement, fluctuations are measured between sawteeth. The spectra are ensembles of many shots, and the error bars are based on the variation for that mode in the ensemble.

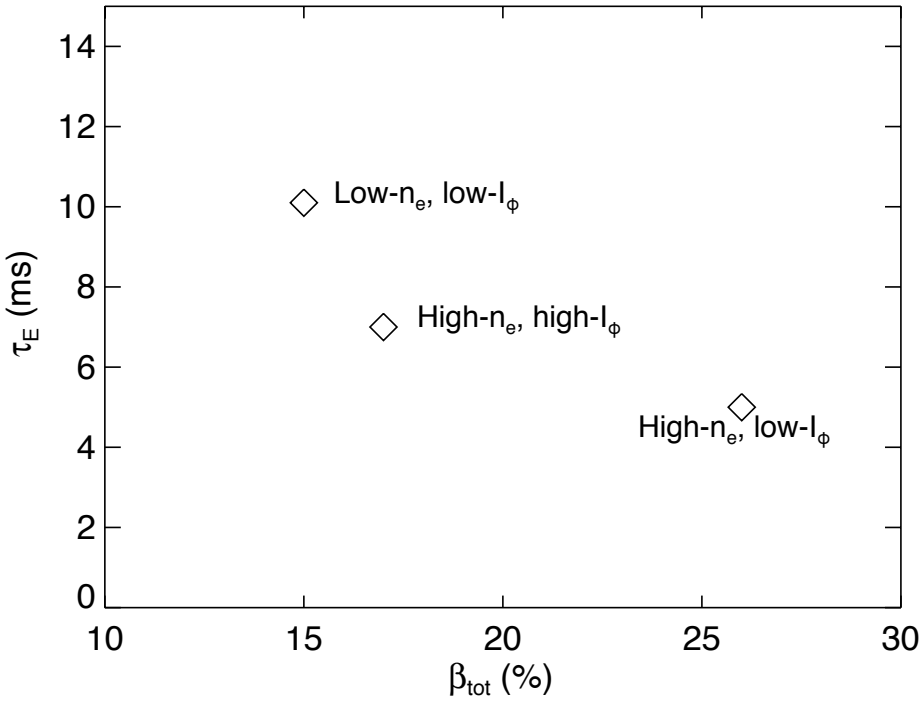

Figure 6.8: Comparison of τ_E and β_{tot} for the best cases reached so far show an inverse relationship between normalized pressure and confinement time. However, the energy confinement time for high-n_e, low-I_ϕ is a lower bound as noted in Chapter 5 and could easily be several milliseconds longer.

compared to a standard discharge. However, the reduction is smaller at high density, reflecting either the increased pressure (Fig. 5.21) or the slight off-axis peaking of the λ-profile (Fig. 5.13). The level of fluctuations at higher density may account for the smaller improved energy confinement time.

6.6 β-limits

Though the pressure may be playing a larger role in the plasma's stability, a disruptive β-limit has not been observed. However, there are indications of a "soft β limit." Even

with a conservative estimate of error bar size ($1 - 2\ ms$), comparison of the best cases show a trade off between β and τ_E (Fig. 6.8). If these limited data are representative, two possibilities immediately emerge - one a local effect, the other global. If interchange instability is induced (but not observed due to diagnostic limitations) then it could be the driving force for a soft β-limit through turbulent transport. But as the confinement scaling based on such a mechanism (resistive interchange turbulence) is exceeded, it is more likely that the larger m = 1 fluctuation amplitudes at higher density (due to the increased pressure) are the source of the reduced energy confinement at higher beta.

6.7 Summary

At low current, a record $\beta_{tot} = 26\%$ for improved confinement RFP plasmas has been achieved, but this does not represent a β-limit. At these pressures, resistive MHD instabilities (local interchange and global tearing) are predicted to be linearly unstable, but disruptions are not observed. The lack of disruptions doesn't discount the possibility of a soft β-limit, however, and an apparent drop in τ_E is observed at higher beta.

Bibliography

[1] B. R. Suydam, in *Proceedings of the 2nd United Nations International Conference on the Peaceful Uses of Atomic Energy, Geneva* Vol. 31, p. 157, 1958.

[2] H. P. Furth, J. Killeen, and M. N. Rosenbluth, Phys. Fluids **6**, 459 (1963).

[3] V. D. Shafranov and E. I. Yurchenko, Soviet Journal of Experimental and Theoretical Physics **26**, 682 (1968).

[4] S. Okamura *et al.*, in *Plasma Physics and Controlled Nuc. Fus. Res. 1994* Vol. 1, pp. 381 – 8, 1994.

[5] T. M. Biewer, *Electron Thermal Transport in the Madison Symmetric Torus*, PhD thesis, University of Wisconsin - Madison, 2002.

[6] S. Gupta, J. D. Callen, and C. C. Hegna, Phys. Plasmas **9**, 3395 (2002).

[7] F. Ebrahimi, S. C. Prager, and C. R. Sovinec, Phys. Plasmas **9**, 2470 (2002).

[8] F. Ebrahimi, Private communication.

[9] D. D. Schnack, D. C. Barnes, Z. Mikic, D. S. Harned, and E. J. Caramana, J. Comput. Phys. **70**, 330 (1987).

. . . and the cheese stands alone.

Omar Little, in *The Wire*

7

Conclusions

7.1 Plasma control developments

The addition of a pellet injector and high-throughput puff valve, as well as an upgrade to MST's fueling system has increased the upper bound on density for MST operation both in standard and PPCD plasmas. Standard plasmas were generally limited to line-averaged densities of $\lesssim 2.5 \times 10^{13}\ cm^{-3}$ due to limitations in the fueling system. Increasing the voltage applied to the valves has increased the upper bound to $\sim 3.5 \times 10^{13}\ cm^{-3}$. Use of a single high-throughput valve has produced $(\triangle<n_e>)/<n_e>\sim 3$ with local densities of $4 \times 10^{13}\ cm^{-3}$. Density profiles are hollow following single valve fueling. Pellet fueling of MST discharges has been able to produce $(\triangle<n_e>)/<n_e>\sim 5$ and local densities exceeding $5 \times 10^{13}\ cm^{-3}$. Density profiles following pellet injection can be peaked, flat or hollow. Finally, the combination of pellet injection and PPCD has resulted in a fourfold increase in density while maintaining low magnetic fluctuations.

7.2 Physics results

The physics results can be categorized thusly: investigation of the RFP beta limit, exploration of ion heating during PPCD, and investigation of the RFP density limit.

7.2.1 Beta limit

The coupling of pellet injection and PPCD has produced discharges where β_{tot} reaches 26%, a record for the improved confinement RFP. No disruptions are observed at this higher beta, but instabilities (both local interchange and global tearing) have been calculated to be unstable. The Mercier criterion is surpassed indicating that local interchange modes will be unstable and fast-growing. These modes are not observed and are either saturated at small amplitude, or the scale of the instability is beyond the resolution of the current diagnostic set. Global tearing modes are calculated to be stable during low density PPCD operation and are observed to be saturated at a low level $\tilde{b}/B \lesssim 0.2\%$. In pellet-fueled discharges, they are calculated to be unstable and are observed to be saturated at higher levels ($\sim$ 0.4%) than at low density. This higher saturation level is attributed to the increased pressure drive for instabilities. While energy confinement is increased compared to standard discharges, pellet-fueled, higher-β plasmas have slightly shorter confinement times than low-density PPCD discharges. This may imply a soft β-limit.

7.2.2 Ion heating

For the first time during improved confinement, the ion temperature is observed to be increasing. This increase is observed at all radii. Though collisional coupling to the

electrons is drastically increased in these higher density plasmas, it cannot be conclusively identified as the sole source of the rising temperature.

Local measurements of heating and ion thermal energy changes are good, but there aren't concurrent measurements of the convective and charge-exchange losses - only estimates. The collisional heating is calculated to be as high at 100 kW/m^3 with the measured $\frac{dW_{th,i}}{dt}$ even higher (150 kW/m^3) indicating that without energy losses through convection and charge exchange, another source is required.

Measurements of the global convective and global charge-exchange losses are good. However, calculation of the global collisional heating and measurements of global ion-thermal energy changes are estimates at best. For the global ion power balance, it remains unclear if there's any anomalous heating of the ions.

7.2.3 Density limit work

In order to observe a Greenwald-like limit, it is necessary to be able to scan both density and plasma current. MST has the capability of producing discharges with plasma currents up to 0.6 MA. However, for gas-fueled discharges, the upper limit of MST capabilities so far is $<n_e> \sim 3.5 \times 10^{13}\ cm^{-3}$. This corresponds to a Greenwald "current" of ~ 0.3 MA, *i.e.,* MST could only really attempt to exceed the Greenwald limit for plasma currents less than 0.3 MA.

The Greenwald limit has been reached both with pellet injection and gas injection. During PPCD, pellet-fueling has produced sustained discharges where the limit is exceeded. Early terminations have been observed for edge-fueled discharges with $N_G \sim 1$ but only for a limited range of plasma currents. Without the ability to scan a larger range of densities, the Greenwald scaling can't be confirmed (or refuted) in MST.

7.3 Future work

7.3.1 Further injector optimization

Future optimization of the pellet injector centers around two points. At high current, it appears possible to inject more material than the injector is currently capable of producing. At low current, there is still variability in pellet speed (and consequently the arrival time), and therefore it remains difficult to ensemble discharges for analysis.

At present the barrels in use on the pellet injector were chosen such that there was a core-penetrating pellet for every operating regime. Now that the ablation characteristics are better understood and barrel-swapping has been streamlined, it would be desirable to reconfigure the injector. It could either be done for maximum coverage of operating regimes or focused on a specific operating regime and then reconfigured for the subsequent run.

At high current, it is desirable to be able to inject more material. A single pellet providing the same number of particles as two pellets would also reduce variability pellet deposition. As such, a single 2.0 mm diameter fast pellet[1] (roughly twice the volume of 1.6 mm pellets) could replace the current combination of two 1.6 mm pellets (one slow and one fast) for high current discharges. However, for experiments with higher densities or for repetitive injection, multiple large, fast pellets (1.3-2.0 mm in diameter) could be used for higher currents ($\geq$ 0.3 MA). This would allow for multiple injections either simultaneously or consecutively.

Lower currents still present a problem in that the core-ablating pellets (punch-propelled) have a large variability in arrival times. The use of snub-nosed or vented barrels, where the

[1]MST is in possession of such barrels, but they have yet to be installed.

variation in breakaway times are similar to fast-pellets, should be revisited with the now-well-established dry-fire technique. Earlier tests showed that these pellets reliably reached speeds of 500-600 m/s. For multiple small-to-moderately sized pellets ($< 1.0\ mm$), this appears ideal for core-penetration at low current. Such a setup could provide $\frac{\triangle n_e}{n_e} \sim 2-3$ as observed for the unreliable 1.6 mm, punch propelled pellet but with the use of more reliable high speed pellets.

7.3.2 Beta limit

It's clear that even with pellet injection, MST has yet to reach a disruptive β-limit. With further optimization of the injector and the lengthening of PPCD (with the soon to be installed programmable B_ϕ supply) increasing β should be possible and surpassing interchange stability could even occur at high current. Use of gas-propelled pellets (be they standard or vented barrels) should also allow for the tailoring of the pressure profile.

Identification of a soft β-limit may be more difficult. A disruptive limit is obvious, but the soft limit would just sneak up on the experimenter. It would require a scan of β values while also measuring τ_E. While time consuming, it is not impossible. Tracing the source of the limit, if it's due to increased m = 1 tearing (pressure or current driven) could simply be a matter of comparing fluctuation levels over a large set of discharges. If the limit is interchange-related, it would be possible to get the pressure profile directly from Thomson scattering measurements possibly with multiple lasers such that ensembling may not be necessary. Otherwise the requirement of ensembling high-β discharges that are locally interchange unstable, *e.g.*, low current, pellet-fueled PPCD discharges would make pellet reproducibility improvements a necessity.

7.3.3 Ion heating

The cause of the temperature rise in pellet-fueled PPCD experiments is still unclear. It's also not necessarily clear why the temperature doesn't rise during low density PPCD experiments except that the collisional heating time scale is an order of magnitude greater than the PPCD pulse length. Regardless, computing the ion power balance is a difficult undertaking. The easiest route for MST may be a global power balance calculation. The Thomson system is now capable of capturing multiple profiles during a discharge. The global calculation needs both ion temperature profiles (the diagnostic capability of MST is limited to the T_i evolution at a single radial point currently) and the time evolution of the electron temperature profile. There is a proposal for a multi-point T_i diagnostic that would solve the former. Currently, the Thomson system can provide T_e-profiles at two time points. Future upgrades to the system may increase that number. Given this, the injector is already capable (at high current) of producing discharges for measuring the heating.

7.3.4 Density limits

Defining a density limit on MST is a difficult task, but higher density operation is key for an RFP reactor. If one dares to look, the use of multiple gas injectors would be necessary to achieve Greenwald numbers greater than unity for all plasma currents. Currently, the single high-throughput valve will accomplish this for plasma current up to 0.25 MA. Two extra valves should be sufficient to breach Greenwald at MST's maximum current of 0.6 MA.

7.3.5 Pellet enhanced performance

Tokamak pellet-fueling experiments have observed improvements in confinement following pellet-fueling due to profile peaking, the so-called "pellet-enhanced performance" or PEP mode [1]. In MST standard discharges, pellet fueling resulted in peaked density profiles and reduced sawtooth behavior as well. Though there is a drop in m = 0 crash activity in these discharges, it is believed that the confinement is unchanged as the m = 1 fluctuation amplitude remains unchanged. The sawtooth behavior may be retarded, but the baseline fluctuation levels remain unchanged indicating the confinement is not enhanced, i.e. no RFP PEP mode yet.

The work on pellet-fueled standard discharges occurred before the advent of improved injector operation. With projected upgrades of the injector, a full examination of the pellet's effects on confinement in standard discharges will be possible. Altering the injector barrel configuration will allow for core deposition at many currents or possibly the ability to get high density (beyond Greenwald) at one particular current (barrels would be switched out for different target plasmas). Using MST full-PFN operating mode, multiple pellets could be injected in sequence during the current flat-top.

Bibliography

[1] B. Tubbing *et al.*, Nuc. Fusion **31**, 839 (1991).

Another flaw in the human character is that everybody wants to build and nobody wants to do maintenance.

Kurt Vonnegut, *Hocus Pocus*

A

Pellet Injector User's Guide

A.1 Introduction

This appendix is meant as sort of a brain-dump of the author's knowledge of all things pellet injector related so that in the event of his departure (planned or not), pellet-fueled MST discharges don't depart with him. First, a more in-depth (than was given in Chapter 2) description of the injector and all its parts will be given. A sizable remainder of the author's pelleteering know-how involves operating procedures which haven't been written down, and will be categorized by the frequency of the task to be performed, be it over the course of a shot cycle, a run day, or performed once in a blue moon. Past problems that have been solved are included so that if the difficulty arises again, the future Pelleteer will have an idea of what (or what not) to do. A few problems have not been solved, and they are included so that future users are aware of them – perhaps they'll fix them? The injector settings for the successful 2006 pellet+PPCD campaigns are presented so that future Pelleteers can take up where the author left off. There is some information that

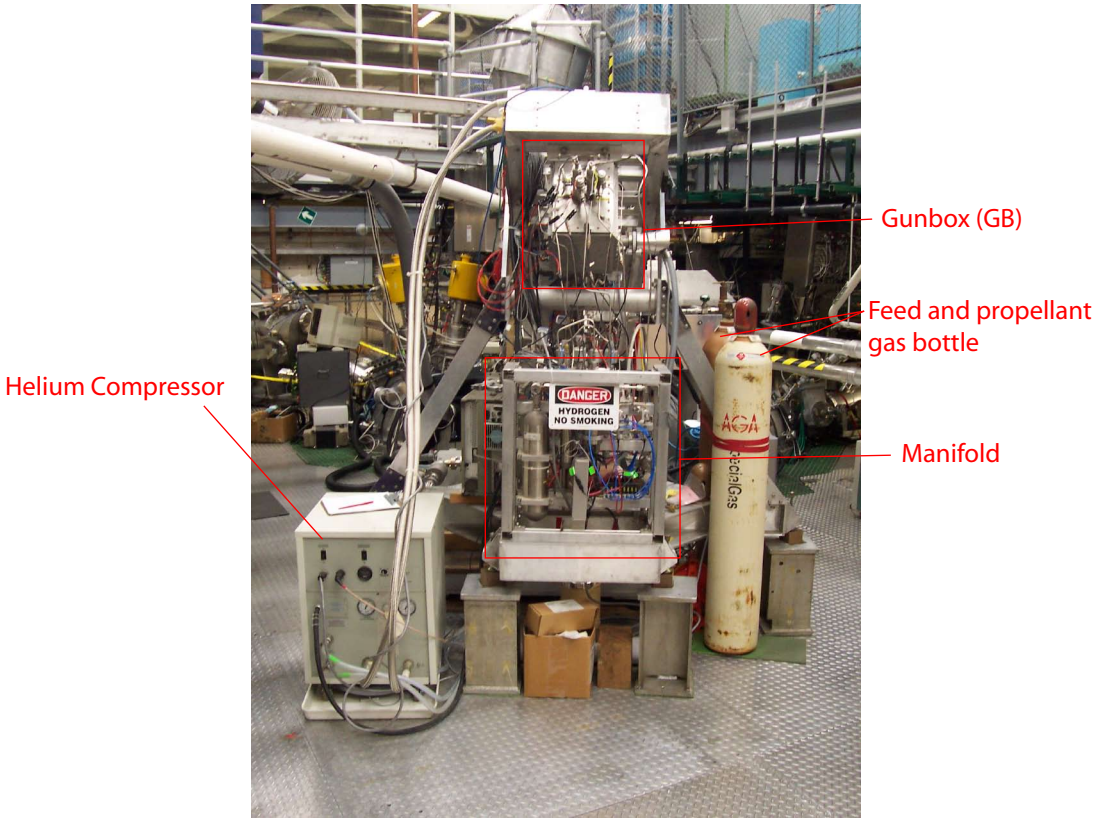

Figure A.1: Injector - rear view

doesn't fall into any of these categories and are included as "Tips 'n' Tricks".

Warning: Use common sense when working around high pressure gases (like the propellant) and the vacuum systems. If you don't trust your common sense or this appendix, talk to Steve Oliva. He'll set you straight. Also, the author is not responsible should the injector rise up and attack its oppressors.

A.2 Detailed layout

The Pellet Injector System (yes, P.I.S) can be subdivided into five parts: the gunbox, manifold, injection line, control rack and cooling system. The first three are located on the 2nd deck of the MST experiment. The control rack can be found in MST's control room, and the cooling system spans MST's 1st and 2nd decks. Multiple views of the 2nd deck residents of the system are shown in Figures A.1, A.2, and A.3. The location of pellet formation (the gunbox), the source of both propellant and feed gases, the contraption that controls the flow of said gases (the manifold), and the device that cools the gunbox (the helium compressor) can all be seen at the rear of the injector (Fig. A.1). Between the gunbox and MST, is the injection line (Figs. A.2 and A.3). The roughing pumps that back the turbo pumps on the injector are all situated on a trampoline (at each corner is a small inflatable "tire" to dampen vibrations) sitting under the injection line. Also situated on or near the injection line are the surge tanks (takes up propellant gas, preventing it from reaching MST vacuum), lightgate/photography station, microwave cavity (provides a relative measure of pellet mass), and the gunbox gate valves [separating the rear surge tank (RST) vacuum from the volume where pellets are formed].

A.2.1 The manifold

The manifold consists of a series of computer controlled pneumatic valves, their controllers, small ballast tanks, a single roughing pump, and the propellant and feed gas bottles. A diagram of the various parts and how they're connected is shown in Figure A.4. The pneumatic valves (PV-XXX) are actuated by compressed air. The needle valves (NV-XXX) are adjustable so that the rate of gas flow can be (manually) varied. Pressure

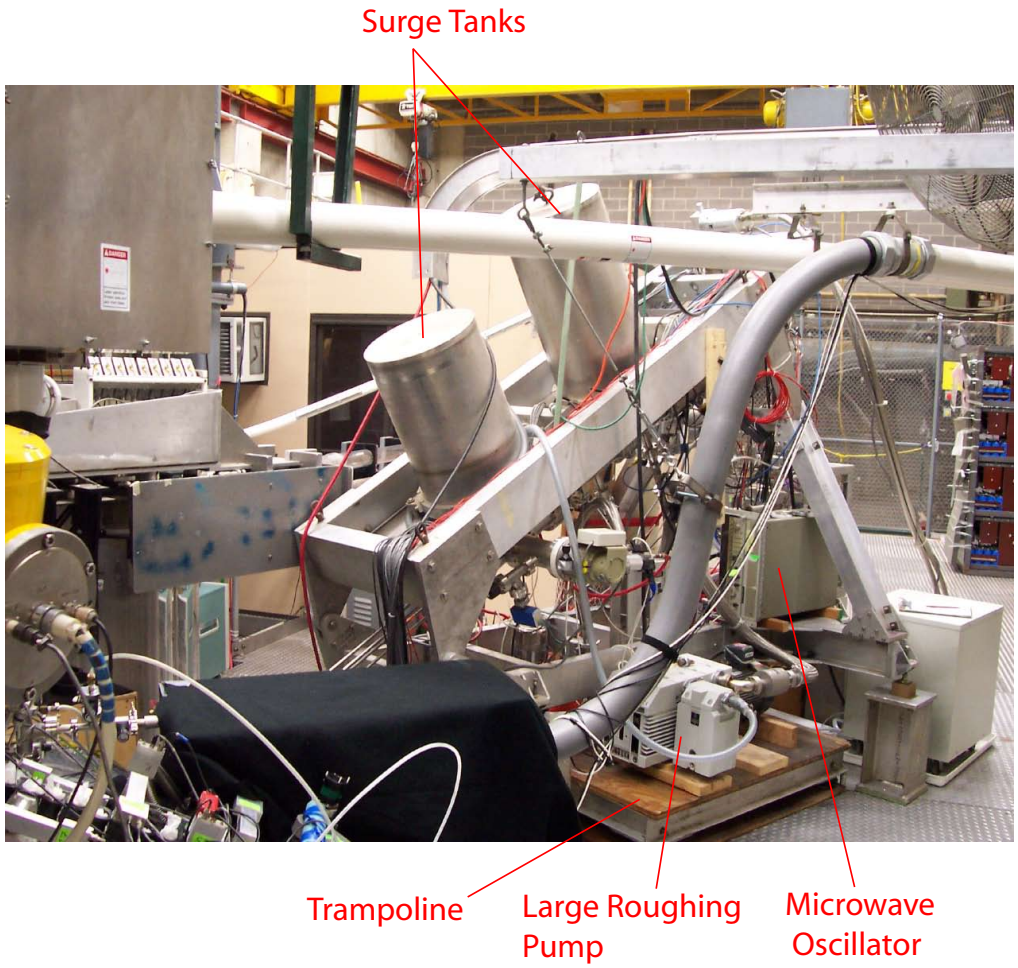

Figure A.2: Injector - side/front view

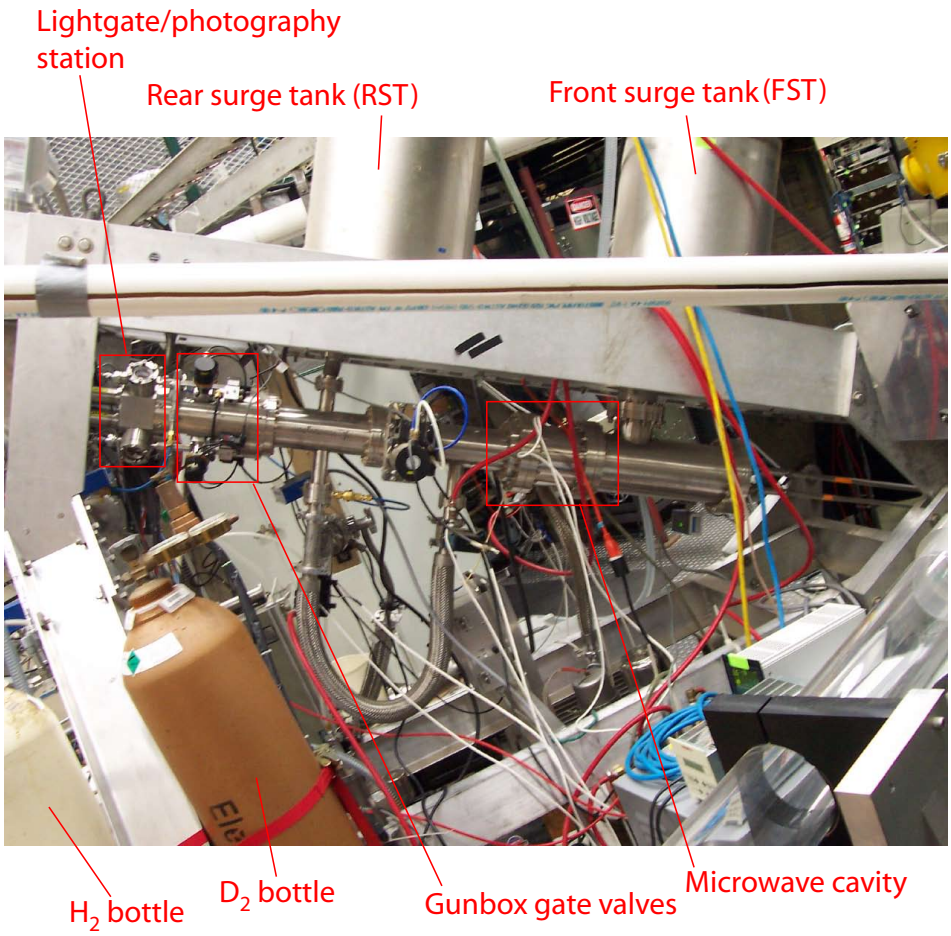

Figure A.3: Injection line

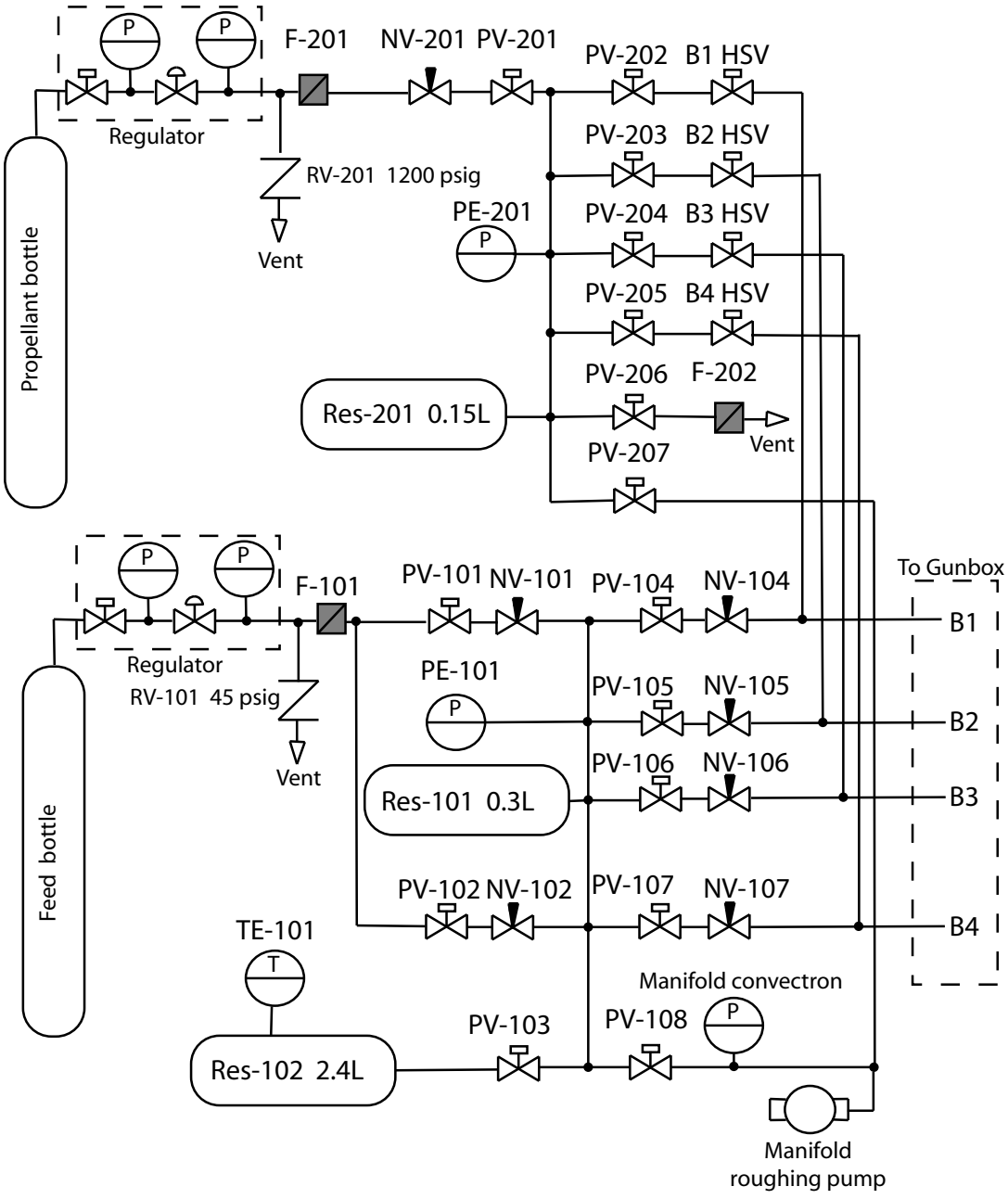

Figure A.4: Manifold diagram

gauges are denoted as PE's or P's. The relief valves (RV-XXX) ensure the manifold pressure doesn't exceed the limits of the manifold's weakest link. The flow in certain parts of the manifold is limited by filters and snubbers (F-XXX). Reservoirs on each side of the manifold ensure large enough ballast of gas for propelling and forming pellets.

From the top of the manifold (Fig. A.5), the feed valves and their respective needle valves can be seen. The feed valves (PV-104 though PV-107) control the flow of deuterium to the barrels. The needle valves (NV-104 through NV-107) control the rate of flow of the gas to the barrels. If gas flow is too fast, there's a risk of poor pellet formation, and if it's too slow, it will just take much longer to form a pellet. There are two supply routes from the bottle to the feed side of the manifold (PV-101 and PV-201). By having their respective needle valves opened to differing sizes, a fast fill and slow fill is accomplished. When forming small pellets the slow fill side can be used, and when forming larger pellets, the faster flow side can be used.

Looking at the manifold from the front (Fig. A.6), the propellant side of the manifold is visible along with the controllers for all the pneumatic valves (PVs) in the manifold. The slow propellant valves (PV-202 through PV-205) control the flow of propellant gas up to the high speed valves for each barrel. Because, the propellant side of the manifold is kept at pressures greater than 1000 $p.s.i.g.$, there is also a venting valve consisting of pneumatic valve (PV-206) and a snubber (F-202). Following venting of the propellant side of the manifold, it can then be pumped down by opening it to the manifold roughing pump via the propellant pump valve (PV-207).

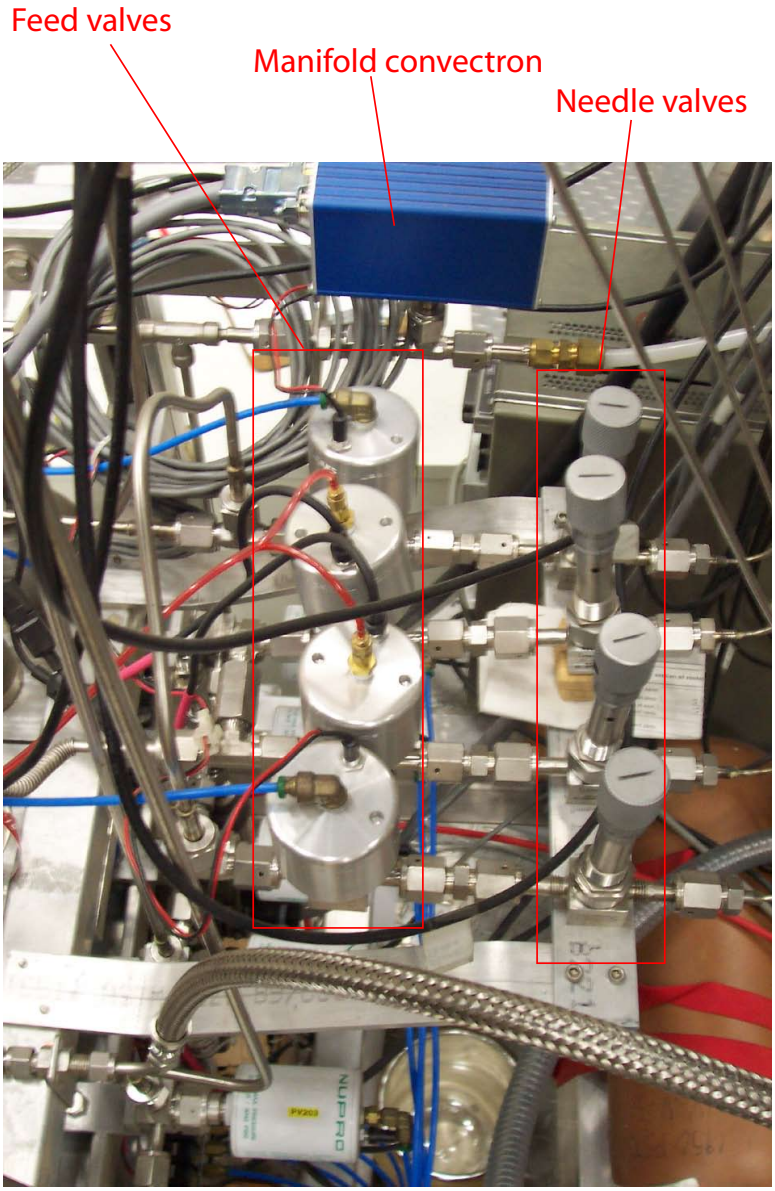

Figure A.5: Manifold - top view

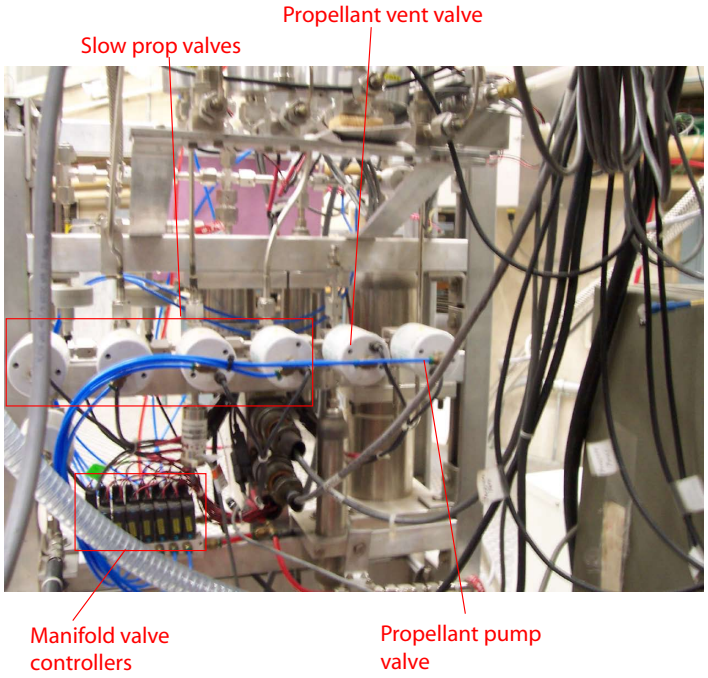

Figure A.6: Manifold - front view

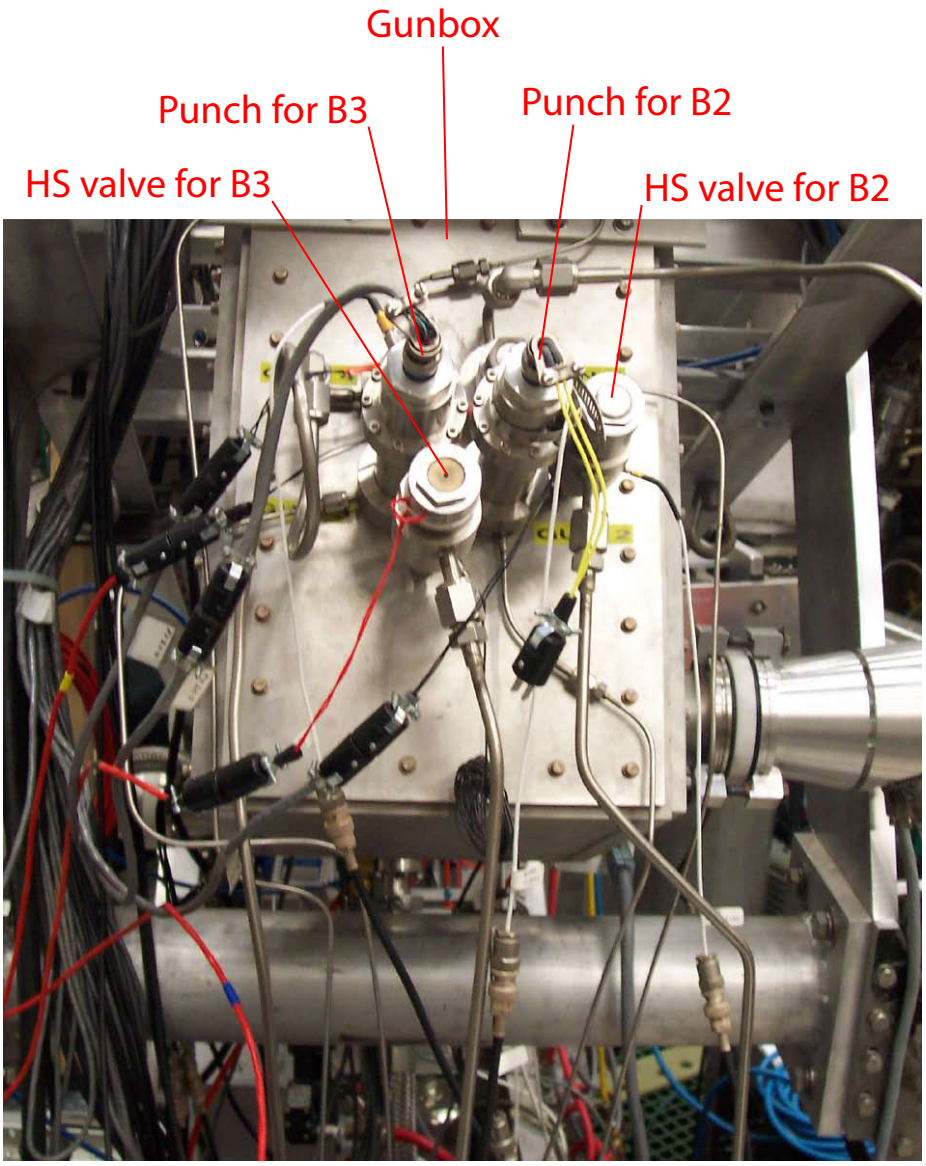

Figure A.7: Gunbox - rear view

A.2.2 Gunbox

At the rear of the gunbox (Fig. A.7), the feed and propellant lines are mated with their respective barrels through the punch/fast-valve housing. In the injectors current configuration, the two lower barrels (2 and 3) are fitted with mechanical punches and external high speed propellant valves. The two upper barrels (1 and 4) are fitted for high speed pellets and have close coupled high speed propellant valves (not visible but are immediately above the punches for barrels 2 and 3).

Access to the inside of the gunbox is achieved through the removal of it's side-plates (Fig. A.8). Each side is held in place by twenty-eight $\frac{1}{4}$" 12-point bolts. The vacuum seal is maintained by rectangular a o-ring whose groove can be seen just inside the face-plate bolt-holes in Figure A.9. Vacuum within the gunbox is the provence of the gunbox turbo. If the barrels 1 or 2 are to be accessed, the turbo side of the gunbox must be opened which requires the removal of the turbo (it's mounted with three large bolts).

Pellets are formed in the gunbox (Fig. A.9) where the coldhead (copper block) contacts the barrels. The heat shorts maintain a steep temperature gradient in order that pellets are formed at this contact point. The shorts are made of braided copper and are held to barrel with zip-ties. The other end of the heat short is connected either to the front of the gunbox or to the punch/fast-valve housing. The lack of precision afforded by the zip-ties are the bane of the Pelleteer. If the heat shorts are to close to the coldhead, then pellets will come out much smaller than expected (if at all). If the spacing is too large, hollow pellets will be formed with can't easily be broken free by the punch or at all by the propellant gas. Rough guidelines for the spacing between the coldhead and point of closest contact of the heat short are given in Table A.1 for various pellet diameters. These are given as a rough estimate, and the Pelleteer may have to experiment a little to ensure

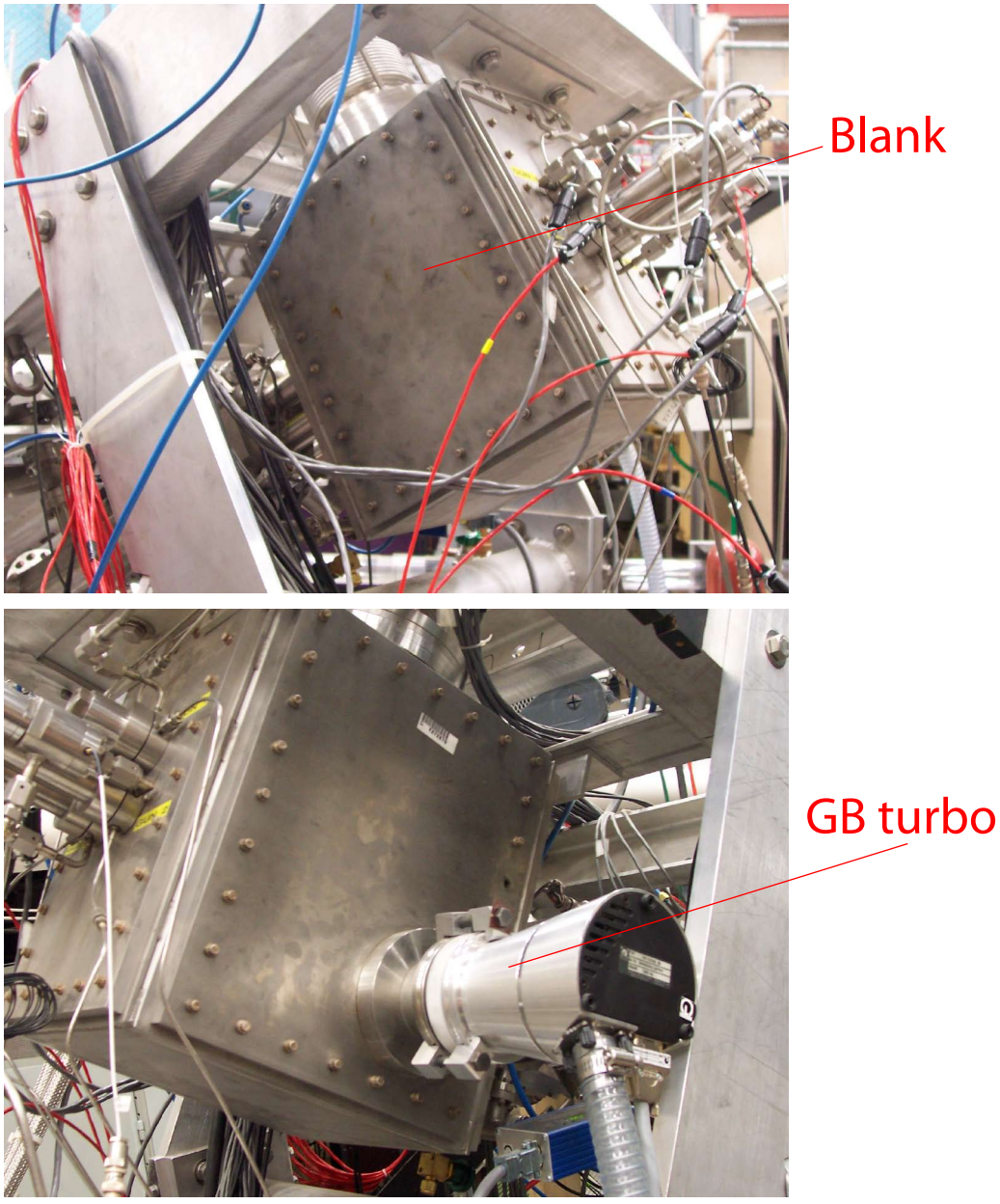

Figure A.8: Sides of gunbox

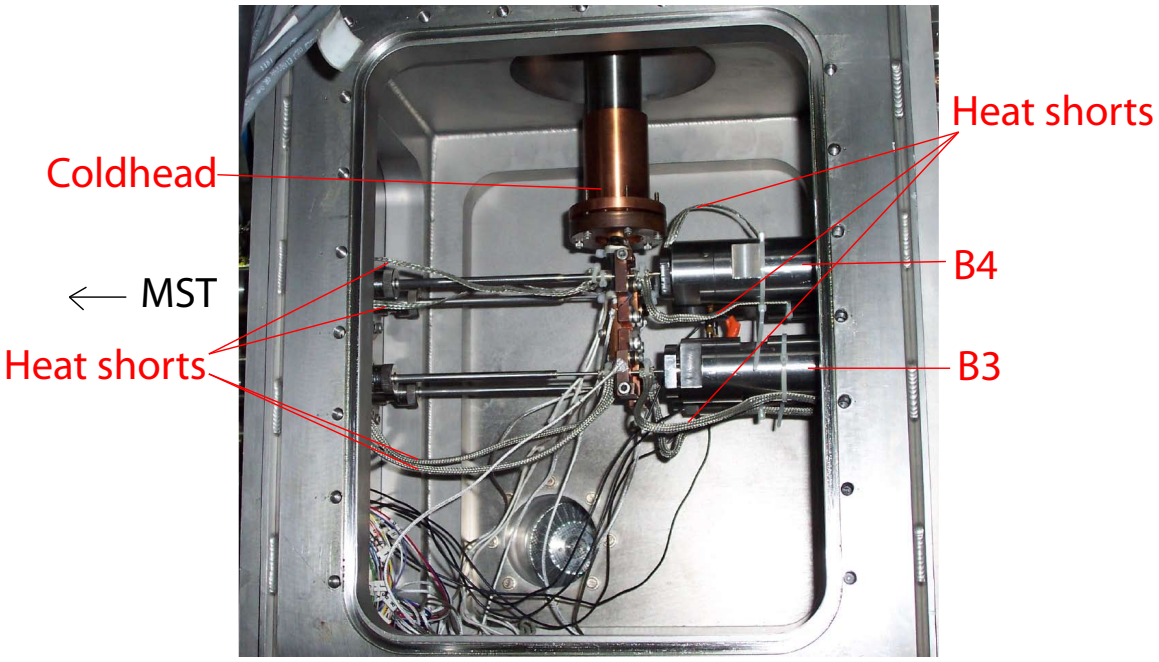

Figure A.9: Gunbox with side cover removed

Table A.1: Heat short spacing guidelines

Pellet diameter	Heat short spacing
1.0 mm	$\sim$ 1/4”
1.3 mm	$\sim$ 5/16”
1.6 mm	$\sim$ 5/16” – 3/8”

reliable pellet formation especially for barrels whose diameters aren't listed.

Also shown in Figure A.9 is a jumble of wires connecting the bottom of the gunbox to the coldhead which are the temperature monitors and heaters. The temperature at five points on the coldhead (each barrel and at the center of the coldhead) is monitored during cooling and heating of the barrels. Heating is accomplished via a heater driver located in the control room.

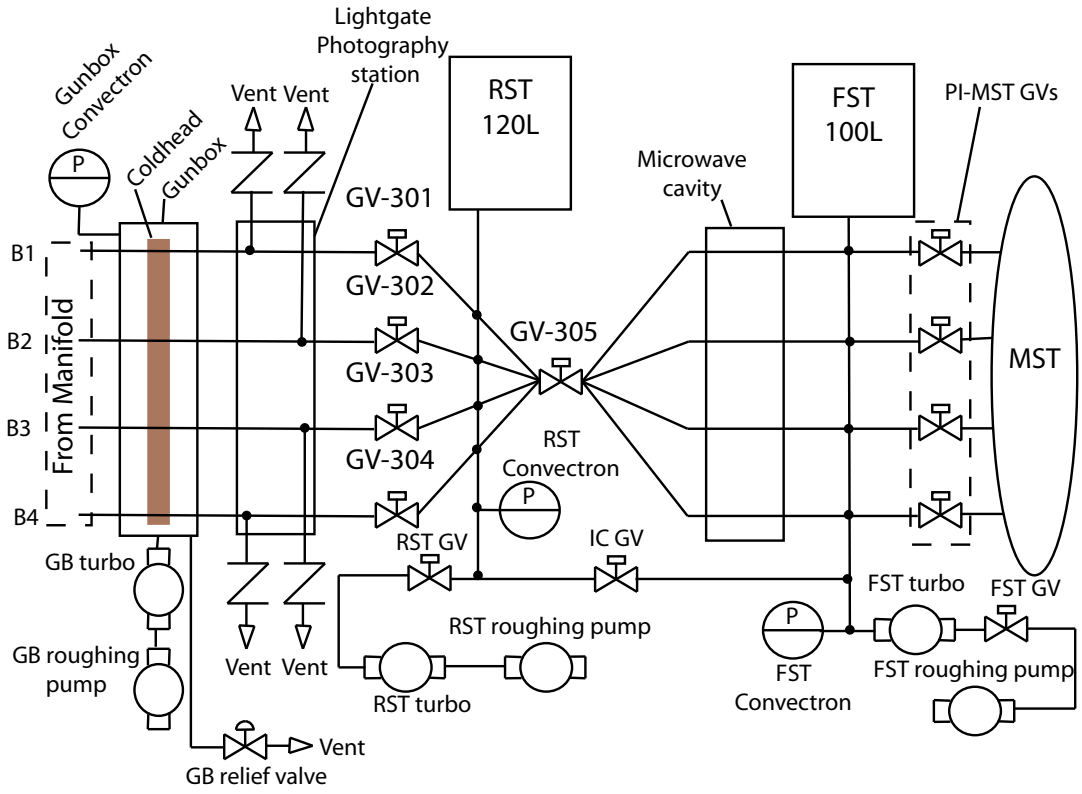

Figure A.10: Injection line diagram

A.2.3 The injection line

Between the gunbox and MST is the portion of the injector referred to as the injection line (shown schematically in Fig. A.10). Just downstream of the gunbox is the lightgate station and the gunbox gate valves (GV-30x, where x = 1 to 4) as seen in Figure A.11. At the lightgate station, there are windows that allow photographing of pellets in flight as they leave the barrels and enter the injection line. Each barrel has a relief (or check) valve to ensure that in the case of excess pressure (*e.g.* the gunbox gate valve is closed during the firing of a high speed pellet) the windows don't crack or break.

The microwave cavity is located just upstream of the front surge tank (Fig. A.12.

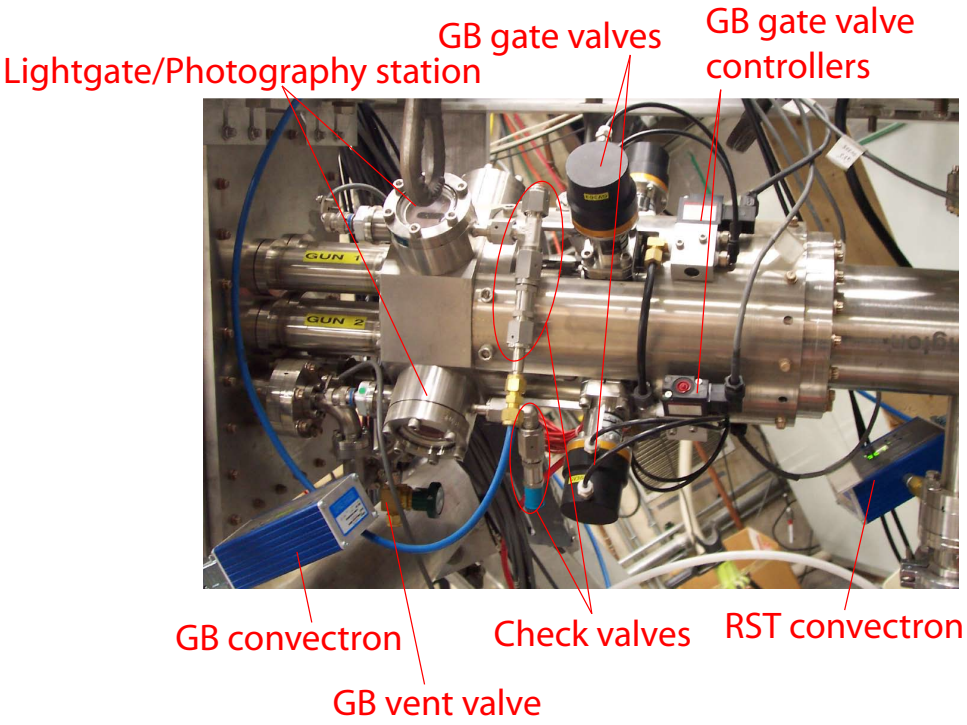

Figure A.11: GV-30X valves and lightgate station

The MST-PI mini-gate valves (Fig. A.13) are pneumatically controlled and can only be opened when interlocks on surge tank pressure are satisfied or when the interlocks are bypassed. During plasma operation, the valves open (and close) automatically one second before (and three seconds after) the discharge. This was accomplished by tying the valve controller (Fig. A.14) to MST's timing system, the PLC. For a valve to be opened it must be armed using the valve controller.

Both the gunbox and front surge tank (FST) turbo controllers are located in the same rack as the valve controller. On top of the rack (but not shown in Fig. A.14) are the RST turbo controller and FST Penning gauge controller. Like the the rear surge tank, the front surge tank has a convectron gauge for monitoring pressure. However, due to the range of measurement for the convectron (down to 1 $mTorr$), a Penning gauge was installed to ensure MST-like pressures ($10^{-8} - 10^{-7}$ $Torr$) in the tank. The convectrons for both surge tanks, the gunbox, and manifold can be monitored from the control room.

A.2.4 Cooling system

The cooling system consists of closed-loop helium compressor (Fig. A.15) which itself is cooled by a closed loop water chiller (Fig. A.16). Within the closed loop of the water chiller are two filters: one for particles and the other is a de-ionizing filter.

The chiller is cooled with building water (Fig. A.17). The flow of building water to the chiller is controlled by manual ball valves on both the supply and return lines. There is also a solenoidal valve on the supply side which is actuated by the chiller controller (Fig. A.18). The controller has three interlocks that can power down the chiller pump and close the building water solenoid: compressor power, PLC water sensors, and chiller

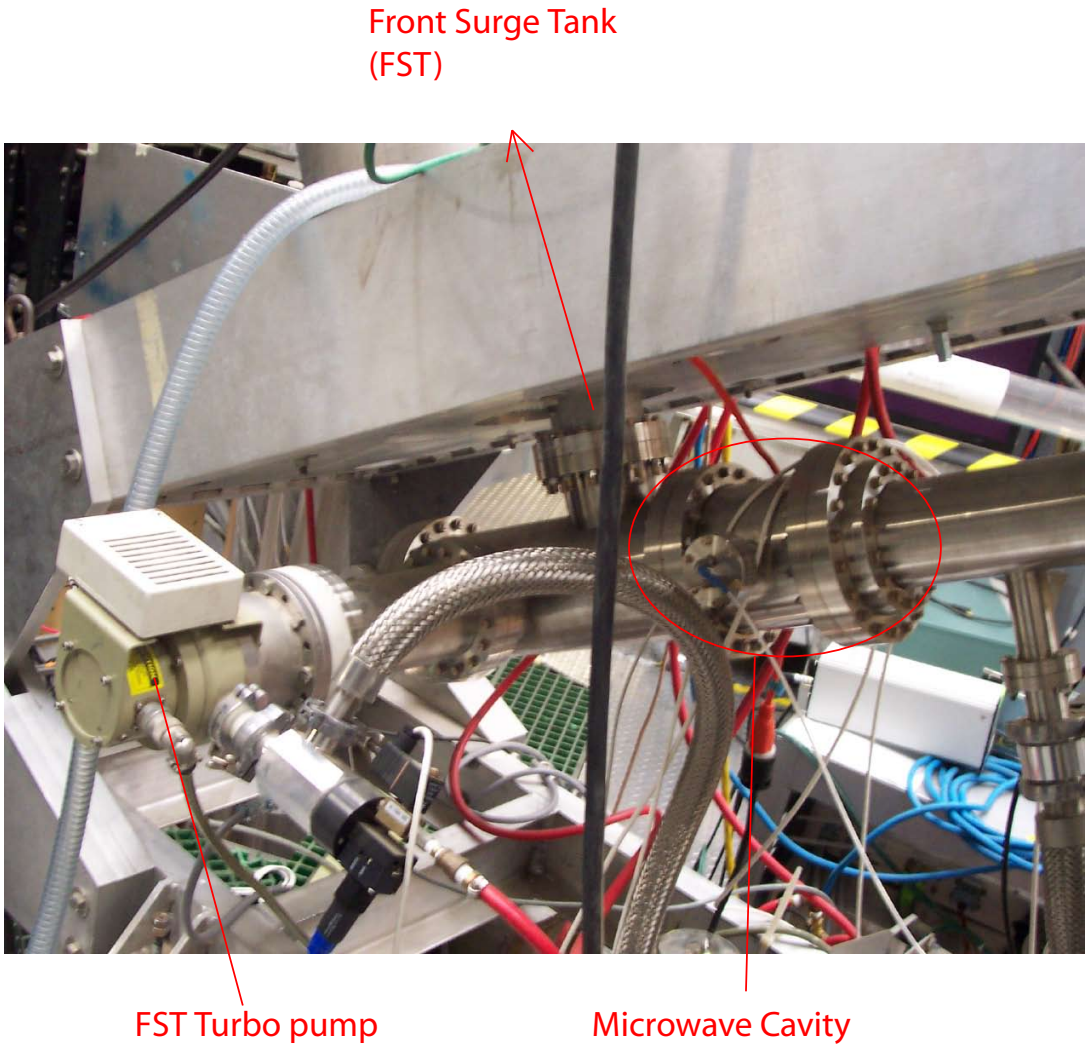

Figure A.12: Microwave cavity and front surge tank turbo pump

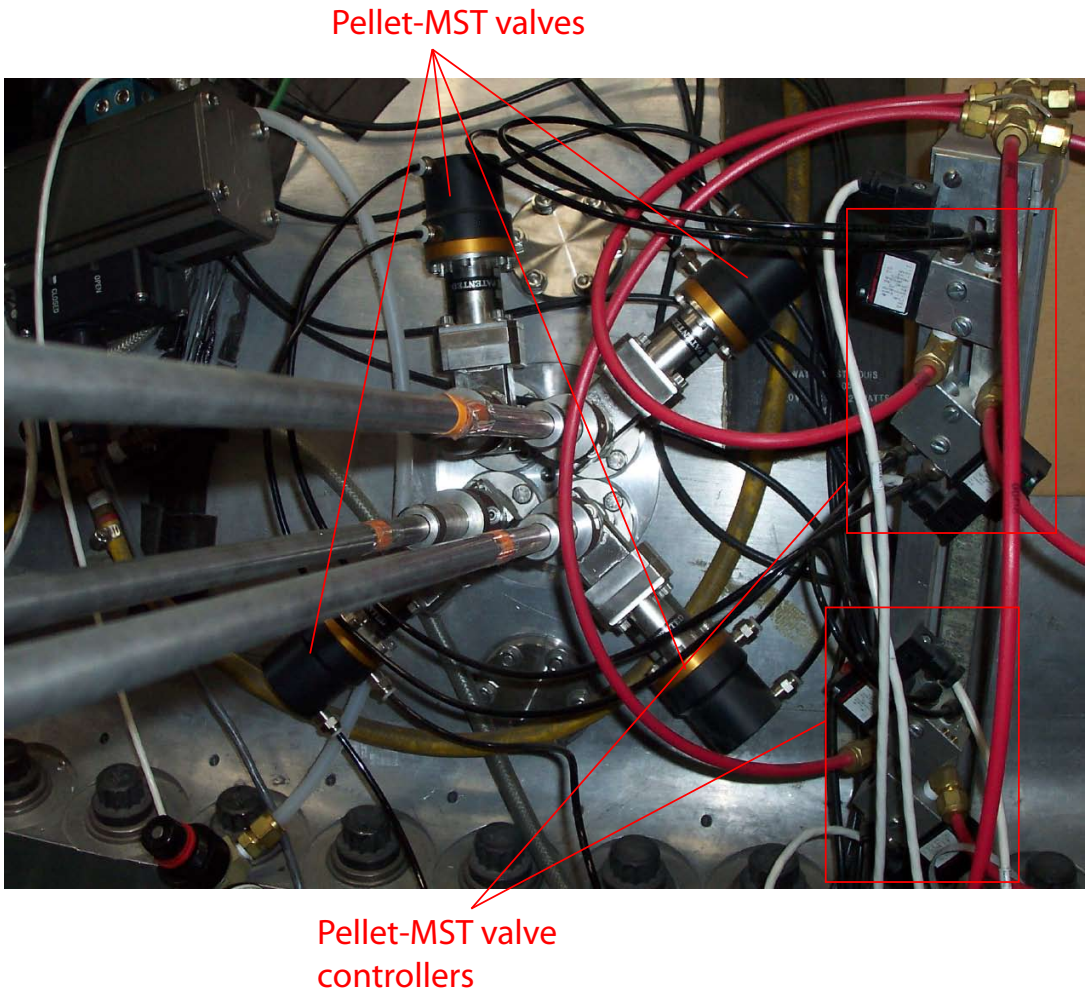

Figure A.13: Injector-MST connection

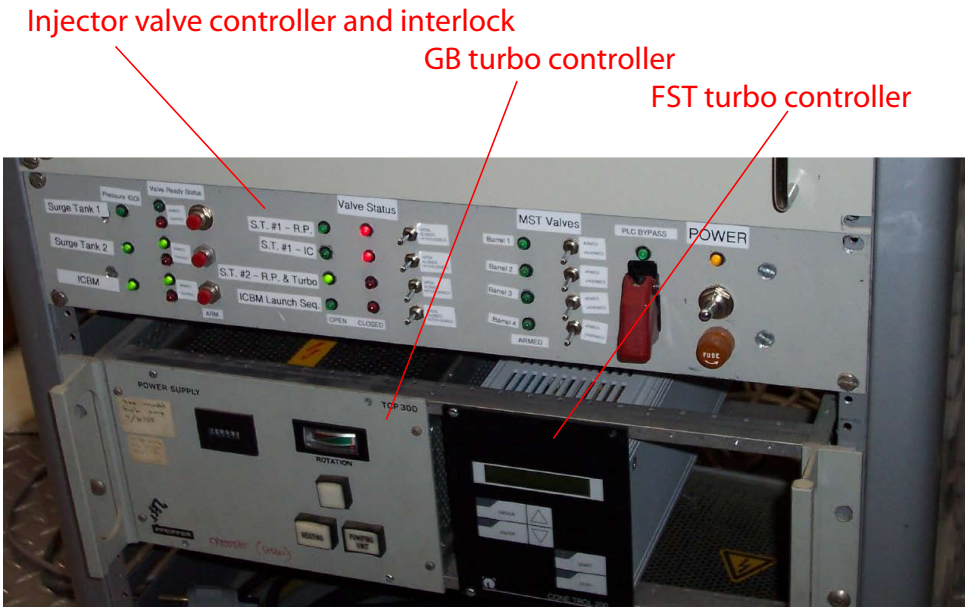

Figure A.14: Injector-MST valve controller

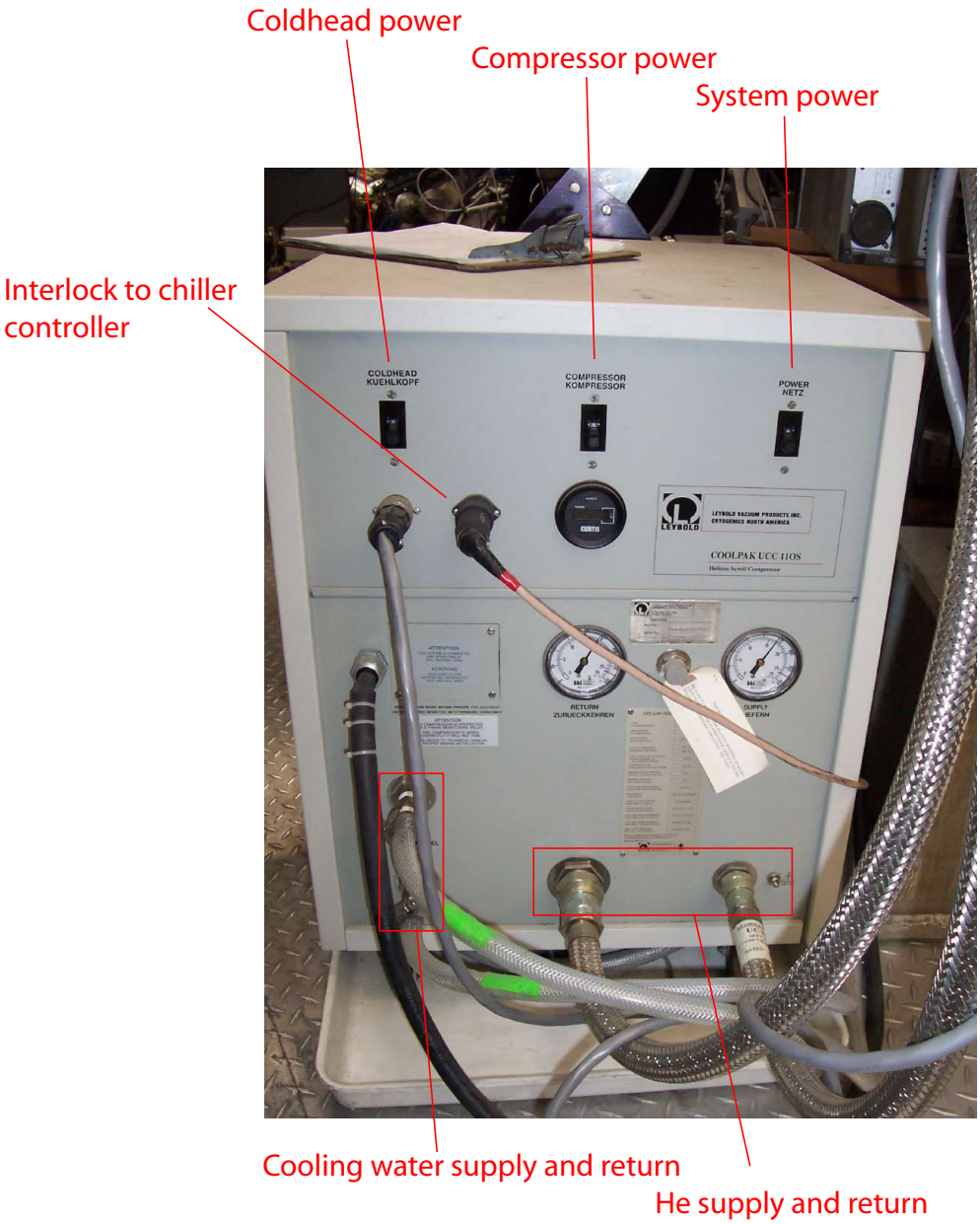

Figure A.15: Helium compressor

Figure A.16: Chiller

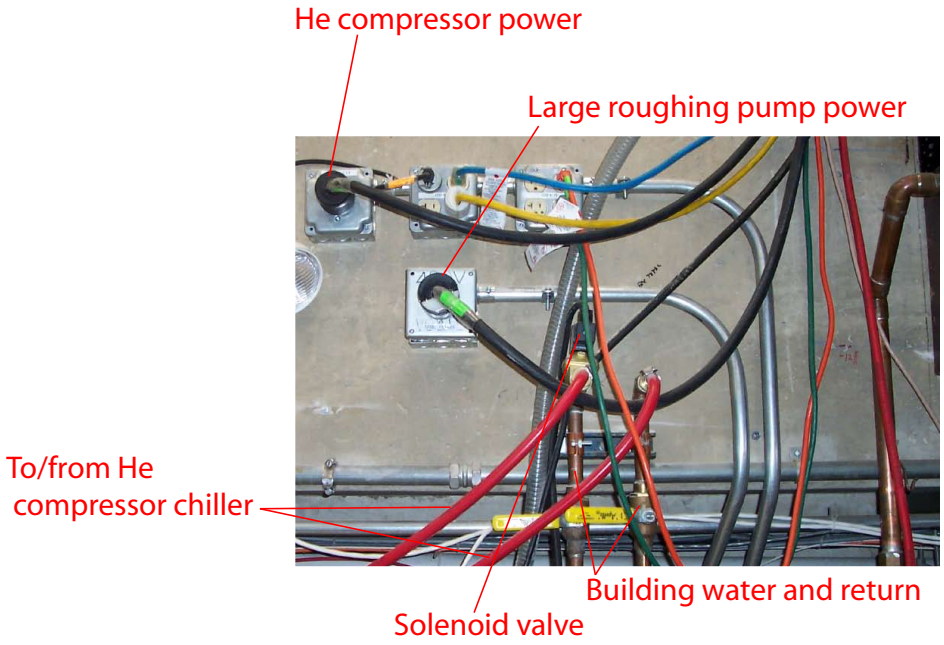

Figure A.17: Water and power connections

Figure A.18: Water controller and interlocks

water temperature. Each interlock can be bypassed, *e.g.* during injector startup, the compressor power interlock must be bypassed. The controller is also interlocked to water sensors at the floor of the chiller and compressor. If there's a leak, the controller closes the solenoid and turns off the chiller pump. The third interlock, chiller water temperature is usually bypassed due to the occasional period of starting and stopping of the pump when the temperature is near the interlock setpoint[1].

A.2.5 The control rack

The central nervous system of the pellet injector is the control rack (Fig. A.19). Located in MST's control room, it consists of the punch and HS valve power supplies, gate valve power supply, lightgate controllers, heater driver controller, coldhead temperature monitor, pressure transducer breakout panel, data aggregator (or "sum-mer"), computer (for issuing commands to valves via a Labview program), and pressure monitor for the propellant and feed sides of the manifold.

The lower half of the control rack (Fig. A.20) consists of the power supplies for the fast valves, mechanical punches, and the injection line gate valves (GV-301 through GV-305). The punch/fast-valve supplies can provide an maximum 180 V for a given time window. The maximum time window is uncertain but for the purposes of the injector is set anywhere from 1.5 ms (for high speed valves) up to 25 ms (for the punches).

The upper half of the control rack (Fig. A.21) consists mainly of transducers and their controllers. The temperatures measured at the coldhead are monitored at the top of the rack. Next to it is the heater driver used to warm up the coldhead between shots. The pressure transducer breakout panel contains the outputs from pressure transducers in the

[1]The setpoint temperature is programmed into the temperature monitor of the chiller (Fig. A.16)

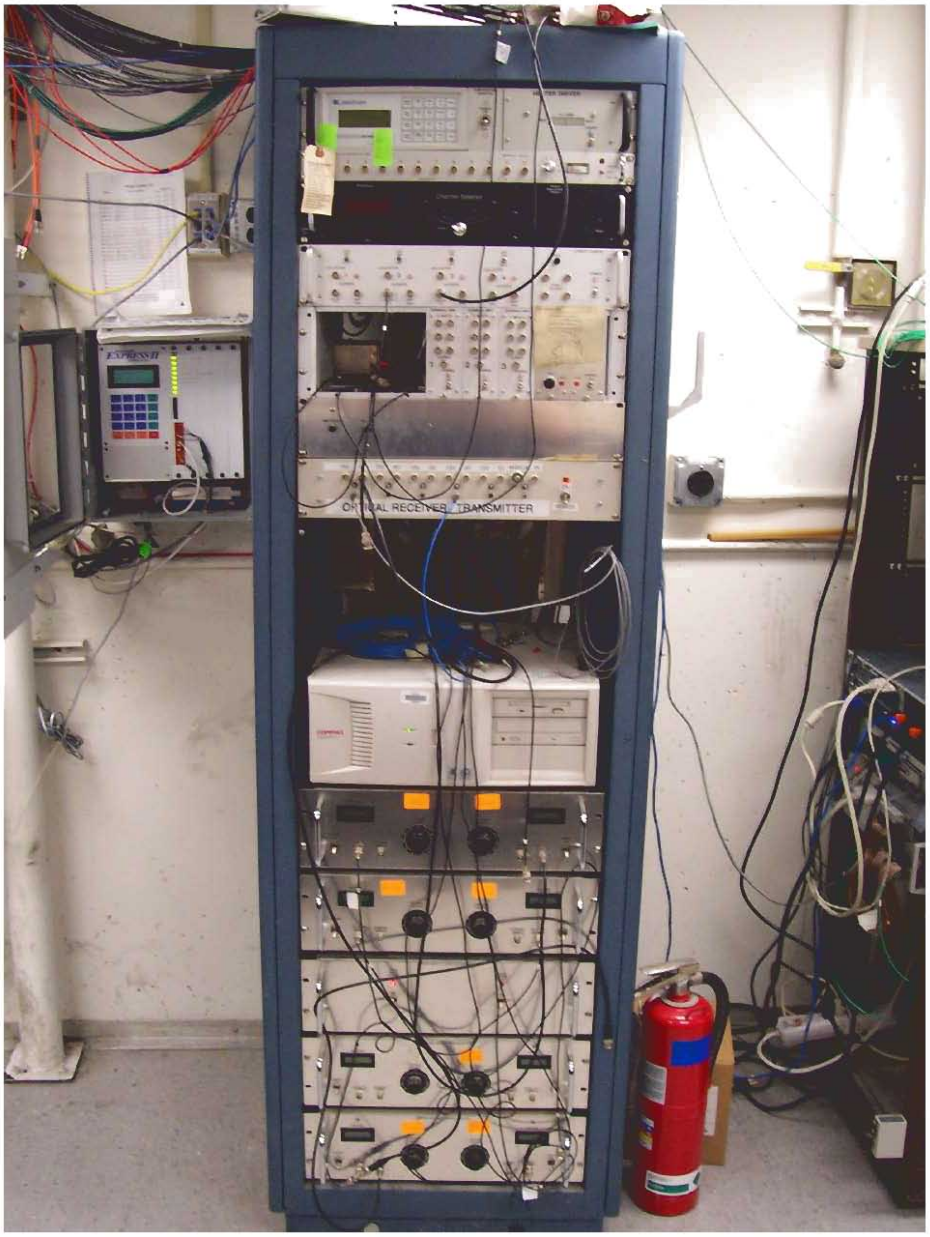

Figure A.19: Control Rack

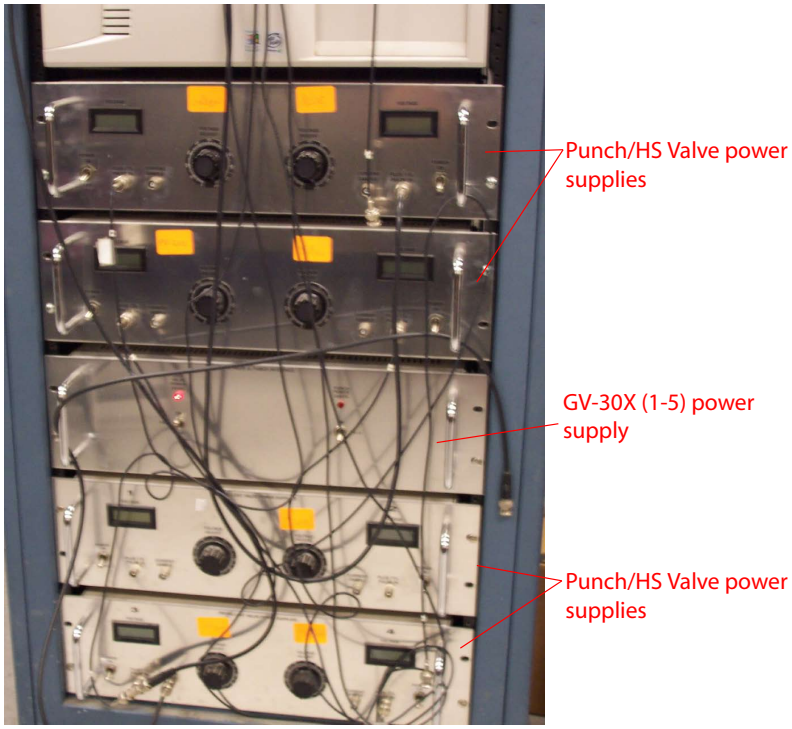

Figure A.20: Control Rack - bottom half

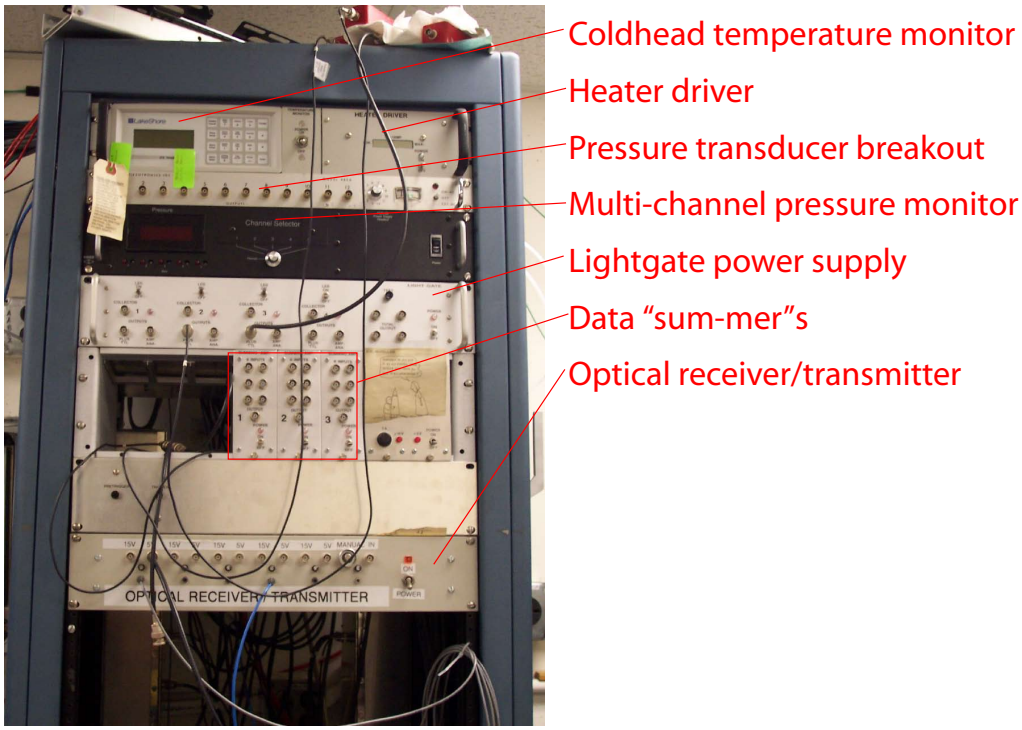

Figure A.21: Control Rack - top half

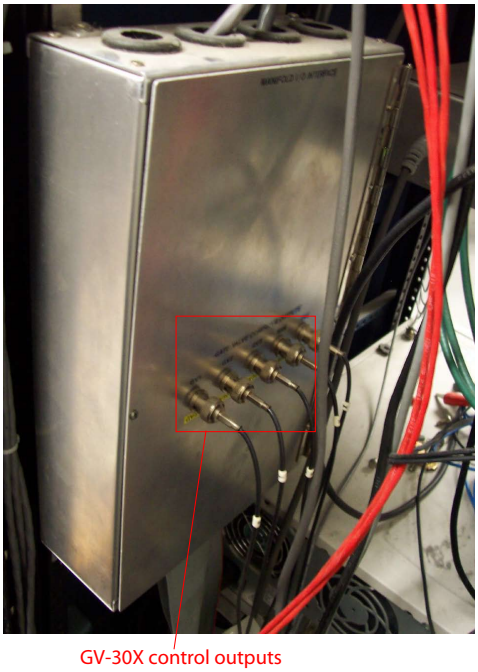

Figure A.22: Control Rack - rear breakout #2

barrels and attached to the punches. The multi-channel pressure monitor reads out the propellant and feed manifold pressures in $p.s.i.$ and $Torr$, respectively. The lightgates for each barrel have their power supplies in the rack. The output signals are part of this supply. There are also three "data sum-mers" which combine multiple signals (if the Pelleteer is short on data acquisition channels). At the bottom of the upper half of the control rack is an optical receiver-transmitter for converting the fiber-optic trigger signal from MST to a TTL pulse (on co-ax) for triggering the injector during a discharge.

The rear of the control rack (Figs. A.22 and A.23) consists mainly of breakout panels for the control of various valves, the triggering inputs, and data inputs. The injection line gate valve control outputs (GV-301 through GV-305) are located in a breakout box

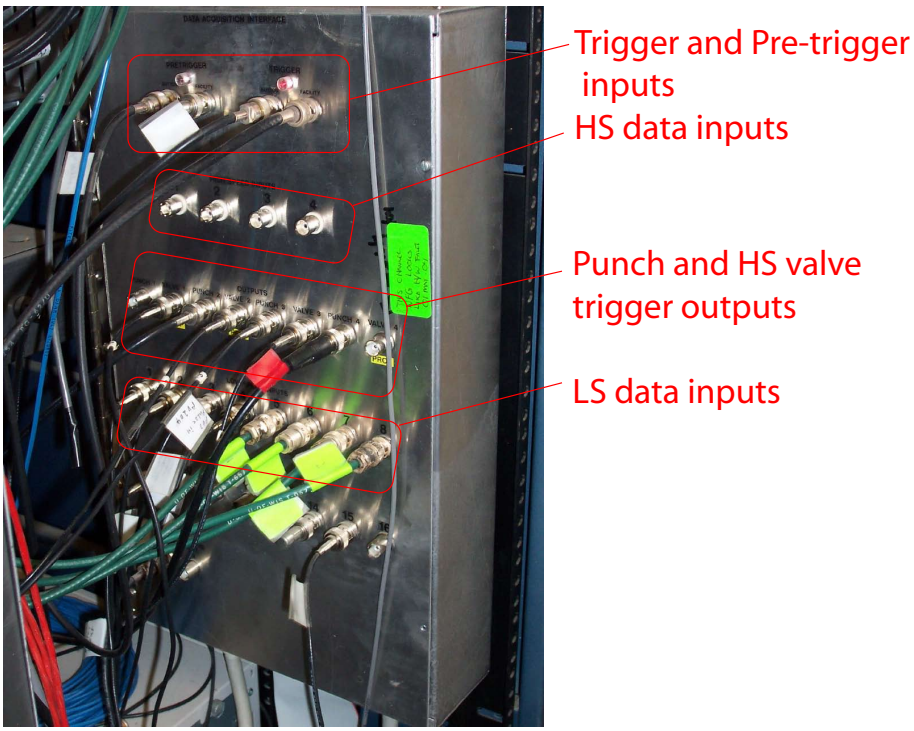

Figure A.23: Control Rack - rear breakout #1

on the left side of the rear of the control rack (Fig. A.22). On the opposite side (Fig. A.23), are the pre-trigger and trigger inputs, high speed and low speed data inputs, and the punch/fast-valve trigger outputs. The punch/fast-valve triggers are run to the power supplies on the front and supply a 5 V pulse whose width corresponds to the length of actuation (roughly 1 to 5 ms for the fast valves and 25 ms for the punches).

A.3 Daily operation

A.3.1 Start of day - Warming up (i.e. cooling down the injector)

At the start of the day, completion of the following task list will get the injector cooling.

1. Ensure that injector pressures are ok: front surge tank, $\lesssim 10^{-7}\ Torr$; rear surge tank, $\lesssim 1\ mTorr$; gunbox, $\lesssim 1\ mTorr$; and manifold, $\lesssim 10\ mTorr$.
2. Open gunbox gate valves (GV-301 through GV-304) using PIS computer.
3. Ensure feed and propellant manifolds are closed off from respective bottles.
4. Open ball valves for building water supply and return (East wall, see Fig. A.17).
5. Bypass helium compressor interlock (chiller controller, see Fig. A.18).
6. Ensure temperature interlock is bypassed (chiller controller).
7. Power up chiller controller, water should begin flowing – After water begins flowing, it may stop as air is flushed from the system. It usually is stopped and restarted multiple times before the flow is constant. If the pump is left running too long with no flow, it will burn out.
8. Turn power on to helium compressor (rightmost switch, see Fig. A.15).
9. Power up compressor (center switch). It will take a moment for the compressor to kick in. When it does, the center display will turn on. Only then, move to the next step.
10. Power up coldhead.
11. Un-bypass helium compressor interlock on chiller controller.

The cooling of the gunbox will take as little at 45 minutes. The temperature is measured at five points on the copper-block the barrels pass through (Fig. A.9) and can be monitored from PIS control rack in the control room (Figs. A.19 and A.21). Once the gunbox

temperature reaches 77 K (nitrogen freezing point), the cooling rate should increase. Occasionally, the cooling process will take longer especially if the gunbox has been opened recently (upwards of two or three hours).

As the injector is cooling, the experimenter can power on the punch and HS valve power supplies (both main power and individual supply power as seen in Fig. A.20). The pressure transducer controller, lightgate station power supply, heater driver power supply and optical transciever should all be powered on as well (Fig. A.21). At this point the feed and propellant bottles may be opened. Typical regulator pressures are $< 5\ p.s.i.g$ and 1150 $p.s.i.g$, respectively. The microwave detector and oscillator can be powered up as well. The microwave oscillator should be set to a frequency of 10.490490 GHz and a range of +10 dBm.

A.3.2 End of day - Cooling down (i.e. warming up the injector)

At the end of the day, both the feed and propellant manifolds are evacuated:

1. Close the feed and propellant bottles.
2. Open gunbox gate valves (GV-301 through GV-304).
3. Close off both the barrel feed and slow propellant valves.
4. Open propellant side of manifold to atmosphere (vent) until pressure is $\lesssim 2\ atm$
5. Close propellant side of manifold from atmosphere and open to manifold roughing pump.
6. Open feed side of manifold to roughing pump.

Next is the turning off of the helium compressor and water chiller:

1. Bypass helium compressor interlock on chiller controller.
2. At compressor, turn off "Coldhead" switch.
3. Turn off "Compressor" switch.
4. Turn off "Power" switch.
5. Wait for chiller water to get below 30° C (upper left wall of chiller, Fig. A.16), and then power down chiller controller.
6. Close ball valves for building water supply and return (east wall).

The control rack supplies and electronics may all be powered down with the exception of the gate valve power supply (left switch, center supply of Fig. A.20).

A.4 Shot cycle procedure

Pellet injection into plasma discharges is an automated process. This process is overseen by a Labview program run on a PC in the control rack which the Pelleteer can manage from the control room.

Before starting the pellet formation cycle, the Pelleteer must configure the injector using the "Setup" procedure in the Labview control program. At this point the barrels to be used are chosen along with the method of propelling the pellets and the pellet size. In this window, the set-point temperatures, feed manifold pressure, and propellant manifold pressure can be set as well. The barrel soak time is also set at this stage, and should be chosen such that length of time between the beginning of the barrel soak and injector initialization is no longer than the MST charge time and no shorter than 10 seconds less than the MST charge time.

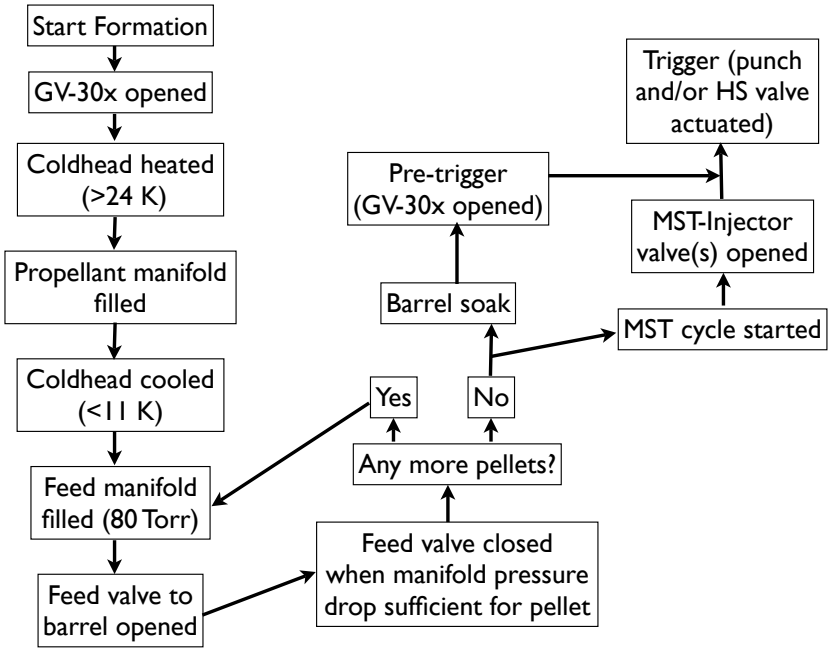

Figure A.24: Shot cycle flowchart

Once the injector is configured, the Pelleteer, may start the formation process. The cycle of a pellet-fueled MST shot is charted in Figure A.24. The first step is to "clean" the barrels. This is a separate procedure from the "dry-fire" cleaning done between shots. During this cleaning process, the gunbox gate valves are opened and the coldhead is warmed up to a set temperature. This temperature (typically $24 - 28\ K$) is chosen to be several Kelvin above the triple point of the hydrogenic gases ($17 - 18\ K$). Once this temperature is surpassed, the heater is turned off, and the propellant manifold filled (if high speed pellets are to be used). Once the coldhead has reached the formation temperature (configurable and usually set to $10 - 11\ K$), the feed manifold is filled with deuterium to 80 $Torr$. The feed valve to the barrel for the first pellet is opened. When the pressure drop corresponds to the programmed pellet size[2], the valve is closed. If any

[2]The pressure drop is determined using the ideal gas law with T being room temperature, V is the

more pellets are to be formed, the manifold is refilled, and the process is repeated for the next barrel. Once all pellets are formed, the barrel soak cycle begins.

At this point the Pelleteer will indicate to the MST operator to begin the charging cycle. For the next 1 – 3 minutes, the injector just sits. The pre-trigger for the injector has been automated so that the Pelleteer can't forget to initialize the injector prior to the plasma discharge. Pre-triggering opens the gunbox gate valves of the barrels in use. Typically the Pre-triggering process takes $8 - 10$ s. A second before the discharge, the MST-Injector valves of the barrels in use are opened. As the MST is discharging, it sends a trigger to the injector instigating the launch of the pellets. The timing of the MST trigger can be programmed to be up to 0.5 s before the start of the discharge, but in practice is usually set in the window of 25 ms before (slow pellets) to 10 ms (fast pellets) after the start of the discharge. Varying the trigger allows the Pelleteer to properly time the arrival of the pellets.

A.5 Occasional maintenance procedures

A.5.1 Barrel installation

The installation of a pellet barrel can be broken down into six parts: (1) Bring the barrels up to air, (2) Accessing the inside of the gunbox, (3) Old barrel removal, (4) New barrel installation, (5) Leak checking, and (6) Closing up the gunbox.

Bringing barrel(s) up to air

1. Close feed and propellant bottles.

volume of the feed manifold reservoir (0.3 L), and N is calculated based on the desired pellet size and deuterium density (0.2 g/cm^3)

2. Close off feed and propellant (slow) valves using Labview control program.

3. Evacuate manifold.

   (a) Close off both the barrel feed and slow propellant valves.

   (b) Open propellant side of manifold to atmosphere (vent) until pressure is $\lesssim 2\ atm$

   (c) Close propellant side of manifold from atmosphere and open to manifold roughing pump.

   (d) Open feed side of manifold to roughing pump.

4. Close off front surge tank from rear surge tank (GV-305 and IC VAT valve).

5. Close off rear surge tank from gunbox (GV-301 through GV-304). May have to power down rear surge tank roughing and turbo pumps depending on state of gunbox gate valves (see Section A.6.2).

Accessing gunbox

1. Power down gunbox turbo pump.

2. Power down gunbox roughing pump.

3. Open gunbox to atmosphere by slowly opening relief valve on front (MST side) of gunbox.

4. Remove gunbox sideplate. If working on barrels 1 or 2, remove turbo from its mount before removing sideplate.

Old barrel removal

1. With gunbox opened, vent manifold.

2. Disconnect feed and propellant lines from barrel (back of gunbox) to be replaced. If working on a punch barrel disconnect external fast valve from housing, leaving fast valve connected to propellant line.

3. Disconnect heat shorts from barrel by cutting zip ties.

4. Loosen barrel retainer nut located at the very front of the punch/fast-valve housing inside the gunbox. Be sure to hold punch/fast-valve housing in place with second wrench.

5. Loosen punch/fast-valve housing spanner nut. On the gunbox's back plate, the housing for punches/fast-valves is held in place with a spanner nut on the inside that sits flush with the plate. Using a pipe wrench or tongue-in-groove pliers to steady the housing outside of the gunbox, use tongue-in-groove pliers to loosen the spanner nut within the gunbox[3].

6. Totally loosen the barrel retainer nut.

7. Totally loosen housing spanner nut.

8. Remove pressure transducer from housing.

9. Slide housing out of gunbox.

10. Loosen Allen-head bolt on coldhead at holds barrel in contact with coldhead.

[3]Though it's a spanner nut, the author has yet to get a spanner wrench in place to loosen the nut. A more practical solution is to use a pair of tongue-in-groove pliers to grip the nut

11. Loosen Cajon fitting at front of gunbox where barrel passes though front plate.
12. Slide barrel out the back of the gunbox.

New barrel installation

1. Slide new barrel through barrel retainer nut, coldhead and into Cajon fitting ensuring copper disc on barrel is flush with coldhead.
2. Slide punch/fast-valve housing through the gunbox backplate and spanner nut, mating it with end of barrel.
3. Lightly screw barrel retainer nut in place.
4. Tighten spanner nut.
5. Tighten barrel retainer nut.
6. Tighten Allen-head bolt on coldhead.
7. Tighten Cajon fitting.
8. Reinstall pressure transducer on punch/fast-valve housing.
9. Reattach heat shorts using spacing guidelines from Section A.2.2.
10. Reconnect feed and propellant lines to punch/fast-valve housing.

Leak checking

If things proceed nicely enough, leak checking may not be necessary.

1. Pump down RST and manifold using their respective roughing pumps

2. Open gunbox gate valves (GV-301 through GV-304). If the pressure doesn't get below $\sim 10\ mTorr$ within several minutes, there might be a leak[4]:

   (a) Close off RST GV.

   (b) Turn off and disconnect RST roughing pump.

   (c) Connect leak checker to RST.

   (d) Proceed to leak check until the leak is fixed or the Pelleteer is satisfied that there is no leak

   (e) Disconnect leak checker.

   (f) Re-connect RST roughing pump.

   (g) Restart RST roughing pump.

   (h) Open RST GV.

3. Turn on RST turbo

4. If the manifold pressure hasn't gotten below $\sim 10\ mTorr$ after an hour or so, it's time to leak check:

   (a) Close PV-108.

   (b) Turn off and disconnect manifold roughing pump.

   (c) Attach leak checker.

   (d) Leak check until leak is found and corrected or until the Pelleteer is satisfied there is no leak.

[4]If the Pelleteer has never leak checked a vacuum system, get educated by a member of the Vacuum Committee.

(e) Disconnect leak checker.

(f) Reattach manifold roughing pump.

(g) Restart roughing pump.

(h) Open PV-108.

Closing gunbox

1. Reattach sideplate. The Pelleteer may find it difficult to keep the o-ring in place while putting the plate back in place. The key(s) to a successful plate reinstall require that the o-ring be thoroughly greased and stretched out. Hasty replacement of the plate after o-ring placement is the final key.

2. Completely bolt up the plate by tightening bolts opposite each other.

3. Re-install turbo (if necessary).

4. Close gunbox vent valve.

5. Start gunbox roughing pump.

6. When gunbox pressure gets below $\sim 10\ mTorr$, turn on gunbox turbo.

A.5.2 Solenoid removal/inspection

Inspection of the punch or high speed valve sealing surface is a simple process compared to barrel installation. The punches and close-coupled high speed valve sealing surfaces are attached to the front of the solenoid. The gunbox needn't be opened for this inspection. The first part of the procedure is similar to barrel installation with the exception that the feed and propellant lines are not disconnected from the barrel(s).

1. Removal

   (a) Close gunbox gate valves (GV-301 through GV-304)

   (b) Evacuate and pump down propellant side of manifold

   (c) Close feed valve (GV-10X, with X = 4-7), slow propellant valve (GV-20X, with X = 2-5) and gunbox gate valve (GV-30X, with X = 1-4) of the barrel to be inspected.

   (d) Loosen spanner nut (may have to use tongue-in-groove pliers) that sits just behind the ring where feed and propellant line enter the punch/fast-valve housing. Use another set of pliers or a pipe wrench to hold front portion of the housing in place

   (e) Once loosened, slide rear part of housing out of front portion exposing the solenoid

2. Inspect punch for kinks or sealing surface for debris

3. Installation

   (a) Clean sealing surfaces on solenoid housing

   (b) Slide solenoid back in place

   (c) Tighten spanner nut

   (d) Pump out barrel by opening gunbox gate valve and manifold feed valve.

A.5.3 Notes on leak checking

Keep a good supply of whiskey at hand. Seriously, ethanol can be used to trace leaks. For leaks that may be to large to warrant the use of the leak chaser, squirting ethanol on

the outside of suspect connection will (if indeed there is a leak) cause a pressure burst as the ethanol makes its way into the vacuum. The whiskey is for the Pelleteer – the MST group has plenty of ethanol but not for the Pelleteer's consumption.

A.5.4 Trampoline upkeep

The air pressure in the four "tires" of the trampoline must be kept high enough to ensure the upper and lower supports don't come into contact. There is a Schrader valve on each tire, and a bike pump is kept near the injector – usually in one of the cubbies created by the structural supports for the injector.

A.5.5 Notes on punches and HS valves

The high speed valves (both close-coupled and those used in conjunction with the punches) only seem to seal properly with several hundred psi of propellant gas behind them. More information on the high speed valves can be found in [1].

The mechanical punch is simply a piece of stiff wire soldered to a bullet shaped piece that screws onto the end of a rod that is moved using a solenoid positioned outside the gunbox. The end of the punch wire sits mere millimeters behind the formation point for the pellet. If air (or any gas with a freezing point above 20 K) gets into the barrel, the punch can freeze in place. If it is noticed that slow pellets aren't breaking away, one possibility is that leak has occurred and the punch is either frozen in place or has been damaged in attempting to propel a nitrogenic pellet.

A.5.6 Pellet testing

Formation and firing of pellets can be accomplished two ways: using the automated Labview system and MST triggering (as one would on a run day) or manually (though still utilizing the Labview program). For the former, the soak time can be shortened (a rule-of-thumb minimum is 20 s) in order to reduce testing time. For the latter, the process of opening and closing the various valves can be done by the Pelleteer using the the Labview program. Manifold pressures can be monitored using the Labview program as well. For pre-triggering and triggering, there are buttons on both the control rack and in the Labview program. The MST data system can be used for accumulating data from the microwave cavity, lightgates, and various pressure transducers, but an oscilloscope can be more efficient. All the data signals can be accessed from the the front of the control rack.

A.5.7 Pump maintenance

The injector's four roughing pumps require that the oil be changed regularly (not sure how regular – Steve O. claims monthly, but they've gone up to 12 months without one). The pumps use either 190 or 195 oil, but not 180.

1. Close off the volume on which the pump is working (except the gunbox - there's no way to close it off from it's pumps).

2. Power down any turbos in line with the roughing pump.

3. Once the turbo (if any) has spun down, turn off the roughing pump.

4. Disconnect the power to the roughing pump.

5. Disconnect the vacuum connection to the roughing pump.

6. Remove drain plug, empty oil into a container and then replace drain plug.

7. Open oil inlet and fill with clean oil.

8. Reconnect vacuum line.

9. Reconnect power and turn on.

10. Open to volume to be pumped, monitor pressure, and when low enough (less than 10 mTorr) turn on turbo (if any).

MST recycles old oil, but the drum in which it is kept tends to move around. Somebody will know where it is.

A.5.8 He compressor cooling system

Occasionally the chiller system will require a "top-off". When adding water (only use de-ionized water), do so by disconnecting one of the two water connections to the compressor (shown in Fig. A.15) and adding from there.

If the filters on the chiller are being changed, they can be closed off from most of the system and then replaced. Following replacement, it will probably be necessary to add water to the system.

Once in a great while, the helium compressor itself will need to be recharged. Talk to Steve O. – he did it the only time it was required during the author's tenure as MST Pelleteer.

A.6 Problems with injector

A.6.1 Past issues (and presumably solved/avoided)

Occasionally choosing the injector configuration for a day's run will require that changing of the power supply connections for the high speed valves and punches. It is imperative that when disconnecting the supplies that they be powered down before either end of the connection is severed. If not, upon reconnection the voltage reading will be zero regardless of knob orientation. The Pelleteer then has to power it down and back up again to get the proper reading. Also of note with the power supplies is that they are generally kept turned all the way up (reading should be in the 170 - 180 V range).

Early in pellet operation, the injector would be triggered by noise. This premature triggering was solved using a fiber optic trigger from MST and an optical receiver on the injector's end (Fig. A.21).

A leak was observed but not isolated in the slow feed fill (PV-101 or NV-101). The problem was avoided by rewiring the controller for PV-101 to actuate PV-201, and to set NV-102 to similar opening as NV-101. In essence, there's no longer a fast fill option for pellet formation. This hasn't proven to be a problem for the largest pellets.

A.6.2 On-going or Impending problems

The microwave cavity has yet to be absolutely calibrated. This would probably require the use of a known mass placed in the cavity. However, data exists on particle delivery to MST to correlate it with the cavity signal. The particle delivery has been measured both during a discharge (using integrated density profiles) and in vacuum (using the pressure increase as measured by a fast-ion gauge). Neither technique has been followed up on due

their own inherent difficulties. During discharges, particle confinement time is similar to the deposition time so particles are lost before the calculation is made. One shouldn't also forget the problem of making interferometry measurements close in time to the ablation (discussed in Chapter 2). As for the vacuum measurement, MST's vacuum system wasn't turned off during the tests, so it is possible that some material lost that way. Again a full study has yet to be done.

There appears to be a leak in the bellows that connect to the gunbox gate valves (they're located on the MST side of the lightgate station). Even with this problem the injector has operated fairly well. In fact the larger part of the data in this thesis was taken after the diagnosis of the leak. They weren't fixed because in order to access them, a portion of the injector would have to be removed - a sort of sheath covering the injection line and also serves a structural element in keeping everything in line. At some point however, it may prove too much, and the bellows will have to be replaced.

A.7 Pellet injector settings

Table A.2 contains the settings for the pellet injector used during the 2006 pellet campaigns. Target arrival times for the pellets were $t = 8 - 12\ ms$ for both high and low current discharges. For this target time, pellets would arrive before the onset on fluctuation reduction.

A.8 Tips 'n' Tricks

It was found (by accident) that if one dry-fires *i.e.* pulsed the propellant valve or punch between shots, the formation of a pellet during the next cycle was more reliable (it was

Table A.2: Pellet injector settings used for Pellet + PPCD campaigns of 2006. Start, arrival and trigger times are relative to MST firing time.

	0.2 MA	0.5 MA	
Pellet diameter	1.6 mm	1.6 mm	1.6 mm
Pellet length	3.2 mm	3.2 mm	4.0 mm
Propeller	punch	punch	H_2 gas
Propeller pulse width	25 ms	25 ms	3.5 ms
Propeller pulse height	$\sim$ 180 V	$\sim$ 180 V	$\sim$ 180 V
Propellant pressure	N/A	N/A	$\sim$ 1100 $p.s.i.$
Barrel soak time	60 s	120 s	
Barrel trigger time	-27 ms	-27 ms	5.5 ms
PPCD start time	10 ms	10 ms	

more likely that a pellet would be formed AND would break free). For the dry-fire, the experimenter can simply start the pre-fire sequence following the completion of the previous firing sequence, and then manually trigger the injector either by depressing the trigger button on the control rack or via the Labview program. No pellet is formed, but whichever barrels are in use will be "cleaned". It is believed (but not yet confirmed) that this technique is most useful for fast pellets and may be of limited benefit for the the slow pellets, but being superstitious, the routine persists.

Bibliography

[1] S. L. Milora, S. K. Combs, and C. R. Foust, Rev. Sci. Instrum. **57**, 2356 (1986).

And all this science I don't understand

It's just my job five days a week

Elton John

B

MST Gas Puff System User's Guide

B.1 The Veeco PV-10 Puff Valve

B.1.1 Characteristics

The Veeco PV-10 puff valve (depicted in Figures B.1, B.2, and B.5) is used for active fueling on MST. It consists of a piezoelectric crystal with a viton "pill" attached to its center. The pill rests against the valve's "volcano" creating a seal. When voltage is applied to the crystal, it retracts, pulling the pill with it and allowing gas to flow through the volcano into the valve's throat and out of the valve.

B.1.2 Testing and Troubleshooting

Occasionally a valve will fail (either open or closed). If it fails to open, the support screws (circled in Fig. B.2) can be tightened until it seals. If the valve fails to open, these same screws can be loosened until the valve leaks and then retightened. In both cases, the user

Figure B.1: Puff valve - side view with cover removed

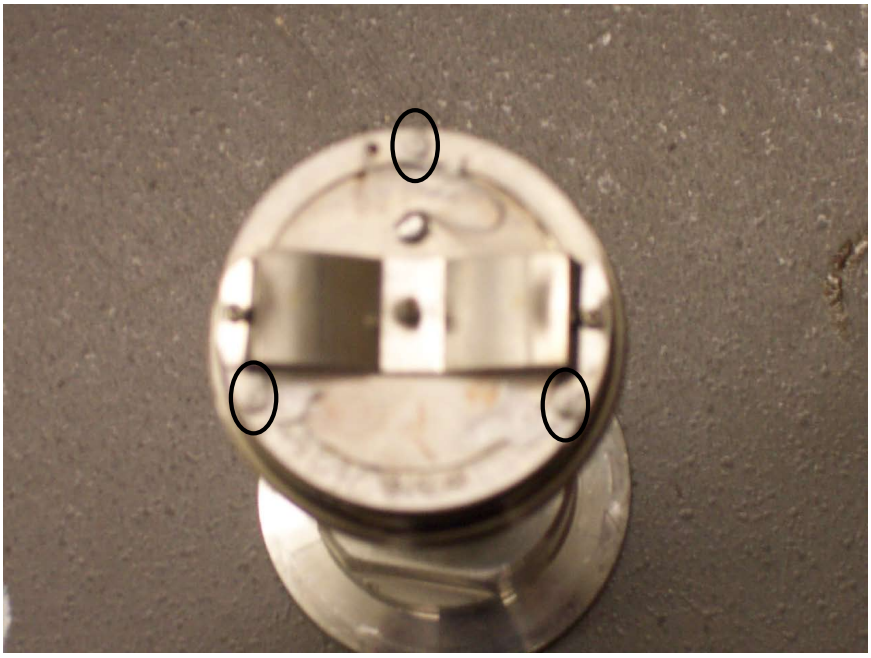

Figure B.2: Puff valve - top view

should then "crack test" the valve following failure.

In the crack test, a valve is connected to a leak checker. The gas input of the valve is left open to atmosphere. In fact the top half of the valve housing can be removed as shown in Figures B.1 and B.2. A variable source is connected to the valve's voltage input. This voltage source should be capable of producing $\sim$ 1 millisecond pulse-lengths with voltages up to 400 V.

The goal of the crack test is to get the valve to open for a one millisecond square pulse that is less than 100 V in amplitude. Once the valve is in place and the voltage source connected, the user should ensure the the valve has sealed and does not leak. If it leaks, tighten the support screws until the valve seals. The height of the crystal above the valve housing should be measured near each of the support screws to ensure evenness. The user then pulses the valve at successively lower voltages (starting at whatever voltage will be

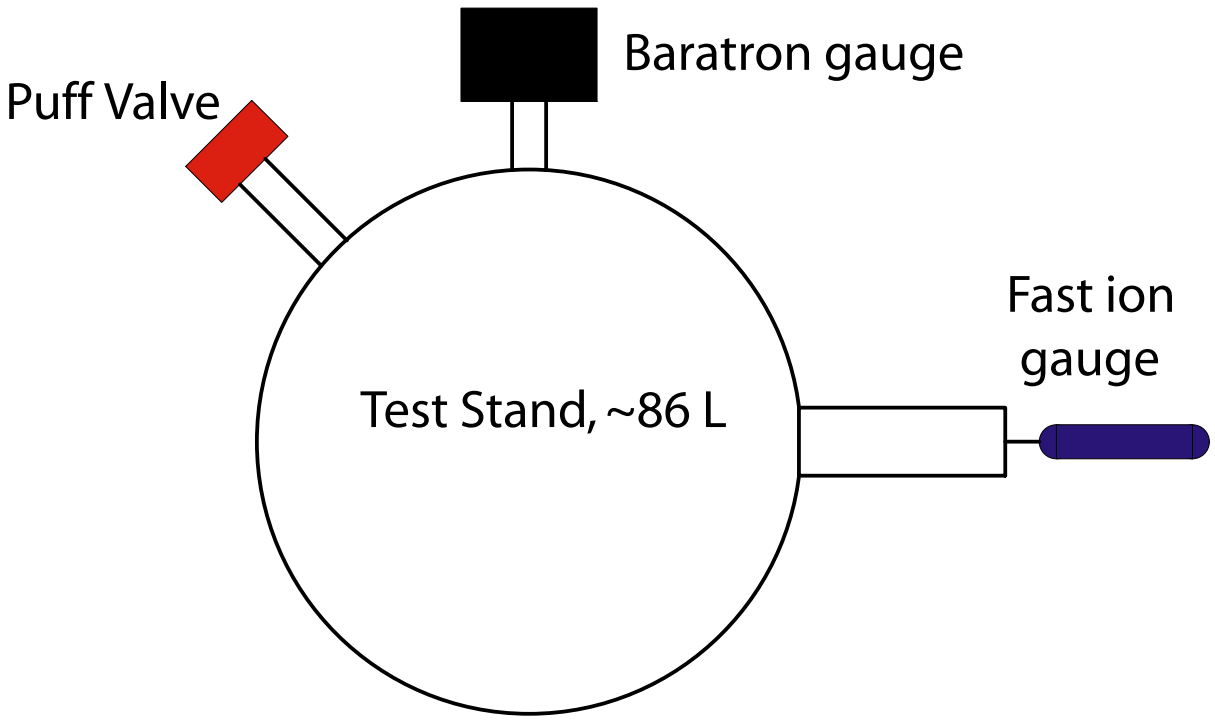

Figure B.3: Flow rate measurements and pressure rise characterizations of single valves were on done on the test stand

used to open it during fueling) until the minimum opening voltage is found. If this voltage is less than 100 V, the crack test is complete. If it's not, the support screws need to be loosened (eighth-of-a-turn increments are the standard) while maintaining the valve's seal. **Note: The power supply should be disconnected when loosening/tightening the support screws.**

The flow rate for a single valve is a measure of the average flow rate for a given square pulse (generally $\sim 10\ ms$). The valve can be attached to the MST test stand (Fig. B.3). Using a baratron gauge, the pressure before and after the gas puff was compared. The

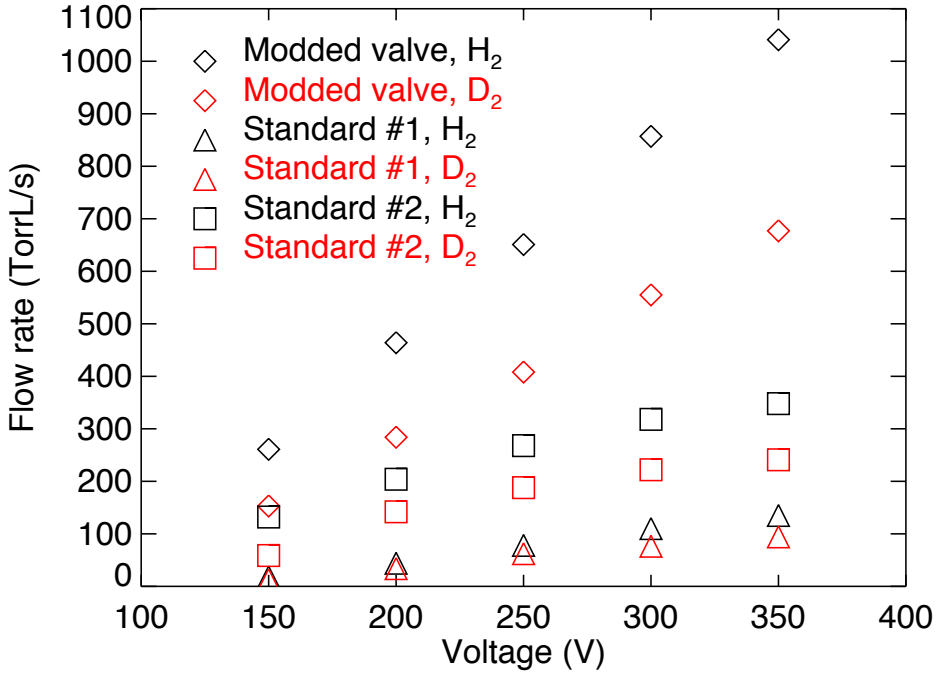

Figure B.4: Puff valve flow rate vs voltage and gas-type with 50 p.s.i fuel-line pressure

volume of the test stand is 86 L. Flow rates $< Q >$ are computed as:

$$< Q > = \frac{\Delta P \cdot V}{\Delta t} \tag{B.1}$$

For 9.9 ms pulse lengths, the flow rates at different voltages for two standard valves and the modified valve are shown in Figure B.4 for both deuterium and hydrogen gas.

B.1.3 Modifications

The modified valve had its throat bored out from the standard 0.019" to 0.042". It is also pulsed at a higher voltage (350 V) than the standard MST puff valve (150 to 250 V), resulting in an order of magnitude increase in flow. Even at the same voltage, the flow is

Table B.1: MST puff valve locations

Valve	Toroidal position	Poloidal Position
1	40°	−105°
2	60°	−135°
3	120°	−135°
4	180°	−135°
5	240°	−135°
6	300°	−135°
7	320°	−105°

improved several times, consistent with the increased throat diameter.

For the purposes of the testing and repairing, the modified valve operates the same as the standard valve. No changes in the crack test or leak checking procedure are necessary when dealing with the high throughput valve.

B.2 MST's Gas Puffing System

Active fueling of MST discharges is done with up to seven Veeco PV-10's spaced toroidally around the vacuum vessel (Table B.1). As valves fail occasionally the number used can fall, but currently stands at six. In the position of Valve #7 (Figure B.5), the high throughput valve has been placed. This occurred for two reasons: (1) Valves #1 and #7 are the easiest to access, and (2) Valve #7 failed during high voltage testing (Figure B.6). Average flow rates for a 10 ms puff for each valve in the MST puff system are show in Figure B.6.

Gas puffing during a discharge is controlled by a Labview program. The program splits the discharge into time windows of five and ten milliseconds. For the period between -20 and 60 ms, the increment is 5 ms. After 60 ms, the increment is 10 ms with the last puff

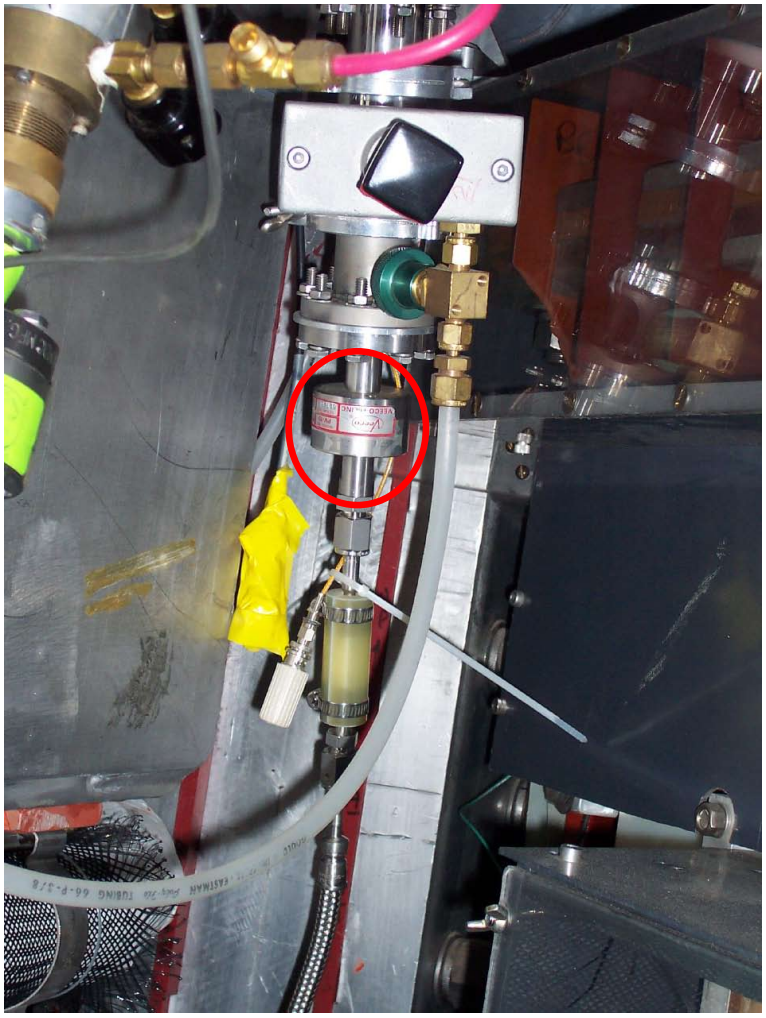

Figure B.5: Valve on MST

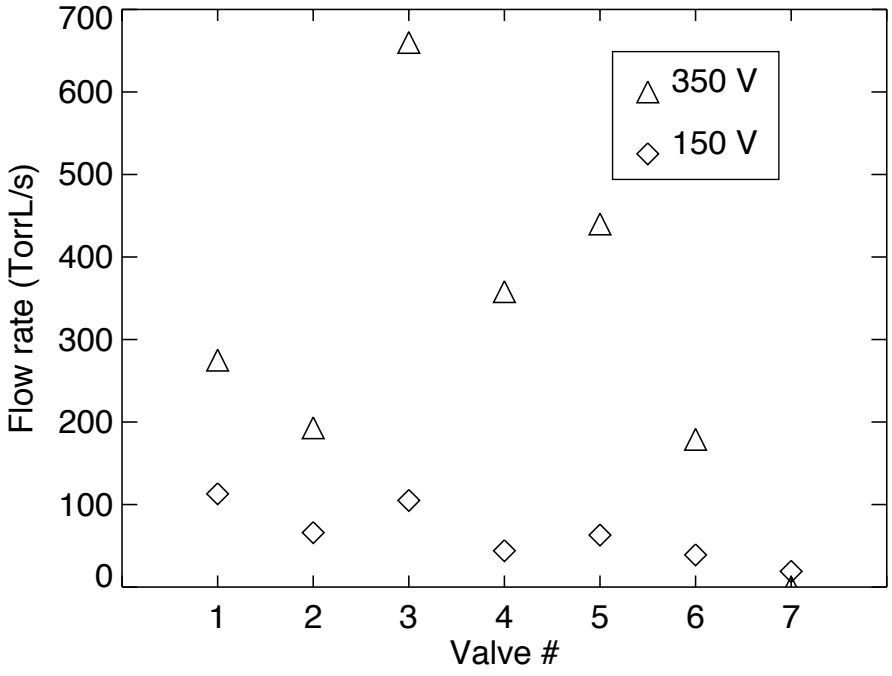

Figure B.6: MST valve flow rates at different voltages with 50 p.s.i fuel line pressure (D_2).

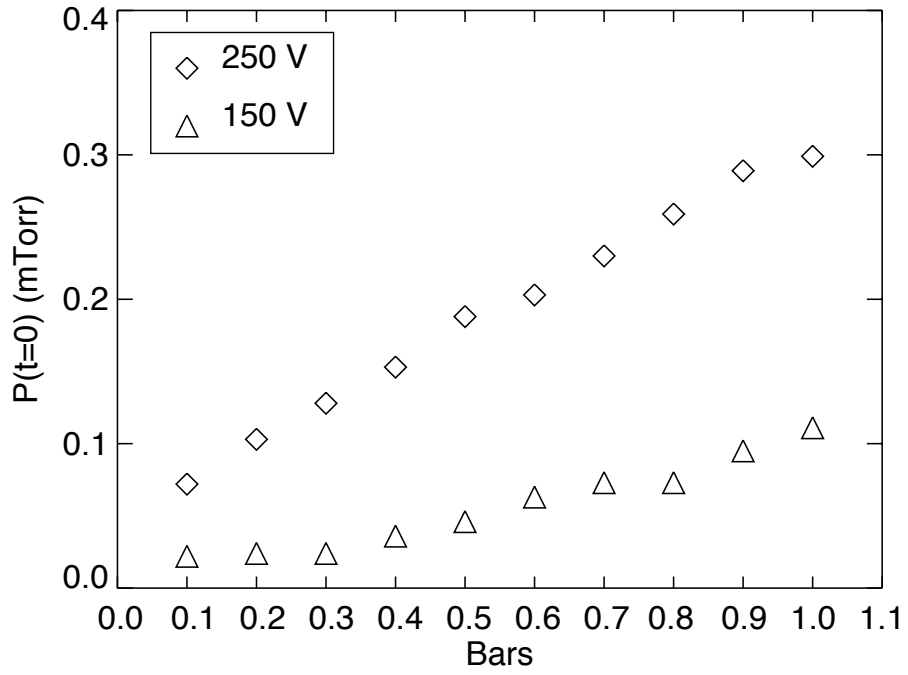

Figure B.7: MST fueling system output vs. pulse voltage at 50 p.s.i. The pressure is measured at the nominal time of the pulse (t = 0). The actual gas puff is programmed to begin at a time such that at the nominal time, the observed pressure rise will be one half of the maximum pressure rise due to the gas puff for a full bar.

at 90 ms. Each window is broken into 2.5 ms subdivisions. The valves can be opened with pulses that start at the beginning of the 2.5 ms subdivision and last the whole 2.5 ms or just some fraction thereof. A full 2.5 ms pulse is referred to as one "bar." In the 250 V pulsing of the valves currently used by MST, the puffing duration is incremented in twentieths of a bar, *i.e.*, the shortest pulse sent to the valves is 0.125 ms. In it's previous 150 V configuration, the pulse increment was 0.25 ms or one tenth of a bar. Figure B.7 shows the pressure rise in the MST vacuum vessel for different length gas puffs for the two pulsing configurations. At 250 V, the puff valve system's response remains linear for shorter gas puffs. For this reason and to gain finer control over the puffs due to the higher throughput at 250 V, the increment size was decreased.

Gas puffs begin several milliseconds before their nominal start time. This was done so that the half-height of the pressure increase was centered on the nominal start time. Figure B.8 shows the pressure rise in the MST vacuum vessel during two such gas puffs (one with the valves pulsed at 250 V, the other at 150 V). In each case the programmed start to the puff is $t = 0$ and lasts 5 ms. Significant pressure increases are seen by the fast ion gauge starting at $t = -6$ ms. The slow rise in pressure before the gas puff is attributed to some sort of leak as the pumps were closed off from the vacuum vessel during testing.

The Veeco PV-10 is limited to 50 p.s.i fuel line pressure. For the sake of completeness, the system throughput at different fuel line pressures was tested in the 250 V configuration (Fig. B.9). The 250 V with 10 p.s.i fuel line pressure has similar output to the 150 V with 50 p.s.i configuration.

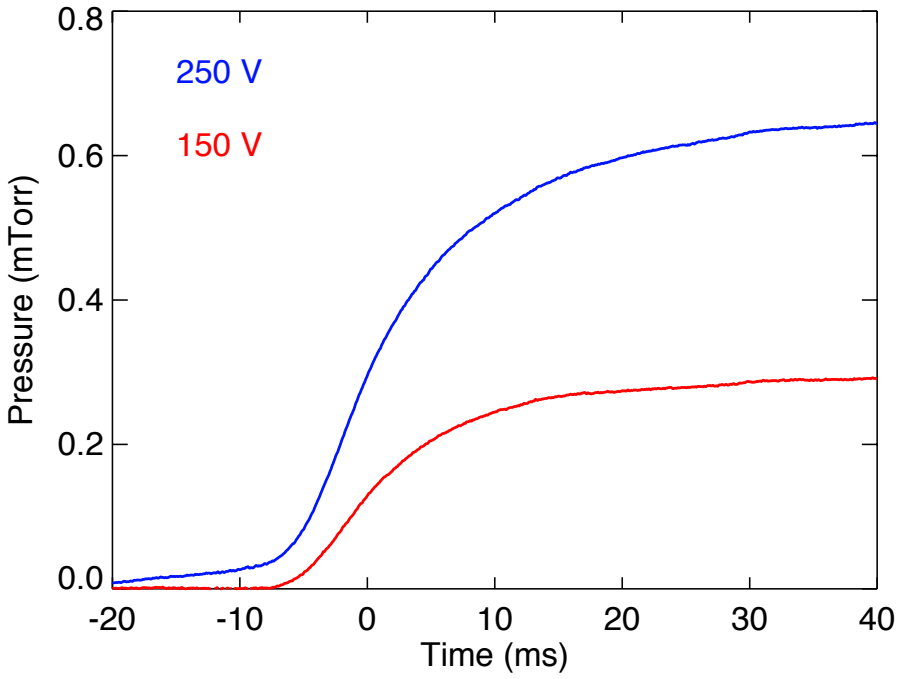

Figure B.8: Pressure rise due to a single gas puff (5 ms in duration) in MST as measured by a fast ion gauge. Shown are the 150 V and 250 V cases. Nominally the gas puff begins at $t = 0$ in both cases. The difference in pre-puff pressure is attributed to a change in leak rate of MST as the two puffs were carried out on separate days.

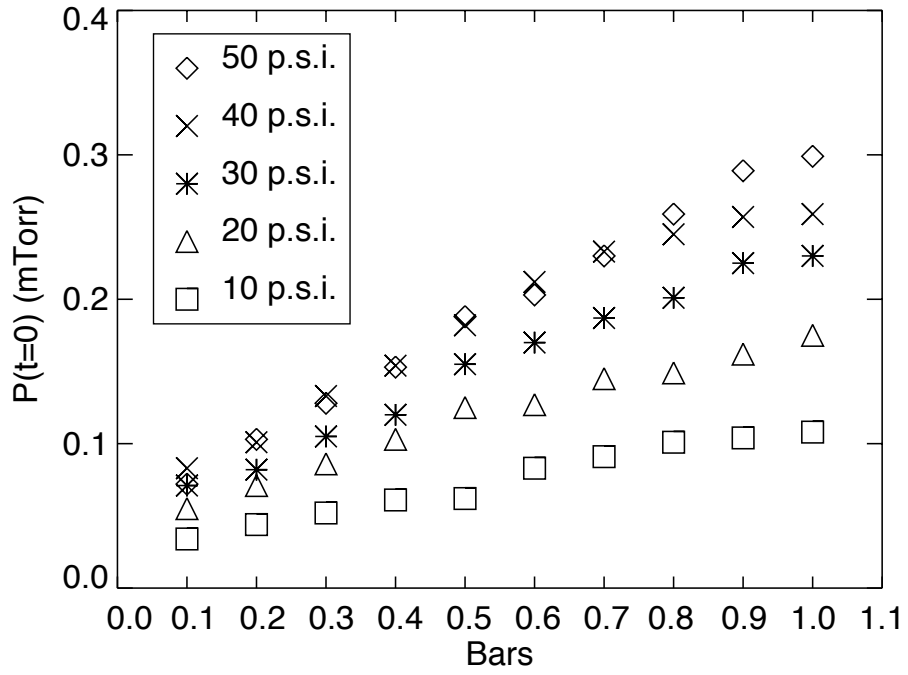

Figure B.9: MST fueling system output for varied fuel line pressures at 250 V. The pressure is measured at the nominal time of the pulse (t = 0). The actual gas puff is programmed to begin at a time such that at the nominal time, the observed pressure rise will be one half of the maximum pressure rise due to the gas puff for a full bar.